Electronic transport and secondary emission in a Hall thruster

Marc Chung To Sang

RÉPUBLIQUE FRANÇAISE
Liberté Égalité Fraternité

Université de Toulouse

Doctorat de l'Université de Toulouse

préparé à l'Université Toulouse III - Paul Sabatier

Transport électronique et émission secondaire électronique dans un propulseur de Hall

Thèse présentée et soutenue, le 2 juillet 2024 par

Marc CHUNG TO SANG

École doctorale
GEETS - Génie Electrique Electronique,Télécommunications et Santé : du système au nanosystème

Spécialité
Ingénierie des Plasmas

Unité de recherche
LAPLACE - Laboratoire PLAsma et Conversion d'Énergie

Thèse dirigée par
Laurent GARRIGUES et Sedina TSIKATA

Composition du jury
M. Gwenael FUBIANI, Président, CNRS Occitanie Ouest
M. Kentaro HARA, Rapporteur, Stanford University
M. Aaron KNOLL, Rapporteur, Imperial College London
M. Luc GIRAUD, Examinateur, Université de Bordeaux
M. Laurent GARRIGUES, Directeur de thèse, CNRS Occitanie Ouest
Mme Sedina TSIKATA, Co-directrice de thèse, Georgia Institute of Technology

Membres invités
M. Fabrice DELUZET, CNRS Occitanie Ouest

UNIVERSITÉ PAUL SABATIER TOULOUSE III

PHD THESIS

Electronic transport and electronic secondary emission in a Hall thruster

---

Author:
Marc CHUNG TO SANG

Supervisors:
Dr. Laurent GARRIGUES
Dr. Sédina TSIKATA

Examiners:
Committee president: Gwenael FUBIANI
"Rapporteur": Aaron KNOLL
"Rapporteur": Kentaro HARA
Committee member: Luc GIRAUD
Guest member: Fabrice DELUZET

A thesis submitted in fulfillment of the requirements for the degree of PhD in plasma engineering

in the

Groupe GREPHE
Laboratoire LAPLACE

July 2, 2024

Declaration on bibliographic methods

I wish to express here my choices regarding bibliographic methods. I am aware of the possible bias of searching for scientific documents and articles on a limited number of databases and through search engines. For this reason, I inform you that I have documented myself in the following ways:

- Through articles provided by my thesis supervisors.
- Through my queries on the search engines Google Scholar, Webofscience, Google.
- Through references in my Master 2 Plasma and Fusion Physics courses.
- Through references quoted in articles and PhD thesis of interest.
- By books available at the Bibliothèque Nationale de France in digital format.

It is quite possible that these databases do not include all the work done on Hall thrusters. It is also likely that many works written in languages other than French and English have not been referenced on the above-mentioned search engines. Finally, given the vast amount of scientific content on this type of thruster, it is possible that some references may have been missed. My choice of quotations is guided by the need to develop a logical and documented reasoning. Consequently, it is not intended to be exhaustive.

À mes parents, ma soeur, ma famille, et à celle qui depuis trois ans épanouit mon coeur.

To those who will take the trouble to read me and make this thesis something other than a grimoire destined for the archives.

UNIVERSITÉ PAUL SABATIER TOULOUSE III

Abstract

École Doctorale GEETS
Laboratoire LAPLACE

PhD in plasma engineering

Electronic transport and electronic secondary emission in a Hall thruster

by Marc CHUNG TO SANG

The boom in satellite space activities has led to the development of numerous electric thruster technologies. Among these, the Hall current thruster is attracting growing interest due to its cost, thrust and specific impulse characteristics. Although this technology has been around for at least fifty years, simulating and understanding its operation remains out of reach. The dynamics of charged particles in the ExB cross-field configuration are rich in instabilities whose role in thruster operation has not yet reached scientific consensus. In this thesis, we propose to take up the "Particle-in-cell" (PIC) approach, which consists in tracking the individual trajectories of charged particles in phase space subjected to an electric field that is a solution of Poisson's equation and calculated on a computational grid. In its explicit version, this numerical method has to meet space and time step constraints that harden with increasing electron density. In three spatial dimensions, the classical PIC algorithm cannot be applied to real thruster conditions. A recent approach, called "Sparse-PIC", circumvents this problem by means of sparse grid methods. It is based on the principle of cancelling grid errors when combining coarse-mesh sub-grids to represent the solution on the fine-mesh grid. The computational performance obtained with the code implemented during the thesis has enabled us to apply this new approach to an ExB cross-field configuration in a reduced Hall thruster model.

Acknowledgements

I would like to extend my warmest thanks to the LAPLACE PhD students and researchers with whom I was able to hold interesting discussions on a wide range of subjects, in particular Clément Guillet on the Sparse method, Gerjan Hagelaar on kinetic approaches, Olivier Pascal on electromagnetic waves in plasma, Gwenaël Fubiani, and many others. These three years were also an opportunity to meet the research teams at the ICARE laboratory, to see the installations on the PIVOINE test facility and the experiments conducted by Thibault Dubois under the supervision of my thesis co-director Sedina Tsikata. I had a great time at the IEPC conference in Boston in June 2022 with teams from CNES, ONERA, start-ups, Stéphane Mazzoufre's team and ICARE PhD students. I would like to thank my thesis supervisors Laurent Garrigues and Sédina Tsikata for the fascinating discussions surrounding the vast subject of Hall thrusters. Finally, I would like to thank CALMIP, GENCI, ENS Paris-Saclay and the French Ministry of Research and Innovation, respectively for allocating computing hours on the OLYMPE and Jean-Zay supercomputers, and for funding my thesis.

Contents

List of Figures

List of Tables

List of Abbreviations

I_{sp}	**Sp**ecific **I**mpulse
SERT II	**S**pace **E**lectric **R**ocket **T**est **II**
ESA	**E**uropean **S**pace **A**gency
LIF	**L**aser **I**nduced **F**luorescence
CTS	**C**ollective **T**homson **S**cattering
ITS	**I**ncoherent **T**homson **S**cattering
JANUS	**J**oint **A**dva**N**ced Prop**U**lsion In**S**titute
PEM	**P**redictive **E**ngineering **M**odel
PIC	**P**article-**I**n-**C**ell
OpenMP	**O**pen **M**ulti-**P**rocessing
MPI	**M**essage **P**assing **I**nterface
BM	**B**reathing **M**ode
ITTI	**I**on **T**ransit **T**ime **I**nstability
ECDI	**E**lectron **C**yclotron **D**rift **I**nstability
MTSI	**M**odified-**T**wo-**S**tream **I**nstability

Physical Constants

Speed of light	$c_0 = 2.997\,924\,58 \times 10^{8}\,\mathrm{m\,s^{-1}}$
Vacuum permittivity	$\epsilon_0 = 8.854\,187\,82 \times 10^{-12}\,\mathrm{F\,m^{-1}}$
Boltzmann constant	$k_B = 1.380\,649 \times 10^{-23}\,\mathrm{J\,K^{-1}}$
Quantum of charge	$e = 1.602\,176 \times 10^{-19}\,\mathrm{C}$
Vacuum magnetic permeability	$\mu_0 = 4\pi \times 10^{-7}\,\mathrm{H\,m^{-1}}$

Chapter 1

Introductory concepts

1.1 The Hall current thruster

1.1.1 Elements of history

The Hall thruster was developed during the 20th century as one of several types of electric thruster. A documented article on the history of electric space propulsion can be found in (Choueiri, 2004). Edgar Y. Choueiri sees five periods of development. He calls the first the era of visionaries between 1906 and 1945. It is marked by the inescapable personality of K. E. Tsiolkovsky (1857-1935) who gave his name to the equation linking the acceleration of a vehicle to the ejection of matter, and therefore of charged matter as well (Tsiolkovsky, 1903). This period marks the beginnings of aerospace, and the principles of electric propulsion for space propulsion purposes are discussed. At the time, interest in accelerating charged particles in order to increase the momentum of ejected matter was conceptualized.

The second period is known as the pioneering era, from 1946 to 1956. This was the crucial moment when the practical foundations of electric propulsion were laid, with the anticipation of certain technical constraints. The increase in on-board mass due to the need for electric power to achieve high ejection speeds is highlighted, in comparison with the mass of fuel required to produce high thrust at slow ejection speeds. This ratio is considered favorable to electric propulsion for maneuvers in stable orbits and in the vacuum of space. It is also considered desirable to use atoms with a high atomic mass, preferring high voltages to high currents. Finally, it is recognized that neutralization of the ion flow by electrons produced by an emissive cathode or other sources is essential. E. Stuhlinger (1913-2008) deeply anchored the study of electric propulsion in the United States with his publications demonstrating the importance of specific power, defined as the ratio of output power to total mass. He also showed that there is an optimum ejection velocity also equivalent to an optimum specific impulse I_{sp} defined as the ratio of ejection velocity v_e to standard gravity g_0 ($I_{sp} = \frac{v_e}{g_0}$) for a given specific power and mission type. It should be noted that most of the works focused primarily on the feasibility of electric propulsion, and less on the purely technical aspects.

Edgar Y. Choueiri then distinguishes an era of diversification and development between 1957 and 1979, during which the Hall thruster was born, and an era of acceptance of these new technologies between 1980 and 1992. He sees the current era as one of application, with electric propulsion systems becoming increasingly common in near- and far-Earth space. However, the 1979 date is not justified in this first

article (Choueiri, 2004). The rest of the article does not seem to have been published, though it is possible to trace it back to the report on the SERT II mission (Space Electric Rocket Test II) (KERSLAKE and IGNACZAK, 1979). This mission used a gridded ion thruster, more popular in the United States of America at the time than the Hall thruster. This type of thruster is based on the electrostatic acceleration of ions through two grids to which a voltage is applied (cf. Figure 1.1). The report refers to successful start-up and operation cycles after nine years in space. The thruster operated for 600 hours, with only eight electrical arcs observed. It should be noted that the time required to start up the thruster, i.e. to create the plasma discharge (a combination of ions and free electrons), eject the first ions and reach nominal thrust is around 15 minutes, which exceeds mission expectations. This also means that a ground-based operator or maneuvering algorithm must take into account a delay between the thruster ignition command and its actual operation. Erosion of the cathode is not considered critical for the thruster, contrary to tests carried out on the ground. Finally, the system's gas leakage losses were kept to very low levels, underlining the importance of the thruster's mechanical design. The success of these tests in the space environment has demonstrated the reliability of these electric propulsion systems for space missions. The era of acceptance referred to by Edgar Y. Choueiri seems to have come to an end with the involvement of the Europeans, through ESA and its EURECA mission launched in 1992, in their very first electric propulsion test in the space environment (Bassner et al., 1994). It was also the very first test called RITA of a radio-frequency ionization electric thruster. The performance observed during the 240 hours of operation corresponds to the tests carried out on the ground, and no effect of the thruster is observed on the rest of the spacecraft. However, the tests ended with the appearance of an electrical arc as the spacecraft passed through a zone known as the "South African anomaly", some 100 km from the Earth's surface, where high-intensity radiation appears to be approaching the Earth. Attempts to restart the engine were unsuccessful, concluding the series of tests. The report's conclusions also mention the importance of these tests as a first step towards a marketable electric propulsion system.

It is interesting to note that electric propulsion was first conceived and designed for manned interplanetary travel, for man's quest for the infinite and for what lies beyond the Earth. Its industrialization, however, was motivated by far more pragmatic motives for maneuvering satellites in near-Earth orbits. Its use for probes exploring the solar system remains the only application close to its initial objective, before perhaps its use for manned Earth-Moon and Mars journeys.

1.1.2 Component parts

The Hall current thruster can be described in terms of its four main components, apart from the power supply needed to maintain its operation. Figure 1.2 shows the distribution of these elements on a PPS-1350ML type thruster:

- Two electrodes, the anode located at the bottom of the thruster channel where the gas to be ionized is also injected, and the cathode on the outside for this model which produces the electrons neutralizing the ion beam as well as the

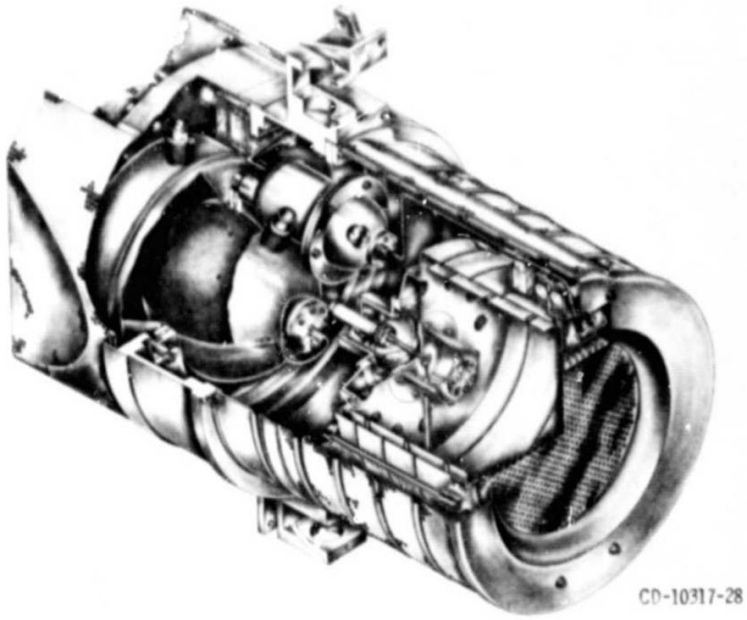

Figure 2. - SERT II Ion Thruster.

FIGURE 1.1: Scheme of an ion gridded thruster used during mission SERT II, after report of the 14^{th} international conference of electric propulsion (SERT II 1979 EXTENDED FLIGHT THRUSTER SYSTEM PERFORMANCE, KERSLAKE and IGNACZAK, 1979).

primary electrons for the discharge. A voltage of around 200-300V is imposed between these two electrodes to produce an axial electric field.

- Walls coated with a dielectric material, in this case boron nitride-silicon dioxide ($BN - SiO_2$), to insulate the rest of the thruster and prevent a too great loss of electrons to the walls.
- External and internal coils within a ferromagnetic circuit to produce a magnetic field conventionally considered radial.

It should also be noted that, in addition to the elements required for its physical operation, the thruster also needs a mechanical design that is sufficiently resistant to vibration during orbiting and operation. The design of its ferromagnetic circuitry can also quickly become complex, and plays an important role in the magnetic field profile (Vilamot, 2012).

1.1.3 Operation principles

The commonly accepted idea behind the Hall current thruster is to maintain a voltage between the two electrodes to create an accelerating electric field in the axial

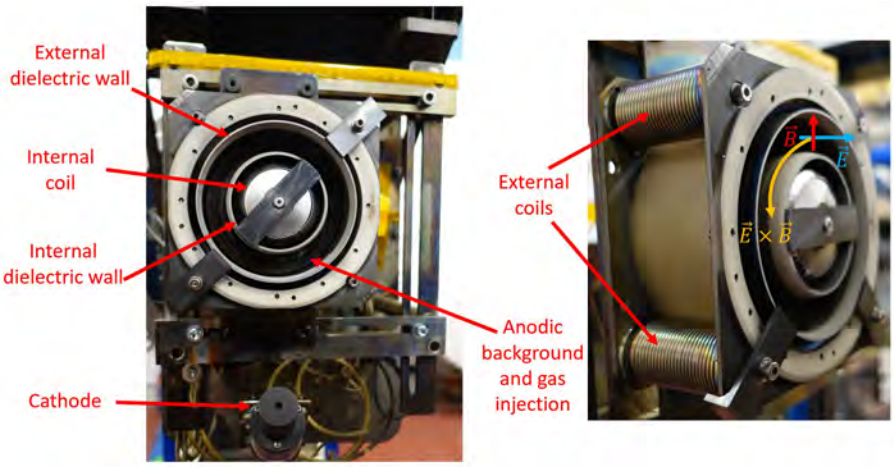

FIGURE 1.2: Main components of a PPS-1350ML Hall thruster (Pictures taken during the test campaign on PIVOINE in January 2021).

direction (see Figure 1.2). The radial magnetic field, strong enough to magnetize electrons but weak enough to consider non-magnetized ions, allows electrons to drift in the ExB azimuthal direction (a current similar to the Hall current) to increase their residence time. These cathode-produced electrons are then heated in the magnetic field zone by the accelerating electric field, giving them sufficient energy to ionize the injected gas - a heavy, easily ionized species, usually xenon. The electrons produced by ionization also follow an azimuthal drift and play a part in ionization. A third source of electrons can be considered when particles collide with the walls, producing secondary electron emission (Villemant, 2018). The ions thus produced are accelerated by the axial electric field, neutralized by the cathode electrons, and produce the desired thrust.

1.1.4 Characteristics

A tour of the thrusters marketed by the main companies will enable us to define an order of magnitude of the specific impulse, thrust and electrical power characteristics of today's thrusters. Specific impulse gives an idea of the efficiency of fuel consumption. The higher the specific impulse, the higher the ejection velocity at the thruster exhaust for a given mass of fuel. Thrust is a parameter linked to mission acceleration requirements. Electrical power gives an idea of the mass of the associated power supply. We can distinguish between low-power thrusters of between 100 and 1000 W, with a specific impulse of between 1000 and 1500 s, and thrust between a few mN and 75 mN, and higher-power thrusters from 1 kW to several tens of kilowatts whose specific impulse varies between 1500 and 2700 s, and thrust between 75 mN and 1 N. All these thrusters are designed to be as compact as possible. The main difference between low-power and high-power thrusters is the use of an external cathode for the former, and a cathode integrated into the centre of the thruster for the latter. The integration of a cathode in the center of the thruster offers a gain in efficiency (Hofer, Gallimore, and Jacobson, 2003; Sommerville and King, 2007;

McDonald and Gallimore, 2009) but is difficult to adapt to small thrusters. We also note that permanent magnets, which are more compact than coils, are only used for low-power thrusters. The difference in magnetic configuration between permanent magnets and coils could be one of the reasons for the use of coils for higher-power thrusters, despite their greater volume. In particular, the magnetic field of the permanent magnets may not penetrate the channel sufficiently as its size increases. In addition, the number of coils increases with the power of the thrusters, suggesting a more significant role for the magnetic field at high power, and in particular its uniformity along the azimuthal direction. Another explanation is the flexibility provided by coils, which enables the magnetic field strength to be varied according to the current flowing through them. The risk of demagnetization of permanent magnets in the case they reach Curie temperature in the space environment could also be a factor. The dielectric material used for the walls is usually boron nitride BN, possibly combined with silicon dioxide $BN - SiO_2$. This choice of material is guided by the desire to reduce the discharge current (Taccogna and Garrigues, 2019, Figure 6 in the review) to optimize the thruster's power consumption.

1.1.5 Recent developments

The subject of Hall current thrusters is vast, and a number of syntheses of previous work can be found, all of them complementary to each other. In particular, there are reviews focusing on the Hall thruster, including recent experimental data on the consequences of electronic secondary emission linked to dielectric walls (Adam et al., 2008; Boeuf, 2017; Hara, 2019; Taccogna and Garrigues, 2019). These reviews highlight the presence of instabilities at kHz and MHz frequencies in these thrusters and their experimental characterization. Details of cathode technologies (hollow cathode, radio-frequency, carbon nanotube or simple heated filaments) and micro-propulsion applications can be found in Levchenko et al., 2018. Levchenko et al., 2020 puts the Hall current thruster in context among other electric propulsion technologies. Kaganovich et al., 2020 and Boeuf and Smolyakov, 2023 focus on the modeling of ExB cross-field configurations that apply notably to the Hall thruster and the magnetron. A didactic and detailed category-by-category introduction to the physics of the Hall thruster can also be found in W. Villafana's recent thesis (Villafana, 2021, Chapter 1). The main points are as follows:

- The classical thruster structure was fixed during the development era between 1956 and 1979, but oscillations and turbulence were observed during Hall current thruster operation. Since then, modeling work has focused on studying, characterizing and understanding these instabilities.
- Comparisons between theoretical and numerical models, and the results of experimental diagnostics, show that the models are not yet sufficiently predictive to accurately describe thruster behavior, but offer good orders of magnitude.
- The complexity of physical phenomena and material configurations is difficult to take into account in its entirety, but recent numerical simulation work is working in this direction (JANUS team within a PEM environment, Wirz et al., 2022, Code AVIP, Joncquières, 2019; Villafana, 2021).

- The use of laser diagnostics by incoherent Thomson scattering (ITS) completes the list of experimental diagnostics applied to the thruster among Langmuir probes, laser diagnostics by "Laser Induced Fluorescence" (LIF) and "Collective Thomson Scattering" (CTS) and antennas. Incoherent Thomson scattering measurements provide access to electronic properties such as density, temperature and drift velocity (Vincent, Tsikata, and Mazouffre, 2020).
- The recent use of antennas to diagnose thruster plasmas at GHz (Mazières et al., 2022) frequencies opens the field to reflections on plasma radiation at these frequencies.
- The barriers to be overcome are theoretical, with developments often based on linear theory, but whose applications are linked to strong plasma perturbations; numerical, with the development of numerical methods that are less costly in terms of computing time, while satisfying the physics equations as closely as possible; and experimental, with the development of methods for better probing of the plasma, and in particular the inside of the thruster channel.

1.2 System of equations of the studied plasma

Which physics are we studying? From coulombic interactions between particles to the notion of mean electric field. From singular events associated with elastic and inelastic collisions to kinetic models in which these events are viewed statistically. From the complexity of particle distribution functions in the space of positions and velocities to the fluid moments resulting from integration in the space of velocities. The approach adopted here is similar to a hybrid point of view, which is the basis of so-called Particle-In-Cell (PIC) simulations. A number of equations are introduced which also take part in the algorithm and the interpretation of results.

1.2.1 Bolztmann - Vlasov equation with collisions

The positions and velocities of particles of a α species over time form a distribution function $f_\alpha(\vec{r},\vec{v},t)$ defined as the number of particles in position space $(\vec{r},\vec{r}+d\vec{r})$ and velocity space $(\vec{v},\vec{v}+d\vec{v})$ at an instant t (continuity approximation). In an electromagnetic field $\vec{E}$ and $\vec{B}$, this distribution function verifies the Vlasov equation with collisions where $C[f_\alpha, f_\beta, ...]$ is a collision term which depends on the type of collisions considered and which may depend on the distribution function of other species (See chapter 4 in Rax, 2005 for different types of collisions):

$$\frac{\partial f_\alpha}{\partial t} + \vec{v}\frac{\partial f_\alpha}{\partial \vec{r}} + \frac{q_\alpha}{m_\alpha}(\vec{E} + \vec{v}\times\vec{B})\frac{\partial f_\alpha}{\partial \vec{v}} = C[f_\alpha, f_\beta, ...] \tag{1.1}$$

where q_α is the charge of a particle of the species α, m_α its mass.

1.2.2 Fluid equations

Integration of the equation (1.1) multiplied by a $\vec{v}^n$ term in velocity space gives the nth fluid moment. The steps leading to the different fluid moments can be found in Melzani, 2017; Lapenta, 2012. The particle density is also defined as:

$$n_\alpha(\vec{r},t) = \iiint_{-\infty}^{+\infty} f_\alpha(\vec{r},\vec{v},t)d^3\vec{v}$$

the mean velocity:

$$\vec{V}_\alpha(\vec{r},t) = \frac{\iiint_{-\infty}^{+\infty} \vec{v} f_\alpha(\vec{r},\vec{v},t)d^3\vec{v}}{n_\alpha(\vec{r},t)}$$

and mean kinetic energy:

$$E_{c\alpha}(\vec{r},t) = \frac{m_\alpha \iiint_{-\infty}^{+\infty} \vec{v}.\vec{v} f_\alpha(\vec{r},\vec{v},t)d^3\vec{v}}{2n_\alpha(\vec{r},t)}$$

For our numerical diagnostics, we consider the fluid moments of the first three orders involved in fluid simulations (Hakim, 2008; Dong et al., 2019).

The 0-order fluid moment is the continuity equation for particle density:

$$\frac{\partial n_\alpha}{\partial t} + div(n_\alpha \vec{V}_\alpha) = \iiint_{-\infty}^{+\infty} C[f_\alpha, f_\beta, ...]d^3\vec{v} \tag{1.2}$$

The first-order fluid moment is the continuity equation of the particle flow, in the direction $i \in [\![1;3]\!]$:

$$\frac{\partial(n_\alpha V_i)}{\partial t} + \sum_{l=1}^{3} \frac{\partial \Pi_{i,l}}{\partial r_l} = \frac{n_\alpha q_\alpha}{m_\alpha}(E_i + \sum_{l=1}^{3}\sum_{\substack{m=1 \\ m\neq l}}^{3} \epsilon_{i,l,m} V_l B_m) + \iiint_{-\infty}^{+\infty} v_i C[f_\alpha, f_\beta, ...]d^3\vec{v} \tag{1.3}$$

where Π is a second-order tensor whose terms are equal to $\Pi_{i,j} = \iiint_{-\infty}^{+\infty} v_i v_j f_\alpha d^3\vec{v}$ for $(i,j) \in [\![1;3]\!]^2$

This tensor contains the inertia and pressure terms for a given species α.

And with $\epsilon_{i,l,m} = \left\{ \begin{array}{ll} 0 & \textit{if at least two indexes are identical} \\ 1 & \textit{if } i,l,m = 1,2,3 \textit{ or any other even permutation} \\ -1 & \textit{if } i,l,m = 2,1,3 \textit{ or any other odd permutation} \end{array} \right\}$

The second-order fluid moment is the heat flow continuity equation, for coefficient $(i,j) \in [\![1;3]\!]^2$:

$$\frac{\partial \Pi_{i,j}}{\partial t} + \sum_{l=1}^{3} \frac{\partial Q_{i,j,l}}{\partial r_l} = \frac{q_\alpha}{m_\alpha}(n_\alpha V_{[i} E_{j]} + \sum_{l=1}^{3} \sum_{\substack{m=1 \\ m \neq l}}^{3} (\epsilon_{i,l,m} \Pi_{l,j} + \epsilon_{j,l,m} \Pi_{l,i}) B_m) + \iiint_{-\infty}^{+\infty} v_i v_j C[f_\alpha, f_\beta, ...] d^3\vec{v} \tag{1.4}$$

where Q is a third-order tensor whose terms are equal to $Q_{i,j,k} = \iiint_{-\infty}^{+\infty} v_i v_j v_k f_\alpha d^3\vec{v}$ for $(i,j,k) \in [\![1;3]\!]^3$

and where $V_{[i} E_{j]} = V_i E_j + V_j E_i$

1.2.3 Maxwell's equations

The electromagnetic field is solved by Maxwell's equations in a vacuum in the presence of sources. Noting ϵ_0 the permittivity of vacuum, μ_0 the magnetic permeability in vacuum, indexes "i" and "e" respectively for ions and electrons, Z the charge number of the ion species, e the quantum of charge, we have:
The Maxwell-Flux equation:

$$div(\vec{B}) = 0 \tag{1.5}$$

The Maxwell-Gauss equation:

$$div(\vec{E}) = \frac{(Zn_i - n_e)e}{\epsilon_0} \tag{1.6}$$

The Maxwell-Faraday equation:

$$\vec{rot}(\vec{E}) = -\frac{\partial \vec{B}}{\partial t} \tag{1.7}$$

The Maxwell-Ampère equation:

$$\vec{rot}(\vec{B}) = \mu_0(\vec{J} + \epsilon_0 \frac{\partial \vec{E}}{\partial t}) \tag{1.8}$$

where $\vec{J} = Zn_i e\vec{V_i} - n_e e\vec{V_e}$

These equations can be reorganized into two wave equations:

$$\Delta\vec{E} - \frac{1}{c^2}\frac{\partial^2 \vec{E}}{\partial t^2} = \vec{\nabla}\left(\frac{(Zn_i - n_e)e}{\epsilon_0}\right) + \mu_0 \frac{\partial \vec{J}}{\partial t} \tag{1.9}$$

$$\Delta\vec{B} - \frac{1}{c^2}\frac{\partial^2\vec{B}}{\partial t^2} = -\vec{rot}(\mu_0\vec{J}) \tag{1.10}$$

where $c = \sqrt{\frac{1}{\mu_0\epsilon_0}}$

The fact that $div(\vec{rot}\vec{B}) = 0$ and that $\vec{rot}(\vec{grad}) = \vec{0}$ leads to introduce the vector potential $\vec{A}$ so that $\vec{B} = \vec{rot}\vec{A}$ and the scalar potential Φ so that $\vec{E} = -\vec{\nabla}\Phi - \frac{\partial\vec{A}}{\partial t}$.

Both potentials require an additional condition to be uniquely defined. If we consider the Lorentz gauge $div(\vec{A}) + \frac{1}{c^2}\frac{\partial\Phi}{\partial t} = 0$, we can obtain two other wave equations for vector and scalar potentials:

$$\Delta\vec{A} - \frac{1}{c^2}\frac{\partial^2\vec{A}}{\partial t^2} = -\mu_0\vec{J} \tag{1.11}$$

$$\Delta\Phi - \frac{1}{c^2}\frac{\partial^2\Phi}{\partial t^2} = -\frac{(Zn_i - n_e)e}{\epsilon_0} \tag{1.12}$$

1.2.4 The electrostatic approach

Tools derived from the theory of electromagnetism are discussed in Jackson, 1999. In particular, the notion of an average electromagnetic field made up of a set of photons is introduced (See its introduction). Electrostatism is presented via experiments to determine the expression of the coulombic force and electric field created by a charged particle, and the generalization of this field to several particles, with the introduction of the notion of charge density. Magnetostatism is presented by introducing Biot and Savart's law relating the magnetic induction field to the current of charged particles in steady state. These notions in the static regime can be applied to the case of the Hall current thruster. Here, we discuss its application within the system of Maxwell's equations presented earlier for the Hall thruster.

The electrostatic approach assumes that electric field generation by time variation of the magnetic induction field is zero, and that magnetic field generation by displacement and polarization currents is also zero. The first case implies that $\frac{\partial\vec{B}}{\partial t} = -\vec{rot}(\vec{E}) = \vec{0}$. The second case implies that $\vec{rot}(\vec{B}) = \vec{0}$. Note that the second condition implies the first if the external magnetic field is also static. This is justified if the magnetic field $\vec{B}_{Hall}$ induced by the Hall current in the thruster is negligible compared with the static external magnetic field $\vec{B}_{ext}$ imposed by means of coils or permanent magnets, $\frac{||\vec{B}_{Hall}||}{||\vec{B}_{ext}||} \ll 1$. In the case of the Hall current thruster, we have $||\vec{B}_{ext}|| \approx 150G$ and $||\vec{B}_{Hall}||$ of the order of a few Gauss according to Garrigues, Mazouffre, and Bourgeois, 2012. Maxwell's equation system then reduces more simply to solving the Maxwell-Gauss equation (1.6), which is equivalent to solving the following Poisson's equation:

$$-\Delta\Phi = \frac{(Zn_i - n_e)e}{\epsilon_0} \tag{1.13}$$

where $\vec{E} = -\vec{\nabla}\Phi$.

1.2.5 Newton-Lorentz's equation

We consider the non-relativistic dynamics of particles (in this case, ions and electrons) in a mean electromagnetic field, using the Newton-Lorentz's equation. For each species of particle α of mass m_α and charge q_α, the relation linking the variation of the momentum of a particle $m_\alpha \vec{v_\alpha}$ to the electromagnetic field $\vec{E}$ and $\vec{B}$ is:

$$m_\alpha \frac{d\vec{v_\alpha}}{dt} = q_\alpha(\vec{E} + \vec{v_\alpha} \times \vec{B}) \tag{1.14}$$

The static approach defined above, coupled with particle dynamics according to the Newton-Lorentz's equation, is the foundation of the electrostatic PIC algorithm presented in Chapter 2. This approach must represent an evolution of the electronic and ionic distribution functions according to the Boltzmann/Vlasov equation (1.1). The system of equations thus posed nevertheless raises several questions. What is the link between a view of the electric field based on coulombic interactions between particles and a view of the electric field based on continuous charge density? In other words, noting N the number of particles with respective charge q_i and position $\mathbf{r}_i$, when can we say that $\vec{E}(\mathbf{r}) = \sum_{i=1}^{N} \frac{q_i(\mathbf{r}-\mathbf{r}_i)}{4\pi\epsilon_0||\mathbf{r}-\mathbf{r}_i||^3}$ is equivalent to $\oiint \vec{E}.d\vec{S} = \iiint \frac{\rho}{\epsilon_0} d^3\vec{r}$? A first answer might be to consider that coulombic collisions are sufficiently rare in the Hall current thruster plasma to be able to neglect interactions within a Debye sphere. The Rutherford scattering model taken from Rax, 2005 (Chapter 4) gives an electron-ion collision frequency of the order of 10 kHz for an electron temperature of 50 eV and an electron density of $10^{17} m^{-3}$, to be compared with a plasma frequency of the order of 2.8 GHz:

$$f_{pe} = \frac{1}{2\pi}\sqrt{\frac{n_e e^2}{\epsilon_0 m_e}} \tag{1.15}$$

where n_e is the electron density. The electric field can therefore be smoothed a priori to represent only the superposition of the distant fields created by the charged particles, thus avoiding singularities at the particle positions. To be more precise, orders of magnitude are calculated for the plasma in the thruster's acceleration zone (See Boeuf and Smolyakov, 2023 for detailed schematics of Hall thruster). On the other hand, how do we define the scale of the mean electromagnetic field, which is also equivalent to the grid step over which the field is calculated? The heuristic justifications given by Dawson, 1983; Birdsall and Langdon, 2004 consider the Debye length associated with electrical plasma screening:

$$\lambda_{De} = \sqrt{\frac{\epsilon_0 k_B T_e}{n_e e^2}} \tag{1.16}$$

where we define the Boltzmann constant k_B, and electron temperature T_e.
In this way, we study collective plasma phenomena whose spatial scale is greater than or of the order of the Debye length.

1.3 Philosophy and objectives of the thesis

Numerous theoretical and experimental studies of the Hall thruster have enabled us to gain a better understanding of it, though not in its entirety as the causes of its dynamics are manifold and difficult to determine and/or model precisely. A multitude of fluid and kinetic models, from one to three spatial dimensions, have been very useful to highlight certain physical wave and transport phenomena. If the aim is to create a reliable, representative simulation of thrusters over the long term, it is necessary to maintain a low level of numerical error and reduce the number of strong assumptions in the models. From this point of view, the particle approach seems to better capture the complexity of physical phenomena, even though fluid models, and in particular two-fluid models, are able to reproduce some of the instabilities potentially present in thrusters (Wang et al., 2022). The three-dimensional nature of the interaction between the plasma and the components of the Hall thruster means that we have to accept this complexity. The difficulty of obtaining acceptable performance from three-dimensional particle calculation codes remains a challenge. W. Villafana's thesis (Villafana, 2021) showed that the electronic cyclotron drift instability (ECDI) could be simulated using a supercomputer over a period of one to one and a half months on a significant part of the thruster in a three-dimensional domain, using a Particle-in-cell (PIC) code coupled to the finite element method. It also highlights the lack of proven modeling of electrodes and dielectric walls which may have an impact on the instabilities present in the Hall thruster at certain operating regimes. Another point on which no scientific consensus has been reached is the exact role of instabilities on the axial transport of electrons, and therefore on the discharge current we wish to reduce in order to lower the electrical power required to operate the thruster. The so-called "anomalous" transport, i.e. not linked to collisions between particles or with the walls, seems to originate in a strong coupling with these instabilities.

It therefore appears necessary to look for alternatives to conventional PIC methods. The classical electrostatic PIC algorithm is described and tested in chapter 2 on a collisionless sheath case to understand how the method's numerical parameters work. The Sparse-PIC method described in chapter 2 is presented as a possible alternative and offers significant time savings at the expense of an error in the resolution of the potential, which we aim to quantify in chapter 3. The application of this relatively recent and little-known method is a risk-taking exercise. It calls on the mathematical tools of sparse grids and the grid combination technique, which are presented in detail in chapter 2. Coupling these tools to the PIC method can give rise to multiple implementations. These are presented in chapter 2, and one of them is specifically tested on an ExB cross-field configuration typical of a Hall current thruster in chapter 3. In general, confidence in simulation results should be systematically assessed. One way of evaluating the combination technique is to apply it to the Poisson equation solving using typical thruster density or electric potential profiles, and to compare it with other solver methods, or to use manufactured solutions. A way to evaluate the results of the complete Sparse-PIC algorithm is to measure the noise level or to compute the various fluid moments. In this complex configuration, the classical PIC algorithm is known not to strictly verify all moments (Birdsall and

Langdon, 2004). These results are shown in chapters 2 and 3 respectively.

One of the advantages of particle-based methods is that they provide numerical diagnostic access to the distribution functions of the positions and velocities of different particle populations or sub-populations. In the context of the study of Hall thruster instabilities, relatively few results on these distribution functions were shown. It is often preferred to use profiles integrated in velocity space, a space that yet includes the complexity of heating mechanisms. In a collisionless plasma, we can consider convection and radiation in the form of electric field waves which can have both physical and numerical causes. Wave physics, which is closer to experimental diagnostics, is more often studied, though theoretical developments are mostly based on linear theory. Some results on mechanisms in the velocity space within an ExB configuration are presented in chapter 3 while also devoting a section to the development of waves in the simulated plasma.

Chapter 4 is dedicated to the role of electronic secondary emission on thruster performance. Its modeling can become quite complex as the physics behind the electronic secondary emission by electron impacts on metallic or dielectric walls is poorly described. Several models based on experimental data have yet been developed. In this chapter, we chose the simplest one and focus on evaluating its role on the electronic transport and the fate of secondary electrons in the position and velocity space.

Finally, Chapter 5 explores a possible interpretation of the experimental results obtained by Thibault Dubois during the January 2021 test campaign on a 1.5 kW PPS-1350ML thruster in the PIVOINE vacuum chamber, using laser diagnosis by incoherent Thomson scattering. Using the Sparse-PIC code implemented during the thesis, the hypothesis of a radially-biased ionization source term is investigated.

Chapter 2

Application of the Sparse method to the PIC algorithm

2.1 The Particle-In-Cell algorithm

2.1.1 The electrostatic explicit version

The electrostatic Particle-In-Cell (PIC) method is a method for modeling the behavior of the distribution function of electrons and ions according to the Boltzmann/Vlasov equation (1.1). To do this, it introduces two types of object: a grid and particles. It solves Maxwell's equations in the electrostatic regime (Sub-section 1.2.4) on the grid and samples the distribution function using particles whose dynamics in phase space is calculated by solving the Newton-Lorentz's equation (1.14). In the approximation where the induced magnetic field is negligible, solving Maxwell's equations is reduced to solving the Poisson's equation (1.13). Coupling occurs from the particles to the grid to calculate the charge density of Poisson's equation, and from the grid to the particles for the calculation of electromagnetic forces. A schematic of the algorithm is shown in Figure 2.1.

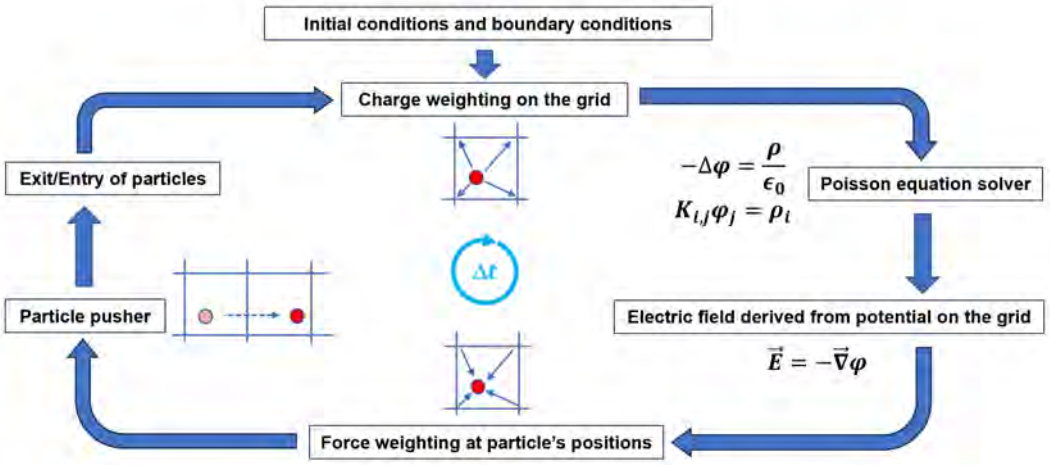

FIGURE 2.1: Electrostatic PIC scheme.

At the initial time, the statistical weight of the particles and their distribution in the space of positions and velocities are determined. The steps of the classical algorithm can be summarized as follows:

- The statistical weight of the particles is deposited on a grid using a Cloud-In-Cell method. (Birdsall and Langdon, 2004).
- The Poisson's equation (1.13) is discretized in matrix form ($K_{\mathbf{i},\mathbf{j}}\Phi_{\mathbf{j}} = \rho_{\mathbf{i}}$ for all $\mathbf{i}$, $\mathbf{j}$ multi-indexes of the grid) and solved on this grid to obtain the potential.
- The electric field $\vec{E} = -\vec{\nabla}\Phi$ is obtained by the finite-difference method on the grid from the potential profile. For a second-order scheme out of boundary conditions, we typically have in the direction i: $E_i(x_i, x_j, x_k) = \frac{-\Phi(x_{i+1},x_j,x_k)+\Phi(x_{i-1},x_j,x_k)}{2\Delta x_i}$.
- The electric field is projected to the particle position using the same shape functions as for charge deposition (Birdsall and Langdon, 2004).
- Particle positions and velocities are updated using a "leap-frog" scheme discretizing the Newton-Lorentz's equation (1.14) (Birdsall and Langdon, 2004), this stage is also known as the "pusher".
- Particles leaving the simulation domain are identified and treated according to the reinjection model.
- Ionization can be processed using a Monte-Carlo type method (Birdsall and Langdon, 2004) or by imposing a source term (Boeuf and Garrigues, 2018).
- Other types of elastic or inelastic collisions can be added using Monte-Carlo methods (See Rax, 2005 chapter 4 for a description of different collisional processes).
- The previous loop is repeated until the end of the simulation time.

Discretization criteria

Each step of the algorithm requires a discretization for its implementation. When choosing the spatial Δx and temporal Δt discretization steps, it is important to check their impact on simulation results. In a didactic approach, Birdsall and Langdon, 2004 justifies the $\Delta t \times \omega_{pe} < 0.2$ criterion by applying the algorithm to a harmonic oscillator where $\omega_{pe} = \sqrt{\frac{n_e e^2}{\epsilon_0 m_e}}$ is the electron plasma pulsation. This criterion preserves the amplitude of the wave (more precisely, $\Delta t \times \omega_{pe} < 2$ is sufficient for the amplitude) and to maintain an error limited to one radian on the wave phase for a few thousand time steps in a periodic domain. This is an order of magnitude for application purposes, and the criterion can be refined according to simulation accuracy requirements and simulation conditions. Similarly, the spatial spacing is generally taken to be of the order of the electronic Debye length $\lambda_{De} = \sqrt{\frac{\epsilon_0 k_B T_e}{n_e e^2}}$. which is the characteristic length of plasma electrical screening. The risk of taking

a too large spatial step is to attenuate the wavelengths of plasma oscillations below $2\Delta x$ but also to create unphysical instabilities (Dawson, 1983; Birdsall and Langdon, 2004). Another constraint linked to particle dynamics is the Courant-Friedrichs-Lewyde (CFL) condition $\frac{\Delta x}{\Delta t} > v_e$. where v_e should be the maximum electron velocity. However, for practical reasons of computational performance, and because the error remains small, we more often consider the thermal velocity of the electrons $v_e = v_{th,e} = \lambda_{De}\omega_{pe} = \sqrt{\frac{k_B T_e}{m_e}}$. Note that if the first two criteria are met, we have $\frac{\Delta x}{\Delta t} > v_{th,e}$. The aim is to ensure that a particle at thermal velocity does not move more than one cell length at each time step, in order to update the electric field on the grid and better calculate its trajectory. Failure to comply with this condition can lead to propagation of the error to the entire grid and unphysical instabilities (Birdsall and Langdon, 2004). Generally speaking, in the case where the explicit PIC method is solved without the electrostatic approach, the electromagnetic field verifies wave equations (1.9) and (1.10) and this criterion becomes de facto $\frac{\Delta x}{\Delta t} > c_0$ with c_0 the speed of light. Since electromagnetic field information propagates at c_0, these numerical parameters need to be adapted to avoid delays in field calculations.

A third numerical parameter is the number of particles in the simulation, and more specifically the number of particles per cell. There is a certain paradox concerning this third parameter. For the first two parameters, discretization implies convergence when grid and time steps tend towards zero. For the number of particles, if we follow the logic of phase space discretization, this number should tend towards infinity. From a physical point of view, this would mean exceeding the actual number of particles. This paradox gives rise to two conceptions of the third parameter. Either we consider a purely continuous vision of the model, which aims to strictly represent the Boltzmann/Vlasov equation (1.1), or we consider that the number of particles in the simulation domain must tend towards the real number of particles, necessarily creating noise of physical origin. In fact, the high frequencies at which particles pass through a cell can create statistical noise leading to density fluctuations (Birdsall and Langdon, 2004). These fluctuations can be exaggerated when the number of particles discretizing the distribution function is small. In certain situations, the absence of particles in certain cells may be due to a small total number of particles in the simulation, resulting in density increments of the order of the weight of a particle. There are no special rules for this third parameter. Nevertheless, convergence of results is expected and observed as the number of particles in the domain increases. In particular, when we assume a random distribution of noise on the electron density, the standard deviation of the electron density, which is also a measure of density fluctuations, decreases according to a $\frac{1}{\sqrt{n_{ppc}}}$ trend, where n_{ppc} is the number of particles per cell. Similarly, the error for charge density follows a trend in $\frac{1}{n_{ppc}} = \frac{1}{Nh^d}$ where h is the space step, N is the number of particles in the domain and d the domain dimension (Tranquilli, Ricketson, and Chacón, 2022, Table 1). We note that for computational performance constraints, this parameter varies from the order of 1000 particles per cell in one space dimension to 120 particles per cell in three space dimensions (Turner et al., 2013; Boeuf and Garrigues, 2018; Villafana, 2021).

A fourth parameter rarely taken into account is the residence time of particles in the domain. Explicit time scheme simulations tend to conserve momentum to the detriment of overall energy conservation. It may therefore be worthwhile to consider configurations where the particles reside in the computational domain for a short time, in order to reduce the effect of these biases on the distribution functions.

It should be kept in mind that all the criteria discussed above must be applied with the aim of representing a particular physics that requires its own degree of precision. The exact criteria that satisfy the needs of simulation are often determined by empiricism and convergence studies. We will strive to select the numerical parameters that best represent the collective phenomena of the plasma.

2.1.2 Validation of a PIC 1D code to a sheath case

The collisionless sheath model of Lieberman and Lichtenberg

We apply the electrostatic explicit PIC algorithm to a one-dimensional sheath case to familiarize ourselves with the method. The sheath is a non-neutral zone at the plasma boundary, allowing quasi-neutrality to be maintained within the plasma (See chapter 6.4 in Rax, 2005). Its size is of the order of a few Debye lengths (1.16). Two species are considered: electrons and xenon ions with a single charge. We consider Dirichlet conditions at the edges of the domain, where $\Phi = 0V$ is fixed. For each ion leaving the domain, an electron-ion pair is re-injected into a pre-defined central injection zone outside the sheath region. Electrons captured at the walls are considered lost. This method maintains the average ion density in the domain equal to the initial density. It has been used successfully in the past (Garrigues and Fubiani, 2023). The diagram in figure 2.2 summarizes the boundary conditions.

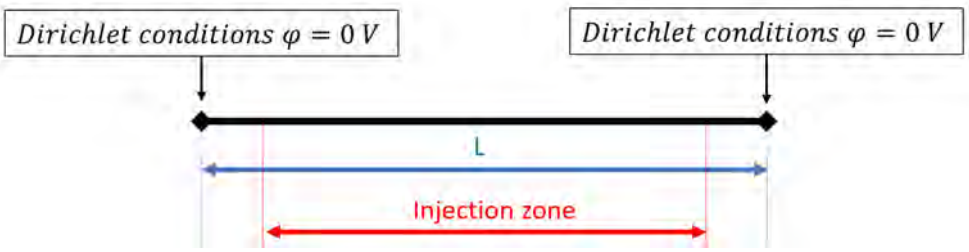

FIGURE 2.2: 1D Boundary conditions for sheath case.

Initially, we consider a uniform distribution of electron-ion pairs over the domain with density equal to $n_0 = 7.5 \times 10^{16} m^{-3}$ and a Maxwellian velocity distribution with an electron temperature of 2 eV and an ion temperature of 0.1 eV. In this configuration, the ions can be considered cold ($T_i \approx 0$) and the sheath model derived from Lieberman and Lichtenberg, 1994 (Chapter 6, page 167, "The collisionless sheath") can be applied. Bear in mind that particle re-injection must take place outside the sheath for the model to apply. Several points of comparison can be drawn from the model. Between the core plasma and the walls represented by the Dirichlet conditions, there are two zones: a pre-sheath, in which near-neutrality

of the plasma is still respected, and in which the ions gain sufficient energy to reach Bohm velocity, and the sheath, where the electron density is necessarily lower than the ion density and the speed of the ions greater than the Bohm velocity. For the sake of simplicity, let us note $T_e[V] = \frac{T_e[eV]}{e}$. If we set the potential at the walls to 0V, the potential at the heart of the domain is equal to:

$$\Phi_{plasma} = \frac{T_e[V]}{2}(1 + ln(\frac{m_i}{2\pi m_e}))$$

In our conditions, $\Phi_{ref,plasma} = 11.55V$.
At the frontier between pre-sheath and sheath, potential is equal to:

$$\Phi_{sheath} = \frac{T_e[V]}{2} ln(\frac{m_i}{2\pi m_e})$$

Or in our conditions, $\Phi_{ref,sheath} = 10.55V$.
There, ion velocity equals Bohm velocity:

$$v_{Bohm} = \sqrt{\frac{eT_e[V]}{m_i}}$$

Or in our conditions, $v_{Bohm} = 1212 m.s^{-1}$.

In practice (Garrigues, Fubiani, and Boeuf, 2016), electrons are thermalized in the injection zone through a fixed frequency such that $\nu_{th} \times \Delta t = 10^{-1}$. In other words, we randomly draw a Maxwellian velocity distribution of fixed temperature (Here $T_e = 2$ eV) for electrons every $\frac{1}{\nu_{th}\Delta t}$ time step. In the absence of thermalization, electrons are cooled by the loss of fast electrons at the walls as shown in figure 2.3. The electrons in this model can remain in the computational domain for several microseconds, and are the least energetic electrons which allows this cooling. The results are then no longer comparable with the sheath theory proposed in Lieberman and Lichtenberg, 1994, which assumes a Maxwellian electron distribution.

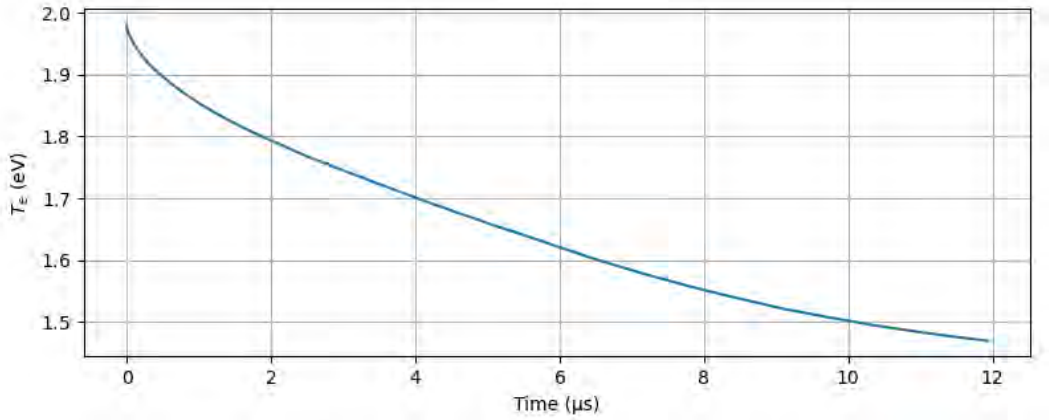

FIGURE 2.3: 1D electron cooling for sheath case when no thermalization occurs.

TABLE 2.1: Parameters for sheath simulation.

Initial density	**Number of particles per cell**	**Grid cells**
$7.5 \times 10^{16} m^{-3}$	1000	1024
L	**Injection zone**	Δt
$2cm$	$0.05cm - 1.95cm$	$1.25 \times 10^{-11} s$
$\omega_{pe} \times \Delta t$	$\frac{\Delta x}{\lambda_{De}}$	$\frac{v_{th,e} \Delta t}{\Delta x}$
0.19	0.51	0.38

Comparison of PIC results with the Lieberman and Lichtenberg model

Figures 2.4, 2.5 show the results of applying the explicit PIC agorithm for numerical parameters summarized in table 2.1 where the discretization criteria mentioned above are also given. The results are time-averaged over one microsecond after 11 microseconds of physical simulation time. Currents stabilize after 4 to 6 microseconds of physical simulation time. The results presented are therefore representative of the stationary regime, which is the regime of interest.

We observe good agreement with the Φ_{plasma} and Φ_{sheath} reference points for the potential, as well as compliance with the Bohm criterion for a break in neutrality associated with the $|n_i - n_e| > \frac{n_e}{10}$ criterion. It should be noted that the results are highly dependent on the injection zone, and deviate from predicted results if the injection zone for electron-ion pairs contains part of the sheath.

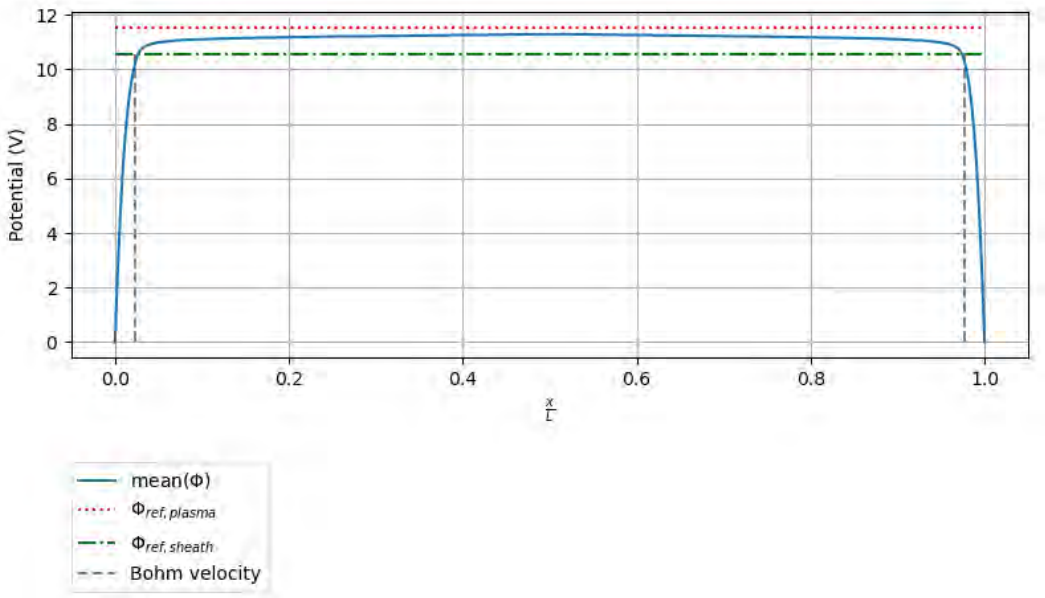

FIGURE 2.4: 1D potential for sheath case with conditions in Table 2.1.

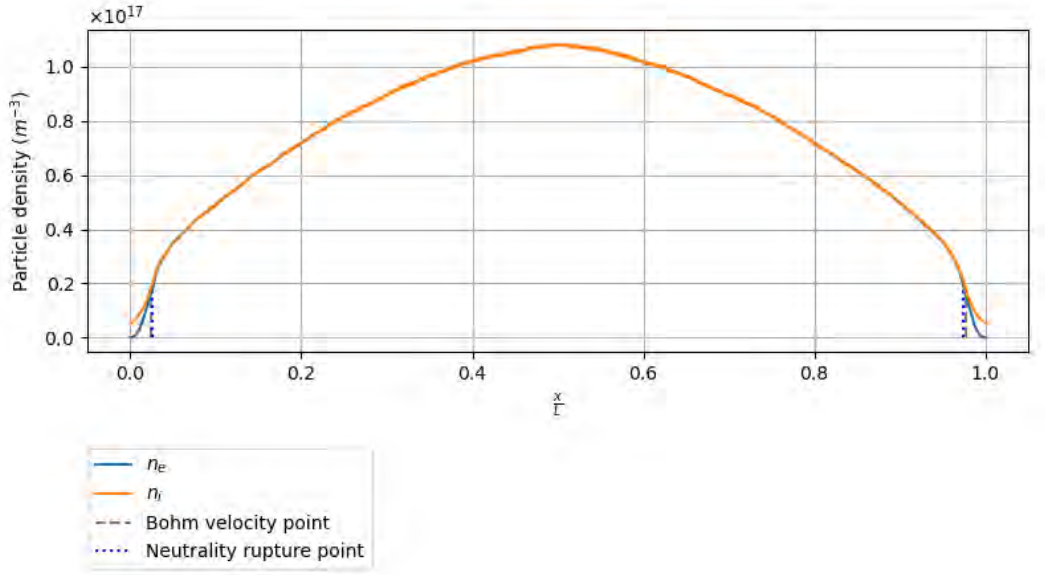

FIGURE 2.5: 1D particle density for sheath case with conditions in Table 2.1.

Dependence of simulation results on discretization parameters

We now seek to determine the dependence of the simulation results on the spatial, temporal and particle discretization parameters under steady-state conditions. We can choose as references the value of the mean electric potential at the center of the domain $\Phi_{ref,plasma} = 11.55V$, the value at which the Bohm velocity is reached for ions $\Phi_{ref,sheath} = 10.55V$, as well as the distance δ between the point at which plasma

quasi-neutrality is broken and the point at which the Bohm velocity is reached for ions which must be zero to verify the Bohm criterion.

We keep the same parameters as in table 2.1 except for $n_{ppc} = 300$, the size of the domain L which we vary to vary the space step Δx and the injection and thermalization zone, which is set between 0.05 cm and $L - 0.05$ cm, i.e. approximately 13 Debye lengths of margin for the sheath. The number of points in the calculation domain is therefore the same, only the Δx grid step changes. Under these conditions, we have $\frac{v_{th,e}\Delta t}{\Delta x} < 1$ for $\frac{\Delta x}{\lambda_{De}} > 0.193$. To better understand the impact of the spatial discretization parameter, we place ourselves in cases where the previous CFL condition is respected. The simulation results obtained are presented in figures 2.6 and 2.7.

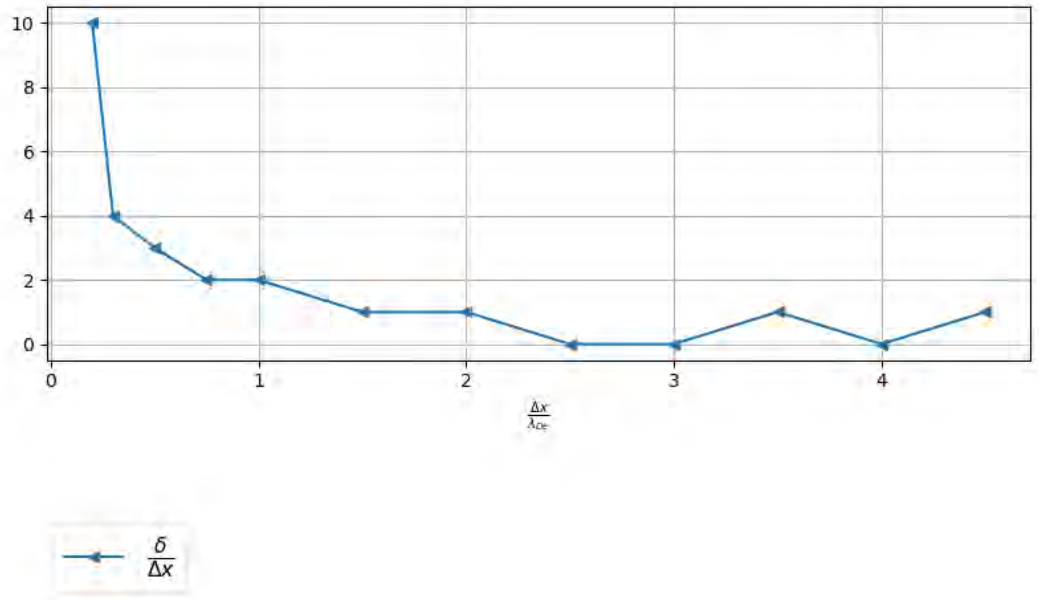

FIGURE 2.6: 1D PIC results with different parameters $\frac{\Delta x}{\lambda_{De}}$ compared with Bohm criteria reference from Lieberman and Lichtenberg sheath model.

The values of $\frac{\delta}{\Delta x}$ are given with a precision of the order of one grid step. Within the range of $\frac{\Delta x}{\lambda_{De}}$ values tested, we observe an influence of the spatial discretization parameter on the compliance with the Bohm criterion. This is degraded for values of $\frac{\Delta x}{\lambda_{De}}$ below 1.5. This can be explained by the CFL condition, which needs to be better solved. In our conditions for $\frac{\Delta x}{\lambda_{De}} > 1.5$, we find the criterion $\frac{v_{th,e}\Delta t}{\Delta x} < 0.13$. For the reference values of the electric potential, the results converge as the grid spacing tends towards zero.

We keep the same parameters as in table 2.1 except for $n_{ppc} = 300$, and we now vary Δt. Recall that $\Delta x = 1.95 \times 10^{-5} m$ under these conditions, and that the ratio $\frac{v_{th,e}\Delta t}{\Delta x} < 1$ for $\omega_{pe}\Delta t < 0.5$. The simulation results obtained are shown in figure 2.8.

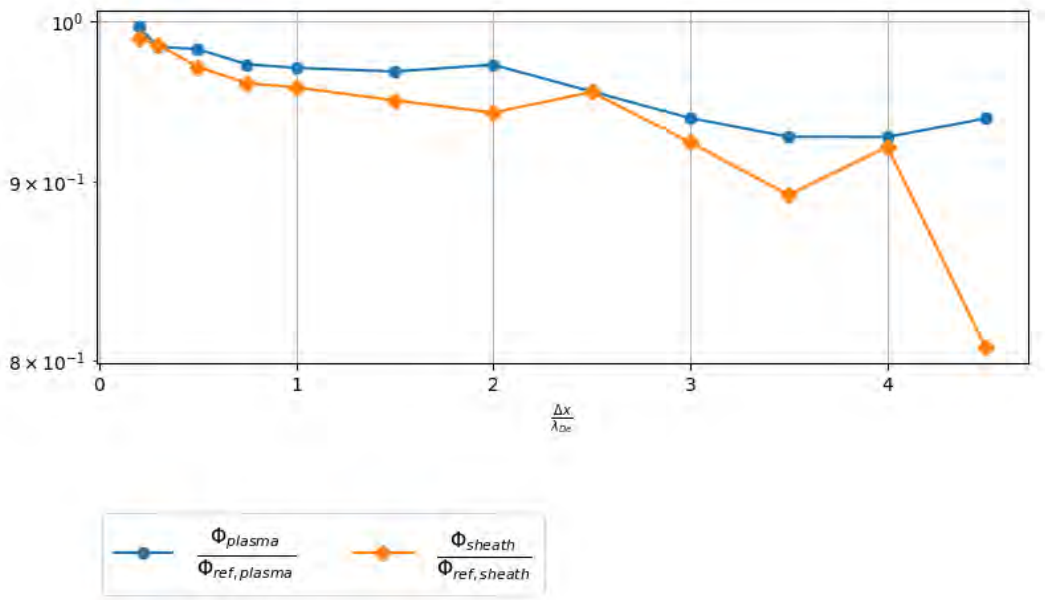

FIGURE 2.7: 1D PIC results with different parameters $\frac{\Delta x}{\lambda_{De}}$ compared with electric potential references from Lieberman and Lichtenberg sheath model.

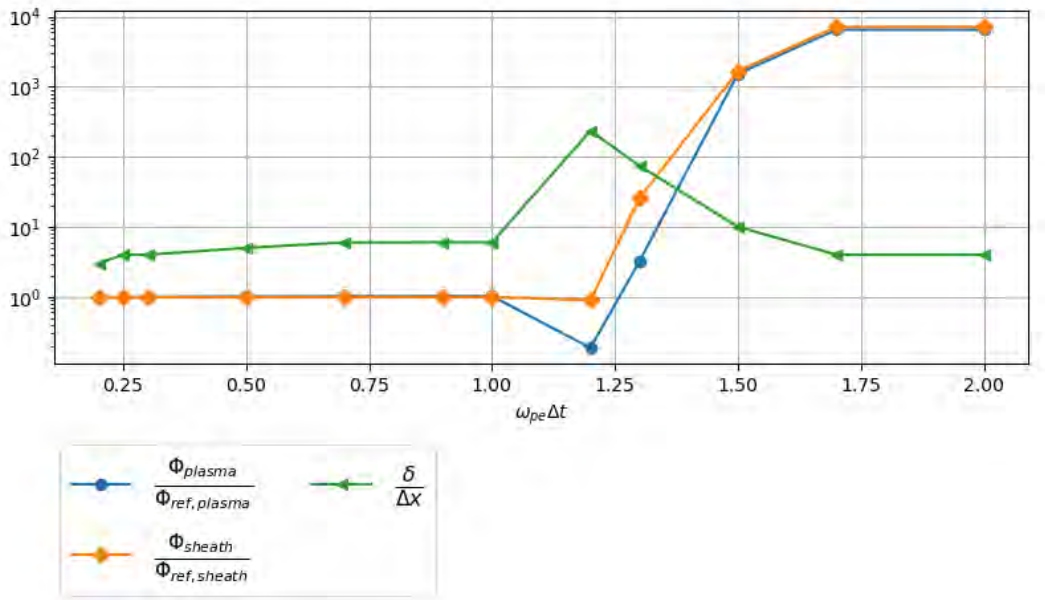

FIGURE 2.8: 1D PIC results with different parameters $\omega_{pe}\Delta t$ compared with references from Lieberman and Lichtenberg sheath model.

We observe that Lieberman and Lichtenberg's sheath model is no longer correctly represented for parameters $\omega_{pe}\Delta t > 1$. also corresponding to $\frac{v_{th,e}\Delta t}{\Delta x} > 2$. The results remain consistent for $\omega_{pe}\Delta t \leq 1$ and seem to converge for both the Bohm criterion and the reference values when the time step tends towards zero. The range of

values tested does not allow us to accurately determine a criterion associated with the CFL condition, except that we observe that at least $\frac{v_{th,e}\Delta t}{\Delta x} < 0.38$ is required.

We keep the same parameters as in table 2.1 and now vary the number of particles per cell at initial time n_{ppc}. The conditions associated with the CFL condition and the other discretization criteria are the same as those presented in table 2.1. The simulation results obtained are shown in figure 2.9.

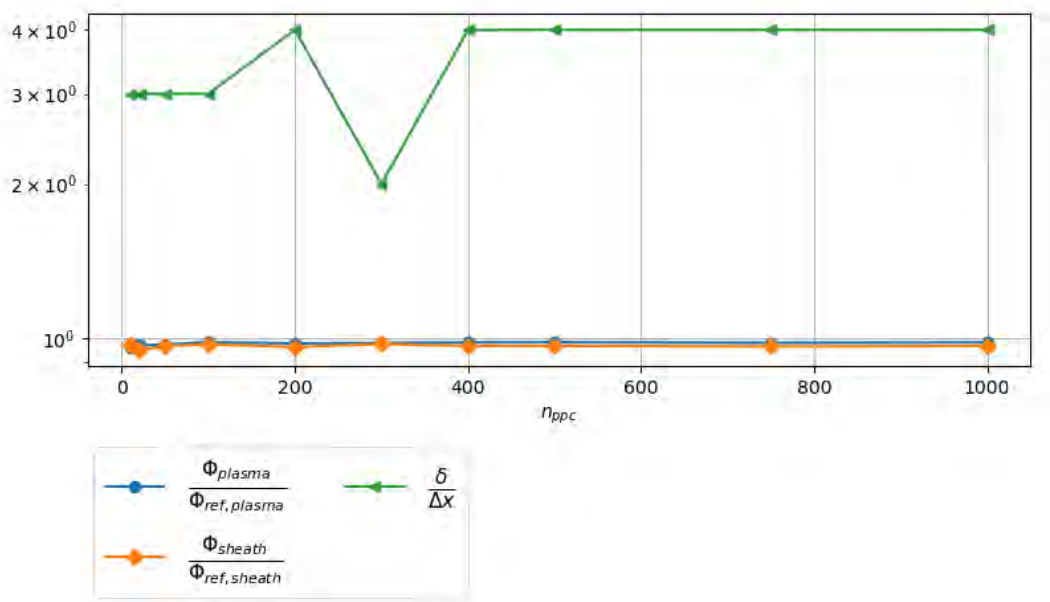

FIGURE 2.9: 1D PIC results with different parameters n_{ppc} compared with references from Lieberman and Lichtenberg sheath model.

Remember that the values of $\frac{\delta}{\Delta x}$ are given with a precision of the order of one grid step. Under these conditions, it appears that the number of particles per cell in the domain at the initial instant does not significantly alter the simulation results for $n_{ppc} \geq 10$. The particle discretization parameter of the phase space does not appear to have a significant impact in the case of the collisionless sheath. We have seen previously that it plays a role in the level of fluctuations in charge density and potential. It could be a significant factor in situations where the particles enter into resonance with a wave, as could be the case for the Hall current thruster. We note that previous simulations have shown an impact of this parameter on transport in reduced models of the thruster (Boeuf and Garrigues, 2018; Tavassoli et al., 2023).

We are also seeking to understand whether these parameters influence compliance with the steady-state fluid moments (1.2), (1.3), (1.4). It is not trivial to establish a reference for evaluating the errors in solving these equations. We prefer to introduce ratios and observe their evolution as a function of discretization parameters. Note (Ox) the axis making up the one-dimensional domain and L the size of the domain. We introduce the temporal mean $< . >_t = \frac{1}{T}\int_0^T .dt$ over time T and the

spatial mean $< . >_x = \frac{1}{L}\int_0^L .dx$. Consider n_0 the average density over the simulation domain at the initial instant and $v_{th,\alpha}$ the thermal velocity of the α species (ion or electron) at the initial instant. We choose to establish the following ratios for the first 0-order moment (1.2) considering that the source term cancels out when the electronic and ionic equations are combined (reinjection by electron-ion pair):

$$\epsilon_{1^{st}}(x) = \left| \frac{\Delta x}{< n_0 v_{th,e} >_t} < \frac{\partial(n_i v_{i,x})}{\partial x} - \frac{\partial(n_e v_{e,x})}{\partial x} >_t \right|$$

For the second moment of order 1 (1.3), the ionization source term introduces a Maxwellian velocity distribution function. Since $\int_{-\infty}^{+\infty} v_i e^{-v_i^2} dv_i = 0$, its average contribution over time is zero, so we introduce the ratio:

$$\epsilon_{2^{nd},\alpha}(x) = \left| \frac{\Delta x}{< n_0 v_{th,\alpha}^2 >_t} < \frac{\partial \Pi_{\alpha,xx}}{\partial x} - \frac{n_\alpha q_\alpha}{m_\alpha} E_x >_t \right|$$

For the third moment of order 2 (1.4), the ionization source term similarly introduces a Maxwellian velocity distribution function. Since $\int_{-\infty}^{+\infty} v_i^2 e^{-v_i^2} dv_i = 0$, its average contribution over time is zero, so we introduce the ratio:

$$\epsilon_{3^{rd},\alpha}(x) = \left| \frac{\Delta x}{< n_0 v_{th,\alpha}^3 >_t} < \frac{\partial Q_{\alpha,xxx}}{\partial x} - \frac{n_\alpha q_\alpha}{m_\alpha} v_{\alpha,x} E_x >_t \right|$$

These ratios should tend towards zero when the spatial and temporal discretization parameters tend towards zero and the number of particles tends towards infinity. For simplicity's sake, we will present the spatial averages of these ratios $< \epsilon_{1^{st}} >_x$, $< \epsilon_{2^{nd},e} >_x$, $< \epsilon_{2^{nd},i} >_x$, $< \epsilon_{3^{rd},e} >_x$, $< \epsilon_{3^{rd},i} >_x$. It should be kept in mind that measuring these quantities at any point in the simulation domain could help with local grid refinement strategies. However, these issues will not be addressed in detail in this thesis. To a lesser extent, we seek to recover the trends observed previously for discretization parameters on simulation results. We therefore place ourselves under the same conditions as previous studies to study the evolution of these ratios as a function of the various discretization parameters. The ratios defined above could then be used as measurement tools in cases where there is no theoretical reference on which to verify the results obtained.

The evolution of the ratios defined above as a function of the $\frac{\Delta x}{\lambda_{De}}$ ratio of grid step to electronic Debye length is shown in figure 2.10.

We observe a significant impact on the ratios defined for the second fluid moment. They decrease as the grid step decreases in the range $\frac{\Delta x}{\lambda_{De}} \in [0.5, 4.5]$, which is consistent with the explicit PIC method. For $\frac{\Delta x}{\lambda_{De}} < 0.5$, the deterioration of the results can be explained by the deterioration of the CFL condition when $\frac{v_{th,e}\Delta t}{\Delta x} > 0.38$. The ratio defined for the third ionic fluid moment seems to show the same trend as the $\frac{\delta}{\Delta x}$ ratio and may therefore, in the sheath case, be an indicator of the compliance with the Bohm criterion. More generally, it could be an indicator of the correct representation of the energetic properties of ions. The use of thermalization for electrons makes the ratio defined for the third electronic fluid moment globally insensitive to

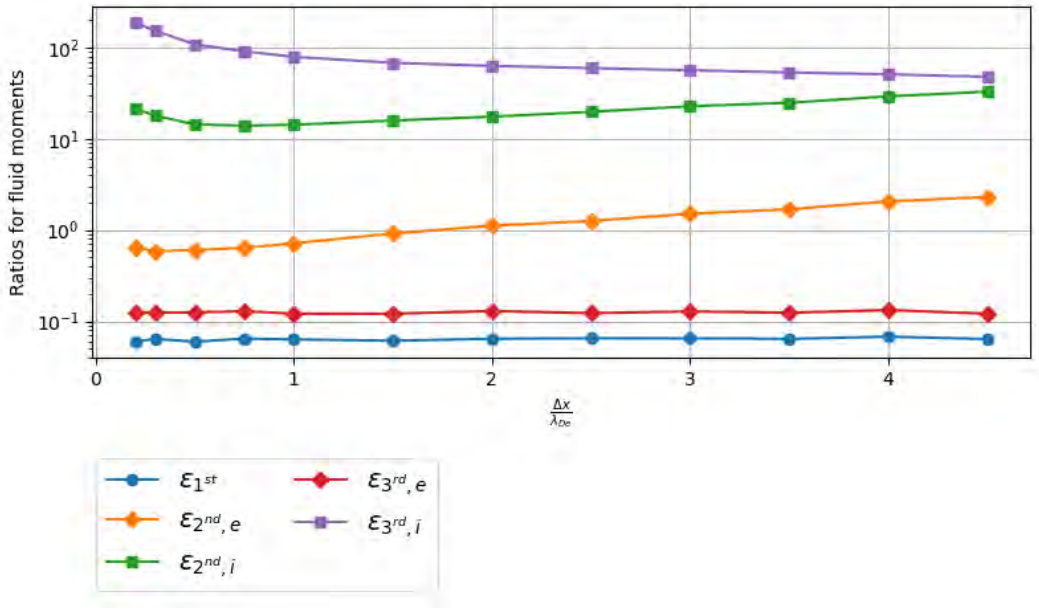

FIGURE 2.10: Ratios for fluid moments with $\frac{\Delta x}{\lambda_{De}}$ for sheath case.

the spatial discretization parameter.

The evolution of the ratios defined above as a function of $\Delta t \times \omega_{pe}$ is shown in figure 2.11.

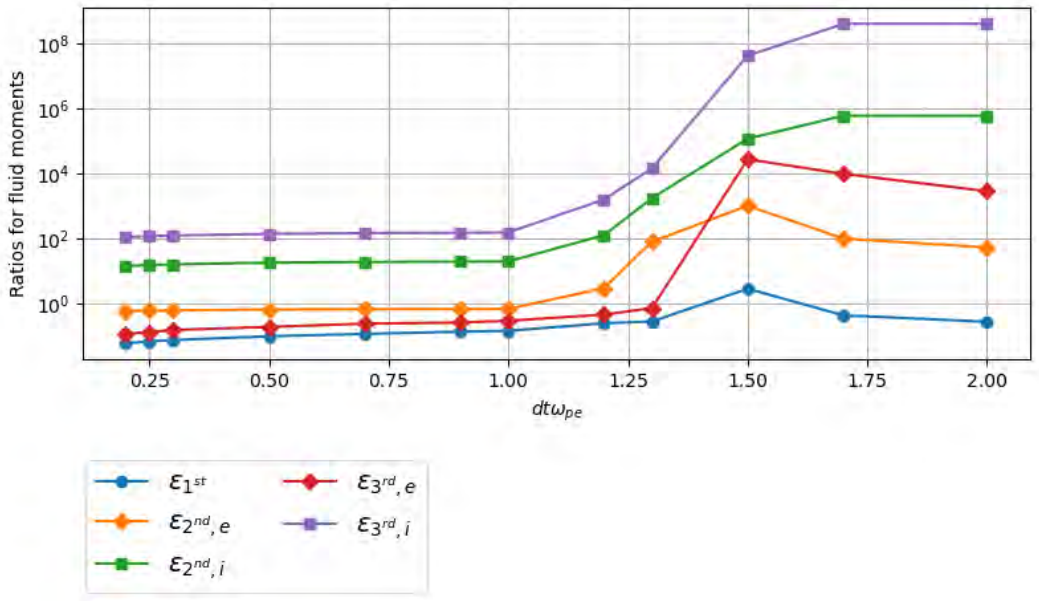

FIGURE 2.11: Ratios for fluid moments with $\Delta t \times \omega_{pe}$ for sheath case.

The effect of the time parameter on the simulation results can be seen in the ratios defined for the first three fluid moments. We observe a significant increase of up

to several orders of magnitude in the ratios defined previously for $\omega_{pe}\Delta t > 1$ and when the CFL condition is no longer respected by a factor of 2, i.e. $\frac{v_{th,e}\Delta t}{\Delta x} > 2$. Such an increase leads to inconsistent results for $\omega_{pe}\Delta t > 1$. For $\omega_{pe}\Delta t \leq 1$, the ratios defined for the fluid moments decrease as the time step decreases, which is consistent with an overall improvement in simulation results compared to Lieberman and Lichtenberg model benchmarks as the time step tends towards zero (cf. Figure 2.8).

The evolution of the ratios defined above as a function of the number of particles per cell at the initial instant is shown in figure 2.12.

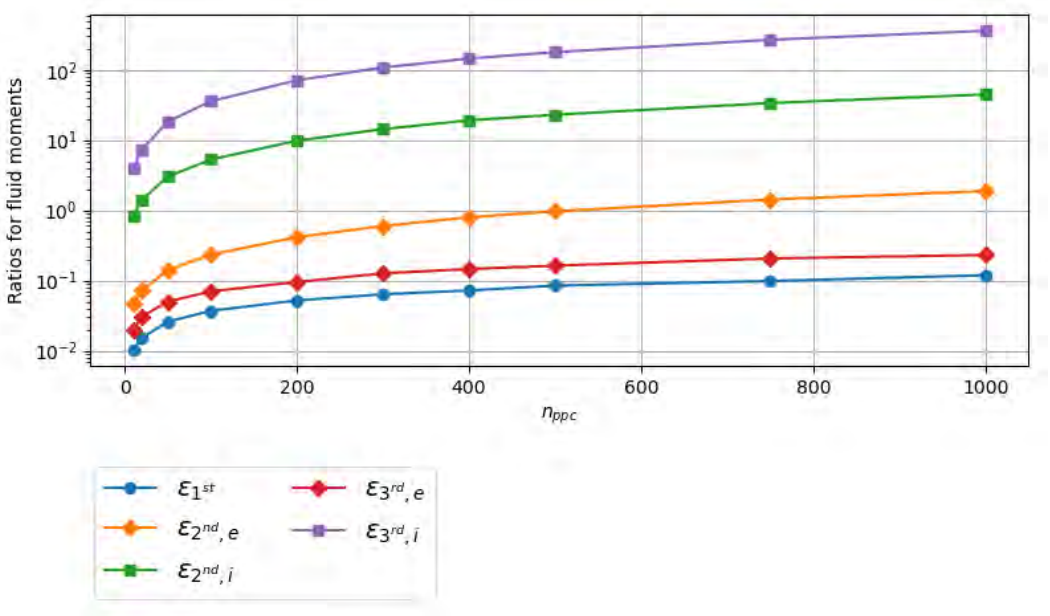

FIGURE 2.12: Ratios for fluid moments with number of particle per cell n_{ppc} for sheath case.

We have already seen that the particle discretization parameter of the phase space does not play a significant role on the simulation results in the collisionless sheath case for $n_{ppc} \geq 10$. However, we observe that this parameter modifies the ratios defined for the different fluid moments, and that these ratios seem to converge as n_{ppc} tends towards infinity. What is more difficult to interpret is that these ratios increase with n_{ppc}. Increasing the number of particles in the domain will help refine the distribution of particles within each cell. The accuracy of gradients linked to the particle distribution function will then be better than that of gradients independent of the number of particles and linked solely to the grid step, as in the calculation of the electric field, which could explain the trend in the ratios defined above. The convergence of the ratios when $n_{ppc} \to \infty$ remains consistent with the idea that this parameter tends to represent phase space.

Fluctuations in electric potential and charge density

We are interested in profiles that are not averaged over time once steady state has been reached. They show temporal variations that can be quantified by calculating a standard deviation. We seek to understand the origin of these oscillations, their evolution as a function of the number of particles per cell and other discretization parameters and discuss the benefits of studying them. Note (Ox) the axis making up the one-dimensional domain. The time average $< . >_t = \frac{1}{T}\int_0^T .dt$ over time T is introduced. The electric potential Φ and charge density $\rho = e(n_i - n_e)$ can be decomposed as follows:

$$\Phi(x,t) = < \Phi >_t (x) + \delta\Phi(x,t)$$

$$\rho(x,t) = < \rho >_t (x) + \delta\rho(x,t)$$

with $< \delta\Phi(x,t) >_t = 0$, $< \delta\rho(x,t) >_t = 0$.

We can define their standard deviations for N_t time sampling points at instants t_i ($i \in [\![1; N_t]\!]$):

$$\sigma_\Phi(x) = \sqrt{\frac{1}{N_t}\sum_{i=1}^{N_t}(\Phi(x,t_i) - < \Phi >_t (x))^2} = \sqrt{\frac{1}{N_t}\sum_{i=1}^{N_t}\delta\Phi(x,t_i)^2} \approx \sqrt{< \delta\Phi^2 >_t (x)}$$

$$\sigma_\rho(x) = \sqrt{\frac{1}{N_t}\sum_{i=1}^{N_t}(\rho(x,t_i) - < \rho >_t (x))^2} = \sqrt{\frac{1}{N_t}\sum_{i=1}^{N_t}\delta\rho(x,t_i)^2} \approx \sqrt{< \delta\rho^2 >_t (x)}$$

These standard deviations allow us to measure the amplitude of fluctuations in potential and charge or particle density $|n_i - n_e|$ at any point in space. If we further assume that:

$$\delta\Phi(x,t) = \sum_{n=1}^{\infty} \delta\Phi_n sin(\frac{n\pi x}{L}) sin(\omega t)$$

Then for an average over a fairly long period of time:

$$\sigma_\Phi = \sqrt{< \delta\Phi^2 >_t} \approx \sum_{n=1}^{\infty} \frac{\delta\Phi_n}{\sqrt{2}} sin(\frac{n\pi x}{L})$$

In our case $\omega = \omega_{pe} \approx 15 \times 10^9 rad.s^{-1}$, a time average over a microsecond is sufficient. The standard deviations of the potential and particle density $|n_i - n_e|$ are given in figures 2.13 and 2.14 for the simulation conditions in table 2.1.

These standard deviations give an order of magnitude to the amplitudes of the fluctuations in potential and particle density $|n_i - n_e|$ respectively of the order of $\sqrt{2}\sigma_\Phi = 0.56V$ and $\sqrt{2}\sigma_{|n_i - n_e|} = 3.5 \times 10^{15} m^{-3}$ for an initial uniform density $n_0 = 7.5 \times 10^{16} m^{-3}$. We find that the dominant mode is the first mode ($n = 1$). This study may prove more interesting in cases where these modes interact with an instability,

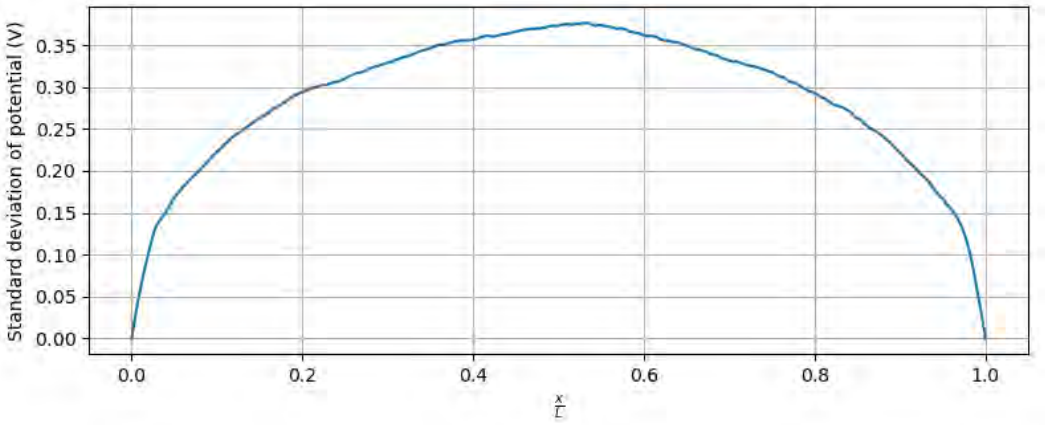

FIGURE 2.13: 1D electric potential standard deviation for sheath case.

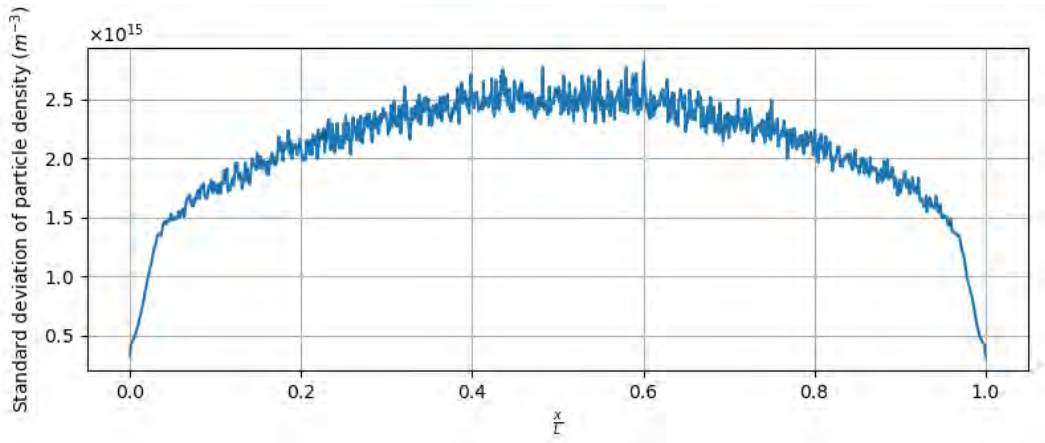

FIGURE 2.14: 1D particle density $|n_i - n_e|$ standard deviation for sheath case.

as might be the case in an ExB cross-field configuration (Perez Luna, 2008; Coche, 2013).

We note that the amplitude of the $|n_i - n_e|$ density fluctuations obtained from the Poisson's equation (1.13) by injecting the potential fluctuation profile in the form of a sum of sines as presented above gives an order of amplitude of $10^{12}m^{-3}$. Potential fluctuations are therefore difficult to read from the standard deviation profile of the $|n_i - n_e|$ density, which is rather of the order of $10^{15}m^{-3}$. In other words, the disordered noise associated with the particles does not contribute on the same scale to the charge density and electric potential profiles. That is to say:

$$-\Delta\sqrt{<\delta\Phi^2>_t} \neq \frac{1}{\epsilon_0}\sqrt{<\delta\rho^2>_t}$$

Even though by definition,

$$-\Delta\delta\Phi(x,t) = \frac{\delta\rho(x,t)}{\epsilon_0}$$

The contribution of noise to particle density $|n_i - n_e|$ can be evaluated using Monte-Carlo theory (Bottino et al., 2007). If we consider a uniform random distribution of this noise, the standard deviation should be reduced by increasing the number of particles per cell according to a $\frac{1}{\sqrt{n_{ppc}}}$ trend, where n_{ppc} is the number of particles per cell. This relation is verified by presenting the evolution of the spatially integrated standard deviation as a function of the number of particles per cell in figure 2.15. The same applies to the standard deviation of the electric potential in figure 2.16.

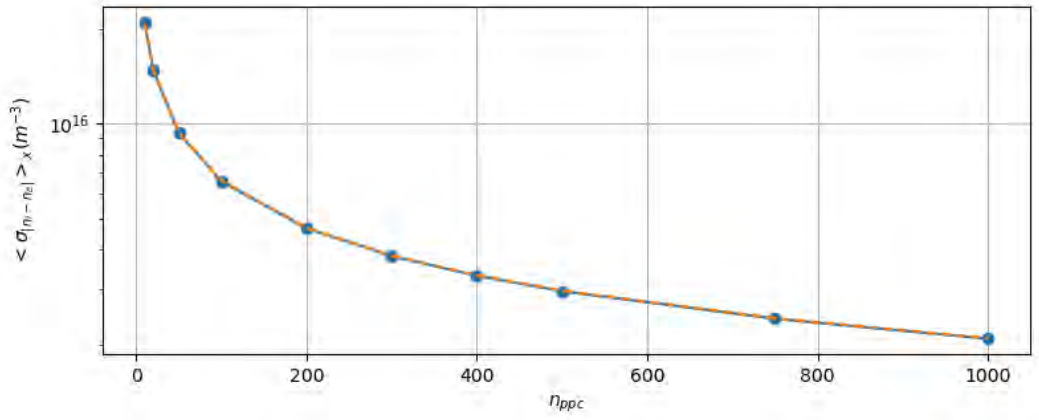

FIGURE 2.15: 1D mean particle density $|n_i - n_e|$ standard deviation for sheath case: results of PIC (dot line), square root fit (dashed line).

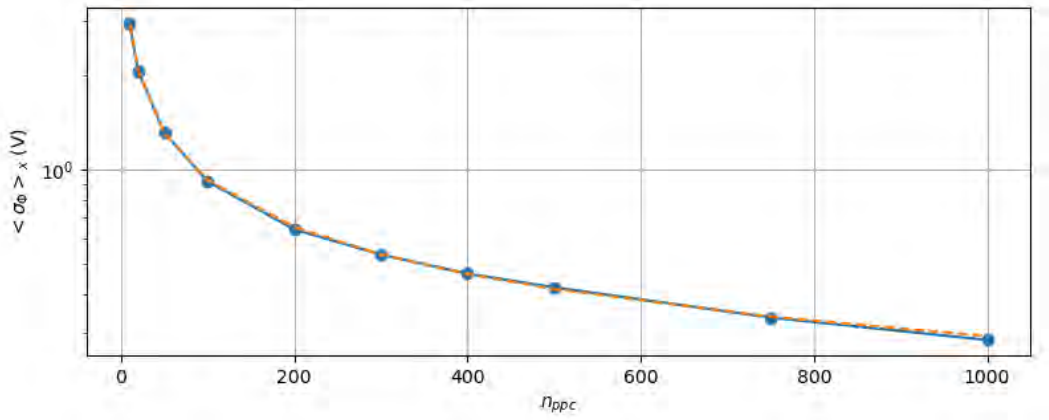

FIGURE 2.16: 1D mean electric potential Φ standard deviation for sheath case: results of PIC (dot line), square root fit (dashed line).

The origin of these fluctuations is therefore linked to the discretization of phase space by a finite number of particles. We also seek to understand whether the fluctuations depend on other temporal and spatial discretization parameters. Figures 2.17 and 2.18 show the variation of the standard deviations of the particle density $|n_i - n_e|$ and the electric potential as a function of the time discretization parameter $\omega_{pe}\Delta t$ for simulation conditions similar to those used in previous studies.

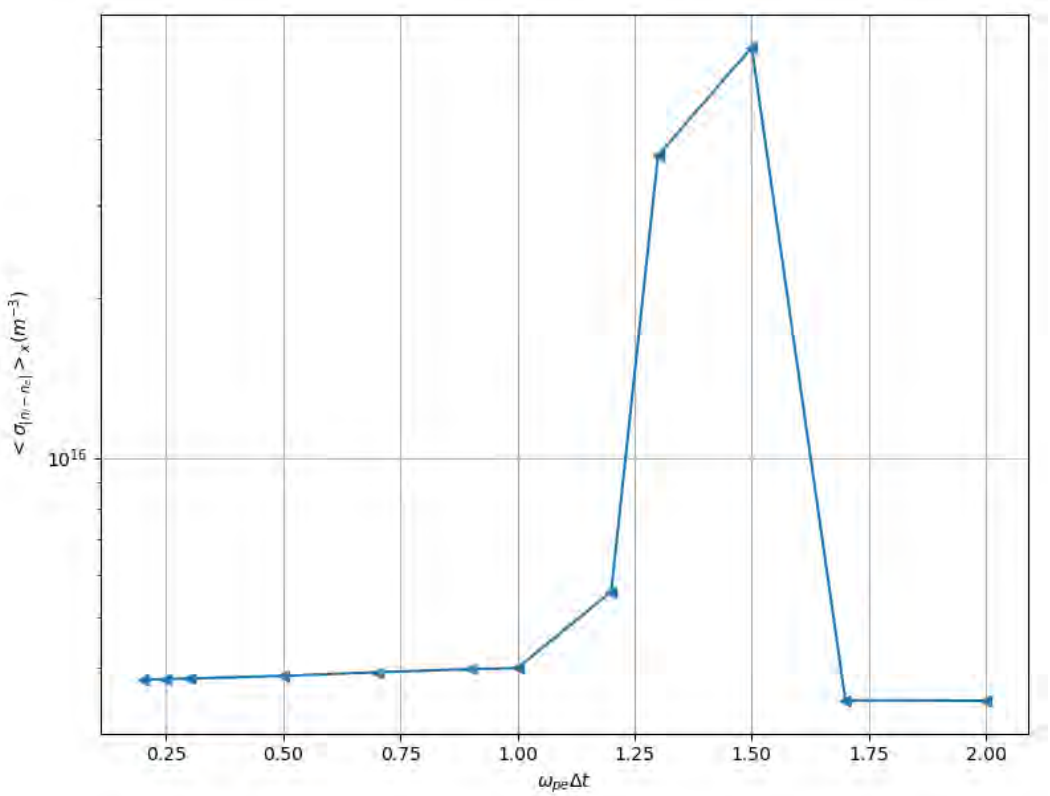

FIGURE 2.17: 1D mean particle density $|n_i - n_e|$ standard deviation with $\omega_{pe}\Delta t$ for sheath case.

The inconsistency of the simulation results can be seen in the values of the standard deviations for $\frac{v_{th,e}\Delta t}{\Delta x} \geq 2$, particularly for the standard deviation of the electric potential. When values are consistent for $\frac{v_{th,e}\Delta t}{\Delta x} < 2$, the time discretization parameter $\omega_{pe}\Delta t$ has little influence on standard deviation values. Figures 2.19 and 2.20 also show the variation in standard deviations of particle density $|n_i - n_e|$ and electric potential as a function of the spatial discretization parameter $\frac{\Delta x}{\lambda_{De}}$.

The spatial discretization parameter has a different effect on fluctuations in charge density and electric potential. This parameter has little influence on charge density fluctuations, of the order of ten percent on the amplitude of fluctuations for the range of values tested. However, it shows that there is an optimum with fixed temporal and particle discretization parameters for reducing charge density noise, which is a balance between a good CFL condition and a small grid spacing. The trend in the potential standard deviation profile shows unambiguously that potential fluctuations cancel out as the grid step tends towards zero. We conclude from

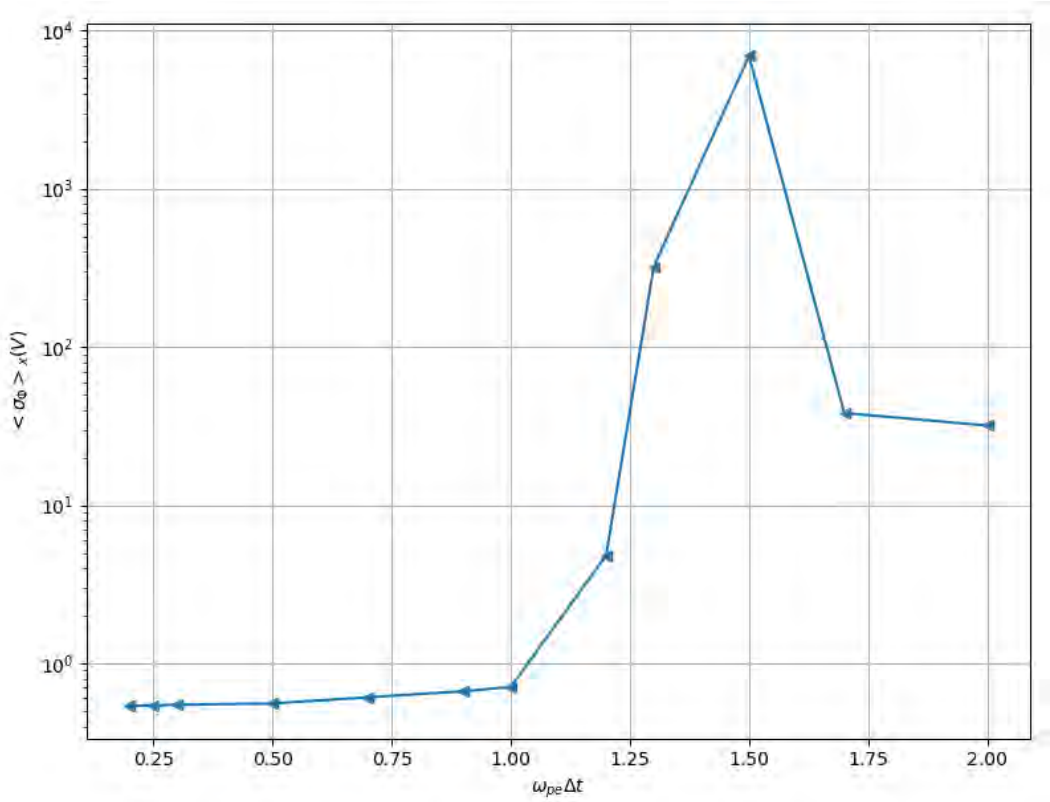

FIGURE 2.18: 1D mean electric potential Φ standard deviation with $\omega_{pe}\Delta t$ for sheath case.

these studies that charge density fluctuations depend mainly on the particle discretization parameter when the CFL condition is good enough to obtain consistent results. For potential fluctuations, both the particle and spatial discretization parameters play an important role.

Does this mean that these fluctuations are purely numerical? The influence of the spatial discretization parameter on potential fluctuations indicates the presence of grid-related modes. These modes therefore have no physical origin. However, the influence of the particle discretization parameter requires further discussion. As discussed in the section on discretization criteria, the number of particles per cell could be interpreted as a parameter that should tend towards infinity or towards the real number of particles. If we opt for the first interpretation, any fluctuation should cancel out as the number of particles tends towards infinity. If we opt for the second interpretation, fluctuations can be an integral part of physics when their level is representative of the real medium. When we imagine situations other than the collisionless sheath case, we can expect there to be privileged modes excited by the particles. The physics of the Hall current thruster introduces instabilities linked in particular to wave-particle resonances (Perez Luna, 2008; Coche, 2013). This is the case with the electron (cyclotron) drift instability (EDI or ECDI, Boeuf and Garrigues, 2018) thought to be responsible for anomalous transport in the Hall current

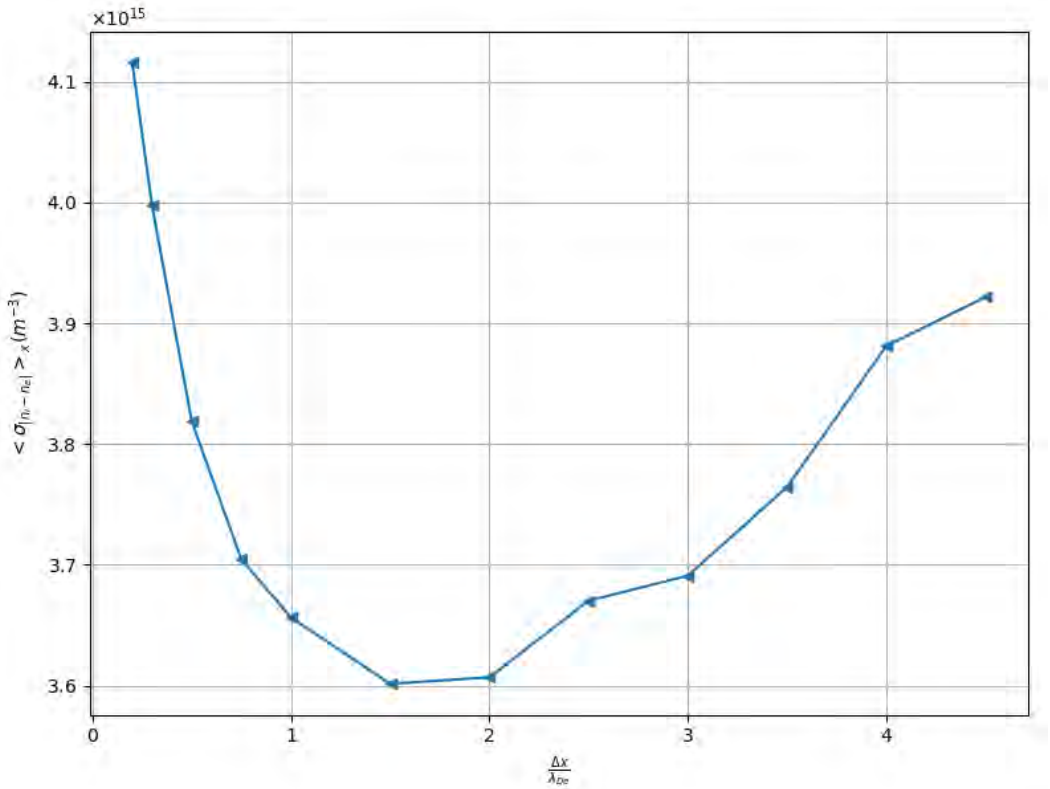

FIGURE 2.19: 1D mean particle density $|n_i - n_e|$ standard deviation with $\frac{\Delta x}{\lambda_{De}}$ for sheath case.

thruster, i.e. the increased transport of electrons across the magnetic barrier despite the low rate of electron-neutral collisions. Fluctuations in these cases are related to resonances, and are superimposed on other fluctuations related to the grid and particle discretization of phase space. The comparison of the PIC method with a solver of the continuous Vlasov equation on this particular case in Tavassoli et al., 2023 illustrates the confrontation of points of view. Solving the continuous Vlasov equation naturally yields results closer to theory. However, the orders of magnitude obtained with PIC could be closer to reality.

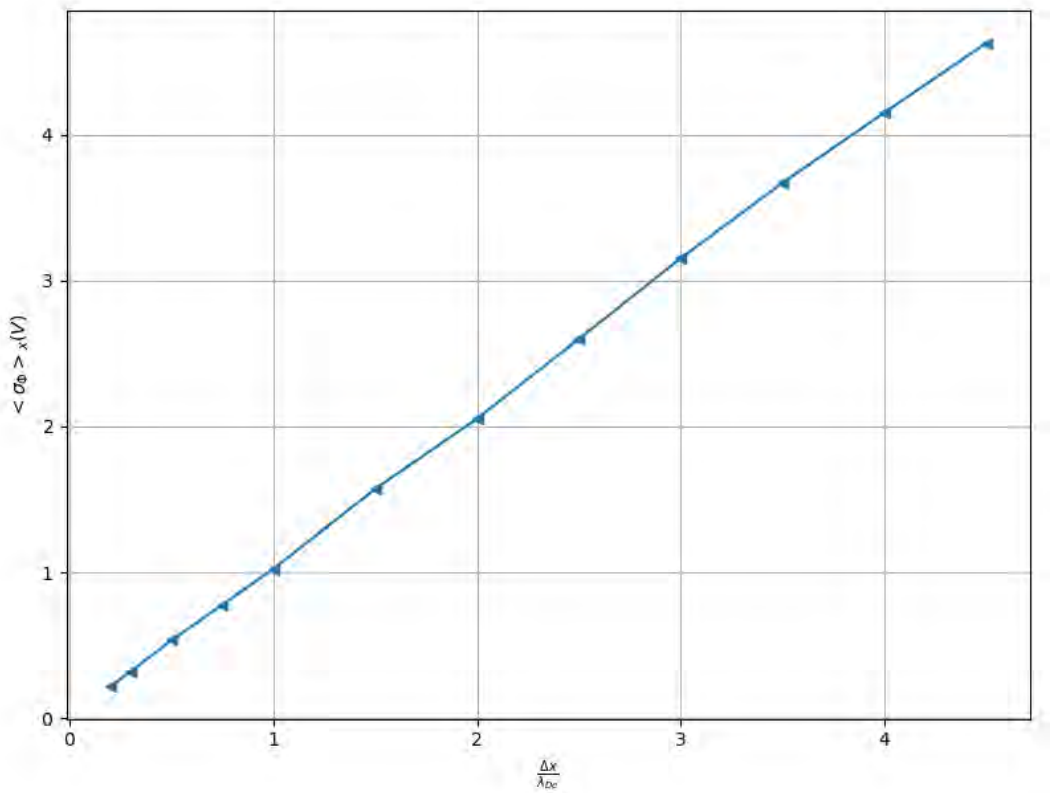

FIGURE 2.20: 1D mean electric potential Φ standard deviation with $\frac{\Delta x}{\lambda_{De}}$ for sheath case.

2.1.3 Variants

The electrostatic approach is not always suited to the problems studied. The PIC algorithm also has an electromagnetic version, which takes into account the electromagnetic waves produced by currents of charged particles, which can propagate throughout space. This involves solving all Maxwell's equations and choosing a gauge to link the scalar potential to the vector potential (Sub-section 1.2.3). An introduction to the different options for implementing Maxwell's equations in the algorithm can be found in Birdsall and Langdon, 2004; Vay et al., 2016. Numerical implementation of the algorithm in a reduced model with one dimension in position and two in velocity can be found in Bonnaud, 2019.

The explicit electrostatic PIC version is designed to conserve particle momentum at the expense of energy conservation for a closed system. There is an implicit alternative that allows energy conservation at the expense of global particle momentum conservation. An example of an implicit implementation can be found in Adam, Héron, and Laval, 2004 for electronic dynamics.

2.1.4 Conclusions on the explicit Particle-In-Cell algorithm

The explicit PIC algorithm was successfully applied to a collisionless sheath case in order to validate the code implementation, to understand the influence of discretization parameters and to evaluate the fluctuations present in the steady-state simulation. In the latter case, we observed that the amplitudes of density fluctuations did not correspond to the amplitudes of potential fluctuations when considering a scaling relationship via Poisson's equation. In fact, the statistical noise on the density completely covers the density fluctuations that would correspond to the potential fluctuations. The relation between these two quantities is therefore more complex. Nevertheless, we observe that the amplitude of both types of fluctuations decreases in $\frac{1}{\sqrt{n_{ppc}}}$ as the number of particles initially in the domain increases. These fluctuations are thus linked to the particle discretization parameter of the phase space. In addition, the fluctuations in the electric potential cancel out as the grid step tends towards zero. The first excited mode in Lieberman and Lichtenberg's collisionless sheath case therefore has a non-physical origin and is purely grid-related. The case of the Hall thruster is more complex, however, and an interaction between excited modes and plasma instabilities is suspected (Perez Luna, 2008; Coche, 2013). Such a study may therefore prove more interesting in the case of the thruster.

It was also possible to verify that the results converge towards the reference solutions derived from the Lieberman and Lichtenberg, 1994 model when the temporal and spatial discretization parameters tend towards zero. The number of particles in the simulation had no significant impact on the simulation results. However, it is expected to be significant in the case of the thruster and the numerical simulation of its instabilities (Boeuf and Garrigues, 2018; Tavassoli et al., 2023). The ranges of values tested for the various discretization parameters showed that the Bohm criterion was assured to within one grid step for:

$$\frac{v_{th,e}\Delta t}{\Delta x} < 0.13$$

When this ratio exceeds 2, inconsistent results were found. This shows that the CFL condition can play a very important role in the validity of results. When the CFL condition is sufficiently satisfied for the results to be consistent, we observe that a grid step verifying $\frac{\Delta x}{\lambda_{De}} \leq 1$ results in only a few percent error on the reference values of the electric potential derived from the Lieberman and Lichtenberg model.

We also try to check that the fluid moments are respected by introducing ratios between quantities that should cancel out and values chosen as a reference for each of the fluid moments. When we compare the trends observed for these ratios with those observed for the validity of the simulation results, we observe a similar behavior for the spatial and temporal discretization parameters. Similar ratios can thus be introduced in three dimensions and for cases with no reference solution, in order to study the influence of numerical spatial and temporal discretization parameters. For the particle discretization parameter, it is preferable to control noise directly by calculating standard deviations of electric potential or charge density. It should also

be noted that it would be possible to determine grid-related modes by measuring the standard deviation of the electric potential as a function of the grid step when the other discretization parameters are fixed.

2.2 The Sparse method

2.2.1 Principle and definitions

The parsimonious grid approach, also known as sparse grids, is based on the principle of representing a space of functions or a function, with a reduced number of degrees of freedom compared to a conventional grid. The idea is to cleverly use a reduced number of approximation functions to represent a high-dimensional solution for which a certain regularity is assumed.
This approach was first applied in Smolyak, 1963 for quadrature problems. It was then developed for applications to the discretization of partial differential equations and also coupled to Galerkin's method in Zenger and Hackbusch, 1991; Bungartz and Griebel, 2004; Pommier, 2008. A summary of the sparse grid approach can be found in Garcke, 2013. However, we recommend a more comprehensive reading of Mario Heene's thesis (Heene, 2018) more focused on the grid combination method, but also Dirk Pflüger's thesis (Pflüger, 2010), whose presentation of sparse grids may help to clarify certain points.

In our study, we introduce the necessary notions from sparse grid theory, with the aim of coupling them to the PIC algorithm. Some commonly used representations of the theory can be modified for numerical application. In this case, the differences in representation will be specified. A number of notations are defined to provide a more rigorous framework for the sparse grid approach. Let be the space of dimension d: $\bar{\Omega} = [0, L]^d$ with L the characteristic length of the domain. In practice, we will restrict ourselves to $d \leq 3$. Note a point in space $\mathbf{x} := (x_1, ..., x_d)$. Let u be a function defined on $\bar{\Omega}$ with real values. The derivation operator is defined as:

$$D^{\mathbf{r}}u := \frac{\partial^{|\mathbf{r}|_1} u}{\partial^{r_1} x_1 ... \partial^{r_d} x_d}$$

where $\mathbf{r}$ is a d-tuple of real numbers $(r_1, ..., r_d)$ and where the norms are defined:

$$|\mathbf{r}|_1 = \sum_{i=1}^{d} r_i$$

$$|\mathbf{r}|_\infty = \max_{1 \leq i \leq d} |r_i|$$

In practice, we consider integer values $(r_1, r_2, r_3) \leq (4, 4, 4)$ and a variable $\mathbf{x} = (x_1, x_2, x_3)$ in three dimensions of space.

We introduce a space of functions for the application of the sparse approach such that the Hölder norm of mixed derivatives is bounded. Let be the set of continuous

functions u such that for any $|\mathbf{r}|_\infty \leq m$ ($m \in \mathbb{N}$), $D^{\mathbf{r}}u$ is continuous and bounded by a constant K:

$$C^{m,K}_{mix}(\bar{\Omega}) := \left\{ u \in C^0(\bar{\Omega}),\ D^{\mathbf{r}}u \in C^0(\bar{\Omega}),\ |\mathbf{r}|_\infty \leq m,\ ||D^{\mathbf{r}}u||_{C^0} \leq K \right\}$$

Let Φ a physical solution on the domain $\bar{\Omega}$ which we assume to belong to $C^{2,K}_{mix}(\bar{\Omega})$. A classical approximation of the solution is based on a Cartesian grid $\Omega_{\mathbf{l}}$ where $\mathbf{l} = (l_1, ..., l_d) \in \mathbb{N}^d$ and defining a grid step $h_{\mathbf{l}} = (\frac{L}{2^{l_1}}, ..., \frac{L}{2^{l_d}})$. For simplicity's sake, we also assume that the solution cancels out at the edges, so that only interior points are considered for the formalism. Taking boundary conditions into account from a numerical point of view will be presented later with the grid combination method. The approximate solution is most often expressed in the basis created by the tensor product of unidimensional bases of hat functions defined for each dimension $j \in [1, d]$ as:

$$\left\{ \psi_{l_j,i_j}(x_j) := \left\{ \begin{array}{l} 1 - |\frac{x_j - i_j \times h_{l_j}}{h_{l_j}}|\ if\ x_j \in [(i_j - 1) \times h_{l_j}, (i_j + 1) \times h_{l_j}] \\ 0\ elsewhere \end{array} \right\}, 1 \leq i_j \leq 2^{l_j} - 1 \right\}$$

whose notation after tensor reconstruction can be summarized as follows:

$$\left\{ \psi_{\mathbf{l},\mathbf{i}}(\mathbf{x}) := \prod_{j=1}^{d} \psi_{l_j,i_j}(x_j),\ \mathbf{1} \leq \mathbf{i} \leq \mathbf{2^l - 1} \right\}$$

The solution can also be approximated using the tensor product of unidimensional hierarchical bases defined as:

$$\left\{ \psi_{\mathbf{k},\mathbf{i}} : \mathbf{1} \leq \mathbf{i} \leq \mathbf{2^k - 1},\ i_j\ odd\ for\ all\ 1 \leq j \leq d,\ \mathbf{k} \leq \mathbf{l} \right\}$$

An example of a unidimensional hierarchical basis is shown in figure 2.21 for $l = (4)$.

The tensor product of unidimensional nodal or hierarchical bases gives an exact reconstruction of the finite-dimensional vector space $V_{\mathbf{l}}$ associated with the grid $\Omega_{\mathbf{l}}$. We can therefore note the expressions of the approximate solutions of the physical solution Φ in the nodal basis:

$$\Phi_{nodal}(\mathbf{x}) = \sum_{\mathbf{i}=\mathbf{1}}^{\mathbf{2^l - 1}} \prod_{j=1}^{d} \alpha_{l_j,i_j} \psi_{l_j,i_j}(x_j)$$

where the sum contains all the indexes of the interior points of the Cartesian grid $\Omega_{\mathbf{l}}$ and where α_{l_j,i_j} are the nodal coefficients,

and in the hierarchical basis:

$$\Phi_{hierarchical}(\mathbf{x}) = \sum_{\mathbf{k}=\mathbf{1}}^{\mathbf{l}} \sum_{\substack{\mathbf{i}=\mathbf{1} \\ i\ odd}}^{\mathbf{2^k - 1}} \prod_{j=1}^{d} \beta_{k_j,i_j} \psi_{k_j,i_j}(x_j)$$

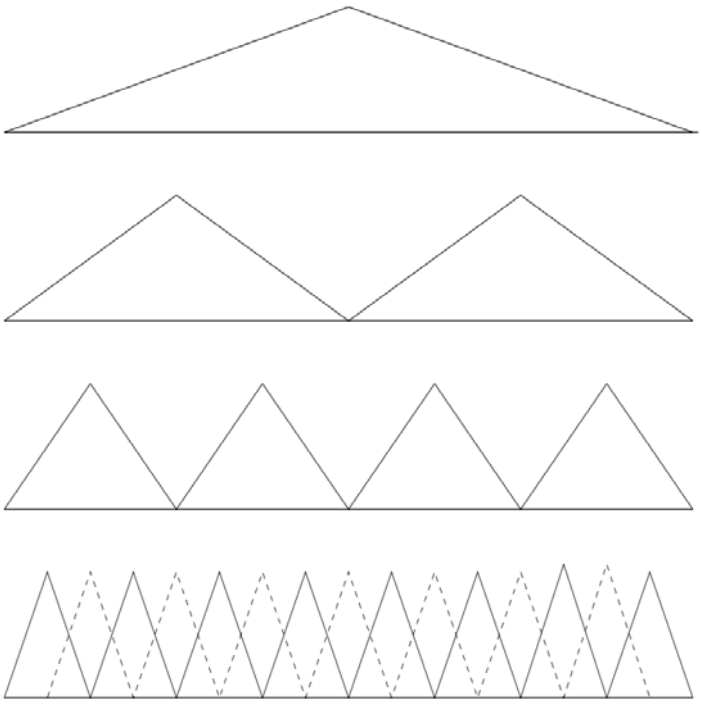

FIGURE 2.21: Hat functions hierarchical basis in solid line ($k = 1$ to 4, top to bottom), bottom level also has the nodal point basis in solid plus dashed line.

where the sums contain all the indexes of the interior points of the Cartesian grid $\Omega_{\mathbf{l}}$ and the β_{k_j,i_j} are the hierarchical coefficients.

Let us take a unidimensional example of a sine function to illustrate the representation of the function in the nodal and hierarchical bases. Let:

$$f := \left\{ \begin{array}{l} [0,1] \rightarrow [0,1] \\ x \rightarrow sin(\pi x) \end{array} \right\}$$

This function can be decomposed in the nodal basis of the finite-dimensional vector space $V_{(3)}$ associated with the grid $\Omega_{(3)}$ as follows:

$$\begin{array}{c} f \approx 0.38\psi_{3,1} + 0.71\psi_{3,2} + 0.92\psi_{3,3} + \psi_{3,4} \\ +0.92\psi_{3,5} + 0.71\psi_{3,6} + 0.38\psi_{3,7} \end{array}$$

Similarly, on a hierarchical basis, it decomposes as follows:

$$\begin{array}{c} f \approx 0.03\psi_{3,1} + 0.21\psi_{2,1} + 0.07\psi_{3,3} + \psi_{1,1} \\ +0.07\psi_{3,5} + 0.21\psi_{2,3} + 0.03\psi_{3,7} \end{array}$$

Figure 2.22 shows the nodal representation of the function f and figure 2.23 shows the hierarchical representation of the function f associated with the grid $\Omega_{(3)}$.

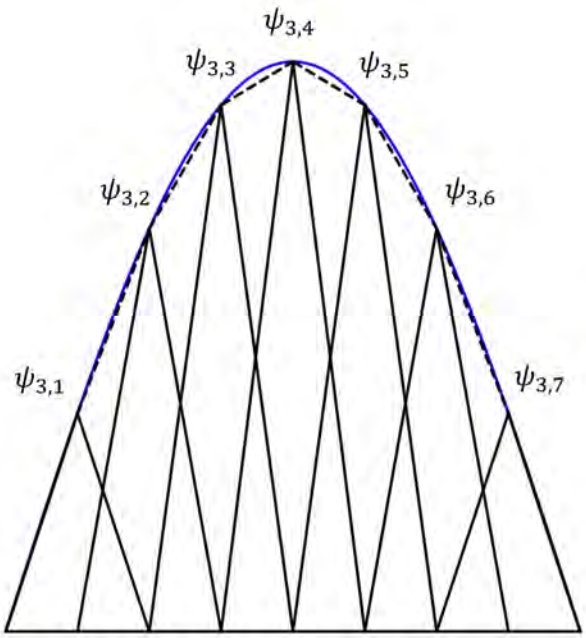

FIGURE 2.22: Nodal basis representation of the sinus function.

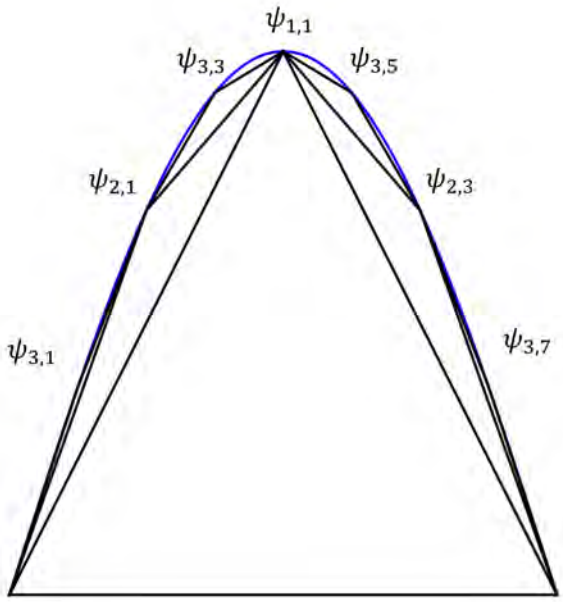

FIGURE 2.23: Hierarchical basis representation of the sinus function.

As previously stated, these two representations of the function are equivalent in one dimension. Hierarchical coefficients are calculated using the algorithm presented below in the sub-section entitled "Hierarchization". Note that for the sine function taken as an example, the hierarchical coefficients decrease with hierarchical level k, so that the coefficients of the next levels can be neglected in front of those of the first levels. While this works for the particular case of the one-dimensional

sine function, this logic is particularly useful in multiple dimensions. In this way, we can take advantage of the hierarchy of basis functions to eliminate certain basis function products in the d-dimensional tensor reconstruction, whose hierarchical coefficients β_{k_j,i_j} are considered negligible compared with those that are retained. Part of the method's efficiency therefore depends on the choice of coefficients to be cancelled out, depending on the type of solution expected. We then present a method for combining sub-grids to reconstruct the physical solution on the nodal grid at a reduced cost. Its practical implementation requires the introduction of a hierarchy of sub-grids.

2.2.2 Hierarchy of sub-grids

We introduce sub-grids associated with levels $\mathbf{1} \leq \mathbf{k} \leq \mathbf{l}$ whose nodes correspond to the tensor product of functions $\psi_{\mathbf{k},\mathbf{i}}$ for odd $\mathbf{i}$ such that $\mathbf{1} \leq \mathbf{i} \leq \mathbf{2^k} - \mathbf{1}$. The choice of which sub-grids to keep affects the choice of which hierarchical coefficients to keep. A sparse grid of level $\mathbf{l} = (n, ..., n)$ contains all subgrids of lower levels $\mathbf{k}$ such that $|\mathbf{k}|_1 \leq n + d - 1$. This choice of sub-grids has been shown to be the most optimal for functions belonging to $C^{2,K}_{mix}(\bar{\Omega})$ in Bungartz and Griebel, 2004. Figure 2.24 illustrates this principle.

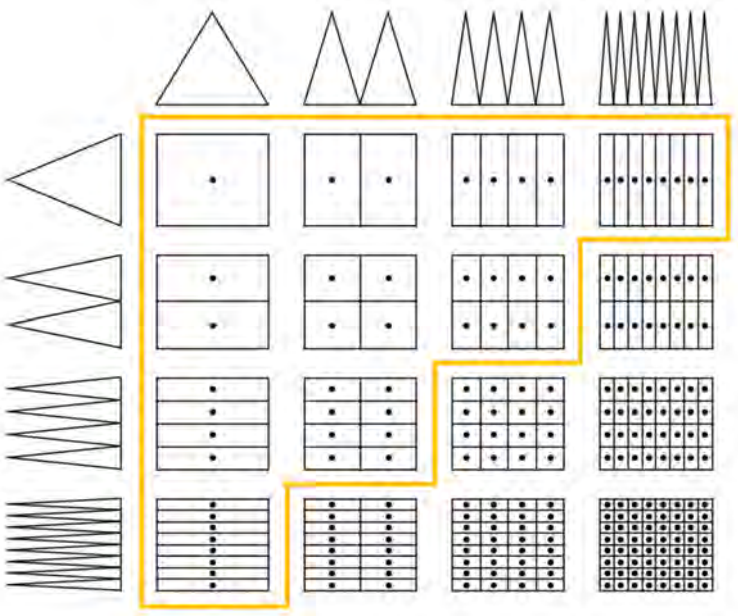

FIGURE 2.24: Choice of sub-grids based on hierarchical basis functions product tensor, example with sparse grid level n=4 containing all sub-grids of lower levels $k_1 + k_2 \leq 5$ for dimension d=2.

An example of the sparse grid thus obtained is shown in figure 2.25 without considering the points at the edges.

This is the most common representation of sparse grids. Note that the sparse grid can be constructed anisotropically by considering different l_j levels in the j directions. Let us take up our example of the sine function presented earlier, but this

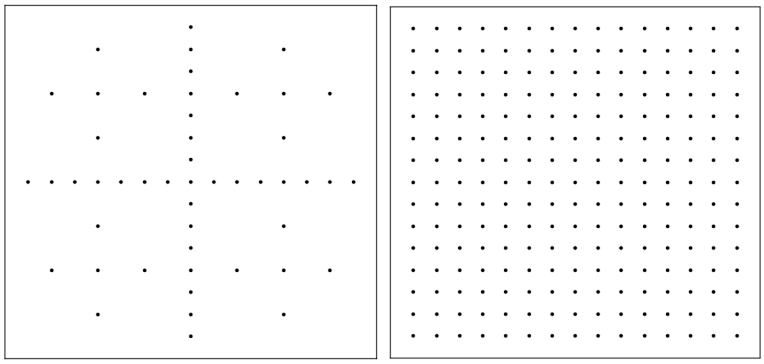

FIGURE 2.25: Isotropic sparse grid with level n=4 (left), nodal basis grid (right) for dimension d=2.

time in two dimensions. Let:

$$f := \left\{ \begin{array}{l} [0,1]^2 \rightarrow [0,1]^2 \\ (x,y) \rightarrow sin(\pi x) sin(\pi y) \end{array} \right\}$$

We calculate the hierarchical coefficients grouped by product of basis functions, let the $\beta_{\mathbf{k},\mathbf{i}}$ such that:

$$\Phi_{hierarchical}(\mathbf{x}) = \sum_{\mathbf{k}=\mathbf{1}}^{\mathbf{l}} \sum_{\substack{\mathbf{i}=\mathbf{1} \\ i\, odd}}^{\mathbf{2^k-1}} \beta_{\mathbf{k},\mathbf{i}} \prod_{j=1}^{d} \psi_{k_j,i_j}(x_j)$$

Each node in figure 2.24 corresponds to a hierarchical coefficient. Figure 2.26 shows the maximum absolute value of the hierarchical coefficients $\beta_{\mathbf{k},\mathbf{i}}$ for all $\mathbf{i} = (i_1, i_2) \in [\![\mathbf{1}, \mathbf{2^k - 1}]\!]$ associated with each sub-grid level $\mathbf{k} = (k_1, k_2)$.

In the particular case of the function f defined above in two dimensions, we observe, for example, that the hierarchical coefficients of the $\mathbf{k} = (2,2)$ level sub-grid are an order of magnitude lower than the hierarchical coefficients of the $\mathbf{k} = (1,1)$ level sub-grid. An optimized construction of the function approximation could be to neglect this sub-grid and therefore the hierarchical coefficients $\beta_{(2,2),\mathbf{i}}$ in its hierarchical basis representation. If we go into more detail, we can neglect certain hierarchical coefficients in each sub-grid. However, applications of the Sparse method does not always allow us to know the type of solution we want to approximate. For this reason, the sparse grid construction method from Bungartz and Griebel, 2004 was presented and gives an optimal construction for any function belonging to $C^{2,K}_{mix}(\bar{\Omega})$.

However, this sparse grid construction is not very practical for application to the PIC algorithm and the solution of partial differential equations. An alternative construction method is presented, which makes use of sub-grids with regular grid steps on which classical differentiation can be used to solve the Poisson's equation.

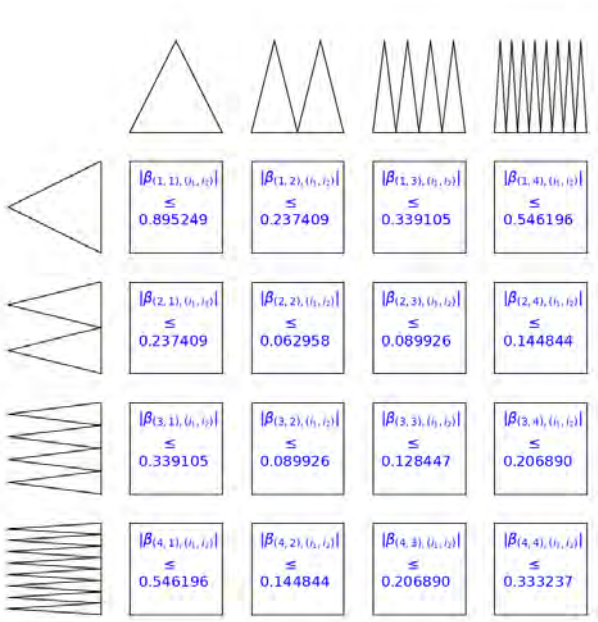

FIGURE 2.26: Maximum absolute value of hierarchical coefficients $\beta_{\mathbf{k},\mathbf{i}}$ for each sub-grid, example with double sinus function and grid level n=4 for dimension d=2.

Another way of constructing the sparse grid is to introduce a sub-grid combination technique. This is based on the principle of error cancellation, noting that sub-grids of level $|\mathbf{k}|_1 = n + d - 1$ and level $|\mathbf{k}|_1 = n + d$ have similar discretization levels in some directions. By combining these sub-grids, these discretization errors can be eliminated, so that only the discretization errors associated with level n remain. This is the method we choose to implement to reconstruct the solution on the grid with a view to coupling it to the PIC algorithm, in a manner similar to that developed in Ricketson and Cerfon, 2016. The differences with the Sparse-PIC algorithm presented in Ricketson and Cerfon, 2016 will be presented in section 2.3. The classical sub-grid combination technique was developed in Griebel et al., 1992 and is inspired by Smolyak's work (Smolyak, 1963). We then use another representation of these sub-grids which includes additional points corresponding to the "ancestors" for each sub-grid that we will define next. These additional points naturally include the domain edges for each sub-grid. Figure 2.27 illustrates the new sub-grids.

The new sparse grid construction is based on knowing the approximated solution in the nodal basis on all the sub-grids selected for the combination technique. Several quantities can be chosen in the PIC algorithm to be approximated with the Sparse method. Note that if only charge density is chosen, no differentiation is used on the sub-grids. If we choose to approximate the potential or the electric field with the Sparse method, we have to solve Poisson's equation on each sub-grid. The adaptation of the Sparse method to the PIC algorithm is developed in more detail

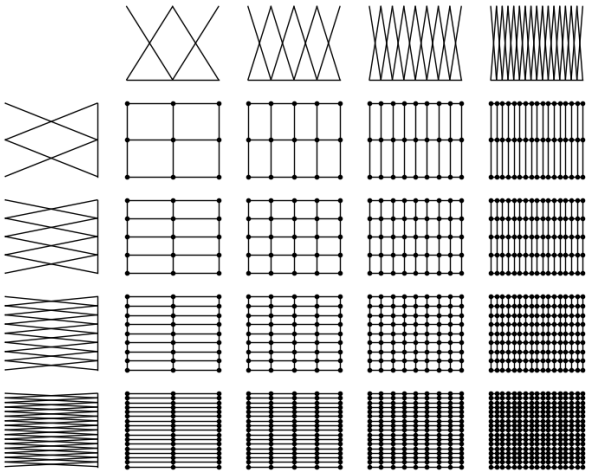

FIGURE 2.27: Sub-grids based on hierarchical basis functions product tensor with ancestors nodes, example with grid level n=4 for dimension d=2.

in section 2.3. The focus here is on the reconstruction of the physical solution on the full regular grid $\Omega_{\mathbf{l}}$ based on the previously defined hierarchy of sub-grids, in three steps. The nodal coefficients of the sub-grids are passed into the hierarchical basis associated with their sub-grid, this is called hierarchization. The sub-grids are combined in the hierarchical basis to obtain the sparse grid. The hierarchical coefficients are passed to the nodal basis to find the solution on the nodal grid, this is called dehierarchization. These three steps are described in detail below.

2.2.3 Hierarchization

We have seen that the physical solution can be expressed in two different bases: the nodal basis associated with the Cartesian grid and the hierarchical basis which, when certain components are removed, is associated with the sparse grid. Adapting the Sparse method to partial differential equations requires the ability to switch from one basis to the other. In particular, we differentiate on the nodal basis, while operations such as addition, subtraction, multiplication and division can be performed more easily on the hierarchical basis. For this reason, sub-grids are combined on a hierarchical basis. Hierarchization is the transition from the nodal basis to the hierarchical basis. Dehierarchization, which we will introduce a little later, is the transition from hierarchical to nodal basis. The change of basis is based on the following unidirectional relation for a grid $\Omega_{\mathbf{l}}$ and for $j \in [1, d]$, $\mathbf{1} \leq \mathbf{k} \leq \mathbf{l}$, $\mathbf{1} \leq \mathbf{i} \leq \mathbf{2^k - 1}$:

$$\beta_{k_j,i_j} = \Phi_{nodal}(i_j \times h_{k_j}) - \frac{1}{2}\left[\Phi_{nodal}(\frac{i_j - 1}{2} \times h_{k_j - 1}) + \Phi_{nodal}(\frac{i_j + 1}{2} \times h_{k_j - 1})\right]$$

where β_{k_j,i_j} is the hierarchical coefficient associated with the point $i_j \times h_{k_j}$ and where we remind you that $\alpha_{k_j,i_j} = \Phi_{nodal}(i_j \times h_{k_j})$ are the nodal coefficients in direction j. The points in the bracketed term $\frac{i_j-1}{2} \times h_{k_j-1}$ and $\frac{i_j+1}{2} \times h_{k_j-1}$ are called **ancestors or hierarchical predecessors** of the point $i_j \times h_{k_j}$. They belong to the lower hierarchical level. In practice, we apply the d-dimensional algorithm 1 found in Jacob, 2014; Guillet, 2023 for each sub-grid.

Algorithm 1 Hierarchization in d dimensions

Require: sub-grid level in each direction $\mathbf{k} = (k_1, ..., k_d)$, values at the nodal grid points stored in array[:]
Ensure: hierarchical coefficients stored in array[:]
  for $j = 1$ **to** d **do**
    for $p = k_j$ **downto** 1 **do**
      for all nodes **x** of hierarchical level (...,k_{j-1},p,k_{j+1},...) **do**
        Let x_l be the left hierarchical ancestor of **x** in dimension j
        Let x_r be the right hierarchical ancestor of **x** in dimension j
        $array\,[\mathbf{x}] \leftarrow array\,[\mathbf{x}] - \frac{1}{2}(array\,[\mathbf{x}_l] + array\,[\mathbf{x}_r])$
      end for
    end for
  end for

A representation of the algorithm applied to a two-dimensional sub-grid of level $\mathbf{k} = (1,2)$ is given in figure 2.28. The arrows point to the updated elements, also circled in red. The elements at the root of the arrows circled in blue are the ancestors of the points circled in red.

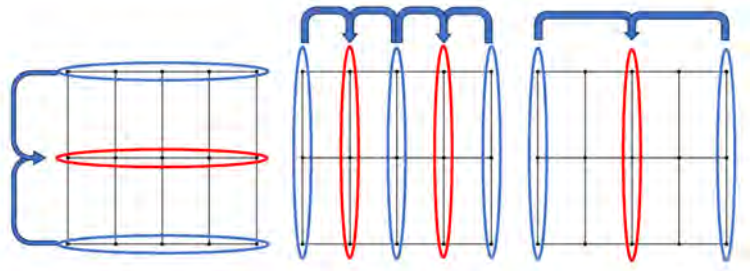

FIGURE 2.28: Hierarchization process on a $\mathbf{k} = (1,2)$ sub-grid, steps going from left to right.

The hierarchical algorithm shows the importance of knowing the boundary conditions of the domain. The first two "ancestors" are the points at the edges of the domain in the hierarchical direction under consideration.

2.2.4 Combination technique

The classical combination technique developed in Griebel et al., 1992 involves a combination of sub-grids as defined above for a regular grid $\Omega_\mathbf{l}$ with $\mathbf{l} = (n, ..., n)$

according to the relation:

$$\Phi_{sparsegrid,\mathbf{l}}(\mathbf{x}) = \sum_{j=0}^{d-1} (-1)^{d-1-j} \binom{d-1}{j} \sum_{|\mathbf{k}|_1 = n+j} \Phi_{subgrid,\mathbf{k}}(\mathbf{x}) \tag{2.1}$$

This relation can be calculated in either the nodal or hierarchical basis. However, the algorithm is potentially faster when the combination is performed in the hierarchical basis. In the nodal basis, the combination operation must be performed for each node of the regular grid $\Omega_n := \Omega_{(n,\dots,n)}$. In a hierarchical basis, only the nodes of the sub-grids associated with the sparse grid are used for the combination. If you choose to combine sub-grids on a hierarchical basis, the previous sub-grid hierarchization step and the subsequent dehierarchization step must be performed. Both methods are equivalent. The relation (2.1) gives in two dimensions:

$$\Phi_{sparsegrid,(n,n)}(\mathbf{x}) = \sum_{|\mathbf{k}|_1 = n+1} \Phi_{subgrid,\mathbf{k}}(\mathbf{x}) - \sum_{|\mathbf{k}|_1 = n} \Phi_{subgrid,\mathbf{k}}(\mathbf{x})$$

and in three dimensions:

$$\Phi_{sparsegrid,(n,n,n)}(\mathbf{x}) = \sum_{|\mathbf{k}|_1 = n+2} \Phi_{subgrid,\mathbf{k}}(\mathbf{x}) - 2 \sum_{|\mathbf{k}|_1 = n+1} \Phi_{subgrid,\mathbf{k}}(\mathbf{x}) + \sum_{|\mathbf{k}|_1 = n} \Phi_{subgrid,\mathbf{k}}(\mathbf{x})$$

An example of combination is given in two dimensions for n=2 in figure 2.29.

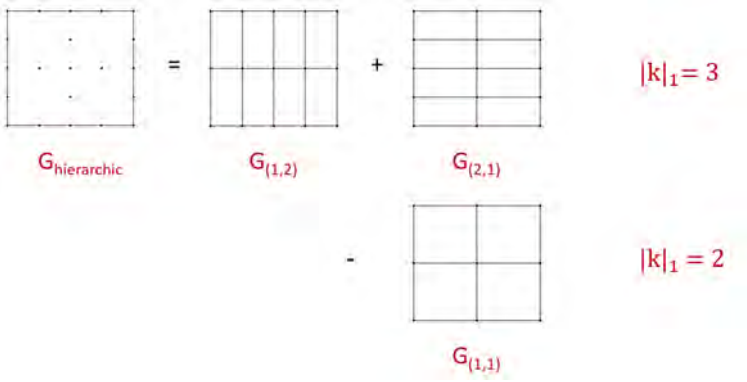

FIGURE 2.29: Combination technique example for n=2 in dimension d=2.

The error associated with the reconstruction of the solution by means of the combination technique for a $C^{2,K}_{mix}(\bar{\Omega})$ function on a Ω_n grid is in the order of $\Phi_{sparsegrid} - \Phi = O\left(h_n^2 |log\, h_n|^{d-1}\right)$. When coupled to the PIC algorithm, several reconstruction options are available, including particle density, potential or electric field. Clément Guillet's thesis (Guillet, 2023) gives an estimate of the dominant error terms for a reconstruction on density and electric field. These terms depend on second-order mixed derivatives for the density and fourth-order mixed derivatives for the electric field. These error terms are summarized in table 2.2.

TABLE 2.2: Density and electric field reconstruction errors for $||.||_\infty$ norm.

Scheme	Dominant term
Density-based reconstruction	$h_n^2 \lvert log\, h_n \rvert^{d-1} \lvert\lvert D^2\rho \rvert\rvert_\infty$
Electric field-based reconstruction	$h_n^2 \lvert log\, h_n \rvert^{d-1} \lvert\lvert D^4\mathbf{E} \rvert\rvert_\infty$

2.2.5 Dehierarchization

The dehierarchization algorithm is very similar to hierarchization. It uses the same unidirectional relation as hierarchization, but from the opposite point of view, let:

$$\Phi_{nodal}(i_j \times h_{k_j}) = \beta_{k_j,i_j} + \frac{1}{2}\left[\Phi_{nodal}(\frac{i_j-1}{2} \times h_{k_j-1}) + \Phi_{nodal}(\frac{i_j+1}{2} \times h_{k_j-1})\right]$$

This relation naturally implies starting the algorithm with the lowest hierarchical level, since we need to know the coefficients of the two hierarchical predecessors. We thus apply the d-dimensional algorithm 2 to the regular grid.

Algorithm 2 Dehierarchization in d dimensions

Require: Regular grid level in each direction $\mathbf{l} = (l_1, ..., l_d)$, values at the nodal grid points updated with hierarchization and combination process stored in array[:]
Ensure: nodal coefficients stored in array[:]
  for $j = 1$ **to** d **do**
    for $p = 1$ **to** k_j **do**
      for all nodes **x** of hierarchical level (...,l_{j-1},p,l_{j+1},...) **do**
        Let x_l be the left hierarchical ancestor of **x** in dimension j
        Let x_r be the right hierarchical ancestor of **x** in dimension j
        $array\,[\mathbf{x}] \leftarrow array\,[\mathbf{x}] + \frac{1}{2}(array\,[\mathbf{x}_l] + array\,[\mathbf{x}_r])$
      end for
    end for
  end for

An example is shown in figure 2.30. Similarly, the arrows point to the updated elements, also circled in red. The elements at the root of the arrows, circled in blue, are the ancestors of the points circled in red.

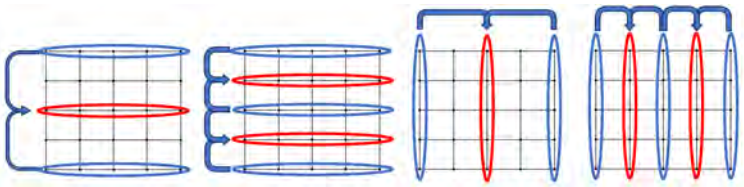

FIGURE 2.30: Dehierarchization process on a $\mathbf{l} = (2,2)$ full-grid, steps going from left to right.

2.2.6 Combination in nodal basis

The combination technique described above can also be implemented on a nodal basis without using the hierarchical basis, i.e. without hierarchization and dehierarchization. The principle is based on projecting at the position of the regular grid nodes (or at the position of the particles in the case of coupling to the PIC agorithm) the components of each of the sub-grids and combine them with the coefficients associated with each sub-grid according to the relation (2.1) but where $\Phi_{sparsegrid,\mathbf{l}}$ is replaced by $\Phi_{nodalgrid,\mathbf{l}}$. An explanatory diagram for a level (2,2) grid is given in figure 2.31.

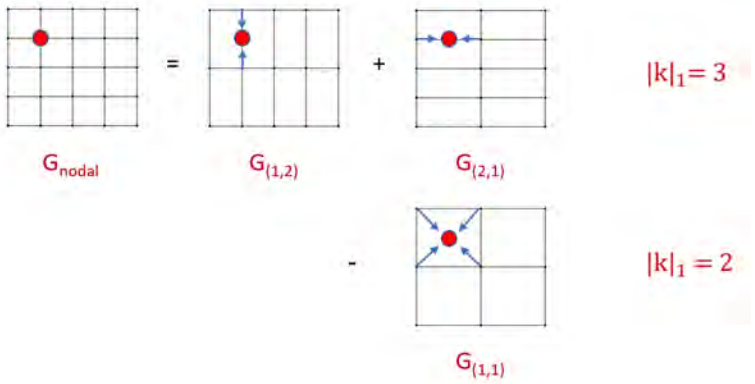

FIGURE 2.31: Nodal combination process on a $\mathbf{l} = (2,2)$ full-grid.

In practice, this combination in nodal basis can quickly become very costly in three dimensions when eight coefficients have to be projected onto a position for each of the sub-grids, whose number quickly reaches a hundred. The number of positions to be calculated is either the number of points in the regular grid or the number of particles in the case of coupling to the PIC algorithm. Although the calculation of projections can be efficiently parallelized, the number of operations is such that the combination technique in hierarchical basis (which can also be efficiently parallelized) is faster for the same cpus architecture, for grid levels equal to or greater than 7. This difference in performance is called into question when we consider coupling to the PIC algorithm (see section 2.3). To get an idea of the scales involved, we give a table 2.3 of the number of points per regular grid level and the number of associated sub-grids in three dimensions.

TABLE 2.3: Scaling of number of nodal grid points and number of sub-grids with grid level in three dimensions.

Grid level	Number of nodal grid points	Number of sub-grids
6	274 625	46
7	2 146 689	64
8	16 974 593	85
9	135 005 697	109
10	1 076 890 625	136

2.2.7 Application to Poisson's equation

The Poisson's equation (1.13) can admit an infinite number of solutions. For example, consider the sum of a particular solution (assuming it exists) and any polynomial of order less than or equal to 1 in (x,y,z) in Cartesian coordinates. To obtain a unique solution, boundary conditions must be imposed at the edges of the domain. The uniqueness of the solution to the Poisson's equation has been demonstrated for Dirichlet and Neumann conditions (apart from a constant which disappears in the calculation $\vec{E} = -\vec{\nabla}\Phi$) or a mixture of the two at the edges of the domain (Jackson, 1999, Chapter 1).
For periodic conditions at the edges of the Ω domain, we impose:

$$\int_\Omega \Delta\Phi d^3\vec{x} = \oint_{\partial S} \frac{\partial\Phi}{\partial\vec{n}} d\vec{S} = 0 = \int_\Omega -\frac{\rho}{\epsilon_0} d^3\vec{x}$$

This weak form of the equation (1.13) therefore imposes constraints on the form of the source term ρ, in particular charge neutrality at the domain scale.
From a numerical point of view, the discretization matrix of the second-order Laplacian operator in three dimensions with periodic conditions is symmetrical positive semi-definite. The numerical Poisson's equation then admits a solution unique to within one constant. When proposing manufactured solutions with periodic conditions, the previous constraint must be verified. Several cases of manufactured solutions are presented here to familiarize ourselves with the Sparse method.
A square domain in two dimensions (y,z) and a cubic domain in three dimensions (x,y,z) with side L are proposed. Several configurations of boundary conditions are considered: mixed Dirichlet-periodic, only Dirichlet, only periodic. In the mixed case, we impose Dirichlet conditions in one direction (Oz) (representing the electrodes in Chapter 3), and periodic conditions in the others (Ox) (Oy). The periodic conditions then impose in two dimensions that:

$$\forall z, \quad \frac{\partial\Phi(y = L, z)}{\partial y} = \frac{\partial\Phi(y = 0, z)}{\partial y}$$

which leads to:

$$\int_0^L \int_0^L \frac{\rho(y,z)}{\epsilon_0} dydz = -(\int_0^L \frac{\partial \Phi(y,z=L)}{\partial z} dy - \int_0^L \frac{\partial \Phi(y,z=0)}{\partial z} dy)$$

A similar relation is found in three dimensions. The mix of Dirichlet and periodic conditions no longer ensures charge neutrality at the domain scale. The charge difference over the domain depends on the outward derivatives of the potential at the boundaries where Dirichlet conditions are imposed. This enables notably the formation of sheaths at electrode boundaries where the electron density is lower than the ion density (Lieberman and Lichtenberg, 1994).

To better understand the Sparse method, we compare the solution reconstructed by the sub-grid combination technique after solving Poisson's equation on each sub-grid with the solution obtained by directly solving Poisson's equation on the regular grid. Thus, density profiles on each sub-grid and on the regular grid are given in input from a fixed theoretical profile, as well as the domain boundary conditions. To better control the results, we test several cases of manufactured solutions. In order to compare only the sparse and direct solving methods, we use the same PARDISO solver ("Parallel Direct Sparse solver", Schenk, Gärtner, and Fichtner, 2000) each time we solve the Poisson's equation.

Manufactured solutions: gradient without source term, mixed Dirichlet-periodic conditions

We first apply the Sparse algorithm to a simple potential gradient, imposing a potential difference between the two "electrodes" represented by Dirichlet conditions and a zero source term. An example of the chosen configuration in three dimensions is shown in figure 2.32.

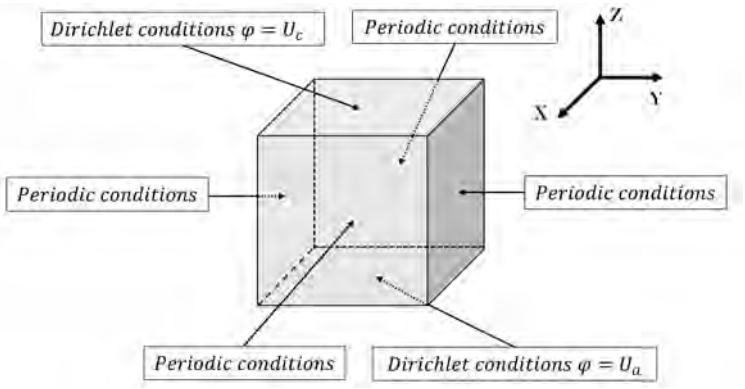

FIGURE 2.32: Mixed Dirichlet-periodic boundary conditions for a gradient test case.

Let us consider a reference solution $\Phi_{ref}(z) = (U_c - U_a)\frac{z}{L} + U_a$ with $U_a = 300V$, $U_c = 0V$, $L = 2cm$ (order of magnitude of the channel length of a PPS-1350ML Hall

TABLE 2.4: Comparison of the errors obtained with PARDISO for the direct solving of the linear system $K\Phi = 0$ and for the solving via the Sparse method. Manufactured solutions: gradient without source term.

Method	Max error	Norm L2 relative error	Norm L1 relative error
Direct 2D	4.74×10^{-13}	2.21×10^{-13}	3.07×10^{-13}
Sparse 2D	2.03×10^{-12}	9.82×10^{-13}	1.37×10^{-12}
Direct 3D	3.45×10^{-12}	1.64×10^{-12}	2.28×10^{-12}
Sparse 3D	2.22×10^{-12}	1.07×10^{-12}	1.49×10^{-12}

thruster) and simply $\rho = 0$. This is compatible with mixed boundary conditions, because:

$$\int_0^L \int_0^L \frac{\rho(y,z)}{\epsilon_0} dydz = -\int_0^L (\frac{\partial\Phi(y,z=L)}{\partial z} - \frac{\partial\Phi(y,z=0)}{\partial z})dy = 0$$

The potential gradient is constant and does not change sign, so the term under the right-hand integral is zero. We define the maximum error as:

$$\epsilon_{max} = max(\frac{|\Phi - \Phi_{ref}|}{\Phi_{ref}})$$

The L1 norm relative error:

$$\epsilon_{r,L1} = \frac{1}{N_g} \sum_{i=1}^{N_g} \frac{|\Phi(i) - \Phi_{ref}(i)|}{|\Phi_{ref}(i)|}$$

The L2 norm relative error:

$$\epsilon_{r,L2} = \sqrt{\frac{\sum_{i=1}^{N_g} (\Phi(i) - \Phi_{ref}(i))^2}{\sum_{i=1}^{N_g} \Phi_{ref}(i)^2}}$$

with N_g the number of grid points.

The potential errors obtained are shown in the table 2.4 for a 128^2-cells grid in two dimensions and a 128^3-cells grid in three dimensions.

The Sparse method fulfils its role in this simple case, and has errors of the same order as a classical solver. If the errors are indeed very small, it may nevertheless be interesting to see how they are distributed on the grid. Figures A.1,A.2 and A.3 in appendix A show the deviations from the exact solution of the potential and from the y and z components of the electric field in two dimensions. Figures A.4 and A.5 show deviations from the exact solution for the potential in three dimensions.

Manufactured solutions: spatial oscillation

We saw in section 2.1 that spatial oscillations in the electric potential could potentially be excited by particles. These oscillations can also be caused by the discretization linked to the computational grid. Uncertainty as to their role and importance has led us to study in greater detail the behavior of the Sparse method in the face of spatial oscillations in charge density. A second case is thus presented, this time considering a non-zero source term with periodic conditions at the boundaries and then with Dirichlet conditions. In the periodic case, we consider $\rho(y,z) = \rho_0 cos(k_y y)cos(k_z z)$ in two dimensions and $\rho(x,y,z) = \rho_0 cos(k_x x)cos(k_y y)cos(k_z z)$ in three dimensions. The integral over the volume of ρ gives in two dimensions:

$$\int_0^L \int_0^L \rho(y,z)dydz = \rho_0 \frac{sin(k_y L)sin(k_z L)}{k_y k_z}$$

and in three dimensions:

$$\int_0^L \int_0^L \int_0^L \rho(x,y,z)dxdydz = \rho_0 \frac{sin(k_x L)sin(k_y L)sin(k_z L)}{k_x k_y k_z}$$

The shape of the potential is (apart from one constant for periodic conditions) in two dimensions:

$$\Phi_{ref}(y,z) = \delta\Phi cos(k_y y)cos(k_z z)$$

and in three dimensions:

$$\Phi_{ref}(x,y,z) = \delta\Phi cos(k_x x)cos(k_y y)cos(k_z z)$$

Periodic conditions require that $k_x = \frac{2\pi m}{L}$,$k_y = \frac{2\pi n}{L}$ and $k_z = \frac{2\pi p}{L}$ with m, n, p integers. These expressions for potential and density verify that:

$$\oint_{\partial S} \frac{\partial \Phi}{\partial \vec{n}} d\vec{S} = \int_\Omega -\frac{\rho}{\epsilon_0} d^3\vec{x} = 0$$

It remains to verify the strong form of Poisson's equation, i.e. $-\Delta\Phi = \frac{\rho}{\epsilon_0}$ at any point in the domain. This imposes in two dimensions:

$$\rho_0 = \delta\Phi\epsilon_0(k_y^2 + k_z^2)$$

and in three dimensions:

$$\rho_0 = \delta\Phi\epsilon_0(k_x^2 + k_y^2 + k_z^2)$$

Similarly, for Dirichlet boundary conditions where $\Phi = 0V$ is imposed, we consider $\rho(y,z) = \rho_0 sin(k_y y)sin(k_z z)$ in two dimensions and $\rho(x,y,z) = \rho_0 sin(k_x x)sin(k_y y)sin(k_z z)$ in three dimensions. Dirichlet conditions require that $k_x = \frac{\pi m}{L}$,$k_y = \frac{\pi n}{L}$ and $k_z = \frac{\pi p}{L}$

with m, n, p integers. The integral over the volume of ρ gives in two dimensions:

$$\int_0^L \int_0^L \rho(y,z)dydz = \rho_0 \frac{(1-cos(k_y L))(1-cos(k_z L))}{k_y k_z}$$

and in three dimensions:

$$\int_0^L \int_0^L \int_0^L \rho(x,y,z)dxdydz = \rho_0 \frac{(1-cos(k_x L))(1-cos(k_y L))(1-cos(k_z L))}{k_x k_y k_z}$$

We can consider the shape of the potential in two dimensions:

$$\Phi_{ref}(y,z) = \delta\Phi sin(k_y y) sin(k_z z)$$

$$\oint_{\partial S} \frac{\partial \Phi}{\partial \vec{n}} d\vec{S} = \int_0^L (\frac{\partial \Phi(y, z=L)}{\partial z} - \frac{\partial \Phi(y, z=0)}{\partial z})dy + \int_0^L (\frac{\partial \Phi(y=L, z)}{\partial y} - \frac{\partial \Phi(y=0, z)}{\partial y})dz$$

$$\oint_{\partial S} \frac{\partial \Phi}{\partial \vec{n}} d\vec{S} = -\delta\Phi(\frac{k_z}{k_y} + \frac{k_y}{k_z})(1-cos(k_y L))(1-cos(k_z L))$$

and in three dimensions:

$$\Phi_{ref}(x,y,z) = \delta\Phi sin(k_x x) sin(k_y y) sin(k_z z)$$

$$\oint_{\partial S} \frac{\partial \Phi}{\partial \vec{n}} d\vec{S} = -\delta\Phi(\frac{k_z}{k_x k_y} + \frac{k_y}{k_x k_z} + \frac{k_x}{k_y k_z})(1-cos(k_x L))(1-cos(k_y L))(1-cos(k_z L))$$

These expressions for potential and density verify that:

$$\oint_{\partial S} \frac{\partial \Phi}{\partial \vec{n}} d\vec{S} = \int_\Omega -\frac{\rho}{\epsilon_0} d^3\vec{x}$$

so that in two dimensions:

$$\rho_0 = \delta\Phi\epsilon_0(k_y^2 + k_z^2)$$

and in three dimensions:

$$\rho_0 = \delta\Phi\epsilon_0(k_x^2 + k_y^2 + k_z^2)$$

The strong form of Poisson's equation $-\Delta\Phi = \frac{\rho}{\epsilon_0}$ is also verified at any point in the domain.

The maximum error is defined as:

$$\epsilon_{max} = max(\frac{|\Phi - \Phi_{ref}|}{\delta\Phi})$$

TABLE 2.5: Comparison of errors obtained with PARDISO for direct solving of the linear system $K\Phi = \rho$ and for solving via the Sparse method. Manufactured solutions: spatial oscillation with periodic conditions.

Method	Max error	Norm L2 relative error	Norm L1 relative error
Direct 2D	2.01×10^{-4}	1.01×10^{-4}	8.21×10^{-5}
Sparse 2D	1.57×10^{-3}	5.28×10^{-4}	4.12×10^{-4}
Direct 3D	2.01×10^{-4}	7.18×10^{-5}	5.25×10^{-5}
Sparse 3D	6.02×10^{-3}	1.64×10^{-3}	1.25×10^{-3}

The L1 norm relative error:

$$\epsilon_{r,L1} = \frac{1}{N_g} \sum_{i=1}^{N_g} \frac{|\Phi(i) - \Phi_{ref}(i)|}{\delta\Phi}$$

The L2 norm relative error:

$$\epsilon_{r,L2} = \sqrt{\frac{\sum_{i=1}^{N_g} (\Phi(i) - \Phi_{ref}(i))^2}{N_g \delta\Phi^2}}$$

with N_g the number of grid points.

Since the potential is defined to within one constant in the case of periodic conditions, the potential profiles are deducted from their mean value for error calculation. We begin by testing the periodic conditions on a simple case. We present the potential errors obtained in table 2.5 for $L = 2cm$, $\delta\Phi = 1V$, $k_x = k_y = k_z = \frac{2\pi}{L}$, a grid of 128^2 cells in two dimensions and 128^3 cells in three dimensions.

The errors obtained for both methods are comparable. Figures A.6,A.7 and A.8 in appendix A show the relative errors for the potential and for the y and z components of the electric field in two dimensions taking the value of the exact field amplitude as a reference.

We now consider the limits of the Sparse method in the periodic case, taking smaller wavelengths, which is equivalent to larger n for $k_x = k_y = k_z = \frac{2\pi n}{L}$ under periodic conditions and $k_x = k_y = k_z = \frac{\pi n}{L}$ under Dirichlet conditions. We can approach the problem posed by fixing either the amplitude ρ_0 or $\delta\Phi$. We consider amplitudes of an order of magnitude close to that determined by the sheath case in sub-section 2.1.2. For the first n modes, we choose to fix $\delta\Phi = 0.5V$ until the corresponding amplitude ρ_0 reaches or exceeds the order of magnitude of the amplitude of density fluctuations, such that $|n_i - n_e| \approx 3.5 \times 10^{15} m^{-3}$. When the previous condition is verified, we set $|n_i - n_e| = 3.5 \times 10^{15} m^{-3}$ equivalent to $\rho_0 = 5.6 \times 10^{-4} C.m^{-3}$ instead of $\delta\Phi$. Such a procedure could be adapted if we succeed in estimating the actual amplitudes of fluctuations in a Hall current thruster.

An experimental estimate of particle density fluctuations using collective light scattering diagnostics for the Hall current thruster (Tsikata et al., 2010) gives an order of magnitude of $10^{15}m^{-3}$ for an average particle density of the order of $10^{17}m^{-3}$. This places us in conditions a priori close to those of the thruster. If we take a closer look at the electron drift instability linked or not to the cyclotron resonance (EDI or ECDI) assumed to be present in the thruster, then preferred modes could be excited. Previous modelling work to determine these modes has been used to establish the scope of our study. Philippe Coche's thesis (Coche, 2013, chapter 5) gives resonant principal modes of less than $n = 12$ in the case of a single-mode spatial oscillation with a collisionless test particle model, and closer to $n = 3$ in a PIC model of the thruster with collisions in a zone of low neutral density of the order of $3.10^{18}m^{-3}$. We thus focus on the first 12 modes and we present the results in two dimensions for the direct and Sparse solving methods in figures 2.33, 2.34 and 2.35 for grids of 128^2, 256^2, 512^2 cells.

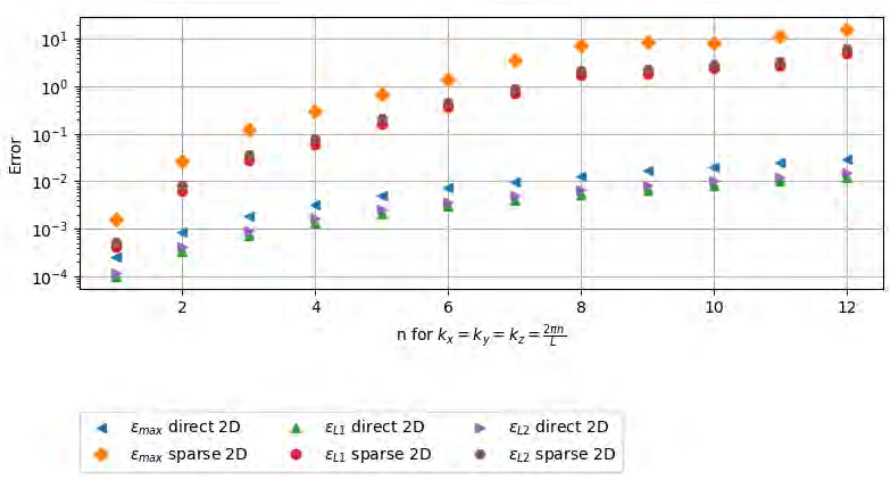

FIGURE 2.33: Relative errors with mode n for a 128^2-cells grid.

Appendix A shows in figures A.9, A.10 and A.11 the potential profiles obtained as a function of mode n for the first twelve modes. For a l-level grid with 2^{2l} cells, we observe a good representation of the electric potential by the Sparse method for the first 4, 6, 8 modes respectively for $l = 7$, 8 and 9.
In three dimensions, the behavior of the Sparse method is different and shows instabilities for the $n = 8$ mode, as shown in figure 2.36.

Only the first two modes are well represented in three dimensions. This suggests that the Sparse method used is of limited interest for the study of small-wavelength spatial oscillations in three dimensions for periodic conditions at the boundaries. However, it is still adequate in two dimensions when the modes studied are smaller than $n = 8$, or else require a higher grid level.

In the case of Dirichlet conditions, the Sparse method gets similar results in two dimensions and slightly better in three dimensions. We thus present the evolution of the L2 norm relative error as a function of modes n according to $k_x = k_y = k_z = \frac{\pi n}{L}$ in figures 2.37 and 2.38 for several grid levels. Note that the modes evolve in

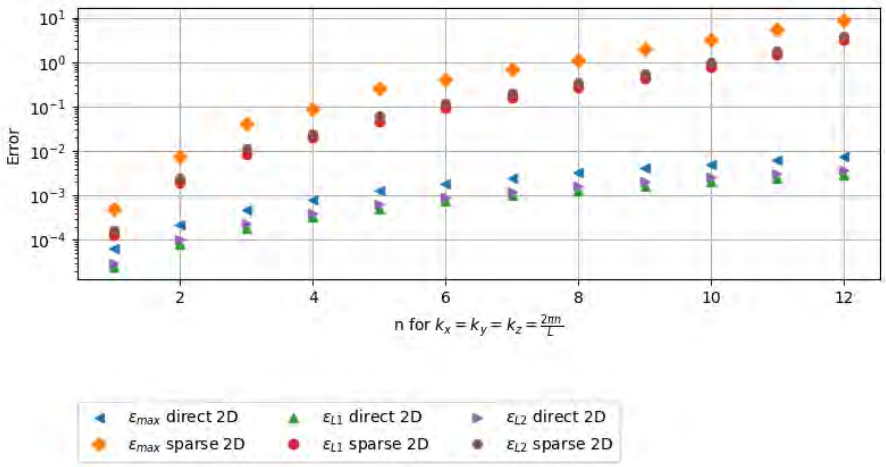

FIGURE 2.34: Relative errors with mode n for a 256^2-cells grid.

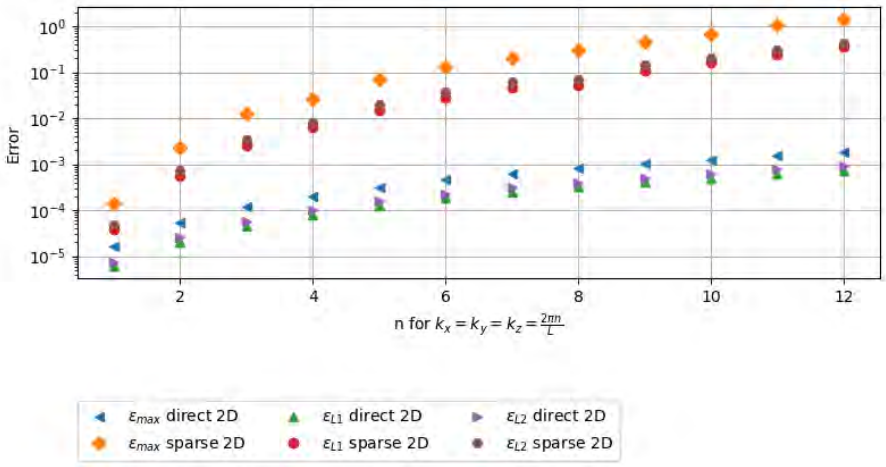

FIGURE 2.35: Relative errors with mode n for a 512^2-cells grid.

multiples of $\frac{\pi}{L}$ instead of $\frac{2\pi}{L}$ for the previous conditions, so we take interest in the first 24 modes.

In two dimensions, the Sparse method correctly represents the potential to within a few percent of L2 norm relative error for the first 8, 12 and 16 modes respectively for grid levels $l = 7$, $l = 8$, $l = 9$. In three dimensions, the Sparse method correctly represents the potential to within a few percent of L2 norm relative error for the first 4, 6 and 7 modes respectively for grid levels $l = 7$, $l = 8$, $l = 9$. Appendix A shows in figures A.12, A.13 and A.14 the potential profiles obtained as a function of mode n for the first twelve modes.

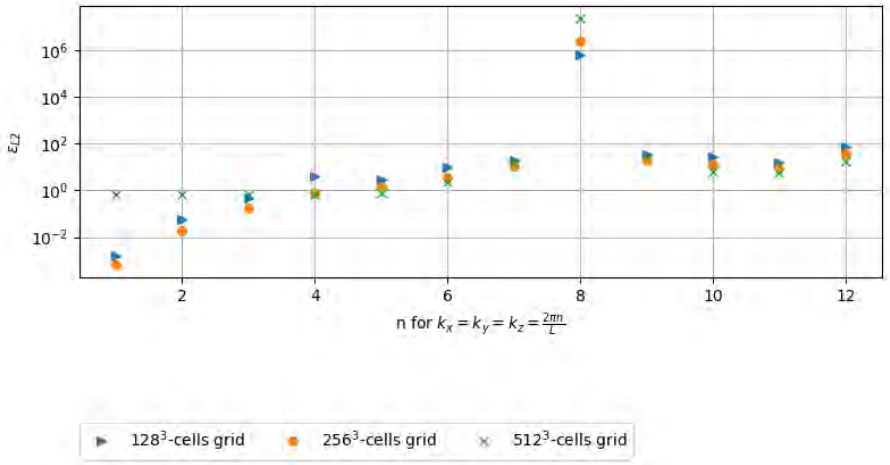

FIGURE 2.36: Relative error L2 with mode n for a 2^{3l}-cells grid ($l = 7$, $l = 8$, $l = 9$) in periodic conditions.

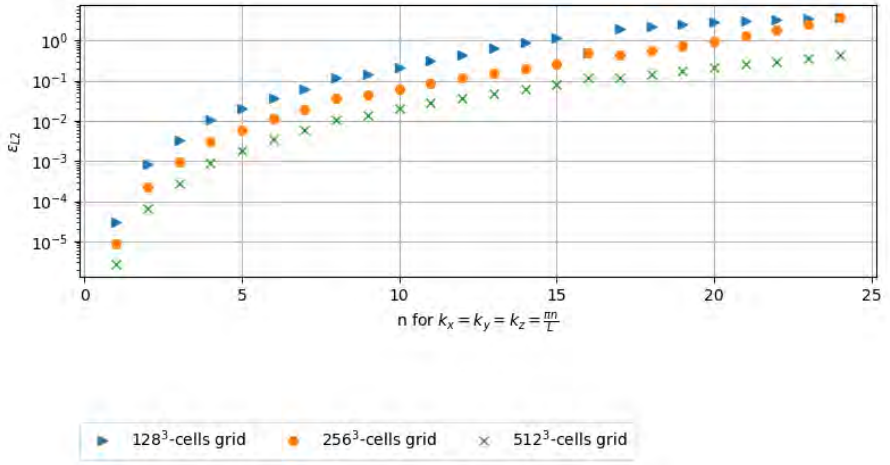

FIGURE 2.37: Relative error L2 with mode n for a 2^{2l}-cells grid ($l = 7$, $l = 8$, $l = 9$) in Dirichlet conditions.

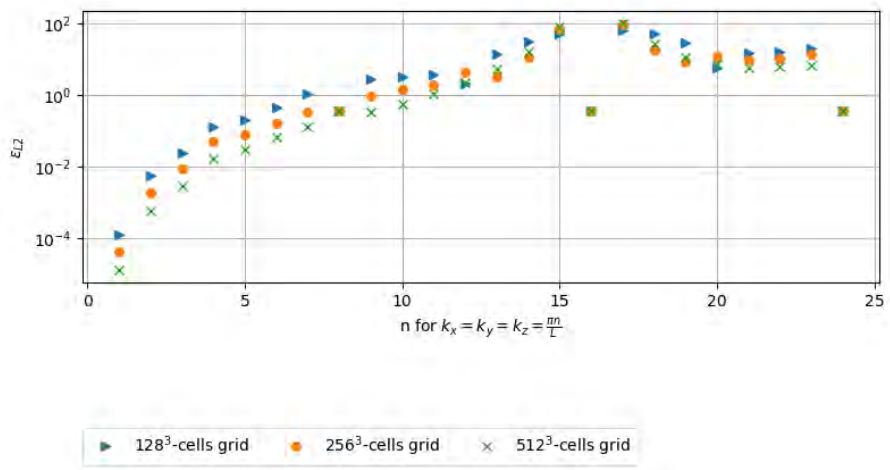

FIGURE 2.38: Relative error L2 with mode n for a 2^{3l}-cells grid ($l = 7$, $l = 8$, $l = 9$) in Dirichlet conditions.

Manufactured solutions: mathematical approximation of PIC simulation results

We can anticipate some PIC results in two and three dimensions for an ExB cross-field configuration typical of the Hall thruster (see Perez Luna, 2008 or chapter 3). It therefore seems more appropriate here to check that these profiles are well resolved by the Sparse method. These results suggest a mean potential in the direction (Oz) of the accelerating electric field (See $\vec{E}$ in figure 1.2) of the form:

$$\Phi(z) = \Phi_0 + \Phi_1 tanh(\frac{2\pi z}{L} - \pi)$$

If we impose Dirichlet conditions on the boundaries representing the electrodes at $z = 0$ (U_a) and $z = L$ (U_c), then we have:

$$\Phi_0 = \frac{U_a + U_c}{2}$$

and:

$$\Phi_1 = \frac{-(U_a - U_c)}{2}$$

considering that $tanh(-\pi) \approx -1$ and $tanh(\pi) \approx 1$. Such a potential profile for $U_a \neq U_c$ gives a density profile:

$$\rho(z) = \frac{8\pi^2\epsilon_0}{L^2}(\Phi(z) - \Phi_0)(1 - \frac{(\Phi(z) - \Phi_0)^2}{\Phi_1^2})$$

Examples of these two profiles for $U_a = 300V$ and $U_c = 0V$ are shown in figures 2.39 and 2.40.

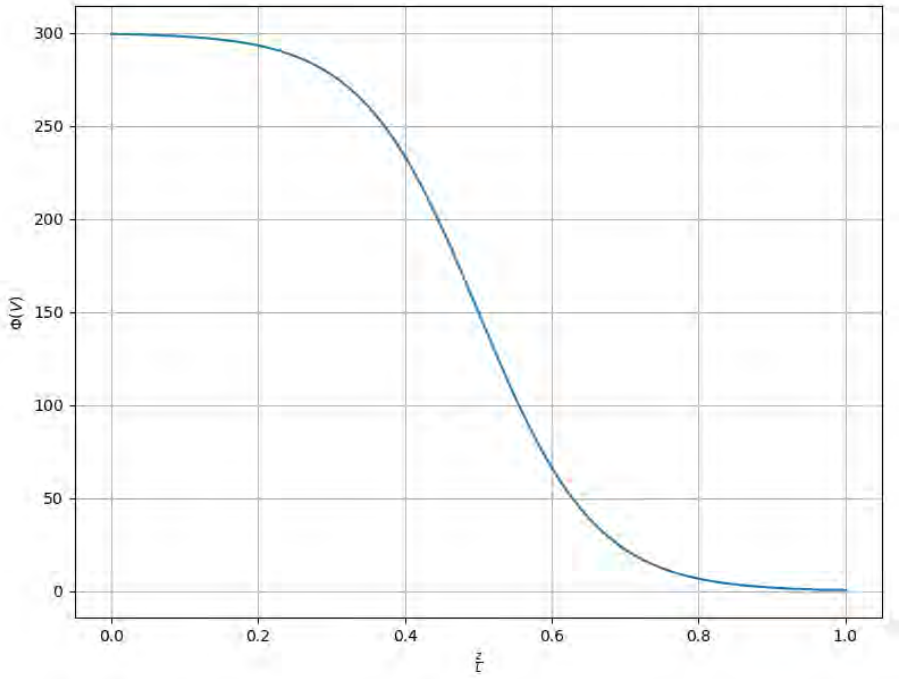

FIGURE 2.39: Hyperbolic tangent approximation of PIC electric potential in a Hall thruster.

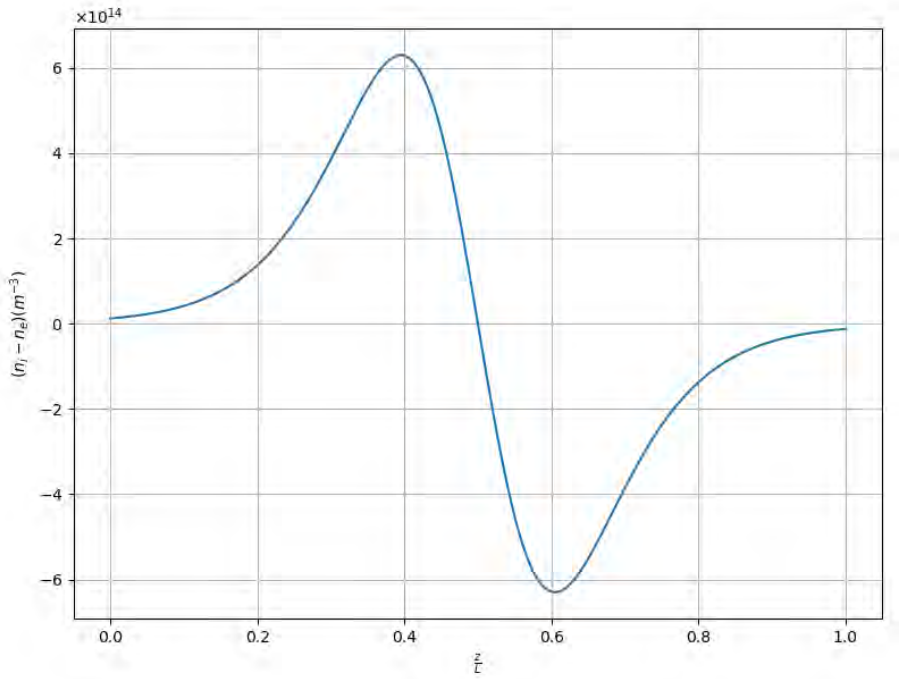

FIGURE 2.40: Density profile $(n_i - n_e)$ associated with the hyperbolic tangent electric potential in a Hall thruster.

TABLE 2.6: Errors obtained in the hyperbolic tangent test case for a 128^d-cell grid.

Method	Max error	Norm L2 relative error	Norm L1 relative error
Sparse 2D and 3D	3.72×10^{-3}	2.20×10^{-3}	1.94×10^{-3}

TABLE 2.7: Computational performance of Sparse method versus Direct method: given time is the mean computational time for a few steps solving Poisson equation.

Grid level	Direct 2D	Sparse 2D	Direct 3D	Sparse 3D
7	$1.4 \times 10^{-3}s$	$3.0 \times 10^{-4}s$	$1.0s$	$3.0 \times 10^{-2}s$
8	$3.5 \times 10^{-3}s$	$1.0 \times 10^{-3}s$	memory issue	$2.7 \times 10^{-1}s$
9	$1.5 \times 10^{-2}s$	$3.5 \times 10^{-3}s$	memory issue	$3.2s$

A first consideration is that statistical noise may cover this density profile so that it may not be directly visible when plotting the mean profile of $(n_i - n_e)$. Nevertheless, we can expect this profile to be correctly resolved by the Sparse method, given its regularity. This is what we verify here. We use the same error definitions as before, replacing $\delta\Phi$ by Φ_1. Table 2.6 gives the errors obtained for the Sparse method in two and three dimensions for a level 7 grid.

The Sparse method gives exact solutions to within one percent of relative error. This type of average electric potential solution obtained in PIC algorithms is therefore regular enough for the Sparse method to be applied.

Comparison of computation times: direct method vs. Sparse method

The above applications give an order of magnitude of the time required to solve the Poisson's equation, which is solved at each time step in the PIC algorithm. The performance of the direct solving method is compared with that of the Sparse solving method, using the PARDISO module ("Parallel Direct Sparse solver", Schenk, Gärtner, and Fichtner, 2000). It should be noted that hierarchization, combination and dehierarchization steps are included in the time computed for the Sparse method. The results are shown in table 2.7. Direct resolution via the PARDISO module in three dimensions does not allow us to handle cases with grid levels equal to 8 and 9 with our implementation. An error message indicating a memory issue is returned. We will note "memory issue" in the table when this occurs. Note that iterative methods exist to overcome this difficulty inherent in direct methods (See the PETSC module, Balay et al., 1998, or any other iterative solver).

There is a clear gain in performance over the direct solving method: a factor of 3 in two dimensions, and for the only data available in three dimensions, a factor of 33. This is not the only aspect of the Sparse method that delivers performance

gains. Coupling the Sparse method to the PIC algorithm also enables us to use fewer particles, as shown in section 2.3.

2.2.8 Variants of the Sparse method

We have seen that the application of the Sparse method is based on the construction of a unidimensional hierarchical basis. The introduction of a hierarchy of sub-grids follows from the tensor products of the hierarchical basis functions. This sub-grid hierarchy then forms the foundation of the sub-grid combination technique. The steps outlined above are based on Smolyak's hierarchical construction (Smolyak, 1963). Alternatives are possible. There are three key tools that can be replaced:

- The unidimensional basis functions.
- The unidimensional quadrature formula introducing a hierarchy of basis functions, which is then used to create the hierarchy of sub-grids by tensor product of these hierarchical basis functions.
- The sub-grid combination technique to eliminate discretization errors.

A final point to be discussed is the use of a 4th-order discretization for the Laplacian operator of the Poisson's equation. Its application to the Sparse method also requires an adaptation of the combination technique.

Change of basis functions

We have been using the hat basis functions ψ_{l_j,i_j} but we mention a possible choice of different basis functions such as B-spline functions of degree p on the support $[0, p+1]$ constructed by recursion (Farin, Hoschek, and Kim, 2002, Chapter 6, Pflüger, 2010, p.27-28):

$$\beta^0(x) := \left\{ \begin{array}{l} 1 \ if \ x \in [0,1] \\ 0 \ elsewhere \end{array} \right\}$$

$$\beta^p(x) := \frac{x}{p}\beta^{p-1}(x) + \frac{p+1-x}{p}\beta^{p-1}(x-1)$$

which gives the gate function for $p = 0$ and the hat function for $p = 1$. Once adapted to the grid, the B-spline functions of degree p become:

$$\psi^p_{l_j,i_j}(x_j) := \left\{ \begin{array}{l} \beta^p(\frac{x_j}{h_{l_j}} + \frac{p+1}{2} - i_j) \\ non-zero \ if \ \ x_j \in [(i_j-1)h_{l_j} - (p-1)h_{l_j+1}, (i_j+1)h_{l_j} + (p-1)h_{l_j+1}] \end{array} \right\}$$

We can also use other polynomial basis functions of degree $p_j \leq l_j + 1$ defined piecewise in each direction j (Bungartz and Griebel, 2004, Section 4.2, Pflüger, 2010, p.23-24). This first category of basis functions is also developed in more detail in Farin, Hoschek, and Kim, 2002, Chapter 6.

Wavelet basis functions constructed by multi-scale refinement using the Deslauriers-Dubuc method (Donoho and Yu, 1999, "interpolet", Bungartz and Griebel, 2004, Section 4.3). Wavelet basis functions whose derivatives at the edges of the supports cancel out ("wavelet", Bungartz and Griebel, 2004, Section 4.4, Pflüger, 2010, p.25-26). Note, however, that the choice of basis functions does not directly affect the construction of the sparse grid.

Quadrature formulas and sparse grid construction

The quadrature formulas also give rise to other types of Sparse grids, such as the Clenshaw-Curtis, Gauss-Patterson Lobatto and Gauss-Legendre grids (see Pommier, 2008 Chapter 2 for examples). Not all of these grids are compatible with the combination technique introduced earlier, and are therefore more difficult to couple with the PIC method. Nevertheless, it is a priori possible to find a suitable combination of sub-grids. Their effectiveness for plasma physics applications has yet to be demonstrated.

Modification of the combination technique: the truncation method

When combining sub-grids, it is possible to get rid of sub-grids whose discretization level is too low. This is the truncation method. Instead of considering the sub-grids resulting from equation (2.1), we use the relation:

$$\Phi_{sparsegrid,\mathbf{l}}(\mathbf{x}) = \sum_{j=0}^{d-1} (-1)^{d-1-j} \binom{d-1}{j} \sum_{\substack{|\mathbf{k}|_1 = n+j \\ \forall m \in [\![1;d]\!],\, k_m >= p_0}} \Phi_{subgrid,\mathbf{k}}(\mathbf{x}) \tag{2.2}$$

where p_0 is the minimum discretization level in each direction. This also reduces the number of points used to approximate the solution. This method is often coupled with the "offset" method introduced next.

Modification of the combination technique: the offset method

The offset method involves using a higher sub-grid level in the combination technique. Instead of using the relation (2.1), we use the relation:

$$\Phi_{sparsegrid,\mathbf{l}}(\mathbf{x}) = \sum_{j=0}^{d-1} (-1)^{d-1-j} \binom{d-1}{j} \sum_{|\mathbf{k}|_1 = n+j+p_1} \Phi_{subgrid,\mathbf{k}}(\mathbf{x}) \tag{2.3}$$

where $p_1 \in \mathbb{N}$, $n + p_1 >= d$ is the hierarchical level offset of the sub-grids.

This method is often coupled with the truncation method to maintain an error level equivalent to the classical combination technique (Heene, 2018, p.13-14).

The 4th-order finite difference scheme

The Poisson's equation can be discretized by 4th-order finite differences and the resulting scheme applied to the Sparse method for each sub-grid. Here we present the centered 4th-order finite-difference scheme from Straalen, 2017 in D dimensions:

$$-\sum_{d=1}^{D} \frac{-\Phi_{\mathbf{i}+2e^d} + 16\Phi_{\mathbf{i}+e^d} - 30\Phi_{\mathbf{i}} + 16\Phi_{\mathbf{i}-e^d} - \Phi_{\mathbf{i}-2e^d}}{12\Delta x_d^2} = \frac{\rho_{\mathbf{i}}}{\epsilon_0}$$

where $\Phi_{\mathbf{i}} = \Phi(i_1\Delta x, ..., i_D\Delta x)$, $\Phi_{\mathbf{i}+e^d} = \Phi(i_1\Delta x, ..., (i_d+1)\Delta x, ..., i_D\Delta x)$.

When applied to the Sparse method, we can expect to obtain better results for solutions with large second derivatives. Note that to use the 4th-order scheme, we need to use the truncation method to set the minimum level in each direction of the sub-grids to 2. We also apply the offset method to compensate for the loss of sub-grids, so that $p_0 = p_1 = 1$ as defined above. An example is given for the test case on spatial oscillations under Dirichlet conditions in figures 2.41 and 2.42 respectively in two and three dimensions for the Sparse method.

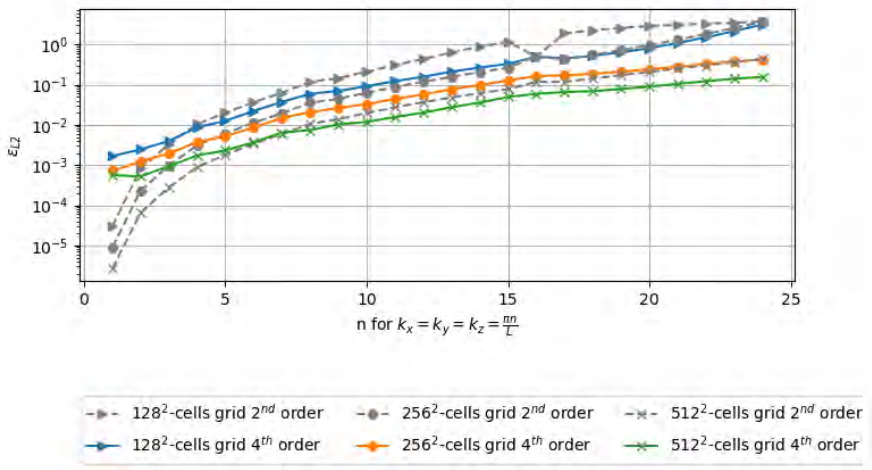

FIGURE 2.41: Relative L2 error in dimension d=2 with the fourth order scheme coupled with truncation-offset technique $p_0 = p_1 = 1$: spatial oscillation Dirichlet case, grey lines show classic Sparse results for reference.

There is a clear improvement in results for modes at shorter wavelengths, particularly in three dimensions. In terms of computational performance, there is a factor of 1.5 to 2 in increasing computation time for the two-dimensional Sparse method, and no significant variation for the three-dimensional Sparse method (see Table 2.7). It may be worth adopting this method for solutions at short wavelengths.

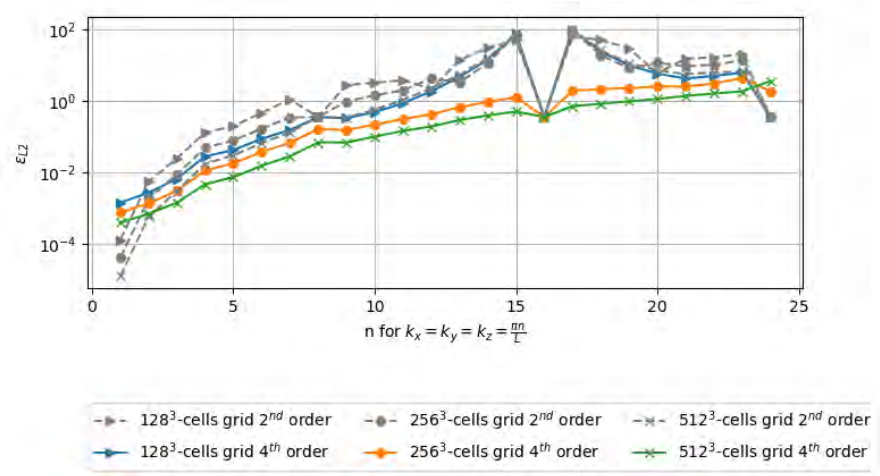

FIGURE 2.42: Relative L2 error in dimension d=3 with the fourth order scheme coupled with truncation-offset technique $p_0 = p_1 = 1$: spatial oscillation Dirichlet case, grey lines show classic Sparse results for reference.

2.2.9 Extension to other geometries

The association of sparse domains

The classic Sparse method presented above is applied to two-dimensional rectangular geometries or three-dimensional rectangular parallelepipeds. As part of the coupling to the PIC method, an extension by "gluing" cubes has been tested in three dimensions. The fact that sub-grids share common points at cube boundaries is used to solve the Poisson's equation over the entire domain for each sub-grid. Hierarchization, combination and dehierarchization steps are performed for each cube. For a sufficiently regular solution such as the electric potential, no significant impact is observed at cube boundaries despite cube-by-cube reconstruction. The simulated domain is shown in figure 2.43. Simulation conditions are similar to those presented in chapter 3 and are therefore not presented in detail here.

An example of the potential and electric field profile obtained are given in figure 2.44.

On less regular profiles, such as the density profile, a cube-by-cube reconstruction results in significant numerical artifacts at the boundaries between cubes. However, reconstruction on this profile is not part of the Sparse-PIC algorithm, so Sparse domain association remains an interesting option for adapting the Sparse method to more complex geometries.

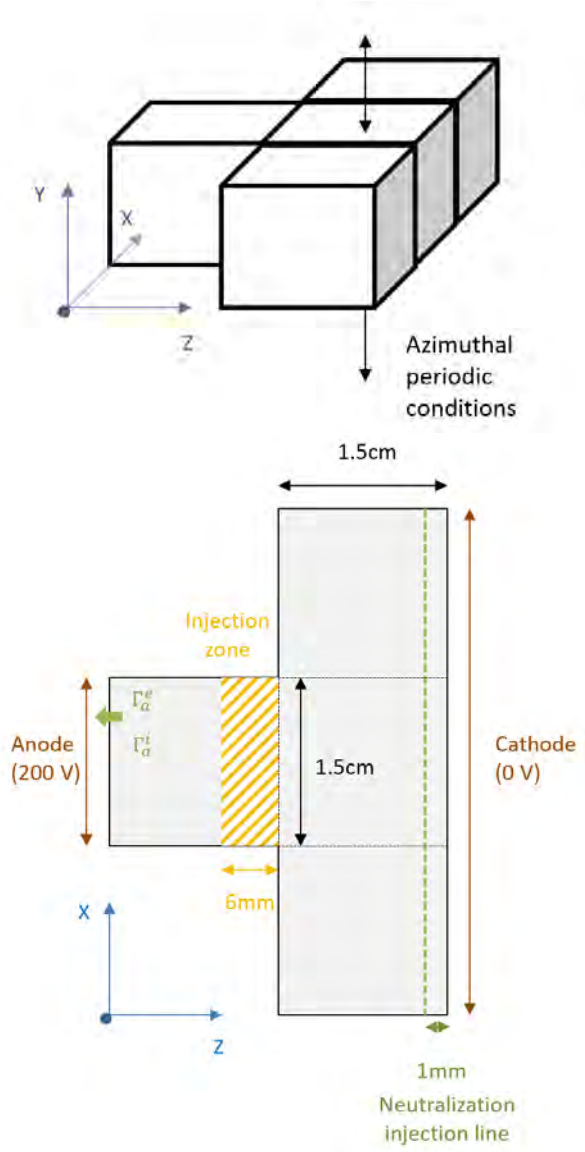

FIGURE 2.43: Four cubes domain in a ExB configuration.

The use of a transformation

Another way of adapting the Sparse method to more complex geometries is to use a transformation function on grids, as found in Weiman and Chaikin, 1979. The properties of this modified method are beyond the scope of this thesis. However, some examples of transformation coupled to the Sparse method can be found in Griebel, 1998; Morozov, Zhuravlev, and Reviznikov, 2021.

2.2.10 Extension to the finite element method

An adaptation of the Sparse method to the finite element method can be found in Pommier, 2008 and an application to the Vlasov/Boltzmann equation in Guo and

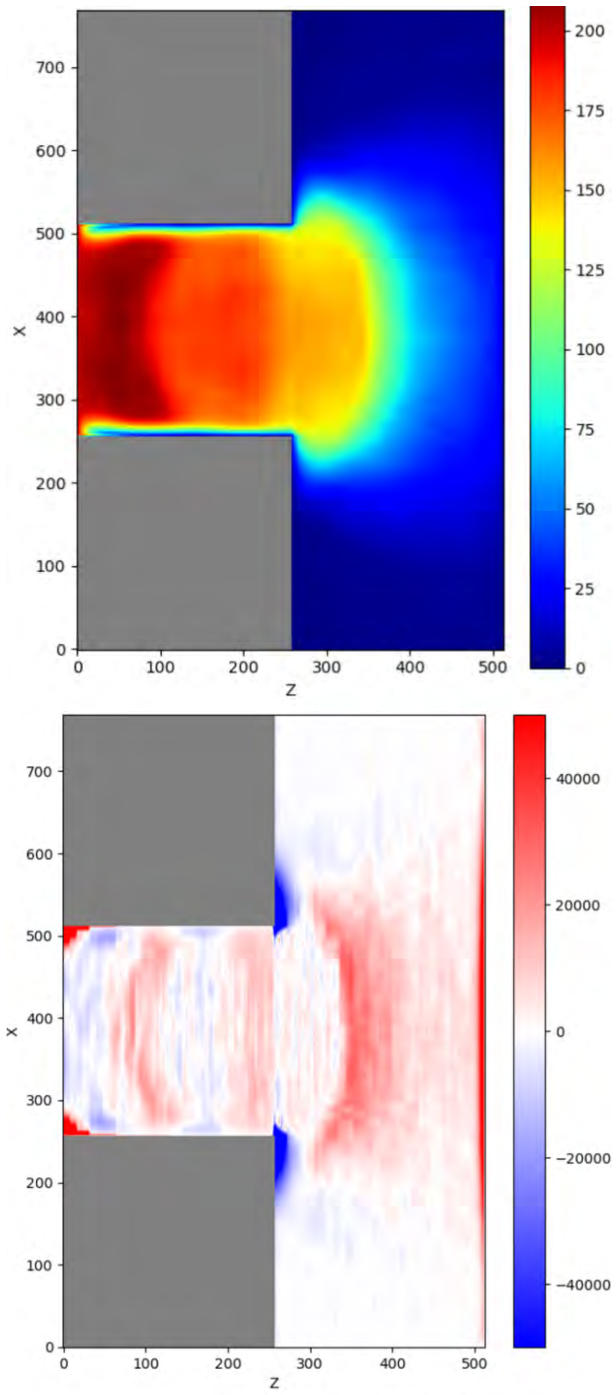

FIGURE 2.44: Electric potential and axial field obtained with a Sparse-PIC method in three dimensions using four sparse cubes in transient state of a ExB configuration.

Cheng, 2016. The results presented conclude that the method is effective for regular solutions, and remains to be tested for less regular solutions. A comparison in terms of computational performance with the Sparse-PIC method is not possible due to lack of data.

2.2.11 Conclusions on the Sparse method

The main tools associated with the Sparse method were presented, and a few tests demonstrated the capabilities of the most common Sparse method. The classical Sparse method poses difficulties in accurately capturing modes at very small wavelengths, particularly in three dimensions. One way of improving the method is to use a 4th-order finite-difference scheme for equivalent computation time in three dimensions and double in two. However, it appears to be sufficiently accurate to capture average plasma properties and important wavelengths in a PIC algorithm applied to the Hall thruster. These results are confirmed in Chapter 3 by comparing the average profiles obtained with a PIC code and a Sparse-PIC code in three dimensions. In terms of computational performance, the Sparse method achieves a gain of a factor of 3 in two dimensions and 33 in three dimensions on the Poisson's equation solving alone, compared with a direct solving method. But it is in coupling with the PIC algorithm that the method finds its greatest interest, notably in reducing the number of particles for the same mesh, as presented in section 2.3. The mathematical framework of the method may hinder its application to more realistic geometries. For this reason, we also addressed this shortcoming of the method by experimenting with a geometric extension of the method by assembling Sparse domains. Cube-by-cube reconstruction of the electric potential seems to work, as the potential is sufficiently regular. Without mathematical proof, however, it is difficult to predict when Sparse domain assembly cannot be used. Reconstruction tests on the electron density profile have shown that there may be numerical effects at the boundaries, as the solution is less regular than the potential. However, its application in a Sparse-PIC algorithm does not appear to have any adverse numerical effects. Other options are available for extending the method to different geometries. These include the use of a transformation or coupling to the finite element method. It should be noted that there are also a number of geometric adaptation algorithms for sparse grids (Griebel, 1998; Morozov, Zhuravlev, and Reviznikov, 2021) that enable the solution to be refined locally or adapted to more complex geometries.

Already coupled recently to the GENE code solving the gyrokinetic plasma equations (Pflüger et al., 2014; Heene, 2018; Pollinger et al., 2023), the Sparse method has proved its usefulness in correctly reconstructing the particle distribution function for given test cases such as the linear simulation of the unstable ion temperature gradient (ITG) mode. Ways of adapting the method to different physics problems associated with turbulence are active research topics. The technique of combining sub-grids has proved numerically unstable for some plasma turbulence simulations (Pollinger et al., 2023). Efforts are focused on testing different basis functions. An example of the use of a wavelet basis in Pollinger et al., 2023 can be found to replace the use of hat functions, which may have led to numerical instabilities in the case studied.

2.3 Coupling the two methods: the Sparse-PIC algorithm

2.3.1 The three options under consideration

The coupling of the Sparse method to the PIC algorithm can take place at three different levels of the algorithm, depending on **the quantity or quantities being reconstructed**. As a first simplification, we consider the reconstruction of **a single quantity** by the Sparse method. Either the density ρ, the potential Φ or the electric field $\vec{E}$ is reconstructed. All three options take advantage of the coarser discretization of the sub-grids to reduce the number of particles required for good sampling in the domain. Clément Guillet's thesis (Guillet, 2023) also provides an overview of the three alternatives for reconstruction on ρ, Φ and $\vec{E}$ under the respective names of PIC-Hg, PIC-NSg and PIC-Sg schemes. We give a graphical representation of the various algorithmic schemes using hierarchical basis reconstruction ("hierarchization-combination-dehierarchization" trio) in figures 2.45, 2.46 and 2.47. The equivalent nodal basis reconstruction algorithms are obtained by replacing the trio of steps hierarchization-combination-dehierarchization by a combination in the nodal basis (See sub-section 2.2.6).

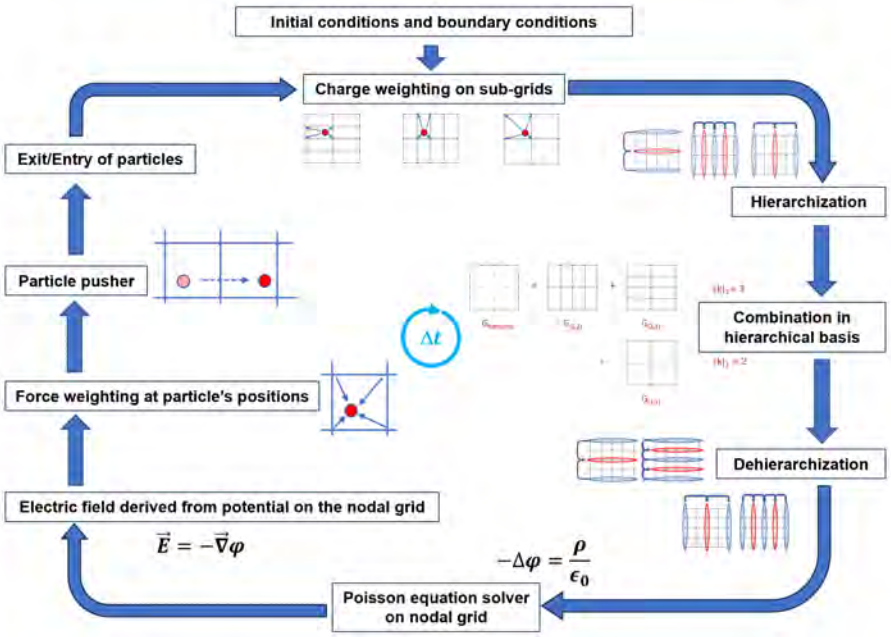

FIGURE 2.45: Sparse-PIC algorithm with hierarchical reconstruction of density ρ.

While these three options may appear similar in appearance, from the point of view of computational performance, memory usage and code parallelization, they are very different. For example, the density reconstruction scheme does not take advantage of the Sparse method for solving the Poisson's equation, and is confronted with the problem of excessively large matrices in three dimensions which requires

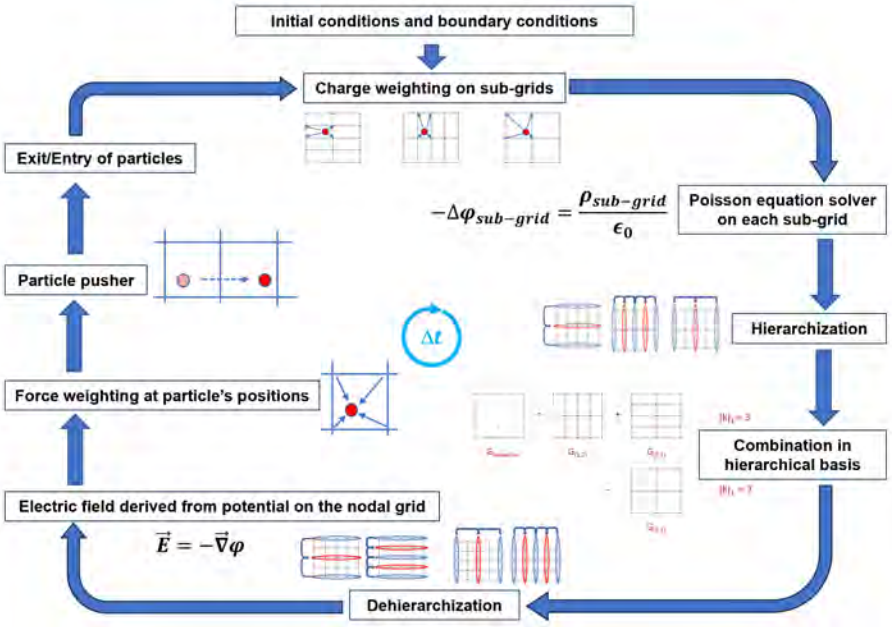

FIGURE 2.46: Sparse-PIC algorithm with hierarchical reconstruction of electric potential Φ.

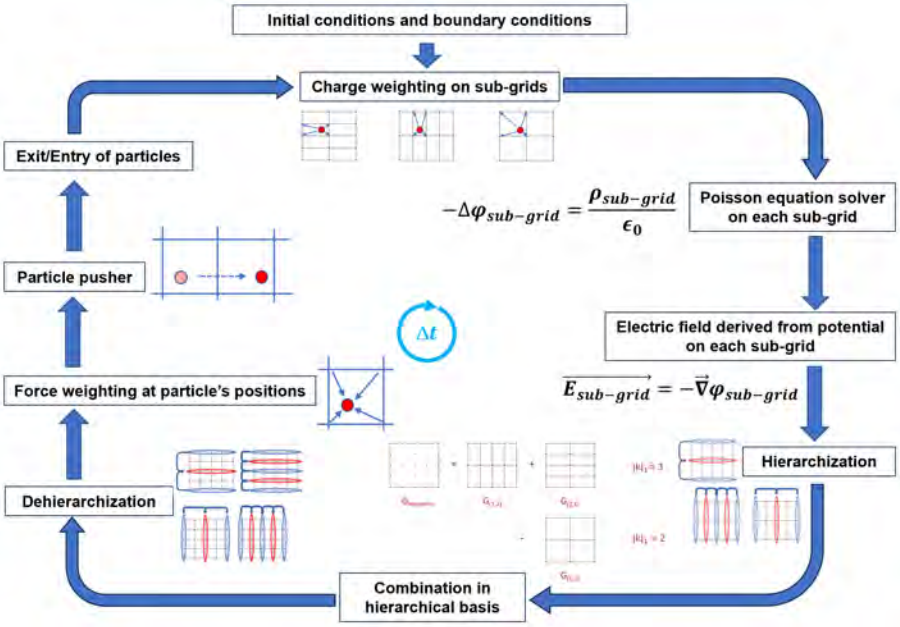

FIGURE 2.47: Sparse-PIC algorithm with hierarchical reconstruction of electric field $\vec{E}$.

special treatment using other matrix algorithms (Fast Fourier Transform solvers, or multigrid approaches, to quote Muralikrishnan et al., 2021). The electric field reconstruction scheme involves either reconstructing the three field components in a hierarchical basis and thus storing the three components on the regular grid or

reconstructing the three components in nodal basis (nodal basis combination) and having to project the three field components at particle positions for all the sub-grids which can number over a hundred in three dimensions for grid levels above 9 (see Table 2.3). The potential reconstruction scheme is a good compromise, allowing us to apply the Sparse method to the solving of the Poisson's equation, while only needing to store one component on the regular grid for hierarchical basis reconstruction. From the point of view of the accuracy of the different options, we obtain different error majorations for these different schemes, which depend on the second-order derivatives for the density and potential reconstruction, and depend on fourth-order derivatives for the electric field reconstruction (Guillet, 2023).

Among other things, this raises the question of nodal versus hierarchical basis reconstruction. While both give exactly the same result, their optimization and performance mainly depend on the ratio between the number of points in the regular grid and the number of particles in the domain. Indeed, hierarchical basis reconstruction considers the entire grid during dehierarchization. The number of positions to be computed in this case is therefore the number of points in the regular grid, whereas in the case of nodal basis reconstruction, the solution can be reconstructed directly at the particle positions and it is the number of particles that matters. For a parallelized architecture, we deduce that the hierarchical basis reconstruction is faster for the first grid levels, after which the nodal basis reconstruction becomes more advantageous, the limit being determined by the previous ratio.

Subsequently, we decided to apply the Sparse-PIC method by reconstructing the potential or the electric field to take advantage of the Sparse method for solving Poisson's equation. The Sparse-PIC-Φ method implies reconstruction on the potential in a hierarchical basis (Algorithm in figure 2.46). The Sparse-PIC-$\vec{E}$ method involves reconstruction on the electric field in nodal basis at particle positions (Nodal combination version of the algorithm in figure 2.47).

2.3.2 Taking the Sparse tool even further

We feel it is necessary to review the differences between the Sparse-PIC algorithm presented in Ricketson and Cerfon, 2016 and the three options (or six if we consider the versions with nodal combination) above. The algorithms presented above use the Sparse tool to reconstruct a single quantity of the PIC algorithm. The Sparse-PIC algorithm presented in Ricketson and Cerfon, 2016 uses the Sparse method to reconstruct both the density ρ and the electric field $\vec{E}$ at particle positions. Figure 2.48 shows a representation of the algorithm as we understand it, assuming a nodal basis combination reconstruction.

The benefit of applying this double reconstruction could be to consider even fewer particles than for the options presented above by taking advantage twice of the error-cancellation principle associated with the sub-grid combination technique. Another argument in favor of a charge density reconstruction is given in Muralikrishnan et al., 2021 to use the Sparse tool as a filter for numerical noise on charge density without necessarily applying it to the whole PIC algorithm. It should be

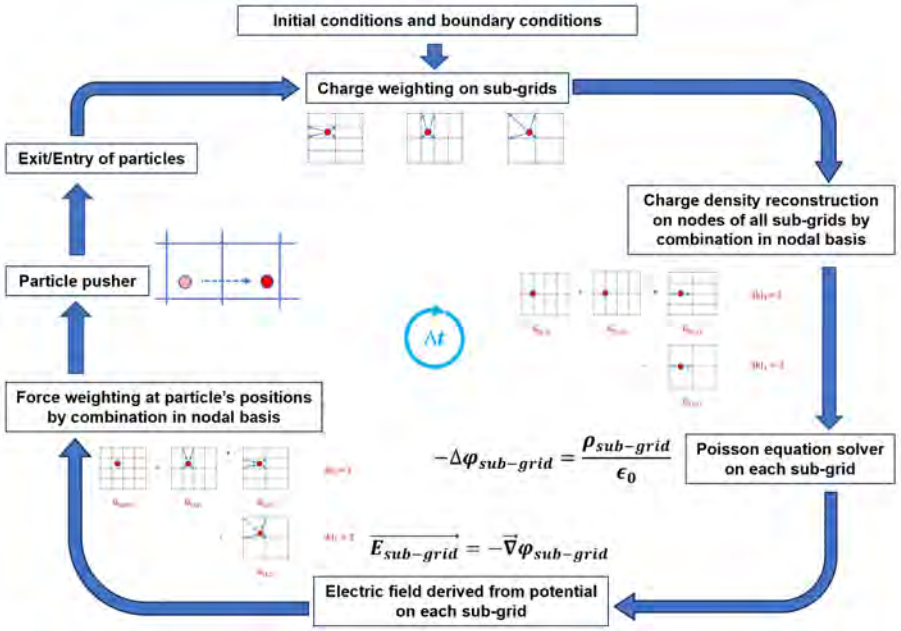

FIGURE 2.48: Sparse-PIC algorithm as understood from Ricketson and Cerfon, 2016.

noted, however, that reconstruction using the classical sub-grid combination technique does not preserve the positivity of solutions, which can be problematic in the case of density-based reconstruction. The question of the most appropriate implementation remains, and invites us to rethink certain quantities.

2.3.3 Rethinking parameters and diagnostics

The number of particles per cell

Traditionally, the number of particles per cell is a parameter used to assess the impact of particle discretization. It is simply defined as the initial ratio of the number of particles N_p in the domain to the number of cells n_c.

$$n_{ppc} := \frac{N_p}{n_c}$$

If we fix a uniform particle density $n_i = n_e = n_0$ initially, the real number N_{real} of particles that each particle in the simulation represents is simply by noting V_{cell} the volume of a cell, or V_{total} the volume of the domain:

$$N_{real} := \frac{n_0\, V_{cell}}{n_{ppc}} = \frac{n_0\, V_{total}}{N_p}$$

For a classical PIC algorithm, each particle represents a weight w_{PIC} in terms of particle density in m^{-3} equal to:

$$w_{PIC} := \frac{n_0}{n_{ppc}} = \frac{n_0\, n_c}{N_p}$$

In the case of the Sparse-PIC method, the number of cells and their volume depend on the sub-grid considered. In a sub-grid with cell volume $V_{cell,sg}$ and number of cells $n_{c,sg}$, each particle represents a weight w_{sg} in terms of particle density equal to:

$$w_{sg} := \frac{n_0\, n_c\, V_{cell}}{N_p\, V_{cell,sg}} = \frac{n_0\, n_{c,sg}}{N_p}$$

The same particle will therefore have a different weight in terms of particle density w_{sg} in each of the sub-grids. In practice, sub-grids with the same sum of levels in each direction have the same number of cells and the same cell volume. There are therefore d different weights, where d is the dimension of the domain of study, as shown by the combination relation (2.1).

One way of defining a parameter to assess the impact of particle discretization is to consider the sum of the number of cells in each sub-grid for N_{sg} sub-grids, so that:

$$n_{ppc,sparse} := \frac{N_p}{\sum_{i=1}^{N_{sg}} n_{c,i}}$$

Each particle in the simulation still represents N_{real} real particles such that:

$$N_{real} := \frac{n_0\, V_{total}}{N_p} = \frac{n_0\, V_{total}}{n_{ppc,sparse} \sum_{i=1}^{N_{sg}} n_{c,i}}$$

A first approximation is to consider that this new parameter $n_{ppc,sparse}$ of the Sparse-PIC method is equivalent to the parameter n_{ppc} of the PIC simulations. However, the total number of cells in the sub-grids $\sum_{i=1}^{N_{sg}} n_{c,i}$ is well below the number of cells in the regular grid n_c for grid levels above 6. This greatly reduces the number of particles in the domain for a given statistic. The order of magnitude of particle gain is summarized in table 2.8 for different grid levels in two and three dimensions.

By setting the parameter $n_{ppc,sparse}$ in the simulation, we also have for each sub-grid:

$$w_{sg} = \frac{n_c}{\sum_{i=1}^{N_{sg}} n_{c,i}} \frac{n_0\, V_{cell}}{n_{ppc,sparse}\, V_{cell,sg}} = \frac{n_{c,sg}}{\sum_{i=1}^{N_{sg}} n_{c,i}} \frac{n_0}{n_{ppc,sparse}}$$

To understand how $n_{ppc,sparse}$ modifies the charge density and potential noise, we take up Lieberman and Lichtenberg's collisionless sheath case, as studied in the section on the PIC algorithm (Section 2.1). We apply it to a cube with mixed Dirichlet-periodic conditions as shown in figure 2.32 in three dimensions and a similar square in two dimensions. Simulation conditions are given in table 2.9.

The results and the noise levels obtained as a function of the number of particles $n_{ppc,sparse}$ are compared with those obtained in one and two dimensions with the

TABLE 2.8: Ratio of number of cells in a regular grid over the total number of cells in all sub-grids $\frac{n_c}{\sum_{i=1}^{N_{sg}} n_{c,i}}$ with grid level.

Grid level	**Ratio 2D**	**Ratio 3D**
6	3.76	33.03
7	6.4	96.95
8	11.13	296.54
9	19.69	936.23
10	35.31	3030.57

TABLE 2.9: Parameters for sheath simulation: comparison between PIC and Sparse-PIC-Φ.

Initial density	**Grid level**	**Electron temperature**
$7.5 \times 10^{16} m^{-3}$	6	$2eV$
L	**Injection zone**	Δt
$3.686 \times 10^{-3} m$	$5 \times 10^{-4} m - 3.186 \times 10^{-3} m$	$1.25 \times 10^{-11} s$
$\omega_{pe} \times \Delta t$	$\frac{\Delta x}{\lambda_{De}}$	$\frac{v_{th,e} \Delta t}{\Delta x}$
0.19	1.5	0.13

classical PIC method and an equivalent number of particles n_{ppc} in figures 2.49, 2.50 and 2.51.

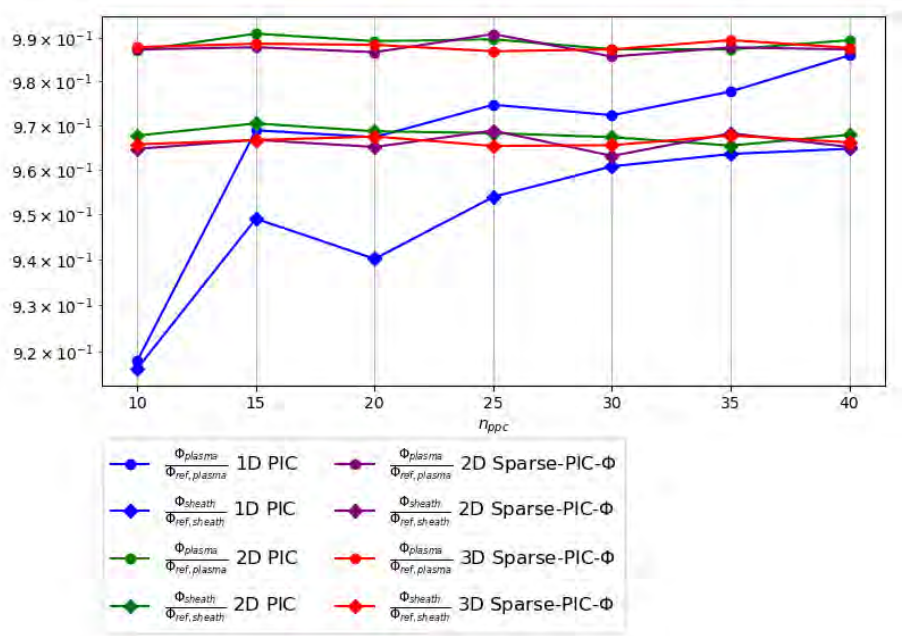

FIGURE 2.49: Electric potential reference points for non collisional sheath with number of particles per cell used in PIC and Sparse-PIC methods.

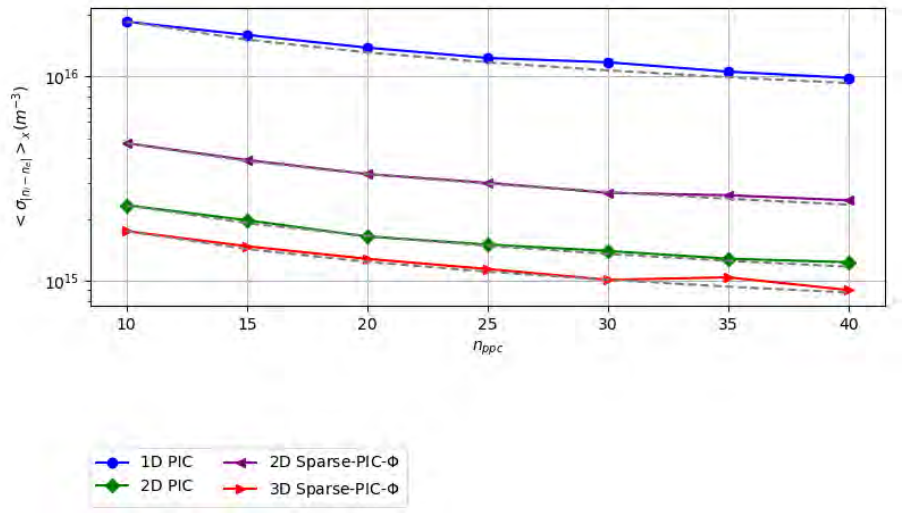

FIGURE 2.50: Noise level on particle density $\sigma_{|n_i - n_e|}$ for non collisional sheath with number of particles per cell used in PIC and Sparse-PIC methods: dashed lines show $\frac{1}{\sqrt{n_{ppc}}}$ tendencies.

The results obtained on the electric potential reference points (Figure 2.49) are not significantly affected by the number of particles in the domain for $n_{ppc} \geq 10$

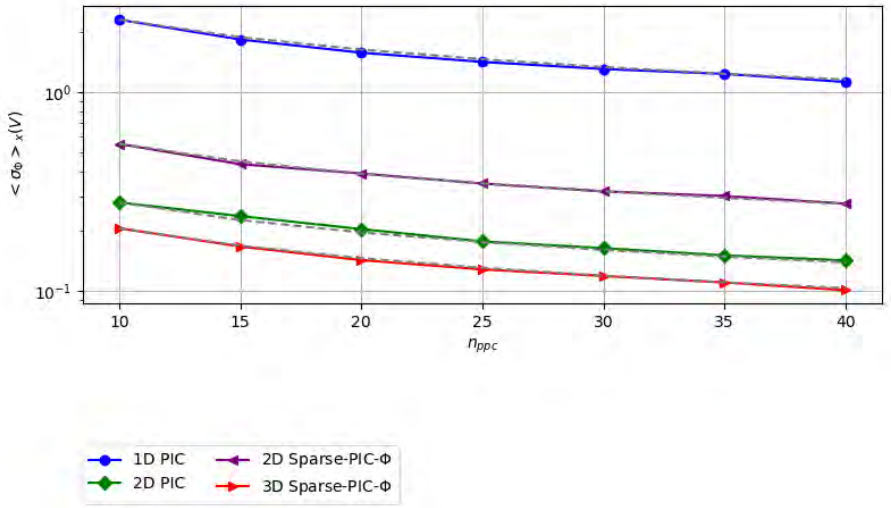

FIGURE 2.51: Noise level on electric potential σ_Φ for non collisional sheath with number of particles per cell used in PIC and Sparse-PIC methods: dashed lines show $\frac{1}{\sqrt{n_{ppc}}}$ tendencies.

except for the unidimensional PIC, which reaches the same level of accuracy as the two-dimensional PIC and the two- and three-dimensional Sparse-PIC methods for $n_{ppc} \approx 40$. This was already observed in figure 2.9 over a wider range of n_{ppc} values for unidimensional PIC. Effective noise reduction is also observed on charge density (Figure 2.50) and on the potential (Figure 2.51) in the case of collisionless sheaths as we go up in dimension always with a tendency to $\frac{1}{\sqrt{n_{ppc}}}$. This is due to the lower frequency of particle cell changes. Comparable noise levels in two dimensions are obtained for both PIC and Sparse-PIC-Φ methods when the parameters for the number of particles per cell follow the relation $n_{ppc,sparse} \approx 4 n_{ppc}$. For a level 6 grid, we have $\frac{n_c}{\sum_{i=1}^{N_{sg}} n_{c,i}} = 3.76$ which leads to a slightly higher number of particles (6% more) for equivalent noise with the Sparse-PIC-Φ method. Thus no particles are gained for the same noise level in the case of a two-dimensional collisionless sheath and a level 6 grid. The same result is observed for a two-dimensional level 7 grid. However, for a level 8 grid in two dimensions, the trend is reversed and we start to gain in particle number with the Sparse-PIC-Φ method for the same noise level. These results are consistent with tests of the Sparse-PIC-$\vec{E}$ method in two dimensions on a $\vec{E} \times \vec{B}$ cross-field configuration (Garrigues et al., 2021b, Figure 4). For the same total number of particles and a level 9 grid, the noise level is reduced by around 50 percent compared with the classical PIC method. Other situations are also more favorable to the Sparse-PIC method. In particular, this ratio is expected to be much more favorable in three dimensions. The noise reduction ratio also depends on the problem studied, as shown in Clément Guillet's thesis (Guillet, 2023) presenting the cases of diocotron instability and Landau damping for which a particle gain of a factor of 75 is obtained. We note that in all cases, the Sparse-PIC-Φ method remains faster than the classical PIC algorithm for the same noise level when using the parallelization strategy presented below and adapted to both algorithms.

Boundary conditions

In the previous section, we tested the Sparse method for Dirichlet, periodic and mixed Dirichlet-periodic conditions. In all cases, these conditions apply when solving the Poisson's equation in the form of additional coefficients in the solving matrix or in the addition of terms to the second member. For Sparse-PIC schemes involving Poisson solving on the sub-grids, these conditions must also be applied to the domain boundaries of each sub-grid. If a hierarchical basis combination is used, after each hierarchization the points at the domain boundaries of each sub-grid are modified by the change of basis algorithm. A correct implementation is therefore to reapply the conditions at the boundaries of each sub-grid before any hierarchization.

The presence of dielectric walls in the Hall current thruster requires the introduction of another type of boundary condition: capacitive walls. This type of boundary condition requires adaptation of the algorithm. For a classical PIC algorithm, the potential variation $dU(\mathbf{x})$ at the capacitive walls is computed by projecting the weights $q \times N_{real}$ of the charges passing through the walls onto each node of the capacitive walls. Noting $dq(\mathbf{x})$ the charge accumulated at the point $\mathbf{x}$:

$$dU(\mathbf{x}) = \frac{dq(\mathbf{x})}{C}$$

where C is the numerical capacitance parameter that can be adjusted to modify the charging rate. For the Sparse-PIC method, the number of particles in the domain is smaller, which reduces the number of particles passing through the walls. The sampling associated with the classical algorithm is not always appropriate.

To maintain consistency with the Sparse-PIC algorithm, a solution is to reconstruct the potential variation dU of a capacitive wall from the potential variation $dU_{sg,\mathbf{k}}$ for each sub-grid of level $\mathbf{k}$ where the particle weight depends on the sub-grid, maintaining the parameter C for each sub-grid. For a domain of dimension $d = 3$:

$$dU(\mathbf{x}) = \sum_{|\mathbf{k}|_1=n+1} dU_{sg,\mathbf{k}}(\mathbf{x}) - \sum_{|\mathbf{k}|_1=n} dU_{sg,\mathbf{k}}(\mathbf{x})$$

where:

$$dU_{sg,\mathbf{k}}(\mathbf{x}) = \frac{dq_{sg,\mathbf{k}}(\mathbf{x})}{C}$$

Reconstruction of numerical diagnostics

Sparse-PIC schemes allow the use of a reduced number of particles. To access Eulerian information on the regular grid, a classical projection onto the nodes of the regular grid is often unsuitable due to the lack of particles. Eulerian properties such as particle density must therefore be reconstructed using the grid combination technique. If we wish to obtain averaged profiles in certain spatial directions or in a domain large enough to contain a high number of particles, we can use a classical projection without significantly altering the results.

2.3.4 Parallelization of the Sparse-PIC method

General introduction to parallelization tools

The parallelization tools used to implement our codes are OpenMP (Open Multi-Processing, Dagum and Menon, 1998) and MPI (Message Passing Interface, Message Passing Interface Forum, 2021). The principle of cpus multi-processor parallelization is to divide up the tasks to be accomplished between several processors in order to save computing time. Supercomputers are organized into nodes, which are groupings of several computing units (cpus). To simplify this first approach, we consider that each node contains computing units sharing the same RAM (Random Access Memory). This allows us to introduce two types of parallelization for cpus: fast parallelization where the memory of the computing units is shared and slower parallelization, where the memory of the computing units is not shared. The first type of parallelization is written in the OpenMP language, the second in the MPI language. An important point to note is that MPI communications, which enable the transfer of information between nodes, are costly in terms of computing time. We therefore aim to avoid these communications as much as possible. Written code is read and executed by each node independently, except when it is instructed to perform an action with other nodes, typically an MPI communication. OpenMP instructions are therefore read and executed independently by each node, enabling cpus on the same node to work in parallel. Interested readers are invited to contact computer centers for more details on these tools.

General parallelization strategy

To take advantage of the double level of parallelization, particle information (position, velocity) is distributed by node (MPI) and by cpu (OpenMP). Because of the potentially large number of sub-grids, sub-grids are distributed per cpu of the same node (OpenMP). MPI communications between nodes are used only to retrieve the charge density on each sub-grid, and for any diagnostics requiring particle information. More advanced parallelization options introducing processor caches and vectorization can be applied to Sparse-PIC schemes, but will not be detailed here.

Achieved performance

Performance tests on our implementations of the Sparse-PIC method for reconstruction in nodal basis (Sparse-PIC-$\vec{E}$) and in hierarchical basis (Sparse-PIC-Φ) for a number of particles per cell $n_{ppc,sparse} = 100$ show nodal basis reconstruction to be faster for grid levels greater than or equal to 8 for a minimum of 180 cpus. This difference in scaling can be explained by the parallelization strategy used and by the ratio between the number of points in the regular grid and the number of particles in the domain which works against the Sparse-PIC-Φ method for regular grids with a high number of points. Provided that cpus resources are sufficient, the parallelized nodal basis reconstruction algorithm should perform better.

TABLE 2.10: Computational time per time step of Sparse-PIC-Φ in dimension d=3 with grid level on a 40 nodes ×36 cpus architecture for $n_{ppc,sparse} = 200$.

Grid level	Computational time per time step (s)
7	2.30×10^{-2}
8	8.20×10^{-2}
9	3.82×10^{-1}

However, in the context of our studies, we consider reduced models of the Hall thruster which require grid levels equal to 7 or 8 to meet discretization criteria. This is why we mainly use the Sparse-PIC-Φ method in configurations that enable us to obtain results rapidly with an optimal number of cpus resources. By way of example, we give the performance achieved by the Sparse-PIC-Φ method in three dimensions for an architecture comprising 40 nodes of 36 cpus, i.e. 1,440 cpus and different grid levels in table 2.10 for a fixed parameter $n_{ppc,sparse} = 200$. These performances do not take into account any diagnostics that may be added to the algorithm. For a level 7 grid, we can see that charge deposit accounts for 72 percent of computation time. Solving the Poisson's equation via the Pardiso module on all sub-grids accounts for only 1.5 percent of the computation time. The hierarchization-combination-dehierarchization trio accounts for 15 percent of computation time, including 11 percent for dehierarchization alone. The particle pusher accounts for 8 percent of computation time. The remaining 3.5 percent is due to particle output/reinjection. For a level 9 grid, the charge deposit accounts for 45 percent of the computation time compared with 47 percent for the hierarchization-combination-dehierarchization trio. We can thus observe that the trio hierarchization-combination-dehierarchization in the Sparse-PIC-Φ algorithm becomes more expensive in terms of computation time than charge deposit for higher grid levels, for the reasons outlined above.

The application of the Sparse method to different algorithms for highly parallelized computing has demonstrated performance gains in terms of both memory usage and computation time which are in line with the development of future Exascale computing architectures (Lago et al., 2020). The development of new algorithms using the Sparse method therefore seems consistent with the constraints linked to high-performance computing and numerical simulation needs.

2.3.5 Conclusions on the Sparse-PIC method

We have presented the different implementations of the Sparse method within the PIC algorithm, according to the quantity(ies) reconstructed using the sub-grid combination technique. Adapting Sparse tools to the PIC algorithm requires rethinking certain parameters such as the number of particles per cell, boundary conditions and the implementation of numerical diagnostics. Standard deviations of density

and electric potential keep decreasing in $\frac{1}{\sqrt{n_{ppc,sparse}}}$ as the number of particles per Sparse cell as defined above increases. Applied to the Lieberman and Lichtenberg collisionless sheath case, the PIC and Sparse-PIC-Φ methods yield equivalent noise levels in two dimensions for the same total number of particles in the simulation domain and grid levels 6 to 8. When the grid level is higher than 8 in two dimensions, we start to gain in particle number for the same given noise level. The gain in particles for a given noise level also depends on the dimension and type of problem studied. It tends to favor Sparse-PIC methods for high grid levels. We have also given a general strategy for parallelizing Sparse-PIC methods for a cpus architecture, using the OpenMP/MPI languages. These tools enable us to apply the Sparse-PIC method to a cross-field configuration typical of a Hall current thruster as presented in the following chapter.

Chapter 3

Numerical results in ExB cross-field configuration

3.1 Studied configuration

3.1.1 Instabilities identified by the state of the art and motivations

The Hall thruster has been the subject of numerous studies, highlighting a wealth of waves and instabilities, valid within the scope of their assumptions. Willca Villafana's thesis (Villafana, 2021, Introduction on plasma waves and instabilities) clearly defines the main instabilities identified:

- "Breathing Mode"(BM) linked to depletion of atoms in the ionization zone. The frequency is linked to the transit time of the atoms in this same region.
- "Ion Transit Time Instability"(ITTI). Axial electric field and density waves propagate from the anode to the thruster plume at a frequency of 100-500 kHz. Although their origin remains uncertain, the frequency is related to the transit time of the ions in the acceleration zone.
- "Electron Drift Instability"(EDI) or "Electron Cyclotron Drift Instability"(ECDI). An instability at MHz frequencies due to the Doppler-shifted electron cyclotron resonance caused by the electron drift in the $\vec{E} \times \vec{B}$ direction and by the ion motion in the axial field $\vec{E}$ direction.
- "Modified-Two-Stream Instability" (MTSI). An instability of the MHz order is present when the ratio of the azimuthal length $L_{azimuth}$ to the radial length L_{radial} of the channel is such that $\frac{L_{azimuth}^2}{L_{radial}} \frac{p}{m^2} \geq \frac{v_d}{f_{ce}}$ (Petronio et al., 2021) where $v_d = \frac{E_{axial}}{B_{radial}}$ is the drift velocity and f_{ce} is the cyclotron electron frequency, p and m are positive integers representing the mth azimuthal mode and the pth radial mode.

For a PPS-1350ML thruster on which Thibault Dubois carried out incoherent Thomson scattering (ITS) measurements during the test campaign on PIVOINE in Orléans in January 2021 under the supervision of Sédina Tsikata (Dubois, 2023), all these instabilities may be present. Insofar as we have experimental data on electron density and temperature at the thruster exit, we have chosen to consider conditions

close to this Hall thruster range. The comparison of simulation results with these experimental results is presented in greater detail in chapter 5.

On the other hand, we have chosen to build on the work carried out by researchers at the LAPLACE laboratory in Toulouse on $\vec{E} \times \vec{B}$ cross-field configurations, and more specifically on the modeling of ionization and acceleration zones of the Hall thruster (Boeuf and Garrigues, 2018). This model has been internationally benchmarked in Charoy et al., 2019 for two-dimensional domains. The Sparse-PIC method developed in the previous chapter enables us to resolve the time scales related to ECDI and MTSI while respecting discretization criteria in a reasonable computation time. However, the three-dimensional configuration and the coupling of the various instabilities make it more difficult to distinguish them in the computational domain. It should be noted that tests of the Sparse-PIC-$\vec{E}$ method in two dimensions have been carried out previously for a case of radio-frequency discharge (Garrigues et al., 2021a) and for the studied cross-field configuration (Garrigues et al., 2021b). The steady-state time-averaged profiles obtained with the classical PIC method were recovered with the Sparse-PIC-$\vec{E}$ method in two dimensions.

Similarly, we compare these profiles in three dimensions obtained by the Sparse-PIC-Φ method chosen previously to the results of the classical PIC method. We use the results of the Electrostatic Parallel PIC code (EP-PIC, Fubiani et al., 2017; Garrigues and Fubiani, 2023) based on a parallel multigrid approach using a successive over-relaxation (SOR) scheme, developed by Gwenaël Fubiani at LAPLACE in Toulouse as a reference for classical PIC.

Measuring the level of fluctuations in particle density and potential in the simulation domain ensures that the results are consistent (see Section 2.1) and can be compared with the level of fluctuations presented in Garrigues et al., 2021b. The particle-based approach used makes it easy to distinguish electron populations according to their origin (cathode, ionization, secondary emission). This advantage can be exploited to study in greater detail the behavior of these populations in the space of positions and velocities to better understand heating and transport mechanisms. To get a better idea of the scales involved, we present several orders of magnitude.

3.1.2 Order of magnitude of spatial and temporal scales of interest

Table 3.1 shows the characteristics of the Hall thruster PPS-1350ML also presented in Jaime Perez Luna's thesis (Perez Luna, 2008).

Based on data from the PPS-1350ML and previous simulations, and for a magnetic field ranging from 30 G (weak magnetic field zone) to 150-200 G (maximum magnetic field), we can give several orders of magnitude for the physical properties of the plasma shown in figure 3.1.

TABLE 3.1: Characteristics of a PPS-1350ML Hall thruster.

Geometrical characteristics	
Length of channel(cm)	2.5
Internal radius(cm)	3.5
External radius(cm)	5
Cathode position(cm from axis)	8

Physical characteristics	
Discharge voltage(V)	300
Xenon flow(mg/s)	5
Discharge current(A)	4.2

Performance	
Thrust(mN)	80
Isp(s)	1700

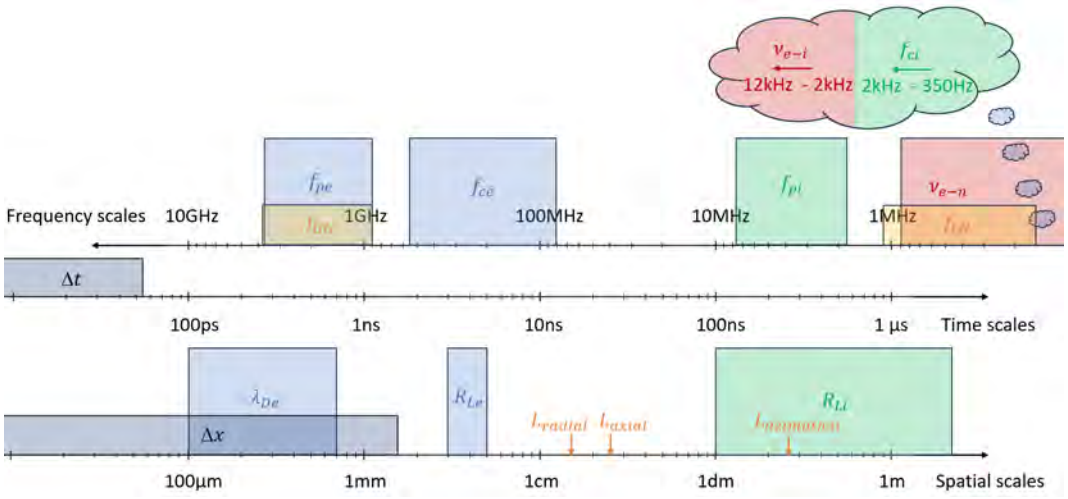

FIGURE 3.1: Frequency, time and spatial scales of interest in the simulated acceleration region of a PPS-1350ML-like Hall thruster: blue zones deal with electron properties, green zones with ion properties, orange zones are hybrid frequencies, red zones are collisions frequencies, and grey zones are numerical parameters.

Let f_{ce} be the electron cyclotron frequency, f_{pe} the electron plasma frequency, R_{Le} the electron Larmor radius and λ_{De} the Debye length. Ion equivalents are subscripted "i" instead of "e". The axial, azimuthal and radial dimensions of the PPS-1350ML are presented on the space chart as L_{axial}, $L_{azimuthal}$ and L_{radial}. Also shown are the Δt time step and Δx grid step, which meet the discretization criteria. The low

hybrid frequency $f_{LH} = \sqrt{f_{ce} f_{ci}}$ and the high hybrid frequency $f_{UH} \approx \sqrt{f_{ce}^2 + f_{pe}^2}$ which correspond to the coupling of the two harmonic oscillators of the electron and ion populations in the vicinity of equilibrium in the electrostatic regime (See Rax, 2005, Chapter 8) are also presented. These frequencies could appear in the thruster. For instance, in the conditions of the azimuthal instability model developed in Chapter 1 in Ducrocq, 2006, a resonance condition involving such frequencies is given $k_y v_d = 2\pi f_{UH}$ where k_y is the wave vector in the azimuthal direction and v_d the azimuthal drift velocity. This relation is notably valid (under the model assumptions) when the electron thermal velocity v_{th} is such that $v_{th} \ll v_d$ and the condition $f_{ce} < \frac{k_y v_d}{2\pi} < f_{UH}$ satisfied. The type of assumptions made in EDI or ECDI instability models will be discussed later in the section dedicated to waves observed in the simulation plasma. We denote ν_{e-n} the frequency of elastic collisions between electrons and neutrals and ν_{e-i} the frequency of Coulomb collisions between electrons and cold ions (considered fixed) as defined in Rax, 2005, Chapter 4. Rigorous definitions of these collision frequencies and associated models are given in the previous reference. For our study, we apply the associated formulas to obtain the orders of magnitude shown in figure 3.1:

$$\nu_{e-n}[Hz] \approx 6 \times 10^{-9} \left[\frac{n_n}{cm^3}\right] \left[\frac{T_e}{eV}\right]^{\frac{1}{2}} \tag{3.1}$$

and:

$$\nu_{e-i}[Hz] \approx 5 \times 10^{-6} \Lambda \left[\frac{n_e}{cm^3}\right] \left[\frac{T_e}{eV}\right]^{-\frac{3}{2}} \tag{3.2}$$

where the Coulomb logarithm Λ is given by:

$$\Lambda \approx \left\{ \begin{array}{l} 23.4 - 1.15 \times ln(n_e[cm^{-3}]) + 3.45 \times ln(T_e[eV]) \ \ if\ T_e \lesssim 50eV \\ 25.3 - 1.15 \times ln(n_e[cm^{-3}]) + 2.30 \times ln(T_e[eV]) \ \ if\ T_e \gtrsim 50eV \end{array} \right\} \tag{3.3}$$

Note that the frequency of elastic collisions between electrons and neutrals ν_{e-n} depends on the calculation position in the thruster, and increases with neutral density and electron temperature. Similarly, the frequency of Coulomb collisions ν_{e-i} increases with electron density and decreases with electron temperature. This trend can be explained by the shorter interaction time between charged particles for the fastest particles, resulting in lower impulse transfer. Orders of magnitude are given for limits associated with points inside the thruster channel:

$$(n_n[cm^{-3}], n_e[cm^{-3}], T_e[eV]) = (2.7 \times 10^{13}, 10^{10}, 35)$$

and at the maximum electron temperature position:

$$(n_n[cm^{-3}], n_e[cm^{-3}], T_e[eV]) = (2.5 \times 10^{12}, 1.7 \times 10^{11}, 70)$$

Neutral densities are taken from Coche, 2013's thesis. Electron density and electron temperature values are taken from the simulation results presented later.

3.1.3 Numerical model

The model developed in Boeuf and Garrigues, 2018 allows us to study a zone of the thruster where anomalous transport, i.e. not related to collisions, must be present. The physical phenomena studied are the instabilities and waves that can appear at the MHz, which gives a physical computation time of the order of twenty microseconds. This time scale effectively neglects Coulombic collisions of frequency ν_{e-i}. This physical time can be reached by Sparse-PIC simulation in three dimensions, while respecting the discretization criteria. Figure 3.2 shows a schematic diagram of the Hall current thruster taken from Boeuf and Garrigues, 2018.

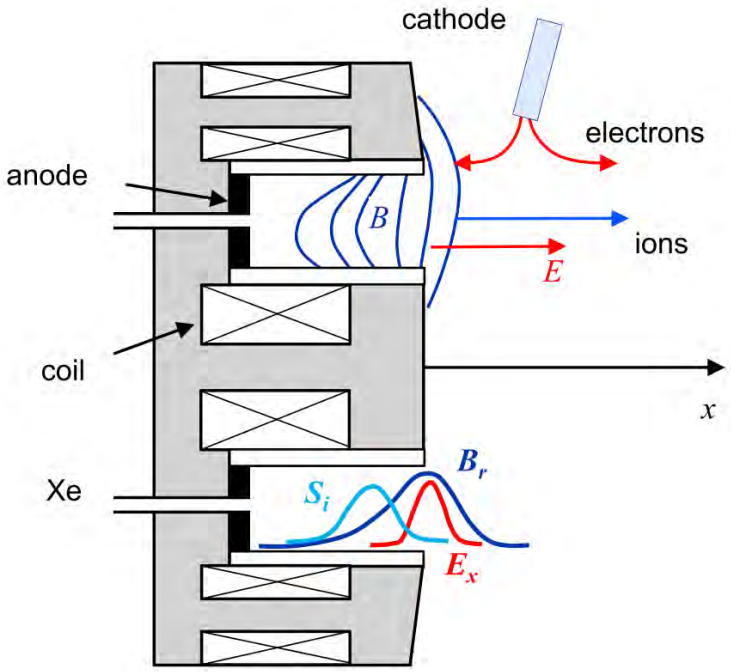

FIGURE 3.2: Hall thruster scheme from Boeuf and Garrigues, 2018.

The **zone modelled numerically** is the zone of the thruster on which are superimposed profiles of the magnetic field $\vec{B}$, the ionization source term S_i and the axial electric field $\vec{E}$. The presence of neutrals is very low (less than $10^{18} m^{-3}$ which gives a frequency of electron-neutral collisions smaller than 100 kHz using the approximation in Rax, 2005) in the right-hand part of the thruster after the ionization peak (See S_i profile in figure 3.2) which allows elastic collisions with neutrals to be neglected. This is not normally the case for the left-hand part before the ionization peak, where elastic collisions with neutrals can thermalize electrons. In this first approach, elastic collisions are not taken into account. A simplification in the studies that follow is to impose a source term for ionization either by fixing a current or by imposing a reinjection model of an ion-electron pair for each ion exit from the domain which keeps the average ion density fixed in the simulation domain. These two types of particle injection to represent ionization are presented in greater detail in Garrigues and Fubiani, 2023. The numerical model used for simulation is similar to that presented in Boeuf and Garrigues, 2018. It is shown in figure 3.3.

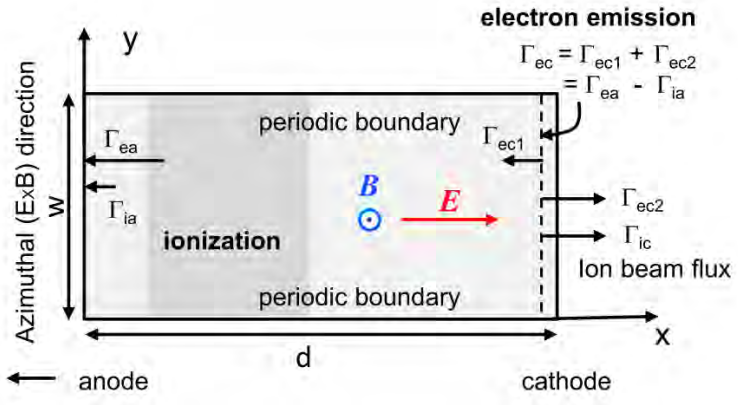

FIGURE 3.3: Hall thruster numerical domain from Boeuf and Garrigues, 2018.

An additional electron source (Γ_{ec}) coming from the cathode must be taken into account in the simulation to neutralize the ion flux accelerated by the axial $\vec{E}$ field. This corresponds to the electron emission plane close to the cathode plane. The difference between the number of outgoing electrons (Γ_{ea}) and the number of outgoing ions (Γ_{ia}) at the anode plane is re-injected to this electron emission plane by randomly drawing their velocity from a Maxwellian distribution of fixed temperatures. Asymptotically, the outgoing electron and ion currents at the cathode plane are equal ($\Gamma_{ic} = \Gamma_{ec2}$). Part of the reinjected electrons therefore neutralizes the ion flow towards the cathode (Γ_{ec2}), while the other part (Γ_{ec1}) flows back towards the anode. Periodic conditions can be envisaged for the Hall thruster in the azimuthal direction (cf. figure 3.4).

The size of the domain in this direction should then be considered as the perimeter of the median circle of the thruster channel. The order of magnitude for a PPS-1350ML type thruster is a domain length of $L_{azimuthal} = 2\pi r_{median} \approx 26.69cm$ in the azimuthal direction. For the sake of computation time, however, we consider a truncated version of this domain in the azimuthal direction. It is also assumed that the discharge has already set up, and we are mainly interested in the stationary state for which an equilibrium is found between the forces, including those of kinetic origin. We start from an initial state where the density of electron-ion pairs is uniform throughout the simulation domain. We also assume a Maxwellian velocity distribution for electrons and ions, with temperatures set at 10 and 0.5 eV respectively. These initial conditions ensure a noise-free start.

3.1.4 Model reduction for diagnostics

Processing data in six or seven dimensions (three spatial, three of velocity and one temporal) can be complicated to implement, given their quantity and representation. We can attest to the existence of solutions for representing data in volume (See Paraview, Ahrens et al., 2005). However, it may be more representative and simpler to consider a preferred direction in the Hall thruster. The transport we are interested in is axial, and as a first simplification, we can consider an axial dependence

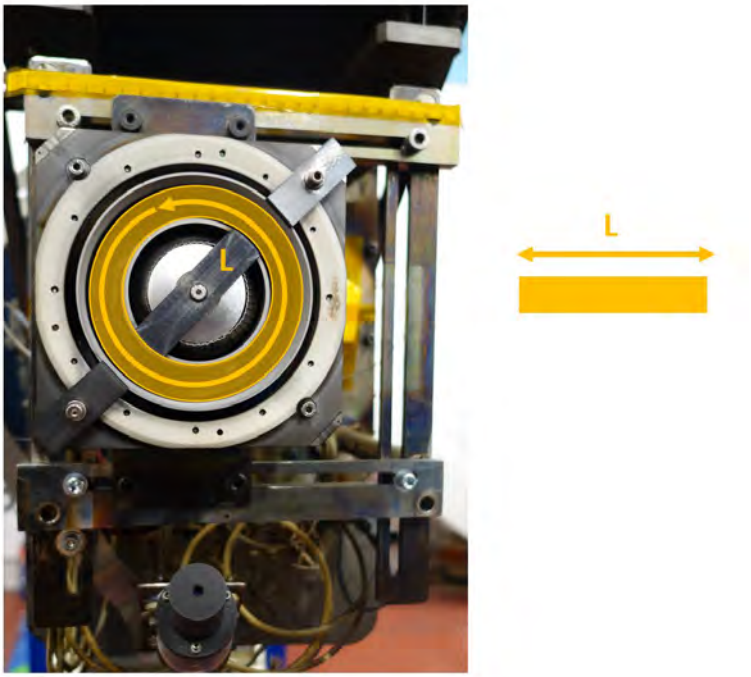

FIGURE 3.4: Periodic boundary in a Hall thruster (left) and truncated model (right).

of the physical simulation parameters (magnetic field, ionization source term, mean electric field). We can thus represent the results as a function of the axial direction, after integrating the quantities diagnosed in the azimuthal and radial directions by slice of thickness of the regular grid axial step. The simulation domain in three dimensions, and the integration volume used for the presentation of profiles reduced to the axial direction are represented in figure 3.5. Let us note U_a the potential fixed at the anodic plane and U_c the potential fixed at the cathodic plane. We consider the axial direction in the (Oz) direction, with reference to notations in cylindrical coordinates, although Cartesian coordinates are used.

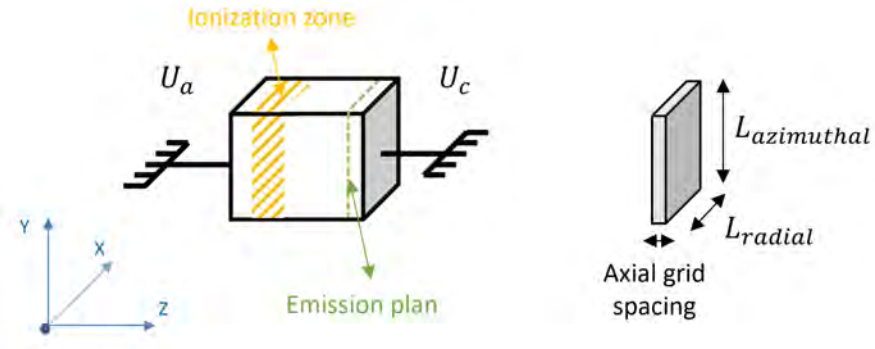

FIGURE 3.5: Hall thruster numerical domain (left) and axial slice for integration in radial and azimuthal directions (right).

As a first step, we consider that several simulation parameters vary only in this direction such as the magnetic field amplitude and the ionization source term. Validation of the results by comparison between the PIC and Sparse-PIC-Φ methods is carried out with mixed Dirichlet-periodic conditions, taking periodic conditions in the azimuthal and radial directions as presented in figure 2.32. This also makes it possible to compare the results obtained with the two-dimensional case, the results of which are presented in Garrigues et al., 2021b. This configuration is not, of course, that of the thruster, but it does provide a point of reference for the work ahead. We then study the impact of walls, and more specifically of secondary electronic emission, in chapter 4.

3.2 Validity of results - Comparison with classical PIC

3.2.1 Simulation parameters

Boundary and initial conditions for the simulation have already been discussed. We consider a cubic domain with Dirichlet conditions in the (Oz) direction and periodic conditions in the other two directions. The injection method used to represent ionization is that of reinjecting an electron-ion pair for each ion exit. The ion density in the simulation domain is therefore constant. The simulation parameters used are shown in table 3.2.

The amplitude profile of the magnetic field is also shown in figure 3.6.

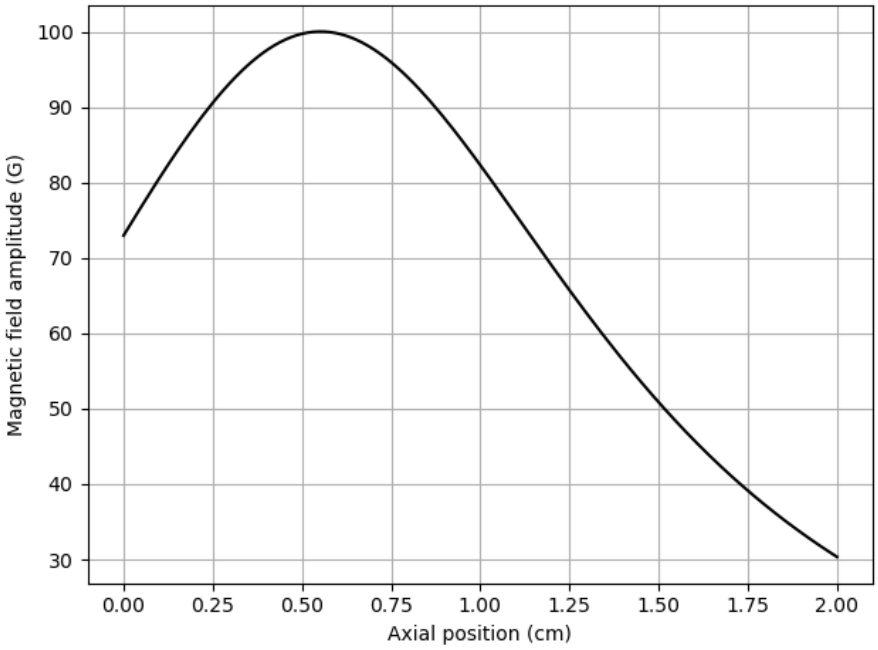

FIGURE 3.6: Axial profile of magnetic field amplitude used for benchmark.

TABLE 3.2: Physical and numerical initial parameters for the benchmark in dimension d=3.

Geometrical parameters	
Length of the cube edge (cm)	2
Axial zone of injection (cm)	0.15-0.75
Axial position of cathode (cm)	1.9
Axial position of maximum of magnetic field (cm)	0.56
Physical parameters	
Maximum of magnetic field (G)	100
Discharge voltage (V)	300
Physical constants	
Electron mass (10^{-31}kg)	9.11
Xenon ion mass (10^{-25}kg)	2.18
Initial conditions	
Plasma density ($10^{16}m^{-3}$)	7.5
Electron temperature (eV)	10
Ion temperature (eV)	0.5
Numerical parameters	
Grid level	7
Number of cells (PIC)	2 097 152
Number of cells (Sparse-PIC-Φ)	21 632
Number of particles per cell (PIC)	50
Number of particles per cell (Sparse-PIC-Φ)	50, 100 and 200
Number of particles per cell (Sparse-PIC-Φ-4^{th})	50
Time step(s)	1.25×10^{-11}
Numerical criteria (using regular grid spacing)	
$w_{pe} \times \Delta t$	0.19
$\frac{\Delta z}{\lambda_{De}}$	1.82
$\frac{v_{th,e}\Delta t}{\Delta z}$	0.10

3.2.2 Time-averaged steady-state profiles

Steady state is considered to be reached when the outgoing ion and electron currents at the anode and cathode evolve around a stable mean value over time. We also check that the electron and ion currents leaving the cathode are equal, attesting to the neutralization of the ion flow. We define these currents at time t_i as the number $N(t_i)$ of charges q having passed through the anode plane (where $U_a = 300V$ is imposed) or the cathodic output plane (where $U_c = 0V$ is imposed) for 2.5 ns of physical simulation time, i.e. 200 time steps such that:

$$I[A](t_i) = \frac{N(t_i)q}{200\Delta t} \tag{3.4}$$

Note that the currents thus defined are negative for electrons and positive for ions. Time sampling is similar to that performed in Boeuf and Garrigues, 2018. This regime is typically reached after 12 to 15 microseconds of physical simulation time for the cross-field configuration under study. An example is given in figure 3.7 for the Sparse-PIC-Φ method and a number of particles per cell of $n_{ppc,sparse} = 200$.

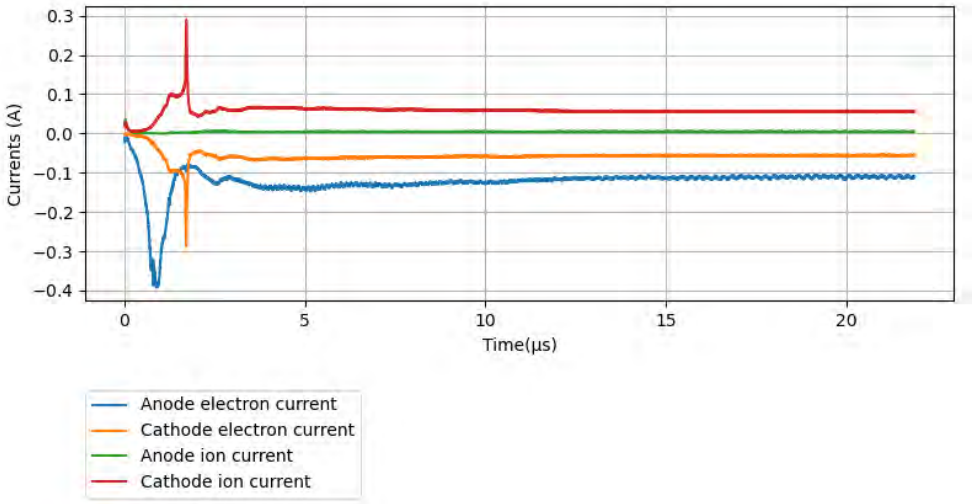

FIGURE 3.7: Exit electron and ion currents at the anode and cathode plans with simulation time: Sparse-PIC-Φ results with $n_{ppc,sparse} = 200$.

We refer to Sparse-PIC-Φ-4^{th} as the Sparse-PIC-Φ method in which we have replaced the finite-difference scheme for solving the Poisson's equation by a fourth-order scheme as described in sub-section 2.2.7 (See Straalen, 2017 for details about the scheme). The profiles of ion density, potential, electric field and electron temperature that are compared are sampled every 100 ns in steady state over ten microseconds of physical simulation time, and are given respectively in figures 3.8, 3.9, 3.10 et 3.11.

We also compare the values of outgoing electron and ion currents at the anode and cathode, as well as the powers lost at the electrodes and associated with the kinetic energy of the exiting particles in table 3.3.

TABLE 3.3: Values of leaving currents and powers lost at the electrodes for the benchmark.

Electron current		
	Anode (mA)	**Cathode (mA)**
PIC ($n_{ppc} = 50$)	-129	-61
Sparse-PIC-Φ ($n_{ppc} = 50$)	-225	-58
Sparse-PIC-Φ ($n_{ppc} = 100$)	-162	-58
Sparse-PIC-Φ ($n_{ppc} = 200$)	-113	-56
Sparse-PIC-Φ-4^{th} ($n_{ppc} = 50$)	-173	-62

Ion current		
	Anode (mA)	**Cathode (mA)**
PIC ($n_{ppc} = 50$)	9	61
Sparse-PIC-Φ ($n_{ppc} = 50$)	11	58
Sparse-PIC-Φ ($n_{ppc} = 100$)	7	58
Sparse-PIC-Φ ($n_{ppc} = 200$)	4	56
Sparse-PIC-Φ-4^{th} ($n_{ppc} = 50$)	9	62

Electron power loss		
	Anode (W)	**Cathode (W)**
PIC ($n_{ppc} = 50$)	16.8	1.7
Sparse-PIC-Φ ($n_{ppc} = 50$)	36.7	2.7
Sparse-PIC-Φ ($n_{ppc} = 100$)	25.8	2.1
Sparse-PIC-Φ ($n_{ppc} = 200$)	15.2	1.6
Sparse-PIC-Φ-4^{th} ($n_{ppc} = 50$)	26.2	2.4

Ion power loss		
	Anode (W)	**Cathode (W)**
PIC ($n_{ppc} = 50$)	0.2	18.1
Sparse-PIC-Φ ($n_{ppc} = 50$)	0.4	18.3
Sparse-PIC-Φ ($n_{ppc} = 100$)	0.1	17.1
Sparse-PIC-Φ ($n_{ppc} = 200$)	0.05	16.3
Sparse-PIC-Φ-4^{th} ($n_{ppc} = 50$)	0.2	18.6

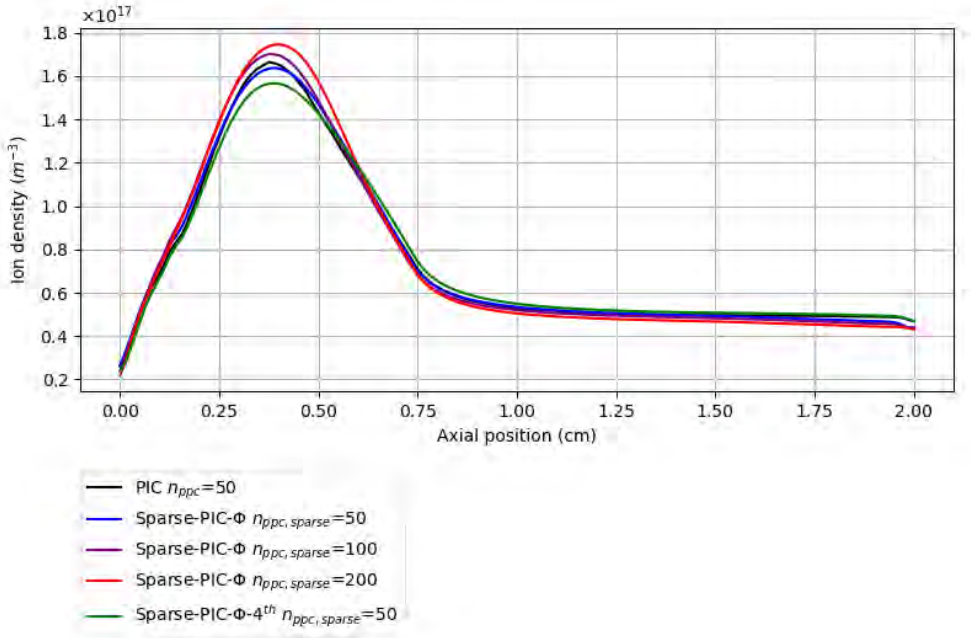

FIGURE 3.8: Axial ion density profiles for benchmarking Sparse-PIC-Φ and PIC methods.

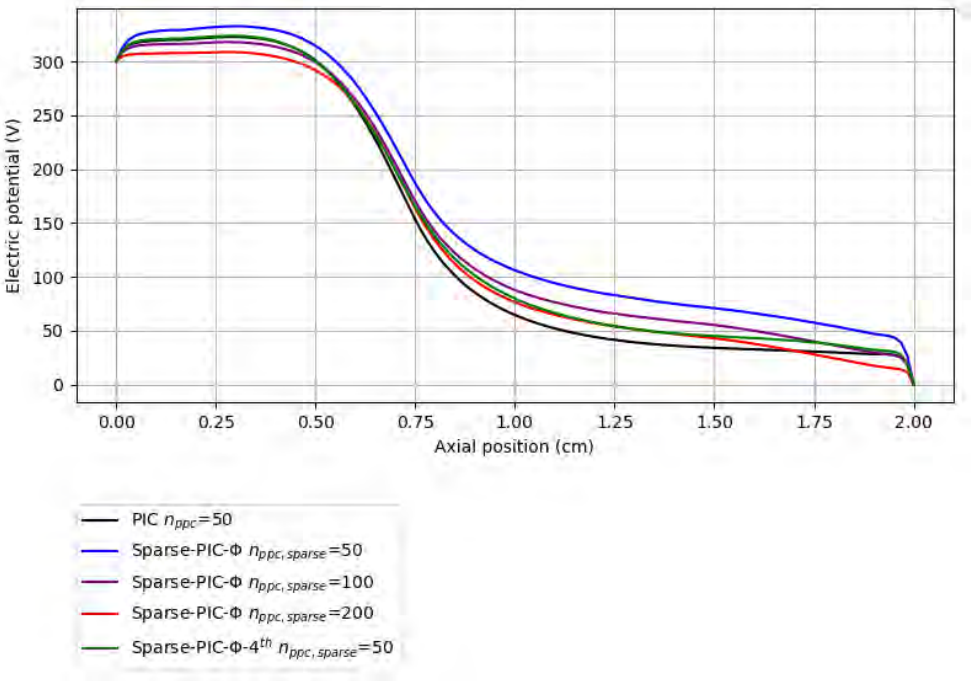

FIGURE 3.9: Axial electric potential profiles for benchmarking Sparse-PIC-Φ and PIC methods.

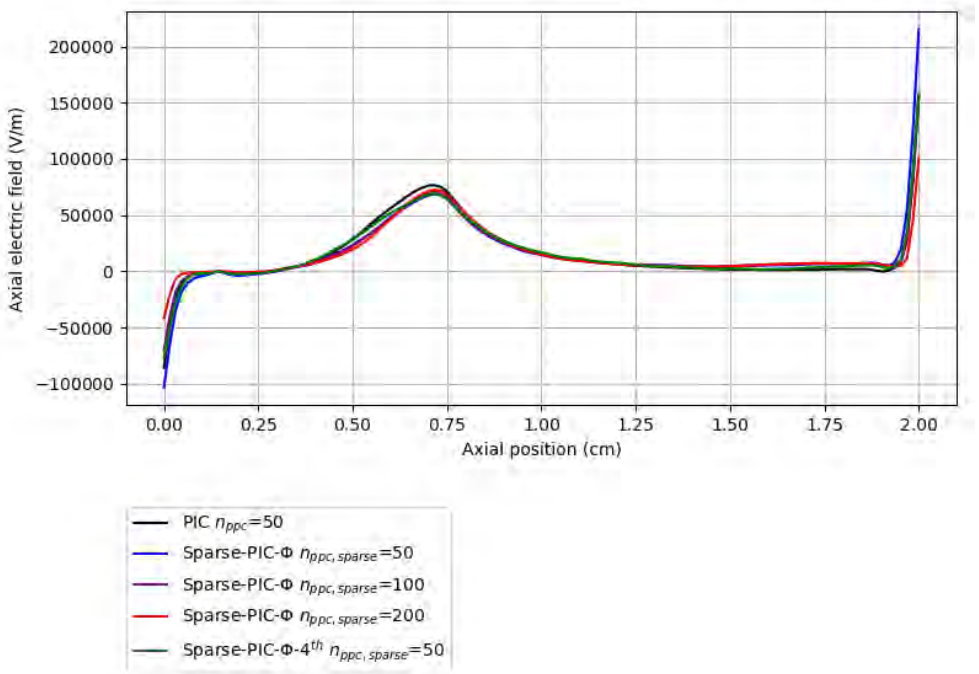

FIGURE 3.10: Axial electric field profiles for benchmarking Sparse-PIC-Φ and PIC methods.

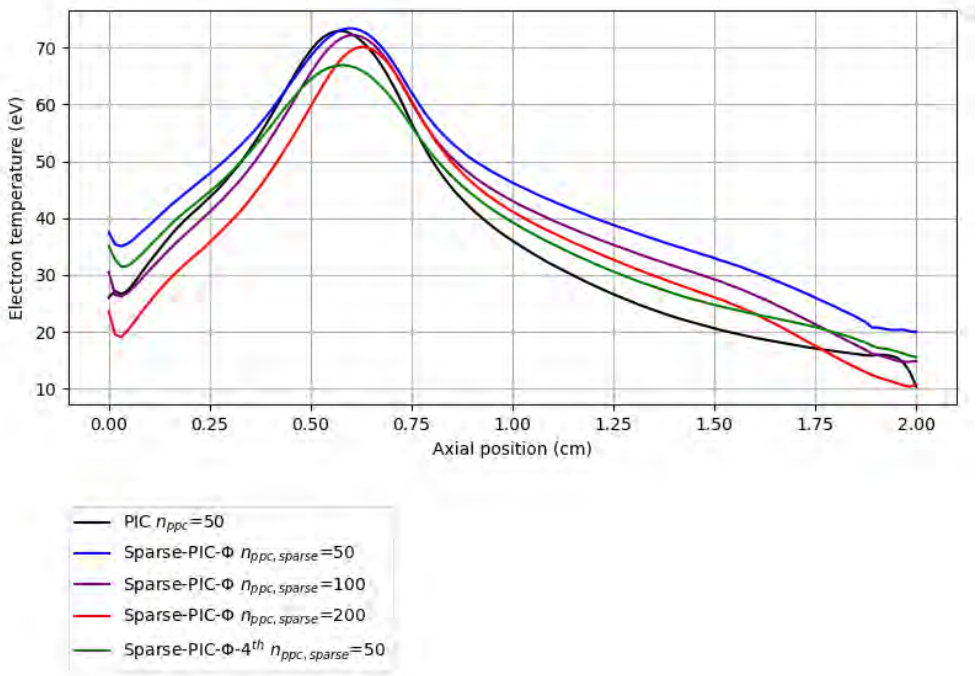

FIGURE 3.11: Axial electron temperature profiles for benchmarking Sparse-PIC-Φ and PIC methods.

TABLE 3.4: Values of $\int E_{axial} dz$ for the benchmark with $U_a - U_c = 300V$.

	Integrated value of axial electric field profile (V)
PIC ($n_{ppc} = 50$)	307.10
Sparse-PIC-Φ ($n_{ppc} = 50$)	310.79
Sparse-PIC-Φ ($n_{ppc} = 100$)	308.77
Sparse-PIC-Φ ($n_{ppc} = 200$)	306.13
Sparse-PIC-Φ-4^{th} ($n_{ppc} = 50$)	308.24

Note that the simulation conditions are one order of magnitude lower than the actual electron density in a PPS-1350ML type thruster, resulting in a lower discharge current measured in the simulation. More realistic conditions can be achieved by leveling up the grid at the expense of simulation time, although it should not change much the observed tendancies.

Results comparable to PIC are obtained with the Sparse-PIC-Φ method in three dimensions, both in terms of current values and power lost at the electrodes, and in terms of the axial profiles of ion density, potential, electric field and electron temperature. Note that the voltage $U_a - U_c$ imposed in the axial direction between the anode and cathode is found to within two or three percent when integrating the average axial electric field profile (See figure 3.10). The $\int E_{axial} dz$ values obtained are summarized in the table 3.4.

Results are improved by refining the numerical scheme for solving the Poisson's equation (Sparse-PIC-Φ-4^{th}) and by increasing the number of particles initially in the domain. It can be seen that the Sparse-PIC-Φ results obtained with $n_{ppc,sparse} = 100$ and $n_{ppc,sparse} = 200$ are close to the average PIC values obtained with $n_{ppc} = 50$, corresponding to a gain in terms of number of particles of a factor between 24 and 48.

Despite the consistency of the results, we note a difference of a few eV in the electron temperature profile between the Sparse-PIC-Φ method and the PIC method. The physical phenomena involved are thus a priori captured in their entirety, but the precision of the results could be improved, in particular with a fourth-order scheme as presented in Straalen, 2017. Compared with the two-dimensional case presented in Garrigues et al., 2021b, the average profiles are closer to the results obtained by PIC for the same grid level. The number of particles per sparse cell also plays a greater role in the results in three dimensions than in two. Its role on the level of fluctuations in the domain is shown next.

3.3 Level of particle density and potential fluctuations

Particle density and potential standard deviations are defined in a similar way to the 2.1 section. For N_t time sampling points at instants t_i ($i \in [\![1; N_t]\!]$), N_x regular grid points in the radial direction at positions x_j ($j \in [\![1; N_x - 1]\!]$) and N_y regular grid

points in the azimuthal direction at positions y_k ($k \in [\![1; N_y - 1]\!]$), the axial standard deviation profile of the potential is given by:

$$\sigma_\Phi(z) = \sqrt{\frac{1}{N_t}\sum_{i=1}^{N_t}\left(< \Phi >_{x,y}(z,t_i) - < \Phi >_{x,y,t}(z)\right)^2} \tag{3.5}$$

where:

$$< \Phi >_{x,y,t}(z) = \sum_{i=1}^{N_t}\sum_{j=1}^{N_x-1}\sum_{k=1}^{N_y-1}\frac{\Phi(x_j, y_k, z, t_i)}{N_t(N_x-1)(N_y-1)} \tag{3.6}$$

The axial profile of the particle density standard deviation is given by a similar relation. Figures 3.12 and 3.13 show the profiles available for the different methods. Time sampling points are taken after convergence of the results (See figure 3.7 and details above) every 4000 time steps (50 ns) for the equivalent of five microseconds of physical simulation time for the Sparse-PIC-Φ and standard PIC methods. Note that the measurement of the level of fluctuations in Boeuf and Garrigues, 2018; Garrigues et al., 2021b is slightly different, involving the mean value of the square root of the fluctuations in the quantity of interest (rms). In our study, we prefer to calculate the standard deviation.

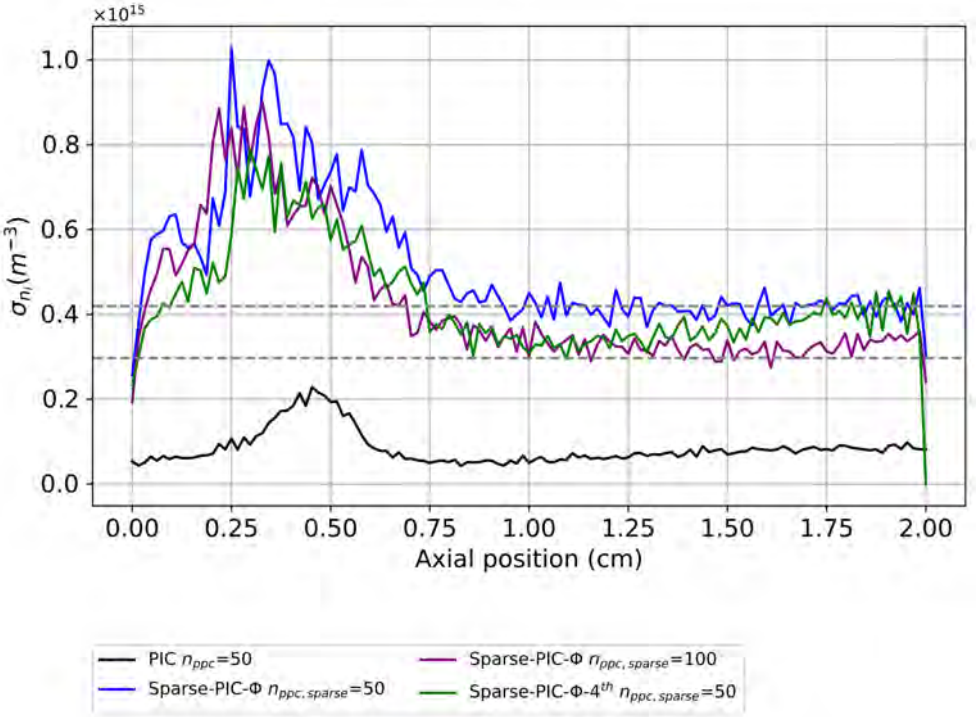

FIGURE 3.12: Axial ion density n_i standard deviation profile for benchmarking Sparse-PIC-Φ and PIC methods: horizontal grey dashed lines show two levels of fluctuations for $n_{ppc,sparse} = 50$ and $n_{ppc,sparse} = 100$ using the $\frac{1}{\sqrt{n_{ppc}}}$ noise reduction.

The level of ion density fluctuations in figure 3.12 is higher by a factor of 3 to

5 on average for the Sparse-PIC-Φ method than for the standard PIC method, for the same number of particles per cell. However, the equivalence of this particle parameter is not exact, as shown in chapter 2 (see figures 2.50 and 2.51). For $n_{ppc} = 50$ and a level 7 grid (benchmark conditions), there are around a hundred times fewer particles in the Sparse-PIC simulation than in the PIC simulation. The Sparse-PIC method therefore reduces the noise at the same initial number of particles in the simulation by a factor of 20 to 30 compared with PIC. A reduction in noise is observed as the number of particles per cell is increased, almost with a $\frac{1}{\sqrt{n_{ppc}}}$ trend, particularly for axial positions greater than 0.75 cm. A density fluctuation level of $4.2 \times 10^{14} m^{-3}$ for $n_{ppc,sparse} = 50$ accordingly gives a density fluctuation level of $2.9 \times 10^{14} m^{-3}$ for $n_{ppc,sparse} = 100$. This order of magnitude is represented on figure 3.12 as grey dotted horizontal lines. The shape of the ion density fluctuation profiles seems to follow that of the ion density profile for the Sparse-PIC method (see figure 3.8). The maximum seen most clearly on the PIC profile corresponds to the center of the ionization zone where ionization is more likely (cf. random draw after Boeuf and Garrigues, 2018, or see representation of ionization term in figure 3.2). The Sparse-PIC-Φ-4^{th} method for $n_{ppc,sparse} = 50$ gives a noise level equivalent to the Sparse-PIC-Φ method with $n_{ppc,sparse} = 100$, except near the cathode, where it achieves a noise level equivalent to the Sparse-PIC-Φ method with $n_{ppc,sparse} = 50$.

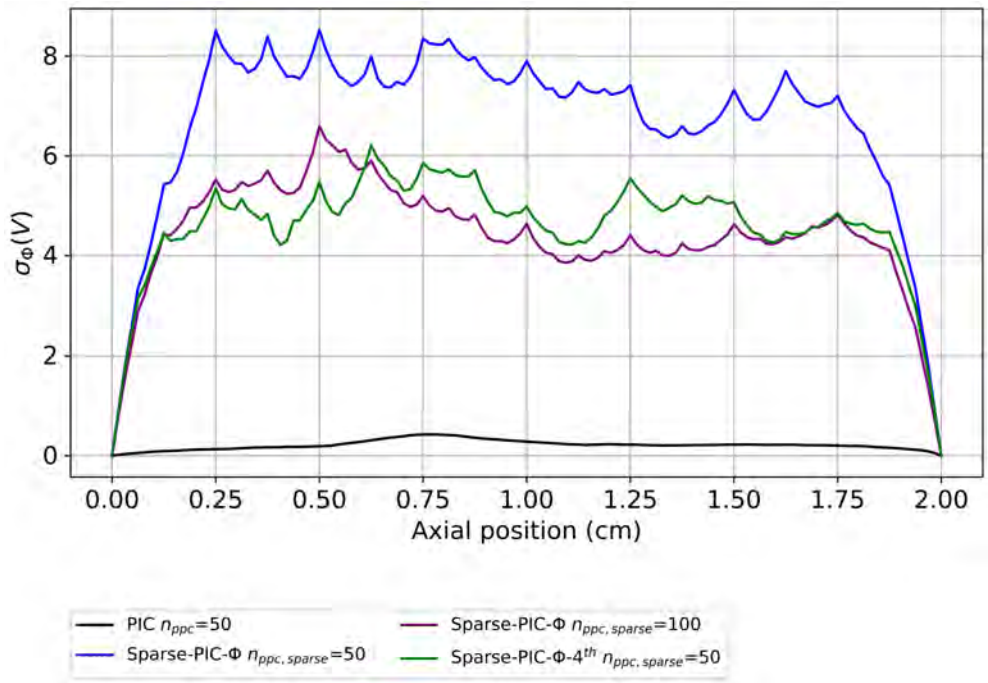

FIGURE 3.13: Axial electric potential standard deviation profile for benchmarking Sparse-PIC-Φ and PIC methods.

In the case of electrical potential, figure 3.13 shows a level of fluctuations of a few volts for the Sparse-PIC method, 8 to 16 times greater than for the PIC method. However, if we refine the time sampling of the Sparse-PIC results by taking a sample every 10 time steps (0.125 ns) for the equivalent of two microseconds of physical

simulation time, we obtain figure 3.14 where a peak of electric potential fluctuations can be seen more clearly around the axial position of 0.75 cm which is close to the position of the maximum azimuthal drift velocity v_d, as well as a level of fluctuations 3 to 5 times higher than for the standard PIC. The order of magnitude of comparison between the two methods in terms of density fluctuations is then similar to that of potential fluctuations.

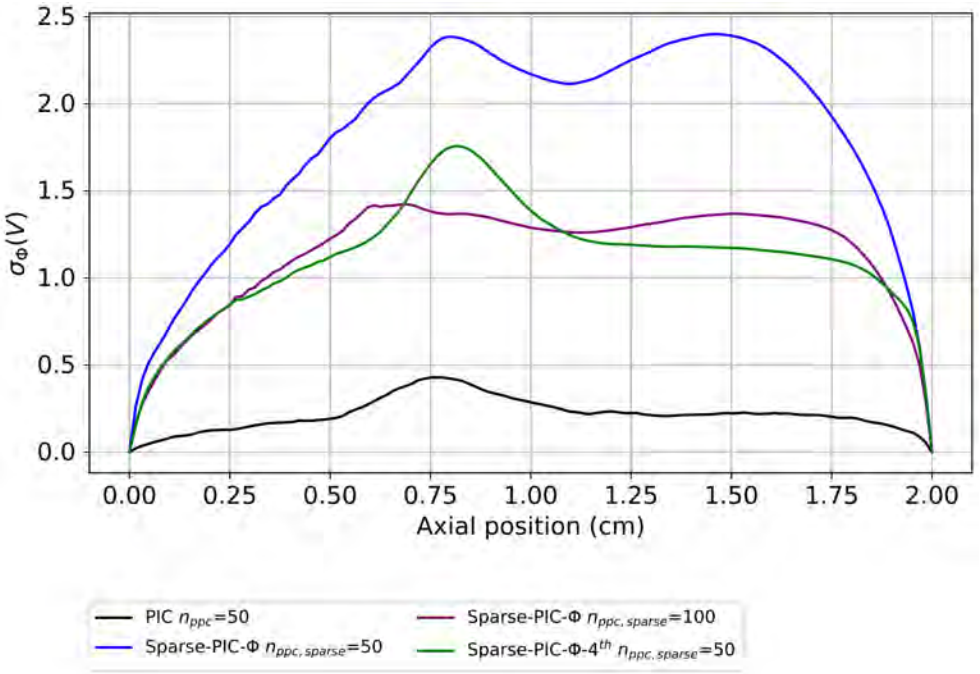

FIGURE 3.14: Axial electric potential standard deviation profile for benchmarking Sparse-PIC-Φ and PIC methods: refined time sampling for Sparse-PIC-Φ results.

The fluctuation levels obtained are of an order of magnitude that remains consistent with the initial density and discharge voltage parameters. The axial profile of the standard deviation of electron density, not shown here, is of the same order of magnitude as that of ion density. This shows that the level of n_e electron density fluctuations is about ten to fifteen times lower in three dimensions than in two dimensions (See figure 9 in Boeuf and Garrigues, 2018). Benchmark results between PIC and Sparse-PIC in two dimensions presented in Garrigues et al., 2021b (Figure 4c) show that the level of fluctuations obtained with the Sparse-PIC method can also be reduced to that of standard PIC by raising the grid level. Those presented in figure 9 in Garrigues et al., 2024 show that the truncation and offset methods presented in chapter 2 (Section 2.2) bring Sparse-PIC results closer to standard PIC. Finally, the test of the Sparse-PIC-Φ-4^{th} method has shown above that the improved integration scheme of Poisson's equation, coupled with the truncation and offset methods, could also reduce the level of noise in the simulation.

3.4 Details by electron population

The configuration studied allows the electron population to be divided into two populations: one created by ionization and the other from the cathode emission plane. To better understand the characteristics associated with each electron population, their respective contribution to the density profile averaged in the axial direction is shown in figure 3.15. The results presented in this section are based on the Sparse-PIC-Φ-4^{th} method. Similar results are obtained for the Sparse-PIC-Φ method.

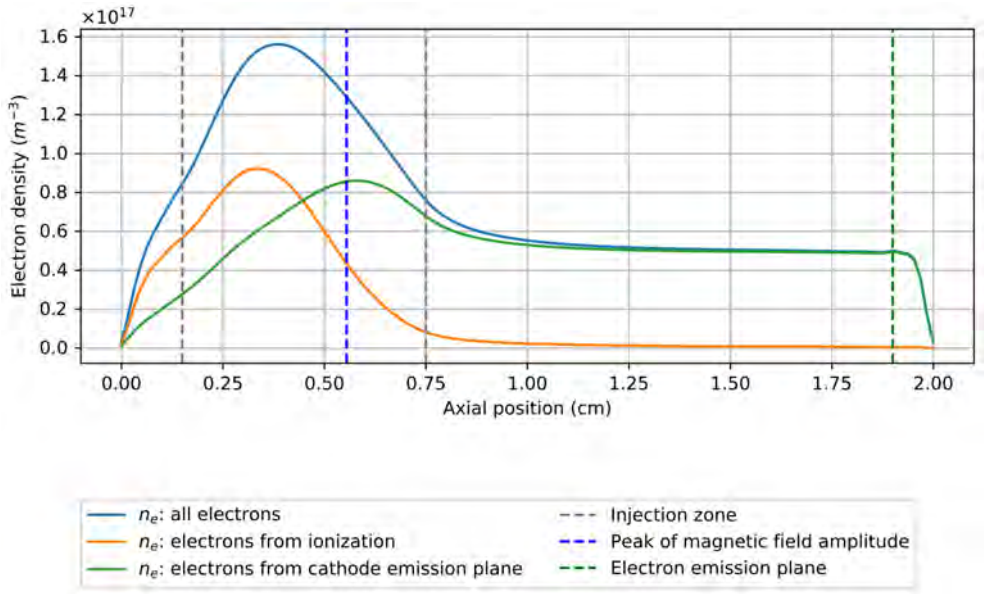

FIGURE 3.15: Electron density axial profiles for different electron populations.

At first glance, the population of electrons coming from the cathode emission plane is concentrated around the peak amplitude of the magnetic field. One interpretation that can be developed with the results of the following section is that the electrons in this population have reached sufficient energy to cross the distance separating them from the anode in less than one cyclotron period, resulting in their smaller presence in the part of the channel close to the anode. In order of magnitude, an electron with a speed of $10^7 m.s^{-1}$ in a magnetic field of 90 G has a Larmor radius equal to 0.6 cm. The peak density of the electron population created by ionization is shifted towards the inside of the channel. The axial pressure gradients associated with each electron population are shown in figure 3.16 and allows us to link several extrema and inflection points to physical simulation parameters.

For the population of electrons created by ionization, the axial pressure gradient has an extremum at the axial position of the maximum magnetic field amplitude. It cancels out at the axial position of the maximum electron density for the profile including all electrons (purple dashed line, or see blue curve in figure 3.15). The axial pressure gradient of the electron population coming from the cathode emission plane also cancels out at this position, and reaches an extremum at the axial position

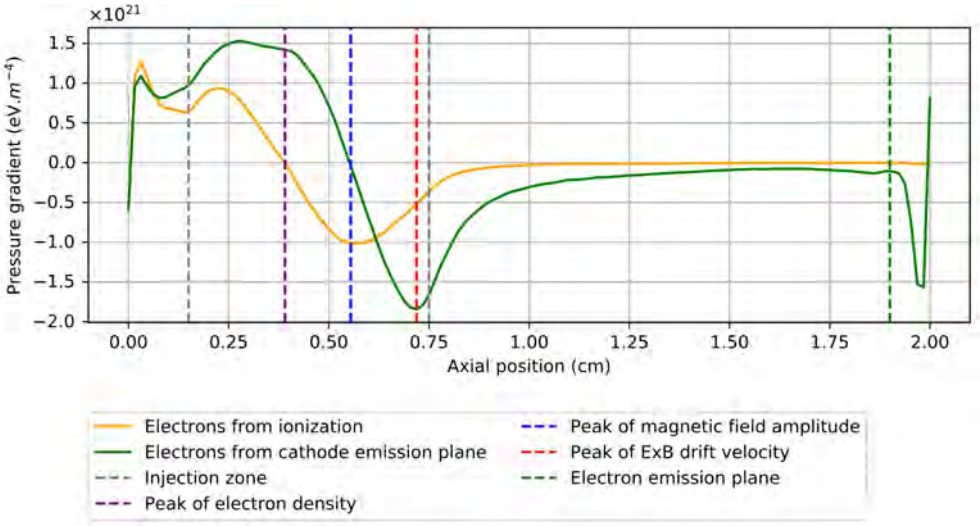

FIGURE 3.16: Axial pressure gradients $\nabla_z p_e$ for the two electron populations.

of the maximum azimuthal drift velocity $v_d = \frac{E_z}{B_x}$. We now plot the sum of the axial pressure gradients associated with each electron population, and observe in figure 3.17 that an equilibrium is found between the electron pressure forces of the two populations at the position where the potential is equal to the potential set at the anode U_a.

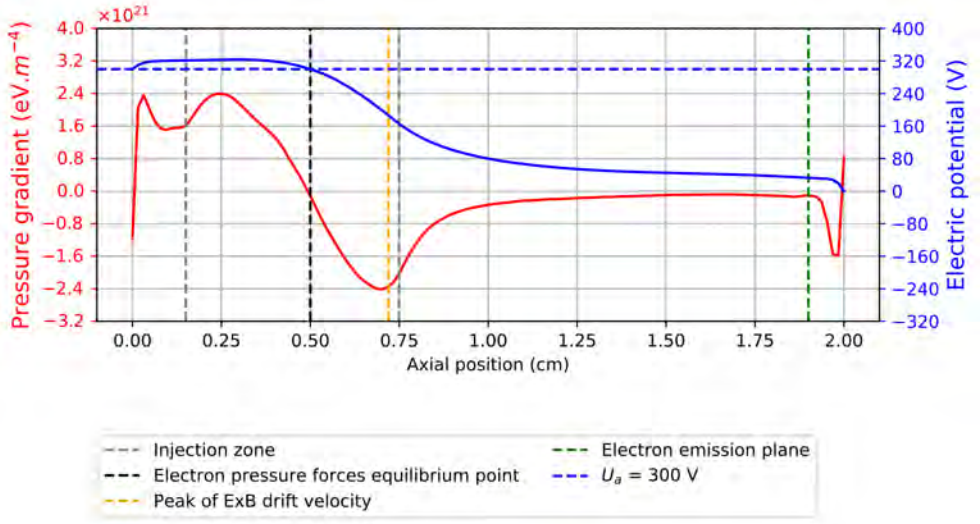

FIGURE 3.17: Sum of axial pressure gradients from the two electron populations: an equilibrium is found where the electric potential is back to U_a.

This axial equilibrium position is also where the electron temperature of the electron population coming from the cathode emission plane is highest, as shown in figure 3.18 (black dashed line). The electron temperature of all electrons is highest

at the axial position of the maximum magnetic field amplitude. The electron temperature of electrons created by ionization is highest between the position of the maximum magnetic field amplitude and that of the maximum v_d azimuthal drift velocity. The distinction between these two electron populations therefore appears to be justified by their characteristics, as described above. The exploration of three-fluid models, two electronic (one for each population) and one ionic, could be an avenue worth developing.

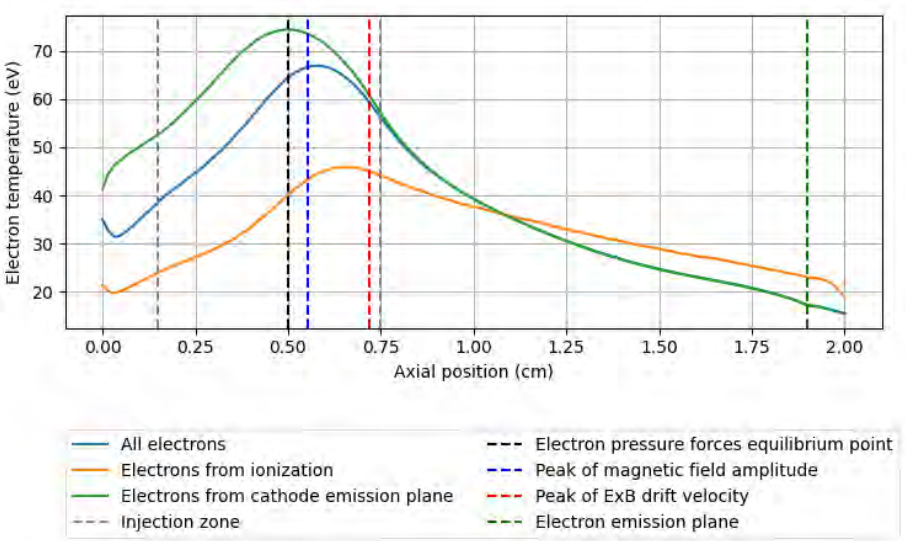

FIGURE 3.18: Electron temperature axial profiles for different electron populations.

3.5 A side note on "Double layer" configurations

This section presents the rudiments drawn from my readings on "double layer" configurations, which seem to be of particular interest for the Hall thruster. Let us take the definition of "double layer" (DL) presented in Schamel, 1986:

> "A DL is defined as a monotonic transition of the electric potential connecting smoothly two differently biased plasmas. This is achieved by a dipole-like charge distribution."

An example of a potential profile and $n_i - n_e$ density profile corresponding to a "double layer" configuration is shown in figure 3.19.

These profiles are similar to those obtained in the benchmark configuration studied to represent the Hall thruster, as shown in figure 3.20. In the case of the thruster, we note that the crossover point between the positively and negatively charged layers is located at the azimuthal drift velocity peak. In addition, the magnetic configuration seems to tend to spread the positively-charged layer. The local minimum density $n_i - n_e$ observed could correspond to the end of the ionization zone at $z = 0.75$ cm. Two other smaller dipole structures can be observed close to the electrodes at

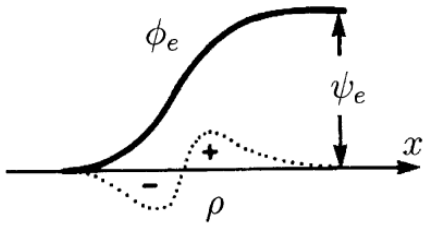

FIGURE 3.19: The electrostatic potential for a stationary double layer (DL), associated with a dipole-like charge density ρ: after Schamel, 1986; Eliasson and Shukla, 2006.

the start of the ionization zone at $z = 0.15$ cm and at the cathode emission plane at $z = 1.9$ cm. These two structures could contribute to electron flow regulation.

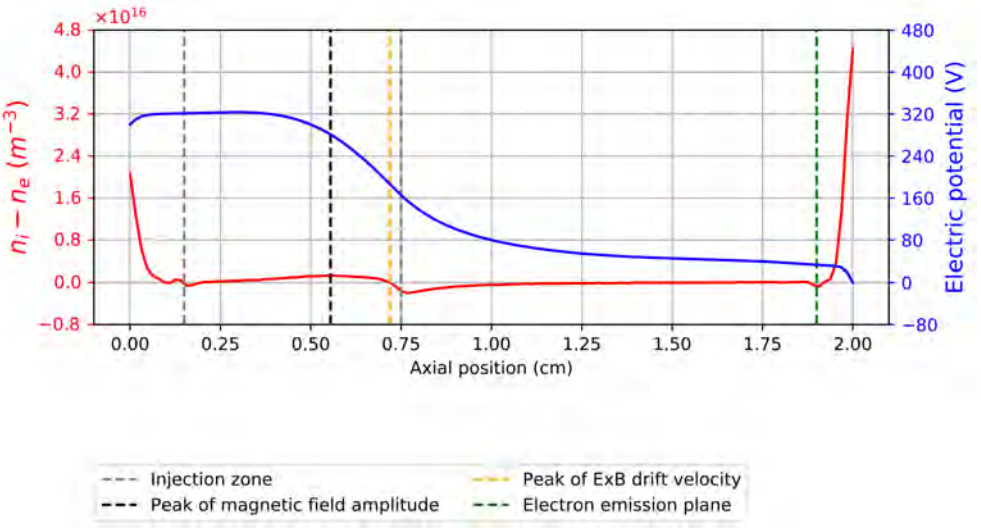

FIGURE 3.20: Electric potential and difference of particle density $n_i - n_e$ in the ExB configuration.

The dipole structure firstly indicates that the quasi-neutrality assumption does not apply to Hall thruster physics. Secondly, it implies particle trapping or reflection, as stated in the article by Schamel, 1986:

> "According to Poisson's equation, $\Delta\phi = -\frac{e(n_i - n_e)}{\epsilon_0}$, a positively charged layer gives rise to a region of negative curvature of ϕ and vice versa, and hence, two oppositely charged layers are needed to build-up the DL structure. Again, trapped particles must be involved, as can be seen by a simple counter argument. Namely, if only streaming (i.e. non reflected) particles would be present, the spatial constancy of each current, $n_j u_j$= const., j = i,e, would imply that the required asymptotic charge neutrality cannot hold simultaneously on both sides of the DL structure. Due to

> the different acceleration each species experiences in the DL, the densities are affected differently: The density of ions (electrons) injected from the high (low) potential side decreases (increases) with decreasing potential. Therefore, if the densities are equal on one side, they have to differ on the other side, and charge neutrality cannot be established there. [...] Spontaneous current disruption caused by electron reflection on a negative potential dip, is the triggering mechanism for a DL."

Applying a potential bias thus seems to lead naturally to a stable dipole structure, although this has not yet been proven theoretically. Laboratory experiments (See references in Schamel, 1986) confirm the existence of such structures in plasma discharges with a potential bias created by electrodes. In the case of the thruster, the magnetic configuration can lead to a reflection of electrons (Observed trajectories in a static electric and magnetic field are periodic and thus bounded) and must be taken into account in addition to reflections linked to electric potential drops. The physics of the Hall thruster could thus benefit from the work carried out on "double layers". It should be noted that fluctuations of the kHz order have been observed on this type of structure under the name of "potential relaxation oscillations" (PRO) (Schamel, 1986):

> "Low frequency fluctuations ($\omega < \omega_{pi}$) with a peak at the center of the DL have also been observed. [...] The oscillatory phenomenon to be discussed here has been observed in many experiments [142.145—153], in which the finite length of the system is of crucial importance. A typical arrangement is a plasma diode (single-ended Q-machine) consisting of a grounded plasma source and a positively biased collector plate terminating the plasma. If the applied voltage is sufficiently large, low frequency oscillations of typically 1—10 kHz are seen."

These fluctuations seem to depend on the distance between the electrodes. A cycle of fluctuations is described in Schamel, 1986, enabling us to link them to the propagation of DL:

> "One readily recognizes two main phases within one cycle of about 400 μs. The first one is characterized by a strong propagating DL which is accompanied by a broad negative potential dip (NPD) on its low potential side, the second one by a fast increase of ϕ in the whole column shortly after the DL has reached the anode. The collected target current is sawtooth-like in time with the decaying phase during the presence of the DL. The oscillation period is correlated with the transit time of the DL which moves with approximately 2—3 times the ion sound speed. This propagation velocity is determined by the speed of the expanding plasma on the low potential side, enabling the DL to satisfy the two Bohm criteria [99]. The second, more rapid phase, is due to an instability of the electron-rich sheath which is formed at the anode after the arrival of the DL. The electrons in this sheath and in the column are quickly lost, and the resultant positive space charge gives rise to an increase of the space potential because the ions cannot respond on this fast time scale."

The case taken as an example in Schamel, 1986 considered an experimental device of almost 40 cm and a discharge voltage of the order of 50 V. The fluctuations present in the thruster (and in the simulation results) at kHz could be of the order of a few hundred kHz if we consider a domain size ten times smaller and a discharge voltage four to six times greater. When we look at the temporal variations in the axial electric potential and density profiles derived from the simulation results, during the first two microseconds, we observe the propagation of a DL which originates in the low-potential zone and propagates to the cathode, as shown in figures 3.21 and 3.22. This could be similar to the first phase of the cycle mentioned above. The end of the first phase of the cycle can be seen in the electron and ion current profiles at the cathode in figure 3.7. High electron and ion currents are observed as the DL passes the cathode at around t = 2 μs. We note that this is also the case in the three-dimensional PIC simulation presented in Villafana, 2021 (see Figure 5.5). We note that the potential then rises throughout the domain and approaches the average static profile shown in red in figure 3.22. This could be the second phase of the cycle described above.

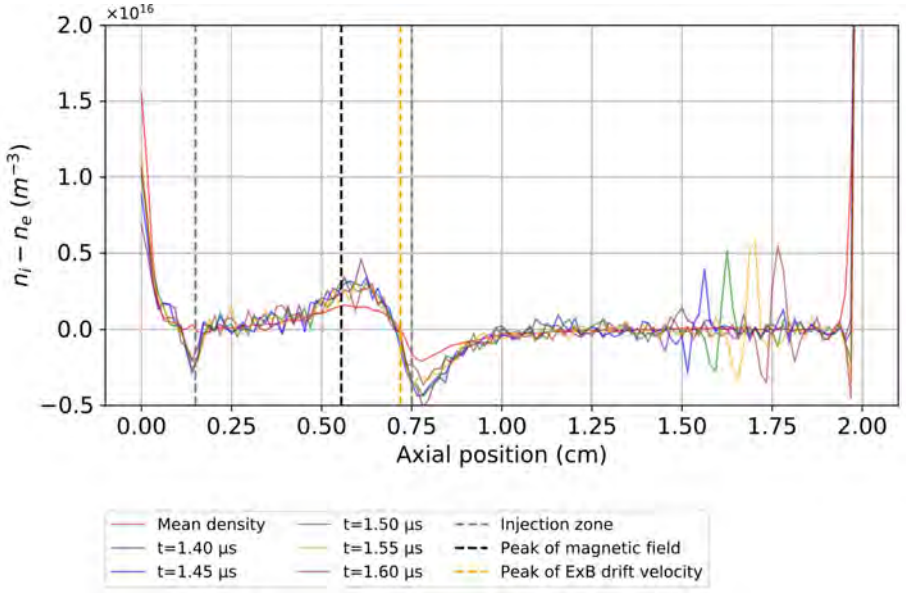

FIGURE 3.21: Axial propagation of a double layer in transient state observed in three-dimensional Sparse-PIC simulations: mean density profile in converged state is also represented in red.

Nevertheless, we note that no further DL propagation of this amplitude appears in the simulation thereafter. The azimuthal drift instability present from the first tens of nanoseconds is disturbed by the propagation of this DL, as described later in the section on waves, but seems to be independent of it. The fluctuations observed at kHz in the simulation begin after the passage of this DL and take place mainly in the azimuthal direction. The origin of this axial disturbance appears to be independent of the magnetic field. The maintenance and transformation of the instability at kHz in the azimuthal direction, on the other hand, seems to depend on it.

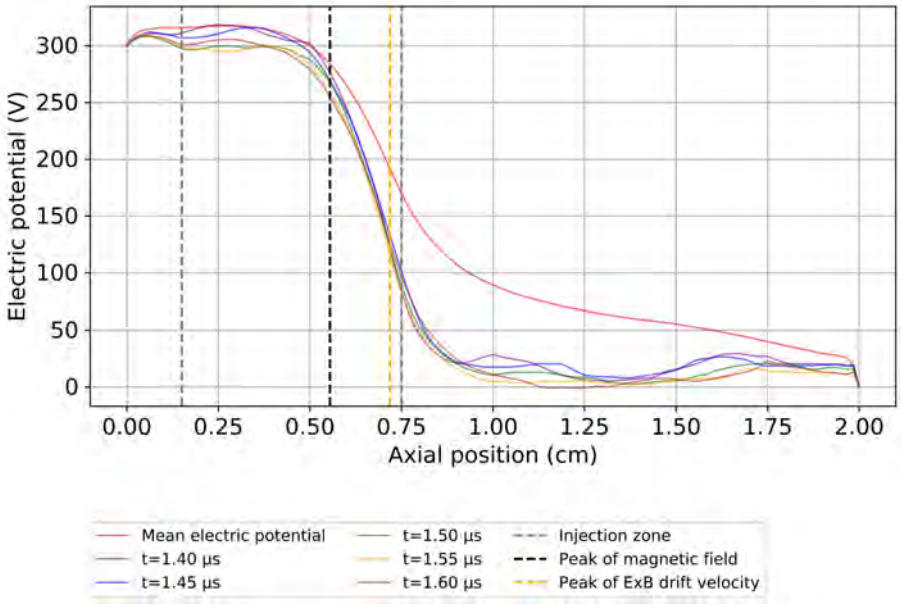

FIGURE 3.22: Axial propagation of a double layer in transient state observed in three-dimensional Sparse-PIC simulations: a potential dip accompanies the propagation of the DL, mean potential profile in converged state is also represented in red.

Other works on space plasmas that mention "double layers" refer to the formation of the main DL (Torvén, Palmadesso, and Papadopoulos, 1979, pages 104-105):

> "It has been argued that double layers might be formed as a result of a local evacuation of the plasma (Alfven and Carlqvist, 1967; Carlqvist, 1969). The principal idea is, that if the plasma is forced to leave a local region at the same time as the current is kept constant - e.g. by means of an inductance - charges of opposite polarity will collect at the boundaries of the evacuated region until the potential drop across the region has grown so large that a space-charge limited current, similar to that described by Langmuir (1929) (see Section 3.2), can start to flow. [...] Several instabilities may give rise to a local evacuation of the plasma. One possibility is that the evacuation is caused by the two-stream instability (Carlqvist, 1973) [...]. The plasma is initially (t = 0) homogeneous (density = n_0) except for a small and local disturbance in the form of a dip in the density. [...] The density dip becomes deeper and more narrow as time passes. [...] However, nothing seems to prevent that the process may work also for other temperature ratios or even by means of other instabilities."

In the case of the Hall thruster, the presence of the magnetic field means that the space charge current introduced by Langmuir cannot be directly applied. However, the principle could be the same. The instability at the origin of plasma evacuation could saturate when the limiting current is reached. Note that the $n_i - n_e$ density dips in the profiles in figure 3.21 are located at the boundaries of the ionization zone and at the level of the cathode emission plane. They could be the result of the growth

of instabilities responsible for the plasma evacuation required to form the DL, and are comparable to the dips shown in Torvén, Palmadesso, and Papadopoulos, 1979 (See figure 3.23).

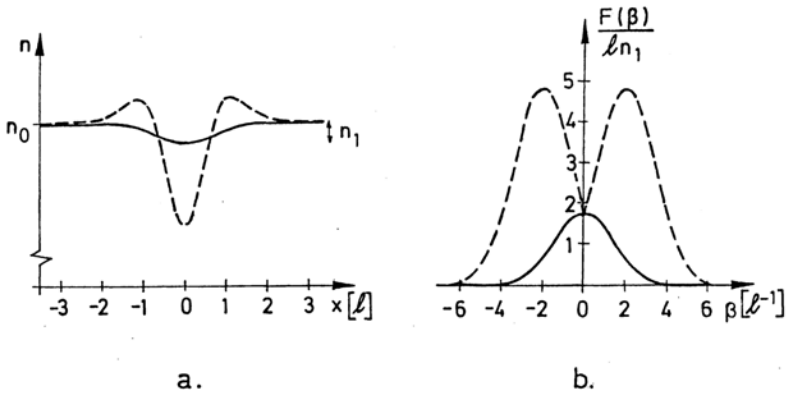

Figure 9. The development of a small disturbance of the density, n(x), and its associated Fourier spectrum F(β) normalized by ℓn_1 is illustrated in a) and b) respectively. The solid curves show the initial state at t = 0 when the density disturbance is assumed to have a Gaussian shape with the amplitude, $n_1 (<< n_0)$, while the dashed curves show the state at a later time $t = t_1$.

FIGURE 3.23: Example of density $n_i - n_e$ dip occurring in the formation of a double layer after Torvén, Palmadesso, and Papadopoulos, 1979.

Only the density dip at the end of the ionization zone at z = 0.75 cm remains noticeable in the "stationary" regime (as defined in previous sections, average profile in red). At this stage, however, it remains difficult to conclude on a link between the azimuthal drift instability and the one at the origin of the plasma evacuation. The next step is to study the plasma's behaviour in phase space, in order to gain a better understanding of the formation of the DL and the role of the azimuthal drift instability. It should be noted that elements of theory have been developed on structures observed in phase space in one spatial dimension (Dupree, 1982; Schamel, 1986; Eliasson and Shukla, 2006; Hutchinson, 2017) and could serve as a basis for the construction of theoretical tools to describe the phase-space behavior of the Hall thruster.

3.6 Velocity distribution profiles as a function of axial position

3.6.1 Energy contours using energy conservation

Before presenting the profiles obtained by simulation, we can attempt to predict the shape of the velocity distribution perpendicular to the radial magnetic field $v_\perp = \sqrt{v_{azimuthal}^2 + v_{axial}^2}$ by conservation of energy. To a first approximation, the magnetic field allows this conservation if gradient effects are neglected. This is true if the ratio of the magnetic gradient drift velocity to the electron thermal velocity is small in front of one. Note the magnetic gradient drift velocity $V_B = \frac{v_\perp^2}{2w_{ce}} \frac{\vec{B}\times\vec{\nabla}B}{B^2}$ and the electron thermal velocity $V_{th} = \sqrt{\frac{2eT_e[V]}{m_e}}$. Under our conditions, we have $\frac{V_B}{V_{th}} < 0.25$ in the entire simulation domain, which justifies this approximation. One consideration is to introduce energy iso-contours perpendicular to the magnetic field considering $E_\perp = \frac{m_e v_\perp^2}{2} - e\Phi$ constant from the mean axial electric potential profile (see figure 3.9). We plot for three initial axial positions, two in the ionization zone (at the center at z = 0.45 cm, at the end at z = 0.75 cm) and one at the cathode emission plane (z = 1.9 cm), energy iso-contours for different initial perpendicular velocities (initial kinetic energy from 0 to 45 eV every 5 eV) in figure 3.24. The perpendicular velocity profiles $v_\perp$ are therefore plotted as a function of the potential profile and of their initial kinetic energy E_{c0} with the conversion:

$$v_\perp[m/s] = \sqrt{\frac{2(e\Phi[V] + 1.602 \times 10^{-19} \times E_{c0}[eV])}{m_e}} \tag{3.7}$$

Note that the electrons produced by ionization to the left of the pressure equilibrium point (See figure 3.17) are trapped in the simulation domain, as their energy contour is cancelled out before they reach the anode. The other electrons are passing through on their way to the anode. Only electrons reinjected at the cathode emission plane and having reached an energy $E_\perp$ associated with the $E_{c0} = 15$ eV contour see their energy contours reach the cathode. They are therefore a priori the only ones able to neutralize the flow of ions towards the cathode. However, this view only shows the influence of the static electric potential. The magnetic field configuration also restricts the axial displacement of particles in the domain. To demonstrate this, let us place ourselves in the previous static electric field configuration, but this time taking the magnetic field into account. For reasons of legibility, we have omitted the axial injection position corresponding to the start of the ionization zone (z = 0.15 cm) in the previous figure. Here we can plot the energy contours achieved under these conditions by particles injected at the three previous axial positions and at the one corresponding to the start of the ionization zone, with initial velocity directed towards the anode in figure 3.25.

A second conclusion is that there can be no currents at the anode and cathode if we do not take into account a time-varying electric field.

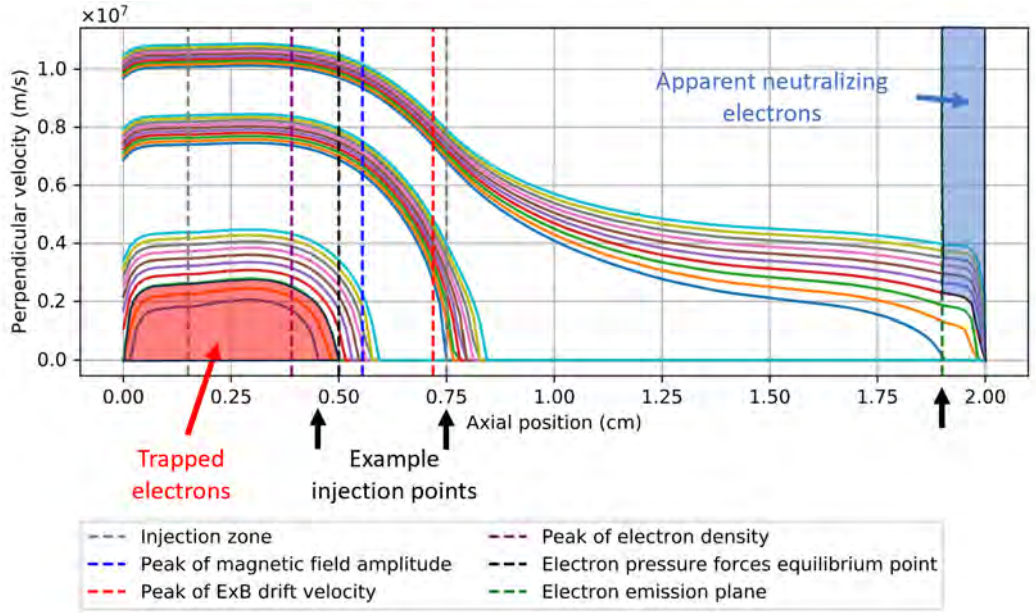

FIGURE 3.24: Perpendicular velocity of particles considering $E_\perp = \frac{m_e v_\perp^2}{2} - e\Phi = constant$ for three injection axial positions (0.45 cm, 0.75 cm and 1.9 cm) and different initial perpendicular energy levels (0 to 45 eV).

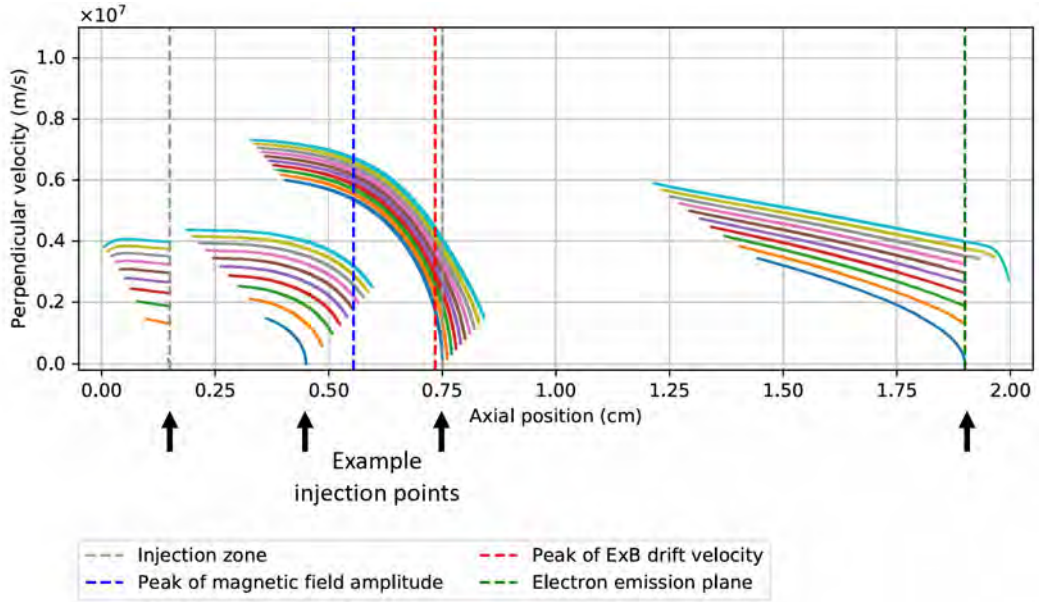

FIGURE 3.25: Perpendicular velocity of particles considering a static axial electric field taken from the mean electric potential in converged state and the influence of the magnetic field on particle trajectories for four injection axial positions (0.15 cm, 0.45 cm, 0.75 cm and 1.9 cm) and different initial perpendicular energy levels (0 to 45 eV).

3.6.2 Computing distribution functions

We are now interested in the electron distribution function in velocity space as a function of axial position z. Consider the profiles $f(z, v_{radial})$, $f(z, v_{azimuthal})$, $f(z, v_{axial})$, $f(z, v_{\perp})$, $f(z, |\vec{v}|)$ where $|\vec{v}| = \sqrt{v_{radial}^2 + v_{azimuthal}^2 + v_{axial}^2}$. These profiles are obtained by considering a volume similar to that introduced in figure 3.5 (slice domain on the right, width depends on the choice of shape function). The one-dimensional shape function is introduced for any axial position z and grid spacing Δz:

$$S_{\Delta z}(z) := \frac{W(\frac{z}{\Delta z})}{\Delta z} \tag{3.8}$$

where $W(z) = max(1 - |z|, 0)$ in the case of hat functions. Similarly, we introduce the one-dimensional shape function for any velocity component v and a step Δv:

$$S_{\Delta v}(v) := \frac{W(\frac{v}{\Delta v})}{\Delta v} \tag{3.9}$$

For a population of $N_e(t)$ electrons with axial position $z_p(t)$ and velocity component $v_p(t)$ ($p \in [\![1; N_e]\!]$), N_t time samples at instants t_i ($i \in [\![1; N_t]\!]$), we compute the distribution function $< f(z, v) >_t$:

$$< f(z, v) >_t := \frac{\sum_{i=1}^{N_t} \sum_{p=1}^{N_e(t_i)} S_{\Delta z}(z - z_p(t_i)) S_{\Delta v}(v - v_p(t_i))}{N_t} \tag{3.10}$$

This quantity $< f(z, v) >_t$ multiplied by the number of particles N_{real} (cf. chapter 2, section 2.3) represented by a macroparticle gives the number of particles in the space $\left(z - \frac{\Delta z}{2} : z + \frac{\Delta z}{2}; v - \frac{\Delta v}{2} : v + \frac{\Delta v}{2}\right)$. We note that two representations of this quantity may be of interest. The first is to normalize this distribution function to one over the entire space (Normalized distribution legend). This gives information on particle distribution in the entire domain as a function of axial position z and velocity component v. The second, by normalizing this distribution function to one over each slice $\left(z - \frac{\Delta z}{2} : z + \frac{\Delta z}{2}; v - \frac{\Delta v}{2} : v + \frac{\Delta v}{2}\right)$ (Normalized space-stepped distribution legend if any). It provides information on the particle distribution in a slice at a fixed axial position as a function of the velocity component v. However, we have chosen to focus on the first representation to avoid any form of repetition.

In addition, we introduce the motion of the fluid particles by computing the acceleration in the direction of the velocity axis and the mean axial velocity in each cell $\left(z - \frac{\Delta z}{2} : z + \frac{\Delta z}{2}; v - \frac{\Delta v}{2} : v + \frac{\Delta v}{2}\right)$ and by plotting it on the distribution function profiles as streamlines. The more exact formulation of this calculation is expressed for the mean axial velocity V_{axial}, provided the denominator is non-zero:

$$< V_{axial}(z, v) >_t := \frac{\sum_{i=1}^{N_t} \sum_{p=1}^{N_e(t_i)} v_{p,axial}(t_i) S_{\Delta z}(z - z_p(t_i)) S_{\Delta v}(v - v_p(t_i))}{\sum_{i=1}^{N_t} \sum_{p=1}^{N_e(t_i)} S_{\Delta z}(z - z_p(t_i)) S_{\Delta v}(v - v_p(t_i))} \tag{3.11}$$

A similar formula is applied to compute the mean acceleration $< a(z,v) >_t$ in the (z,v) plane. The representation of the streamlines further requires us to divide the mean axial velocity by the axial grid step Δz and the mean acceleration by the velocity step Δv so that the vector $(\frac{<V_{axial}(z,v)>_t}{\Delta z}, \frac{<a(z,v)>_t}{\Delta v})$ represents the displacement vector in the (z,v) plane. Time sampling is taken every 10 time steps (0.125 ns) during two microseconds of physical simulation time for profiles in the "stationary" regime.

3.6.3 Transient regime

We have seen previously that DL formation could be explained by plasma evacuation due to an instability. The first two microseconds of simulation allow us to observe the evolution of the plasma between the initial homogeneous state and the situation where neutrality is broken. We present the profiles $f(z, v_{radial})$, $f(z, v_{azimuthal})$, $f(z, v_{axial})$, $f(z, v_\perp)$, $f(z, |\vec{v}|)$ obtained for ions and all electrons at regular intervals of 500 ns of physical simulation time. The results presented in this section come from the Sparse-PIC-Φ method for $n_{ppc,sparse} = 100$. Similar results are observed for the Sparse-PIC-Φ-4^{th} method and for $n_{ppc,sparse} = 50$ and $n_{ppc,sparse} = 200$.

Figures 3.26 and 3.27 show the distribution functions in the initial state, more precisely at the first time step ($t = 1.25 \times 10^{-11} s$). Streamlines are added on the distribution function profiles to provide information for the fluid motion. The plasma is initially homogeneous and the velocity distributions are Maxwellian, with temperatures of $T_i = 0.5$ eV for the ions and $T_e = 10$ eV for the electrons.

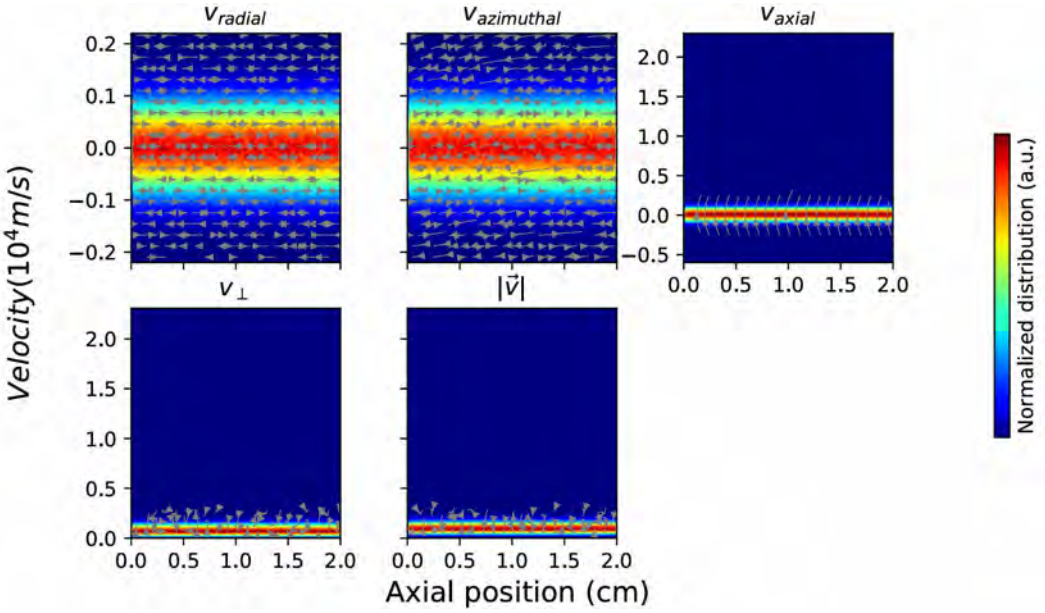

FIGURE 3.26: Axial profile of velocity distribution $f(z,v)$ at initial state: ions (normalized distribution), streamlines are also represented with grey arrows.

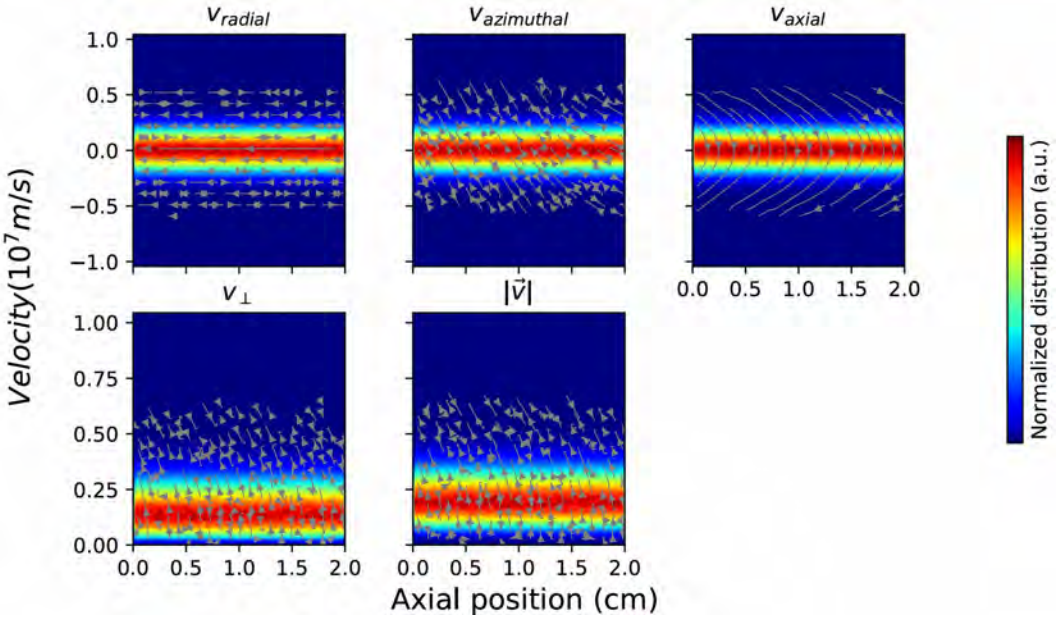

FIGURE 3.27: Axial profile of velocity distribution $f(z, v)$ at initial state: all electrons (normalized distribution), streamlines are also represented with grey arrows.

During the first 500 nanoseconds, sheaths form near the electrodes (represented by Dirichlet conditions). This results in a reduced presence of particles, as can be seen in figures 3.28 and 3.29. The axial velocity of ions begins to increase in the direction of the cathode, particularly near the magnetic field maximum, indicating the appearance of an axial electric field and the start of DL formation. It can be seen that the field lines corresponding to the fluid motion of the ions in the $(z, v_{azimuthal})$ space tend to heat the ions in the azimuthal direction in most of the domain. However, the azimuthal velocities of the ions remain an order of magnitude lower than their axial velocities at maximum.

The electrons, for their part, see the formation of two trapping zones in the (z, v_{axial}) plane, marked by the closure of the lines of fluid motion. The first, at the level of the magnetic field maximum (z = 0.5625 cm), corresponds to the formation of the main DL. The second, to its right, corresponds to the electrons following the ions being evacuated by the formation and axial propagation of another DL. At this stage, the DLs are hardly distinguishable on the density profile, as shown in figure 3.30 (t = 0.5 μs). Nevertheless, it can be seen in detail that a zone of positive density begins to form between z = 0.25 cm and the position of the magnetic field maximum (z = 0.5625 cm) as well as a negative density dip around z = 0.75 cm corresponding to the end of the ionization zone. The other planes of the electron distribution functions show rather disordered lines of motion. It is only in the "stationary" regime that we find distinct structures in these planes. These structures are shown in the dedicated sub-section.

At t = 1 μs, the main DL has formed (cf. figure 3.30). The plasma concentrates

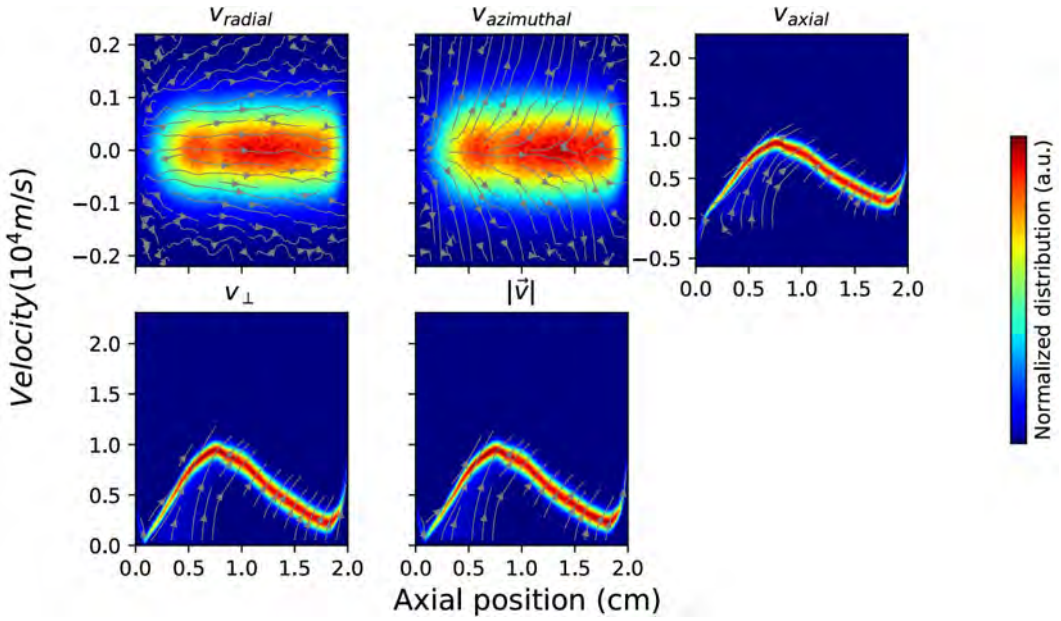

FIGURE 3.28: Axial profile of velocity distribution $f(z, v)$ at $t = 0.5\mu s$: ions (normalized distribution), streamlines are also represented with grey arrows.

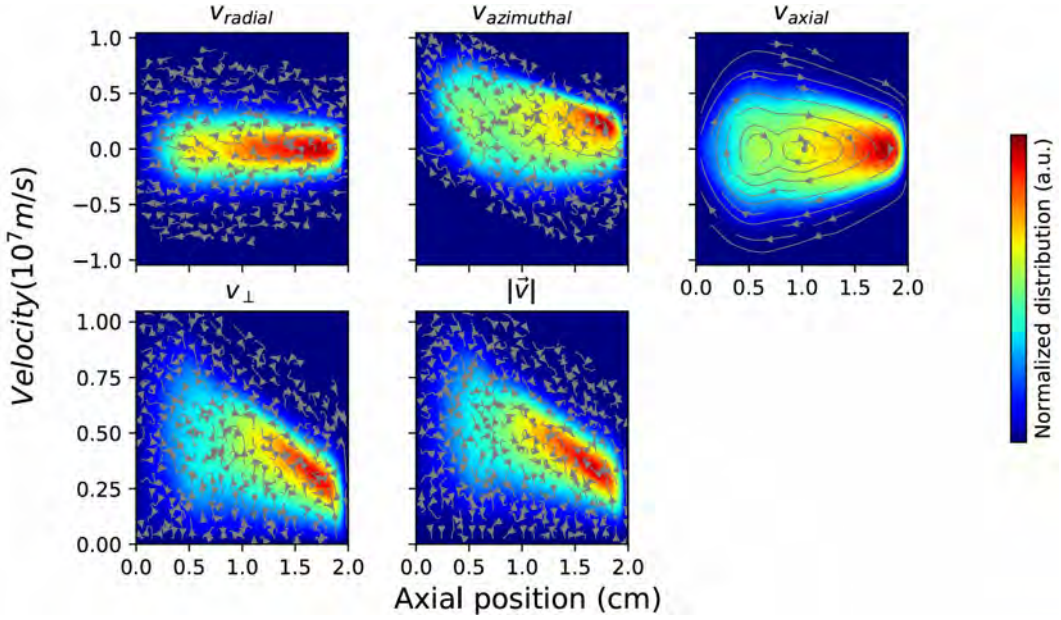

FIGURE 3.29: Axial profile of velocity distribution $f(z, v)$ at $t = 0.5\mu s$: all electrons (normalized distribution), streamlines are also represented with grey arrows.

close to the cathode, as shown by the ion and electron distribution functions in figures 3.31 and 3.32. The two trapping zones in the (z, v_{axial}) plane of the electron distribution function are clearly visible. Electrons injected at the cathode emission

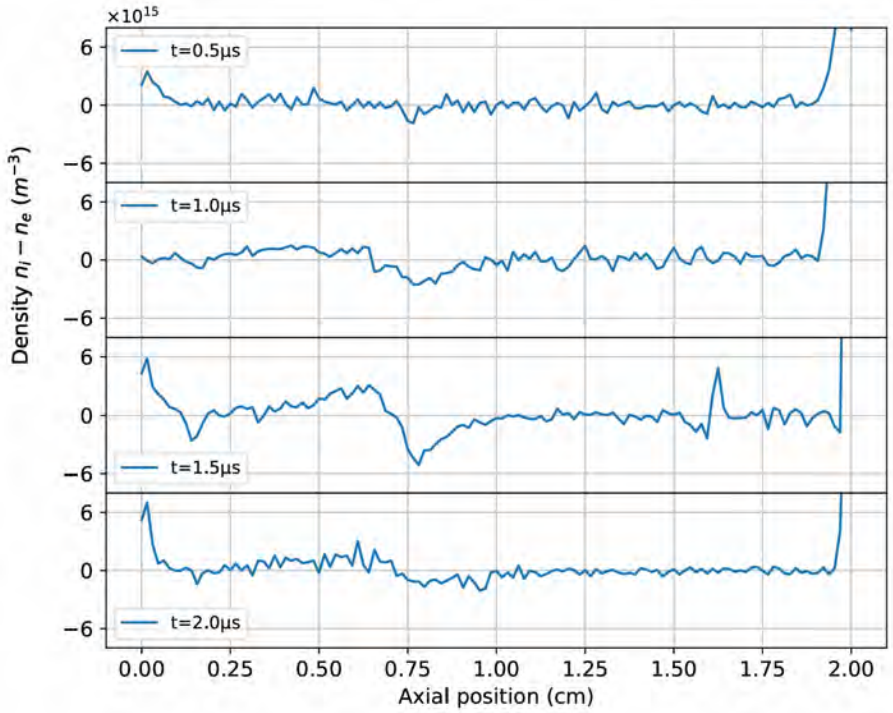

FIGURE 3.30: Axial profile of density $n_i - n_e$ at t = 0.5 μs, 1 μs, 1.5 μs and 2 μs.

plane give the shape of the distribution function close to the anode. However, the plasma can only be evacuated once another DL has formed and propagated.

This new DL forms around t= 1.3 μs (cf. figure 3.21) and propagates towards the cathode, dragging along a large part of the plasma. At t = 1.5 μs, the main DL is increased by an instability (cf. figure 3.30) and the other DL of opposite direction propagates towards the cathode. We also note a density dip around the position corresponding to the start of the injection zone at z = 0.15 cm. The ion and electron distribution functions in figures 3.33 and 3.34 clearly show the ongoing evacuation of plasma at the cathode. This plasma evacuation can be associated to an abrupt axial variation of the distribution functions. The electron distribution function near the cathode is narrower than that at t = 1 μs. Ions leave the domain at the cathode with an almost constant axial velocity close to 10^4 m/s, which is not the Bohm velocity.

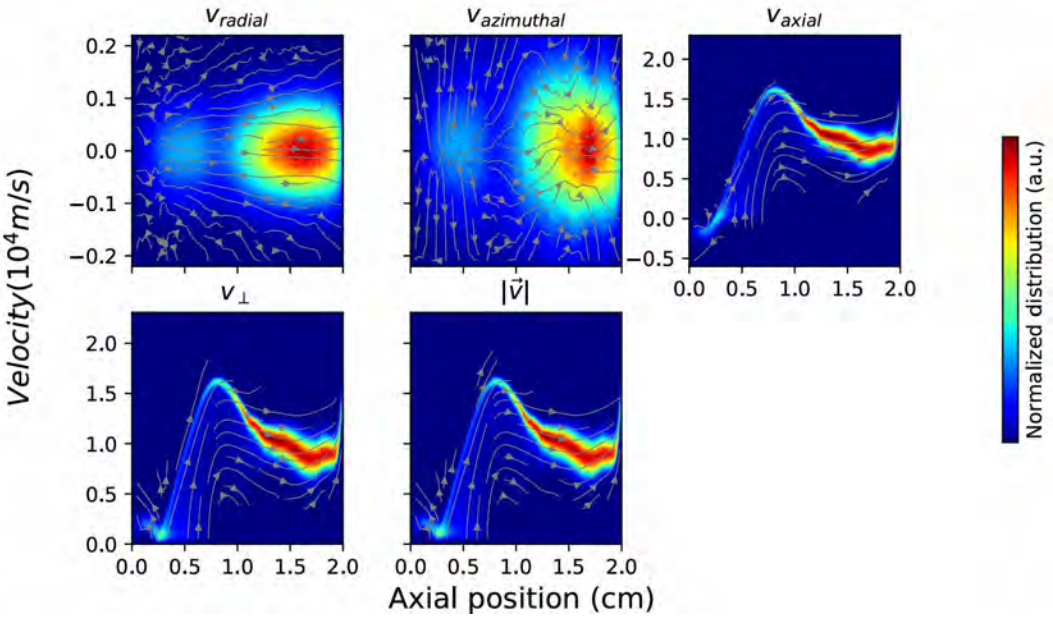

FIGURE 3.31: Axial profile of velocity distribution $f(z, v)$ at $t = 1\mu s$: ions (normalized distribution), streamlines are also represented with grey arrows.

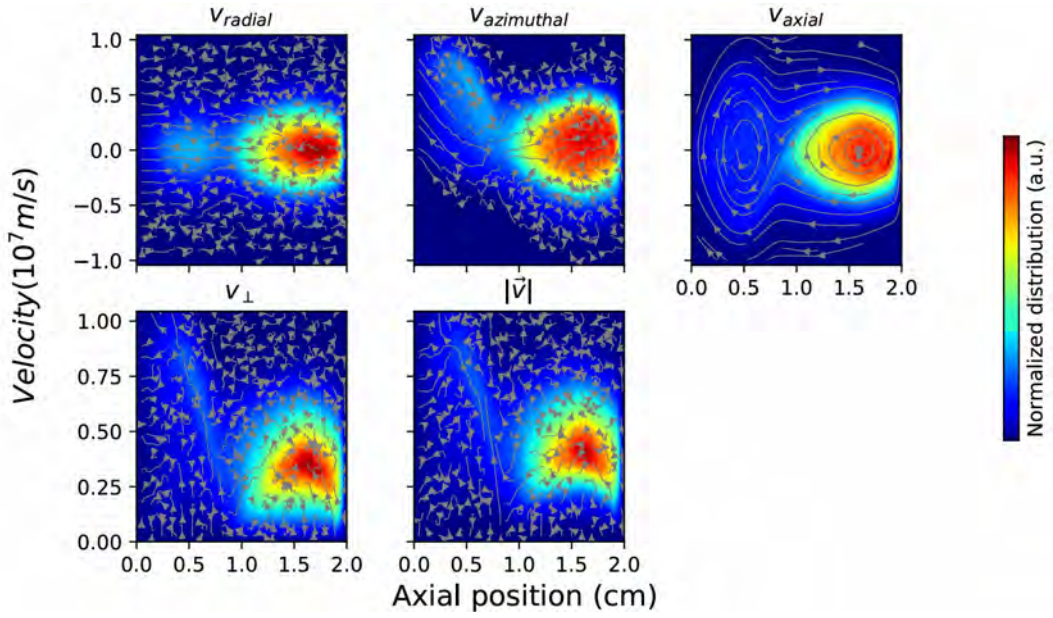

FIGURE 3.32: Axial profile of velocity distribution $f(z, v)$ at $t = 1\mu s$: all electrons (normalized distribution), streamlines are also represented with grey arrows.

At t = 2 μs, most of the plasma has been evacuated at the cathode, and according to the particle injection conditions, ions are re-injected with electrons into the ionization zone. Most of these ions see the potential drop associated with the main DL

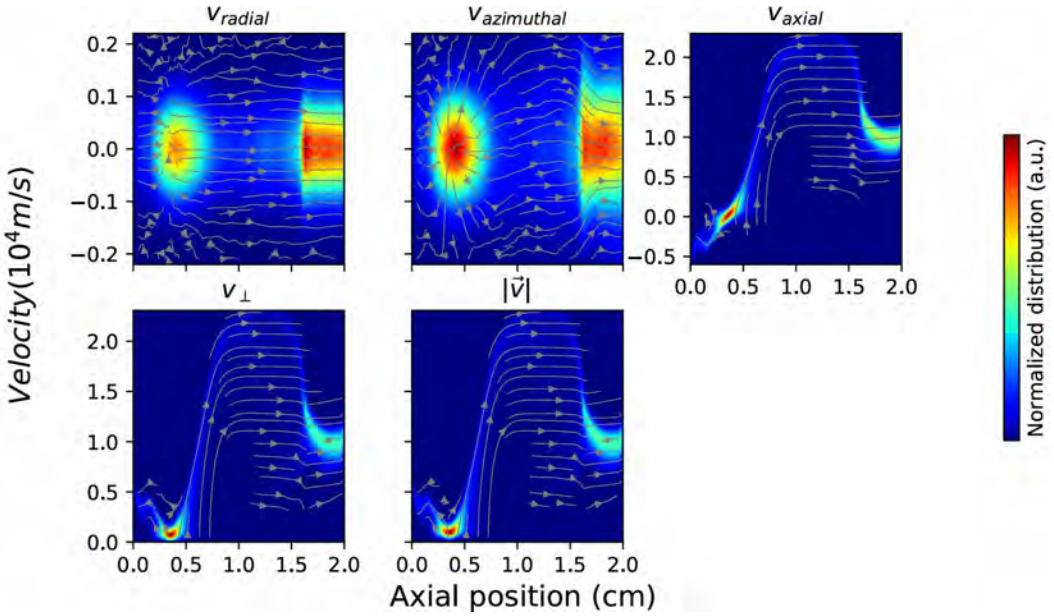

FIGURE 3.33: Axial profile of velocity distribution $f(z, v)$ at $t = 1.5\mu s$: ions (normalized distribution), streamlines are also represented with grey arrows.

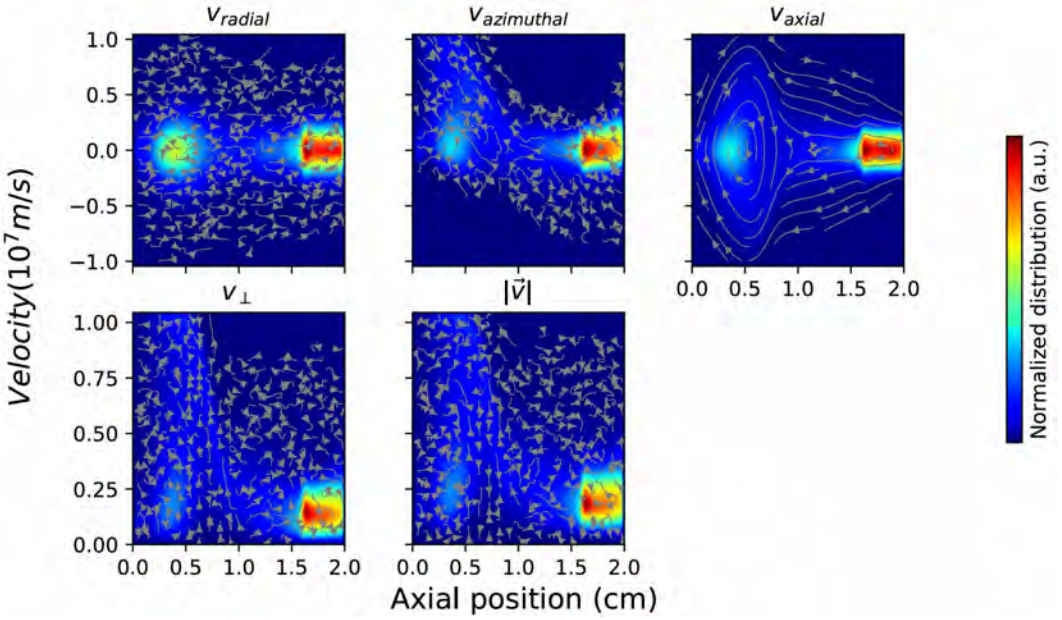

FIGURE 3.34: Axial profile of velocity distribution $f(z, v)$ at $t = 1.5\mu s$: all electrons (normalized distribution), streamlines are also represented with grey arrows.

and gain an axial velocity equivalent to to $\sqrt{\frac{2eU_d}{m_i}} \approx 2.2 \times 10^4$ m/s where $U_d = 320$ V is the voltage between the plasma core and the cathode (See figure 3.9). Note that U_d is greater than the voltage imposed between the electrodes. This could be

explained by the formation of sheaths at the electrodes, particularly at the anode, which require a pre-sheath potential drop to accelerate the ions. It can also be noticed that the break in neutrality does not correspond to the ion Bohm velocity at the electrodes. We also note that an azimuthal perturbation is still present on the ion distribution profile in the $(z, v_{azimuthal})$ plane. The electron distribution profile in this plane also shows disordered movements. In the (z, v_{axial}) plane, only the trapping zone linked to the main DL can be distinguished.

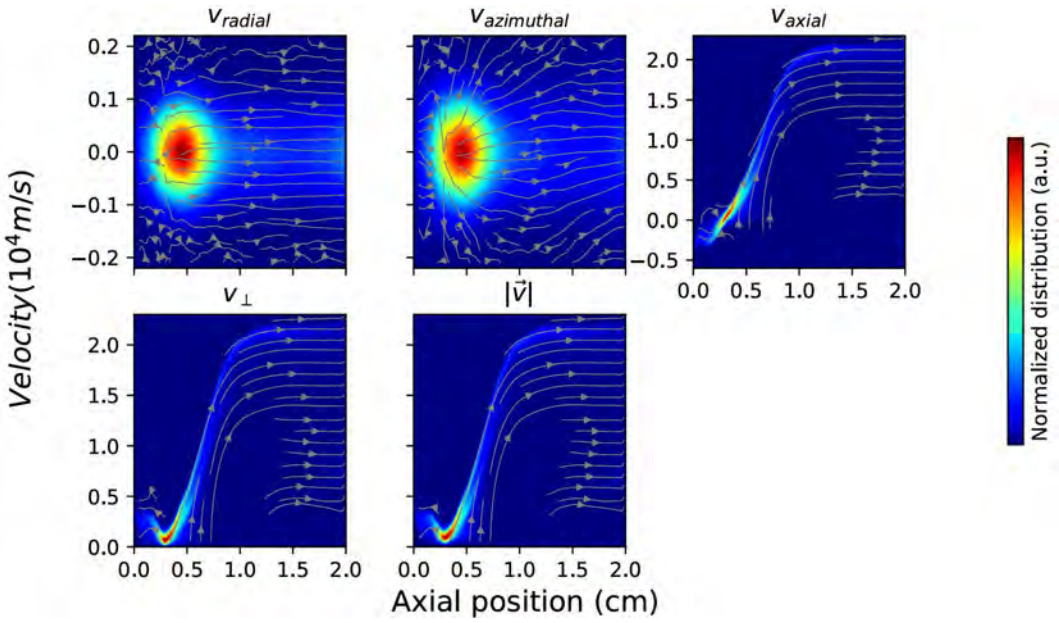

FIGURE 3.35: Axial profile of velocity distribution $f(z, v)$ at $t = 2\mu s$: ions (normalized distribution), streamlines are also represented with grey arrows.

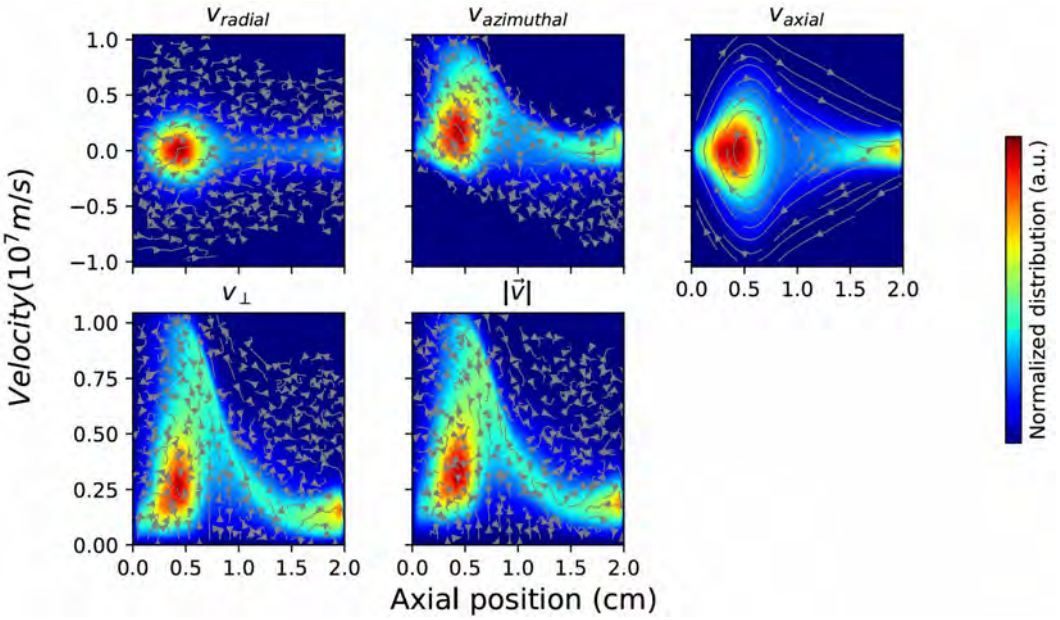

FIGURE 3.36: Axial profile of velocity distribution $f(z, v)$ at $t = 2\mu s$: all electrons (normalized distribution), streamlines are also represented with grey arrows.

3.6.4 "Stationary" regime

In the "stationary" regime, as defined in section 3.2, the electron velocity distribution profiles in figure 3.37 show wider radial velocity diffusion than at $t = 2\mu s$, and almost equivalent to axial velocity diffusion. Velocity diffusion peaks close to the magnetic field maximum. The lines of fluid motion in the (z, v_{radial}), $(z, v_{azimuthal})$, $(z, v_\perp)$ and (z, v) planes are ordered and show that the electrons neutralizing the ions at the cathode are those which have gained sufficient energy $E_\perp$ or $E_{total} = \frac{m_e v_e^2}{2} - e\Phi$, if we assume that neutralizing electrons follow streamlines going towards the cathode. This last conclusion is in line with the observation made on the energy contours in figure 3.24 which shows that only electrons produced at the cathode emission plane with an energy $E_\perp$ or E_{total} greater than that associated with E_{c0} =15 eV can neutralize the ion flux at the cathode.

The structure of the electron trapping zone in the (z, v_{axial}) plane, linked to the main DL and marked by the closure of the lines of fluid motion, can still be seen. This can also be seen on the distribution profiles when we look at the details of each electron population, those produced by ionization and those from the cathode emission plane (See figures 3.38 and 3.39). Most of the electrons produced by ionization are concentrated inside the channel before the magnetic field peak. This distribution can be explained by the electrostatic trapping of low-energy electrons in this zone (See figure 3.24). The electrons produced at the cathode emission plane tend to follow the $E_\perp$ and E_{total} energy iso-contours. The density of these electrons is lower close to the cathode, and can be explained by their high kinetic energy perpendicular to the magnetic field when approaching it. For example, an electron with a perpendicular velocity of $10^7 m.s^{-1}$ in a magnetic field with an amplitude of 90 G

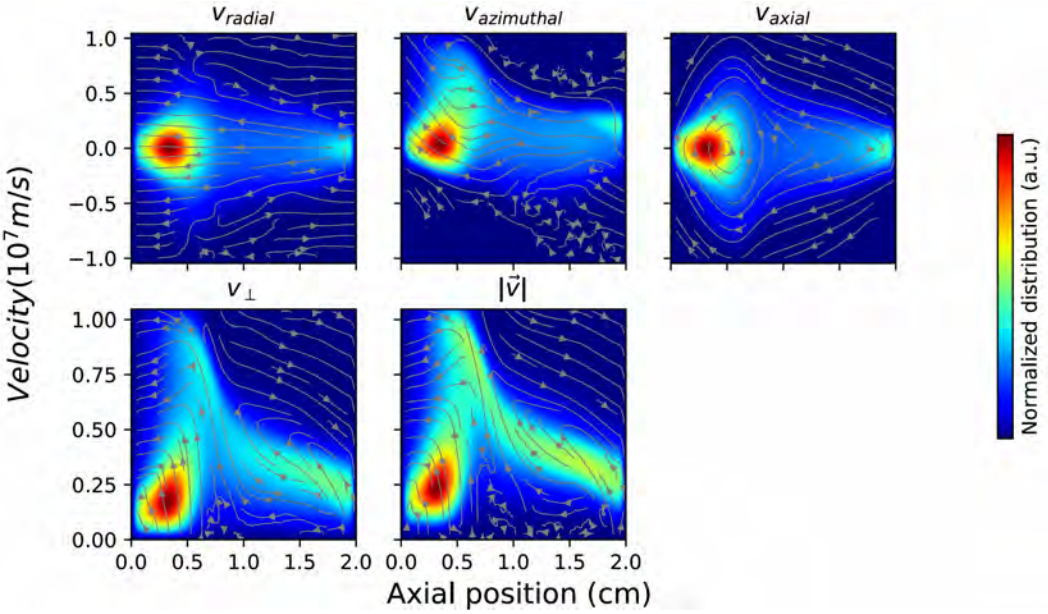

FIGURE 3.37: Axial profile of velocity distribution $f(z, v)$ in converged state: all electrons (normalized distribution), streamlines are also represented with grey arrows.

has a Larmor radius equal to 0.6 cm. These energetic electrons therefore only stay in the simulation domain for a short time. The distribution functions also show that some of the electrons produced at the cathode emission plane lose energy perpendicular to the magnetic field $E_\perp$ and to a lesser extent E_{total}, in the vicinity of the magnetic field peak, and join the $E_\perp$ and E_{total} energy levels rather associated with electrons produced by ionization.

The previous observation and the continuity of the distribution functions observed in figure 3.37 despite the difference in energy $E_\perp$ and E_{total} of electrons coming from the cathode emission plane and those produced by ionization suggest perpendicular or total energy exchanges between the different electron populations. Thus, we note the presence of a vortex structure of fluid motion lines in the $(z, v_{azimuthal})$ plane in figure 3.38 for electrons produced by ionization, marking the presence of the azimuthal instability. Note that it is not directly visible on the profiles associated with electrons coming from the cathode emission plane (Figure 3.39, $(z, v_{azimuthal})$ plane). This indicates that some of the electrons coming from the cathode emission plane are not affected by this mechanism. This vortex structure, whose center is close to the axial position corresponding to the magnetic field maximum allows perpendicular energy exchange between electrons coming from the cathode emission plane and those produced by ionization. Examples of trajectories derived from Sparse-PIC simulation are shown in figures 3.40 and 3.41.

Some of the electrons produced by ionization gain energy perpendicular to the magnetic field $E_\perp$ as they pass through the vortex structure to exit the domain at perpendicular energy levels associated with electrons coming from the cathode emission plane. The reverse phenomenon also affects some of the electrons produced at the cathodic emission plane, which lose energy perpendicular to the magnetic field

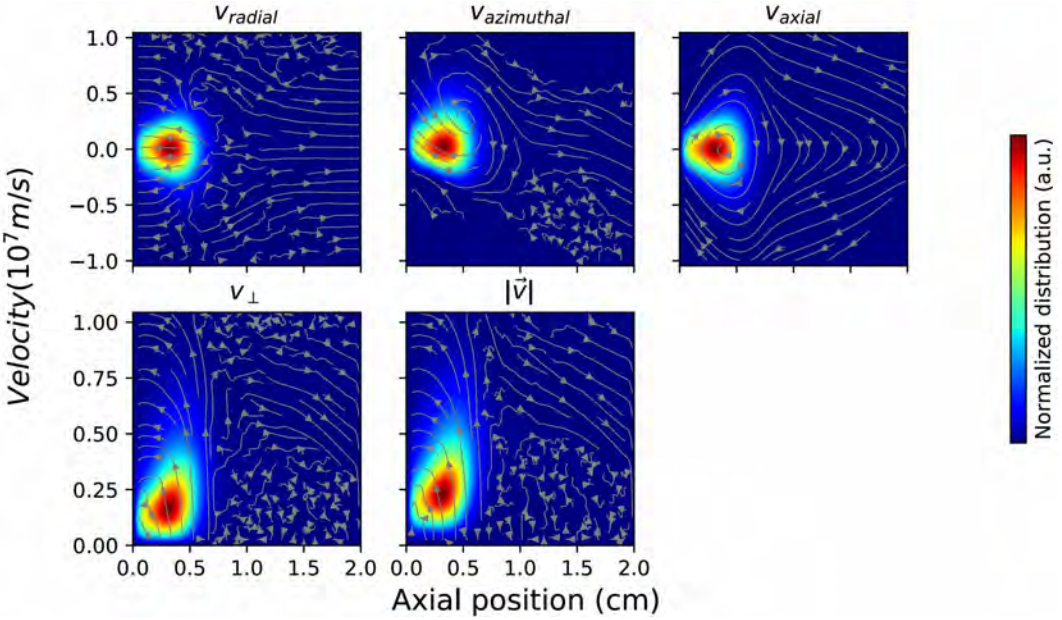

FIGURE 3.38: Axial profile of velocity distribution $f(z, v)$ in converged state: electrons from ionization (normalized distribution), a vortex structure can be observed in the $(z, v_{azimuthal})$ plane showing clear signs of an azimuthal instability.

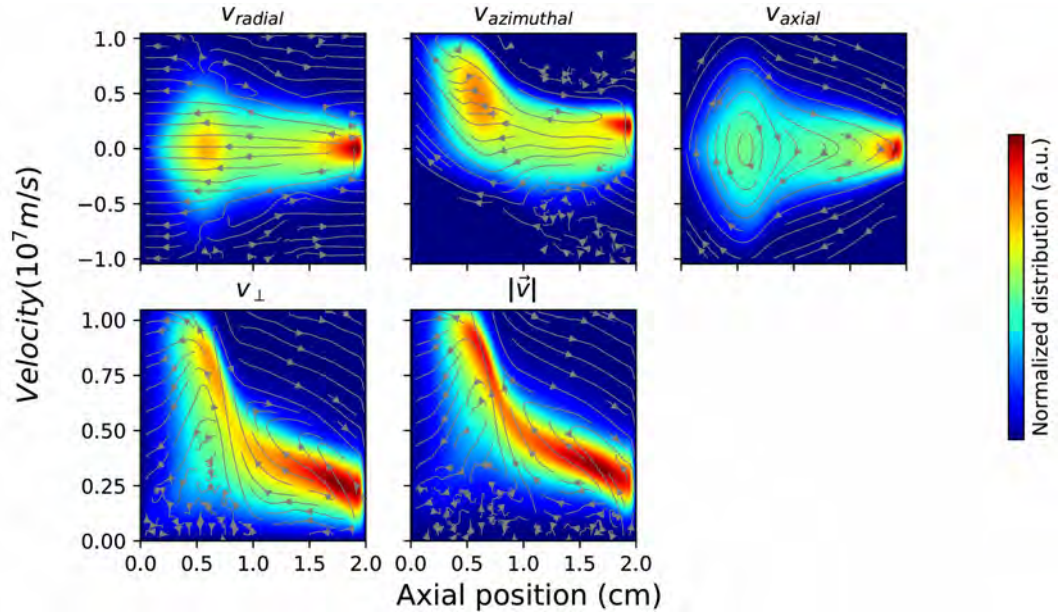

FIGURE 3.39: Axial profile of velocity distribution $f(z, v)$ in converged state: electrons from cathode emission plane (normalized distribution).

$E_\perp$ as they pass through the vortex structure, leaving the domain at perpendicular energy levels associated with electrons produced by ionization.

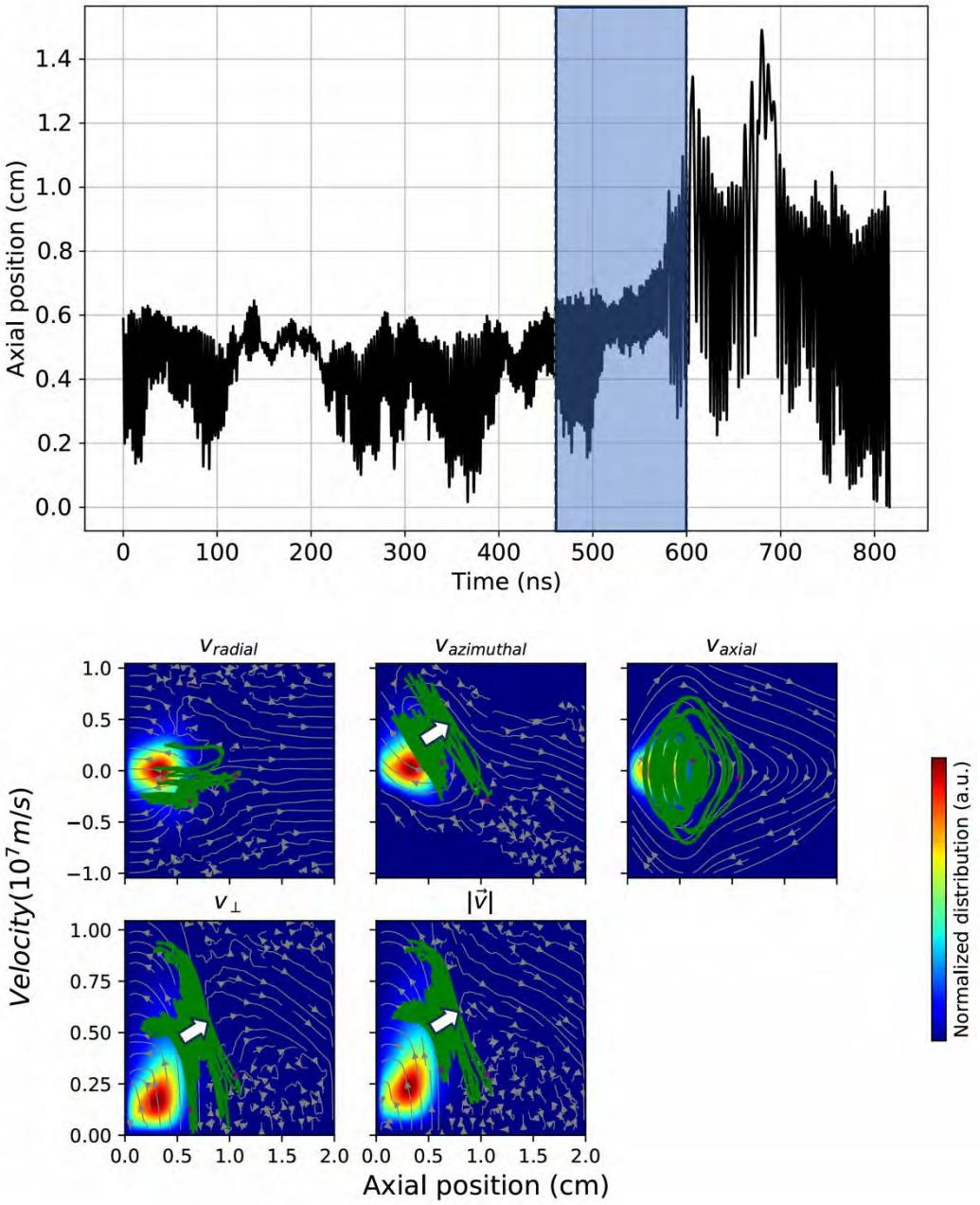

FIGURE 3.40: Trajectory of an electron from ionization extracted from the Sparse-PIC simulation: axial position with time, the blue zone is detailed just after (up), part of the trajectory in green showing the particle going through the vortex structure as it gains perpendicular energy $E_\perp = \frac{m_e v_\perp^2}{2} - e\Phi$ and total energy $E_{total} = \frac{m_e v_e^2}{2} - e\Phi$ (down), direction is represented by a white arrow, distribution functions f(z,v) of the electrons from ionization are represented as a framework (normalized distribution).

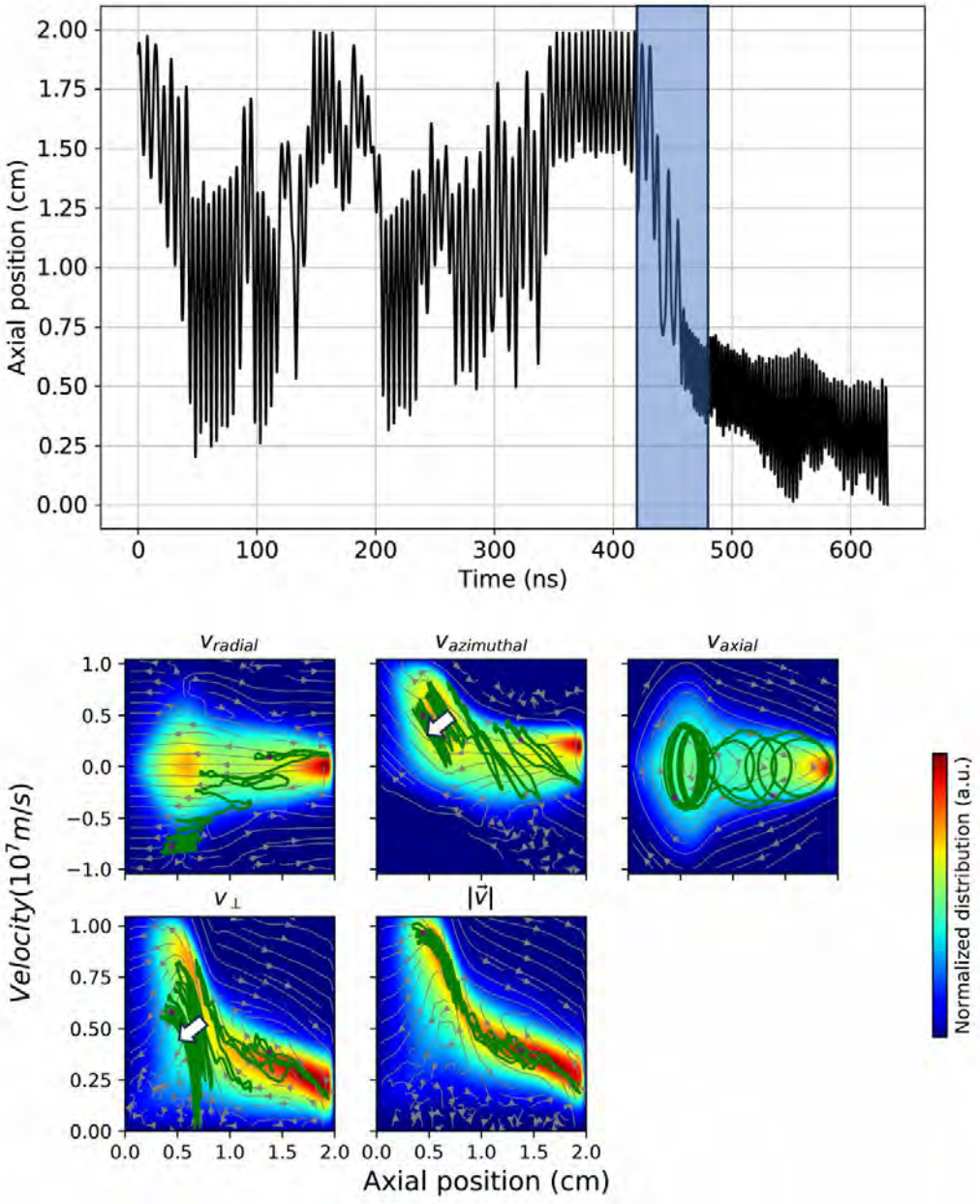

FIGURE 3.41: Trajectory of an electron from the cathode emission plane extracted from the Sparse-PIC simulation: axial position with time, the blue zone is detailed just after (up), part of the trajectory in green showing the particle going through the vortex structure as it loses perpendicular energy $E_\perp = \frac{m_e v_\perp^2}{2} - e\Phi$ (down), direction is represented by a white arrow, distribution functions f(z,v) of the electrons from the cathode emission plane are represented as a framework (normalized distribution).

The relative stability over time of the azimuthal instability therefore seems to be linked to the permanent exchanges of energy perpendicular to the magnetic field

$E_\perp$ between the two electron populations. Note that in the case of the electron trajectory coming from the cathode emission plane as it passes through the vortex (figure 3.41), the particle's kinetic plus potential energy E_{total} appears to remain almost constant. Indeed, the trajectory follows the energy iso-contour of the f(z,$|\vec{v}|$) profile similar to those shown in figure 3.24. This could explain the diffusion of radial velocities. Electrons from the cathode emission plane losing energy perpendicular to the magnetic field $E_\perp$ as they pass through the vortex could compensate for this loss by gaining energy in the direction parallel to the magnetic field $E_\parallel = \frac{m_e v_\parallel^2}{2} - e\Phi$, in this case radial. This difference in behavior between the two populations could be linked to the velocity differential. Faster electrons from the cathode emission plane would have time to exchange adiabatically whereas electrons produced by ionization would suffer instability without being able to adapt. However, this interpretation requires further investigation to be validated, and will be left to future work.

The electron trajectories obtained from the simulation also suggest different types of resonance to explain the passage of the magnetic barrier and the transit of electrons from the cathode to this barrier. The absence of a fluctuating electric field would prevent any current flow in this ExB cross-field configuration. Consequently, the jumps in axial displacements observed on the trajectories of electrons coming from the cathode emission plane every 100 to 200 ns could indicate the presence of resonance at the ion plasma frequency, while the passage of the magnetic barrier (magnetic field maximum) would rather be linked to electron cyclotron resonances with the mechanism of perpendicular energy exchange between the two electron populations described above. The link between the vortex structure and the cyclotron resonance will be developed later in the wave section (See figure 3.59).

On the ion side, the distribution profiles in figure 3.42 are close to those observed at $t = 2\mu s$. Radial and azimuthal velocities are more diffused than at $t = 2\mu s$, with the appearance of almost annular streamline structures in the (z, v_{radial}) and $(z, v_{azimuthal})$ planes.

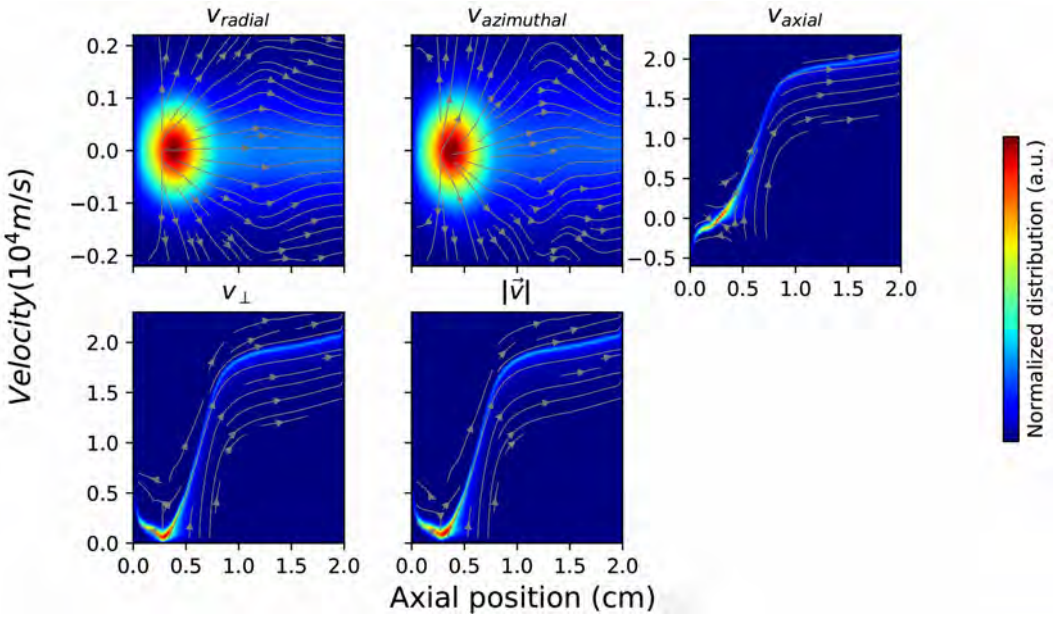

FIGURE 3.42: Axial profile of velocity distribution $f(z, v)$ in converged state: ions (normalized distribution).

3.7 Profiles in velocity space by transport zone

The presentation of the previous profiles with lines of fluid motion revealed a trapping structure linked to the main DL and a vortex structure in the $(z, v_{azimuthal})$ plane linked to the azimuthal instability. Another representation of the electron distribution function in velocity space can be made by axial transport zone and allows us to observe other fluid motion structures. For this purpose, we focus on the time-averaged axial electron flow profile shown in figure 3.43. Time sampling is taken every 100 ns for the last 12 microseconds of physical simulation time (from t = 10 μs to t = 22 μs). Compared with figure 3.20, we can divide this profile into six transport zones:

- two zones at the edges of the simulation domain correspond to sheaths and pre-sheaths,
- a zone in the channel corresponding to the formation of a secondary dipole, in which a decrease in electron flow towards the anode is observed, around the axial position corresponding to the start of the ionization zone (z = 1.5 cm),
- a positively-charged zone straddling the channel and the plume, in which electron flow to the anode increases,
- a negatively-charged zone in the plume in which electron flow to the anode decreases; together with the preceding zone, it forms a dipole whose axial delimitation corresponds to the maximum azimuthal drift velocity,
- a quasi-neutral zone in which electron flow is nearly constant.

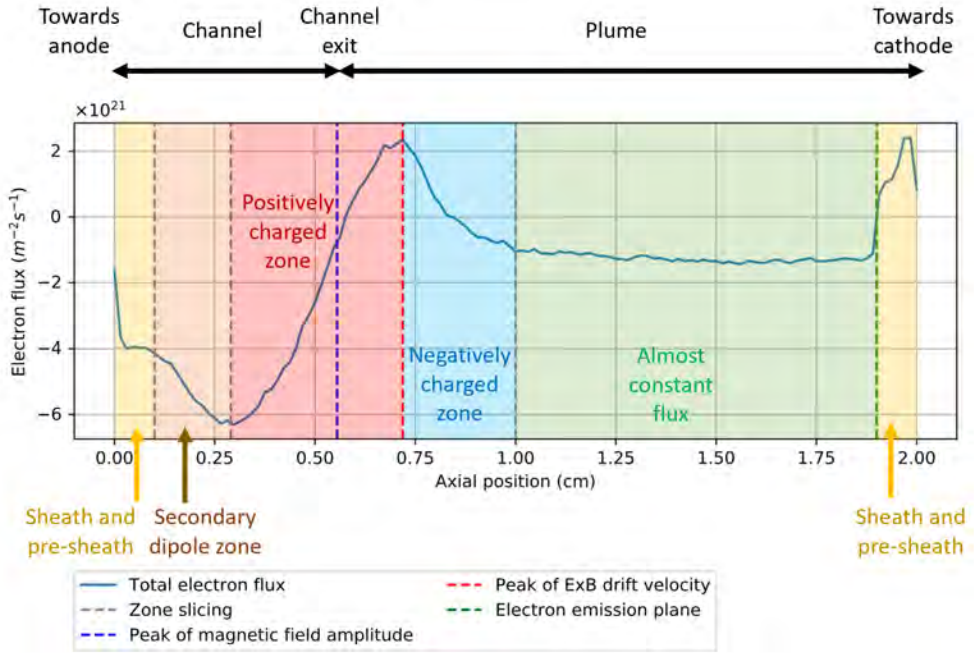

FIGURE 3.43: Axial electron flux: zone slicing for numerical diagnosis.

The figure 3.43 also shows the zones corresponding to the thruster channel, the plume and the electrodes as a function of axial position. Note that in this configuration, the electron flux gradient is not zero and seems to vary according to the dipole structures. We return to this observation later. While the main DL structure seems justified by previous works on plasmas with potential biases (see references in section 3.5), the secondary dipole zone that appears around the axial position corresponding to the start of the injection zone may be questionable. Indeed, one of the limitations of the model chosen to represent the thruster is that it does not take into account collisions, particularly with neutrals in the channel. These collisions tend to thermalize the electrons in the secondary dipole zone, which makes the presence of this structure less likely in reality. The transition between the anode zone and the thruster acceleration zone is present here in the form of an anode sheath due to Dirichlet conditions. This transition should be more complex, and the sheath strongly perturbed by the transit of neutrals. Despite these limitations, the ExB configuration studied should provide valid results for the Hall thruster, particularly around the main DL.

3.7.1 Fluid motion structures in velocity space

The $(v_{azimuthal}, v_{radial})$ plane of the electron distribution function is the seat of fluid recirculation movements, similar to vortices, which affect both electrons produced by ionization and electrons coming from the cathode emission plane. Figure 3.44 shows this dynamic for electrons produced by ionization. Two vortices can be seen, quasi-symmetrical with respect to the azimuthal velocity axis on the lines of fluid motion in the positively-charged zone of the main dipole (top right figure).

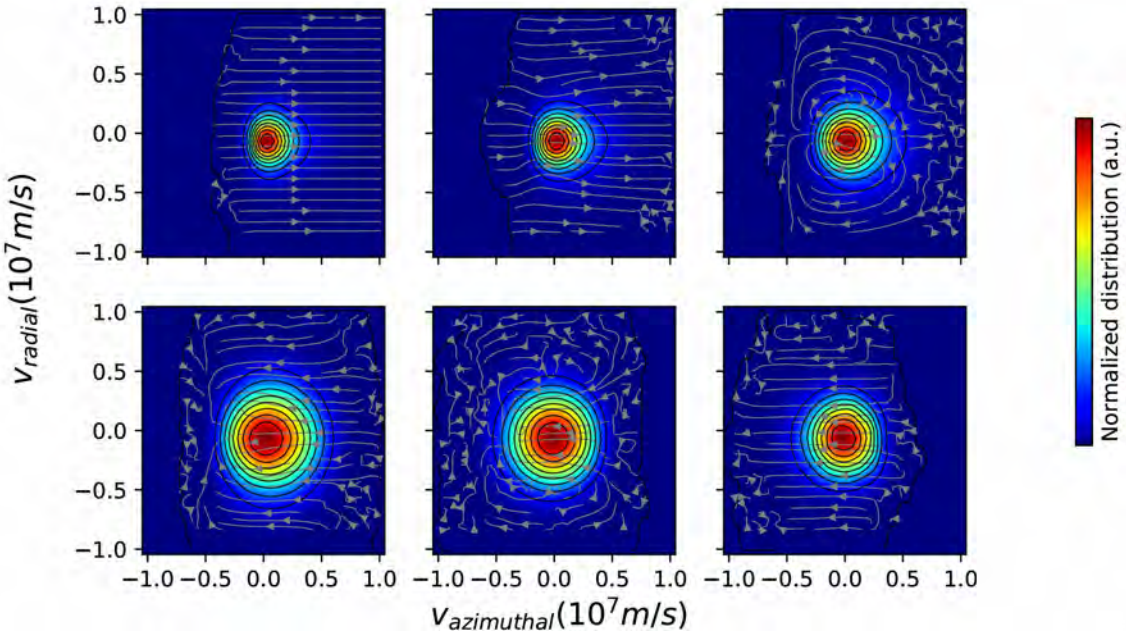

FIGURE 3.44: Azimuthal-radial profile of electron velocity distribution by transport zone for electrons from ionization: anode sheath (top left), secondary dipole (top middle), positively charged zone (top right), negatively charged zone (bottom left), almost constant electron flux (bottom middle), cathode sheath (bottom right).

Figure 3.45 shows its equivalent for electrons produced at the cathode emission plane. Note that vortices are clearly present in the main dipole zone, regardless of charge (top right and bottom left figures), but also in the zone of almost constant electron flux (bottom middle figure). In the positively-charged zone of the main dipole, the center of the vortices is located around radial velocities equal in absolute value to 5×10^6 m/s for electrons produced at the cathode emission plane, while it is located around radial velocities equal in absolute value to 2×10^6 m/s for electrons produced by ionization. Since the vortices circulate in the same direction for both electron populations, the offset of the centers in the radial velocity axis results in opposite movements in the $(v_{azimuthal}, v_{radial})$ plane, which could indicate an exchange of momentum between the two populations.

The presence of such structures in the $(v_{azimuthal}, v_{radial})$ plane indicates a necessarily different dynamic between the two-dimensional and three-dimensional cases, although there may be many points in common. These structures are also traces of instabilities that develop jointly in the azimuthal and radial directions. The anode sheath and secondary dipole zones in figure 3.45 (top left and top middle figures) also enable us to distinguish two subpopulations among the electrons produced at the cathode emission plane. One has continued towards the anode along the isoenergetic contour, while the other has been caught up in the instability and trapped in a low-energy zone.

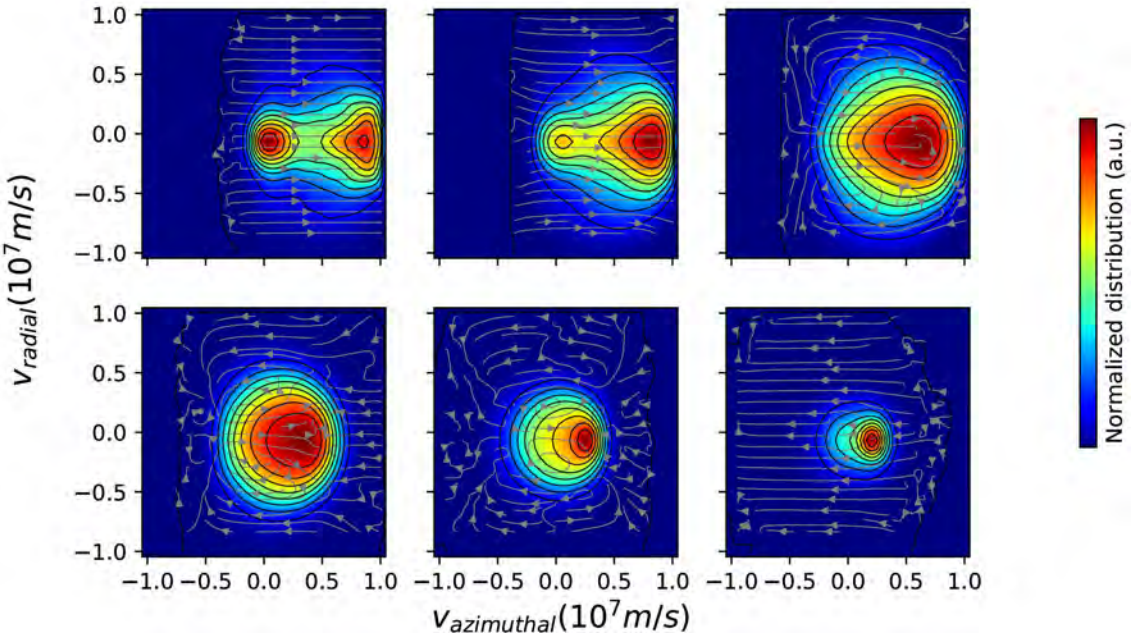

FIGURE 3.45: Azimuthal-radial profile of electron velocity distribution by transport zone for electrons from ionization: anode sheath (top left), secondary dipole (top middle), positively charged zone (top right), negatively charged zone (bottom left), almost constant electron flux (bottom middle), cathode sheath (bottom right).

Another plane (v_{axial}, $v_{azimuthal}$) allows us to visualize a fluid movement that circulates around a specific azimuthal velocity value, the drift velocity $v_d = \frac{E_z}{B_x}$ averaged over each transport zone. This is illustrated in figure 3.46 showing the fluid motion lines superimposed on the distribution functions of all electrons per transport zone.

This observation invites us to consider the average cross-field drift velocity as a constant reference point in steady state.

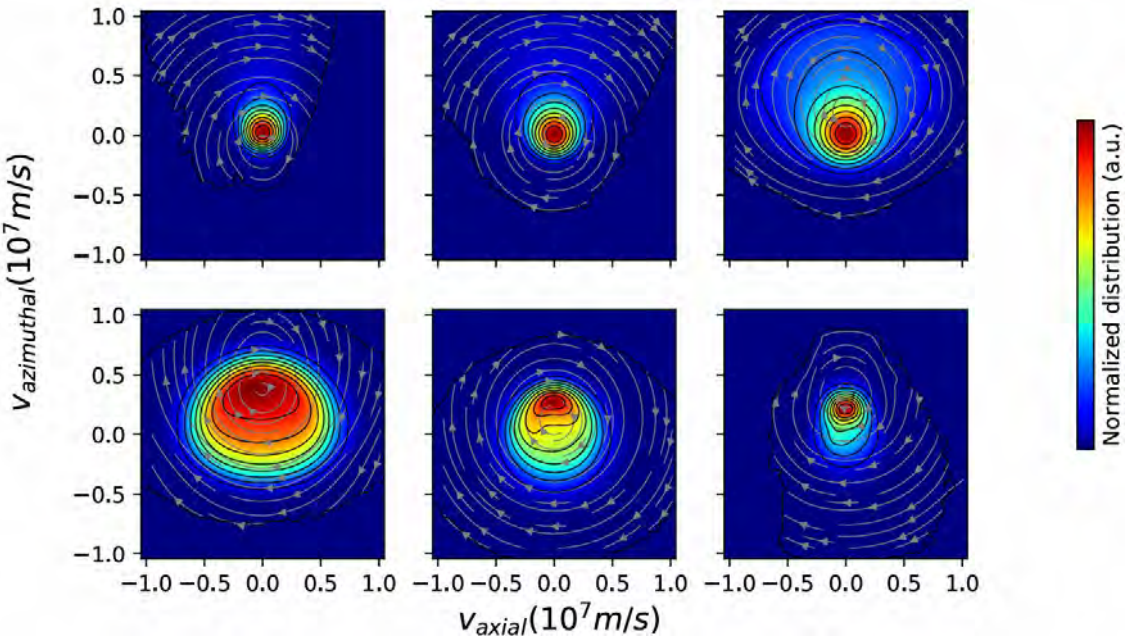

FIGURE 3.46: Axial-azimuthal profile of electron velocity distribution by transport zone: anode sheath (top left), secondary dipole (top middle), positively charged zone (top right), negatively charged zone (bottom left), almost constant electron flux (bottom middle), cathode sheath (bottom right).

3.7.2 An approximation of the axial electron transport

"Anomalous" transport (See Janes and Lowder, 1966, Yoshikawa and Rose, 1962) is based on the inclusion of a virtual collision term in the fluid equations (equivalent to viscosity or friction) resulting in an anomalous mobility term in the transport equation. This type of model is derived from the kinetic theory of gases and the terms associated with elastic collisions. However, electron-neutral collisions are negligible in the acceleration zone of the Hall thruster, particularly at the level of the magnetic field maximum (see figure 3.1). The term "anomalous" was used because electron transport across the magnetic barrier could not be explained by elastic collisions. A more physical interpretation of this non-collisional term is therefore necessary. For this reason, we investigate the nature of the non-collisional term through our simulation results.

The figure 3.43 presented at the beginning of this section shows the presence of non-zero terms to the right of the flux continuity equation (1.2), otherwise, the electron flux gradient would be zero and the electron flux constant throughout the domain. More precisely, when averaged in the radial (Ox) and azimuthal (Oy) directions (periodic conditions here), $\int_0^{L_x} \frac{\partial(n_e v_{e,x})}{\partial x} dx = 0$, $\int_0^{L_y} \frac{\partial(n_e v_{e,y})}{\partial y} dy = 0$, over time in steady state, $< \frac{\partial n_e}{\partial t} >_t = 0$, the ionization and injection of electrons at the cathode emission plane alone cannot explain the profile obtained, and kinetic terms must be

added to complete the fluid equation. This gives us:

$$\begin{aligned} < \frac{\partial(n_e v_{e,z})}{\partial z} >_{x,y,t} = & < \iiint_{-\infty}^{+\infty} C[f_e, f_i, ...] d^3\vec{v} >_{x,y,t} \\ & + < \iiint_{-\infty}^{+\infty} \frac{-e}{m_e}(\vec{E} + \vec{v} \times \vec{B}).\frac{\partial f_e}{\partial \vec{v}} d^3\vec{v} >_{x,y,t} \end{aligned} \tag{3.12}$$

The first term on the right-hand side of equation (3.12) combines the contributions of ionization and electron injection at the cathode emission plane. By definition of the injection conditions, these are restricted respectively to the injection zone between z = 0.15 cm and z = 0.75 cm and to the cathode emission plane at z = 1.9 cm. These contributions to the first fluid moment equation can be estimated by diagnosing the number of particles injected in the Sparse-PIC simulation. Ionization electron production at steady state for a number of particles per cell equal to 100 is equivalent to an ionization rate of $2.62 \times 10^{23} m^{-3} s^{-1}$ distributed over the ionization zone. We note that this is close to that imposed in the two-dimensional benchmark of Charoy et al., 2019 for slightly different conditions where $S_0 = 5.23 \times 10^{23} m^{-3} s^{-1}$. The electron emission rate at the cathode emission plane is equivalent to a source term of $1.53 \times 10^{25} m^{-3} s^{-1}$. The second term on the right-hand side of equation (3.12) is the kinetic term. The fact that it is non-zero implies an asymmetry of the electron distribution function f_e in at least one direction of velocity space. From the distribution function profiles f(z,v) presented in the previous section, we can assume symmetries in the direction of radial velocities (Ov_x) and axial velocities (Ov_z), which cancels out their respective integrals. Therefore $\int_{-\infty}^{+\infty} \frac{\partial f_e}{\partial v_x} dv_x = 0$ and $\int_{-\infty}^{+\infty} \frac{\partial f_e}{\partial v_z} dv_z = 0$. This implies that:

$$\begin{aligned} < \frac{\partial(n_e v_{e,z})}{\partial z} >_{x,y,t} = & < \iiint_{-\infty}^{+\infty} C[f_e, f_i, ...] d^3\vec{v} >_{x,y,t} \\ & + < \iiint_{-\infty}^{+\infty} \frac{-e}{m_e}(E_y + v_z B_x) \frac{\partial f_e}{\partial v_y} d^3\vec{v} >_{x,y,t} \end{aligned} \tag{3.13}$$

This expression of the first fluid moment is difficult to develop without further assumptions. However, it does indicate that dynamics in the azimuthal direction play a major role in axial electron transport. Then, we would like to understand the link between the $n_i - n_e$ density profile, particularly at the central dipole, and the axial electron flow gradient suggested by figure 3.43. A comparison is made in figure 3.47 by dividing the axial electron flux gradient by the cyclotron pulsation. It can be seen that in our axis conventions, in the main dipole zone, the electron flux gradient is of the same sign as the excess charge, as shown in figure 3.47.

This in itself is quite intuitive, since a negatively-charged zone will tend to slow down electrons moving in its direction, and vice versa. The contribution of the electron source term linked to the cathode emission plane in terms of density is also visible on the axial electron flux gradient profile divided by the cyclotron pulsation at z = 1.9 cm. It is of the order of $1.3 \times 10^{16} m^{-3}$ distributed over two axial cells for a cyclotron pulsation of $5.77 \times 10^{8} rad.s^{-1}$, which is equivalent to the previous estimate of the cathode emission rate. The one linked to ionization is of lower amplitude and

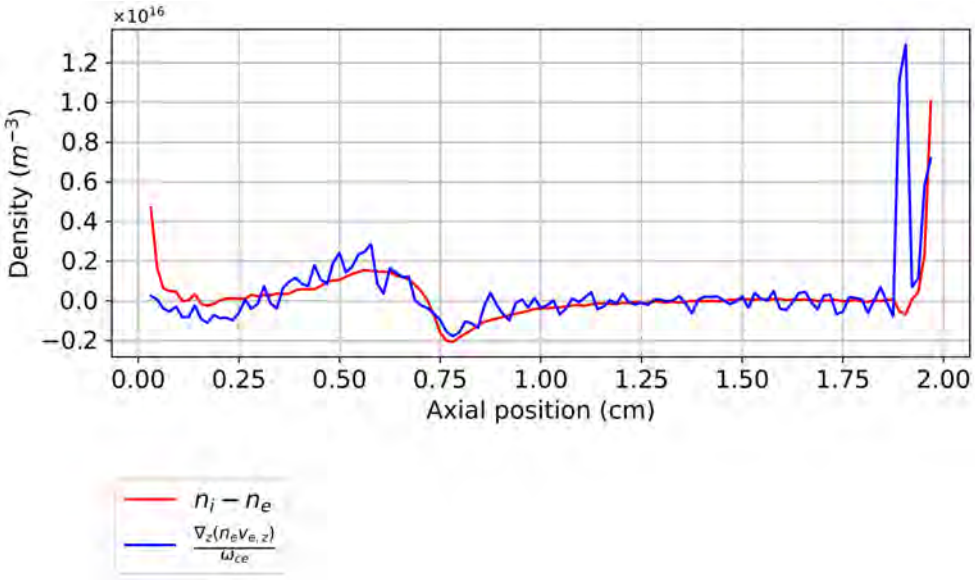

FIGURE 3.47: Axial density $n_i - n_e$ compared to axial gradient of electron flux over cyclotron pulsation.

has little effect on the profile. Its contribution in density equivalence is shown in figure 3.48.

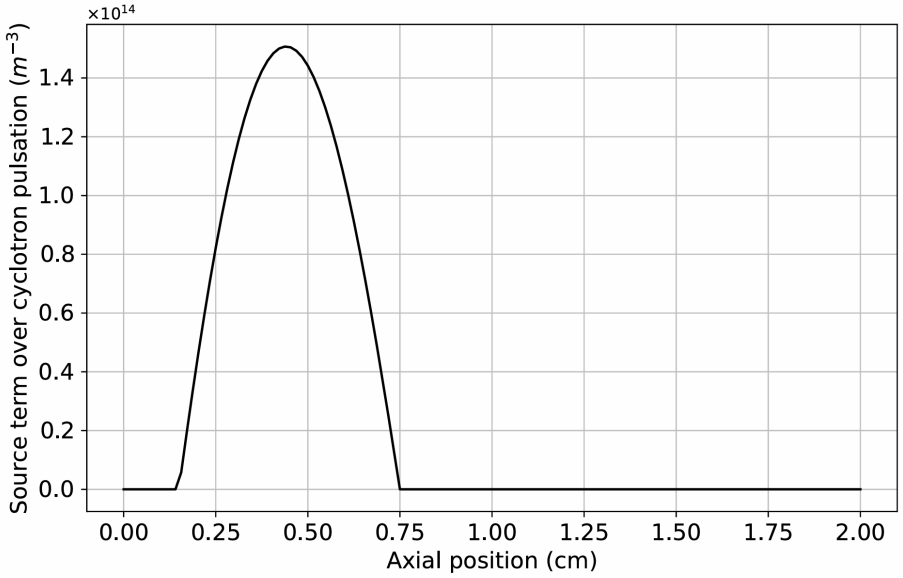

FIGURE 3.48: Contribution of ionization source term over cyclotron pulsation in stationary regime, it can be neglected when compared to the profiles of density and of axial gradient of electron flux over cyclotron pulsation.

The contribution of the ionization source term to axial electron transport is therefore an order of magnitude lower, and is negligible in the equation of the first fluid

moment compared to the other terms. Excluding the cathode emission plane, we note that we have, on average over time and integrating in the radial (Ox) and azimuthal (Oy) directions:

$$< \frac{\partial(n_e v_{e,z})}{\partial z} >_{x,y,t} \approx \omega_{ce} < (n_i - n_e) >_{x,y,t} \tag{3.14}$$

This trend can be observed both in the benchmark conditions presented at the beginning of the chapter and in the benchmark conditions in Charoy et al., 2019. Changing numerical simulation parameters such as the number of particles per cell or the grid level gives the same results. Assuming this approximation to be true, this means that the expression (3.13) gives a relation between the term of kinetic origin of the first fluid moment and the main dipole:

$$< \iiint_{-\infty}^{+\infty} \frac{-e}{m_e}(E_y + v_z B_x)\frac{\partial f_e}{\partial v_y} d^3\vec{v} >_{x,y,t} \approx \omega_{ce} < (n_i - n_e) >_{x,y,t} \tag{3.15}$$

While this observation brings us closer to a relation between the magnetic configuration of the Hall thruster and the axial transport of electrons, it is not sufficient to link the characteristics of electron transport to the engineering parameters. The relation between the density or potential profile (converted by Poisson's equation) with the magnetic field and the voltage imposed between the electrodes is unknown.

3.8 Electron drift with regard to cyclotron motion

This section is the result of attempts to describe the wave-particle resonance mechanism by studying electron drift with regard to cyclotron motion. Although it provides less information than particle trajectories, it supports the idea that this mechanism does indeed occur. Cyclotron resonance occurs when the electric field is in the same direction as the particle velocity during cyclotron rotation as shown in figure 3.49, or when this is true on average over a cyclotron period.

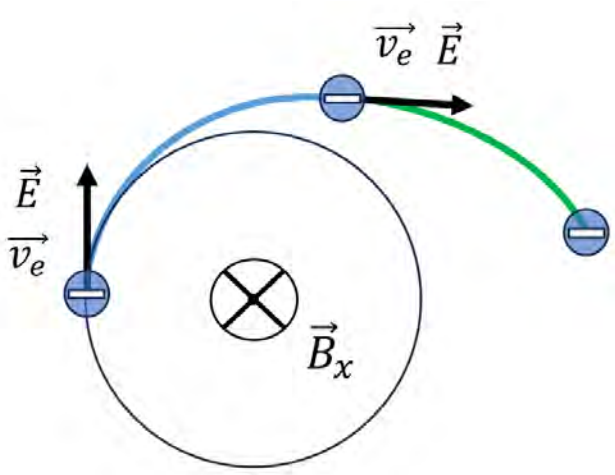

FIGURE 3.49: Schematics of cyclotron resonance process and associated drift from cyclotron trajectories.

Electron trajectories taken as examples (figures 3.40 and 3.41 in section 3.6) have shown jumps in axial displacements, and losses or gains of energy perpendicular to the magnetic field $E_\perp$ when passing through a vortex structure in the $(z, v_{azimuthal})$ plane. These events mark the presence of resonances of potentially different natures. If we are interested in cyclotron resonance, we can calculate the drift of electrons with regard to cyclotron trajectories.

Recall that the magnetic field considered is strictly radial, i.e. in the (Ox) direction, and that its axial amplitude profile is given in figure 3.6. Note $R_{Le,p}$ the electron Larmor radius, $\omega_{ce,p}$ the electron cyclotron pulsation at the position of an electron at time t_0. An electron with azimuthal velocity v_{y0} and axial velocity v_{z0} at this instant t_0 therefore has an equivalent Larmor radius:

$$R_{Le,p} = \frac{\sqrt{v_{y0}^2 + v_{z0}^2}}{\omega_{ce,p}} \tag{3.16}$$

Note (y_0, z_0) the position of the electron at time t_0 in the axial-azimuthal plane (Oyz). Note ψ_0 the phase at time t_0 assuming a cyclotron trajectory:

$$\psi_0 = arcsin\left(\frac{v_{z0}}{\sqrt{v_{y0}^2 + v_{z0}^2}}\right) \tag{3.17}$$

The position of the electron $(y_{th,ce}, z_{th,ce})$ at the next instant $t_0 + \Delta t$ if following a cyclotron trajectory is given in the axial-azimuthal plane (Oyz) by:

$$\left\{ \begin{array}{l} y_{th,ce} = y_0 + R_{Le,p}sin(\omega_{ce,p}\Delta t + \psi_0) - R_{Le,p}sin(\psi_0) \\ z_{th,ce} = z_0 - R_{Le,p}cos(\omega_{ce,p}\Delta t + \psi_0) + R_{Le,p}cos(\psi_0) \end{array} \right\} \tag{3.18}$$

To quantify the drift of electrons with regard to cyclotron motion in the axial-azimuthal plane (Oyz), we calculate for all electrons the distance δ_e at a time t_0 between the position $(y_{th,ce}, z_{th,ce})$ and the observed position (y_{obs}, z_{obs}) at the next instant $t_0 + \Delta t$, that is, for one particle:

$$\delta_{e,p} = \sqrt{(y_{obs} - y_{th,ce})^2 + (z_{obs} - z_{th,ce})^2} \tag{3.19}$$

This displacement $\delta_{e,p}$ can be normalized by the distance traveled during a time step, assuming a cyclotron trajectory, that is, by $R_{Le,p}\omega_{ce,p}\Delta t$. A summary diagram of the calculation is shown in figure 3.50.

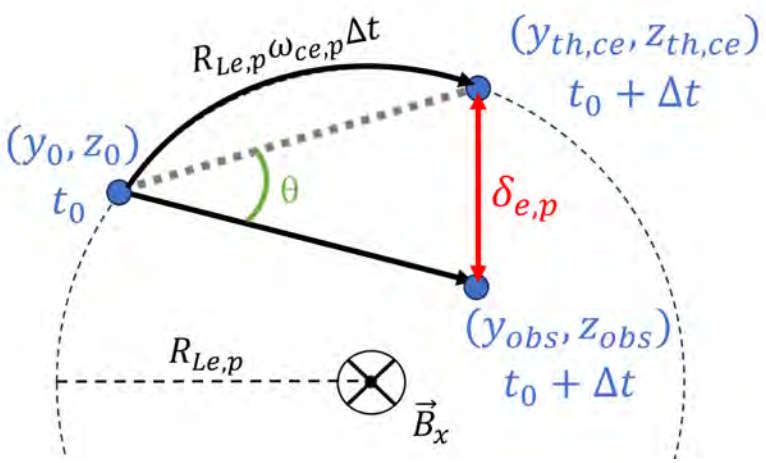

FIGURE 3.50: Computation of drift $\delta_{e,p}$ from electron cyclotron trajectory.

Recall the definition of the one-dimensional shape function for any axial position z and grid step Δz:

$$S_{\Delta z}(z) := \frac{W(\frac{z}{\Delta z})}{\Delta z} \tag{3.20}$$

where $W(z) = max(1 - |z|, 0)$ in the case of hat functions. For a population of N_e electrons of axial position z_p ($p \in [\![1; N_e]\!]$), we calculate the mean ratio $< \frac{\delta_e}{R_{Le}\omega_{ce}\Delta t} >$:

$$< \frac{\delta_e}{R_{Le}\omega_{ce}\Delta t} > (z) := \frac{\sum_{p=1}^{N_e} \frac{\delta_{e,p}}{R_{Le,p}\omega_{ce,p}\Delta t} S_{\Delta z}(z - z_p)}{\sum_{p=1}^{N_e} S_{\Delta z}(z - z_p)} \tag{3.21}$$

We obtain the axial profile averaged over all electrons present in each volume slice $2\Delta z \times L_{radial} \times L_{azimuthal}$ centered at position z. The same is applied to the population of electrons created by ionization and the population of electrons introduced at the cathodic emission plane. This profile is shown in figure 3.51.

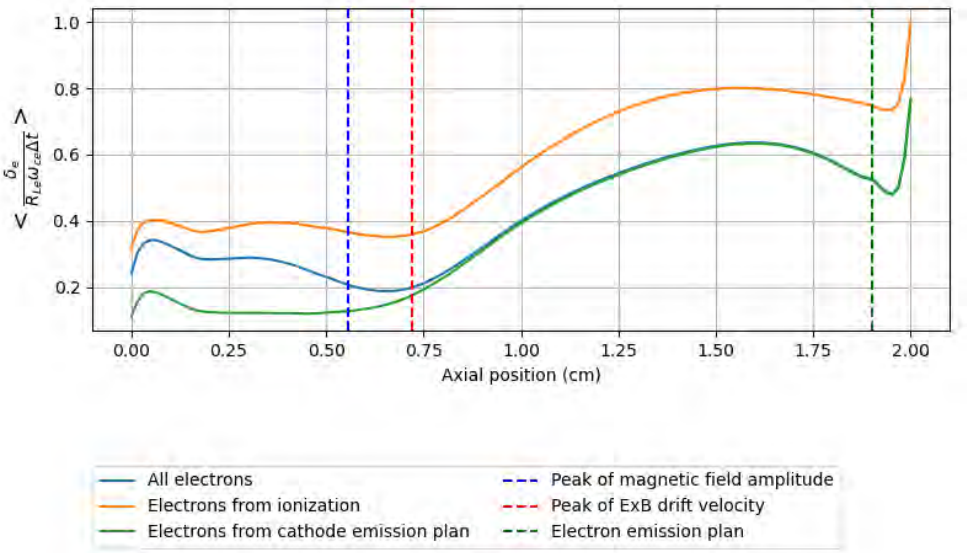

FIGURE 3.51: Drift ratio $< \frac{\delta_e}{R_{Le}\omega_{ce}\Delta t} >$ from electron cyclotron trajectory: axial profiles.

We observe that cyclotron trajectories are most perturbed in regard to electron velocity in low-amplitude magnetic field zones, and especially in the plume once the azimuthal drift velocity peak $v_d = \frac{E_z}{B_x}$ has been passed. They are least perturbed on average for all electrons in the zone between the magnetic field peak and the drift velocity peak. However, this is also a zone where electrons are more energetic. Impulse exchange could therefore be important here, as suggested by the presence of fluid motion line vortices in the $(z, v_{azimuthal})$ and $(v_{azimuthal}, v_{radial})$ planes, and by the electron trajectories highlighted in the previous sections. In the absence of collisions, the cyclotron trajectories of electrons coming from the cathode emission plane remain weakly perturbed inside the channel ($\frac{\delta_e}{R_{Le}\omega_{ce}\Delta t} \leq 0.2$ before the peak of ExB drift velocity).

Another way of representing the ratio $< \frac{\delta_e}{R_{Le}\omega_{ce}\Delta t} >$ is to take into account the angle θ between the vector $((y_0,z_0),(y_{th,ce},z_{th,ce}))$ and the vector $((y_0,z_0),(y_{obs},z_{obs}))$ as defined above (see Figure 3.50). If a form of cyclotron resonance is present, then we must observe a joint drift of electrons at the same given angle. To achieve this, we

calculate the ratio:

$$< \frac{n_e}{n_0} \frac{\delta_e}{R_{Le}\omega_{ce}\Delta t} > (\theta) := \frac{\sum_{p=1}^{N_e} \frac{\delta_{e,p}}{R_{Le,p}\omega_{ce,p}\Delta t} S_{\Delta\theta}(\theta - \theta_p)}{N_e} \tag{3.22}$$

The results obtained by integrating on the domain are shown in figure 3.52.

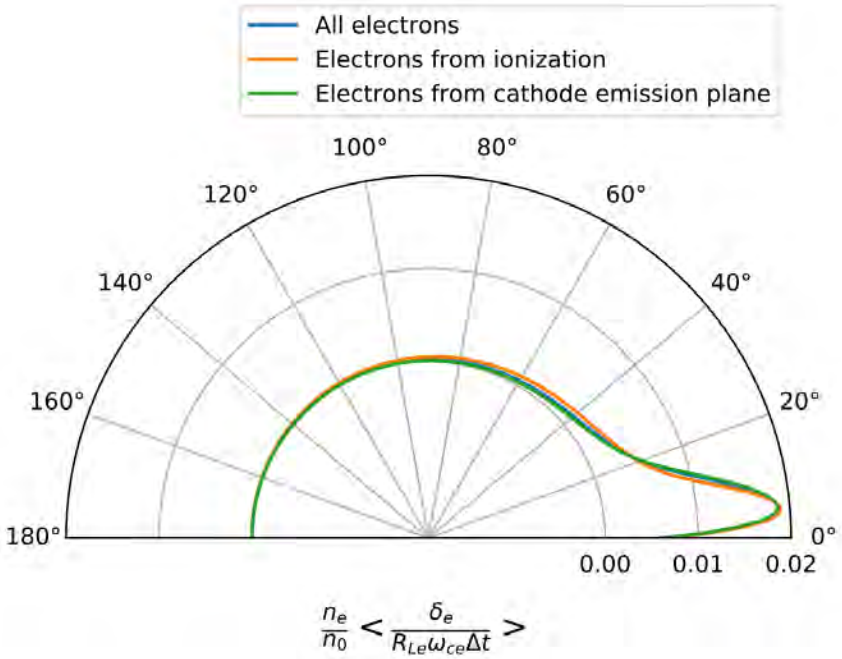

FIGURE 3.52: Drift ratio $< \frac{n_e}{n_0} \frac{\delta_e}{R_{Le}\omega_{ce}\Delta t} >$ from electron cyclotron trajectory with drift angle.

A low-angle θ peak of the order of 5 degrees is indeed observed for all electrons, consistent with a form of electron cyclotron resonance. Further work is required to determine the precise links between resonance and electron drift with respect to their cyclotron trajectory, and could be carried out in the future.

3.9 Waves present in plasma

We first describe the wave characteristics observed in the simulation results. A discussion of wave models follows. A simple approach to processing simulation data efficiently is to consider the quantities of interest integrated in two spatial directions as a function of time. Quantities are sampled every 100 ns of physical simulation time. In particular, we present the electric field and $n_i - n_e$ density profiles, which indicate the presence of a MHz wave, and the ion density profiles which indicate the presence of a wave at MHz and another at kHz in figures 3.53, 3.54, 3.55, 3.56 and 3.57. Electron density and electron velocity profiles are presented in appendix B.

Figure 3.53 shows the ion density profiles. The azimuthal profile identifies two wave frequencies, one at MHz corresponding to the average ion plasma frequency $f_{pi} = 4.8$ MHz and the other on the order of 200 kHz. To give another order of magnitude, the average transit time of ions from the ionization zone to the cathode is one microsecond and therefore cannot explain this second wave frequency. The MHz wave propagates in the azimuthal direction in the same direction as the drift velocity $v_d = \frac{E_z}{B_x}$. with a wavelength λ_{MHz} of the order of 1.4 mm, that is, an azimuthal wave vector k_y of the order of 4500 $rad.m^{-1}$. This wavelength within the framework of the method of characteristics used in Lafleur, Baalrud, and Chabert, 2016, assuming a uniform plasma, and a Maxwellian electron and ion distribution shifted by the azimuthal drift velocity, is equal to $2\pi\lambda_{De}\sqrt{2} = 1.65$ mm. The frequency of the azimuthal drift wave developed in this framework is equal to $\frac{f_{pi}}{\sqrt{3}} = 2.8$ MHz. It can be seen that these elements of theory are of the order of the characteristics of the MHz wave in the simulation, though different, which seems normal given the assumptions of the theoretical model of azimuthal drift instability. The differences raise the question of whether the perceived wavelength λ_{MHz} in the simulation is not related to other physical quantities. In particular, the vortex structure present in the $(z, v_{azimuthal})$ plane (see figure 3.38 in section 3.6) has its center close to the magnetic field maximum. The wavelength at MHz λ_{MHz} could depend on the physical parameters at this axial position. Note that at this position $T_e \approx 67$ eV (see figure 3.18 in section 3.4) and $\lambda_{MHz} \approx \frac{c_s}{f_{pi}}$ where $c_s = \sqrt{\frac{T_e[eV]e}{m_i}} \approx 7000$ m/s is the ion bohm velocity. The azimuthal wave at MHz thus has characteristics close to those of an ion acoustic wave. We also note the presence of the MHz wave on the radial profile of the ion density. It propagates in both positive and negative radial directions. On the other hand, the kHz wave propagates in the azimuthal direction, but with a spatial period equal to the length of the simulation domain. More precisely, we observe a deficit of ions propagating in the azimuthal direction from the first microsecond of physical simulation time. This ion deficit is accompanied by an electron deficit (Profile for electrons is also presented in annex B) such that the density profile $n_i - n_e$ in figure 3.54 is not significantly perturbed by this wave at kHz. The appearance of this wave at kHz coincides with the formation of the main DL, as can be seen on the density profile or in section 3.6 (see figure 3.30), and with the propagation of an axial DL as shown in section 3.5. In other words, the axial evacuation of plasma during the first two microseconds of physical simulation time led to the propagation of a

plasma deficit in the azimuthal direction, the frequency of which can be equal to the displacement velocity of this deficit over the azimuthal length of the domain. Under our conditions, the average displacement velocity of this plasma deficit is of the order of 4000 m/s. Note that this dip moves faster than ions in the azimuthal direction and slower than electrons.

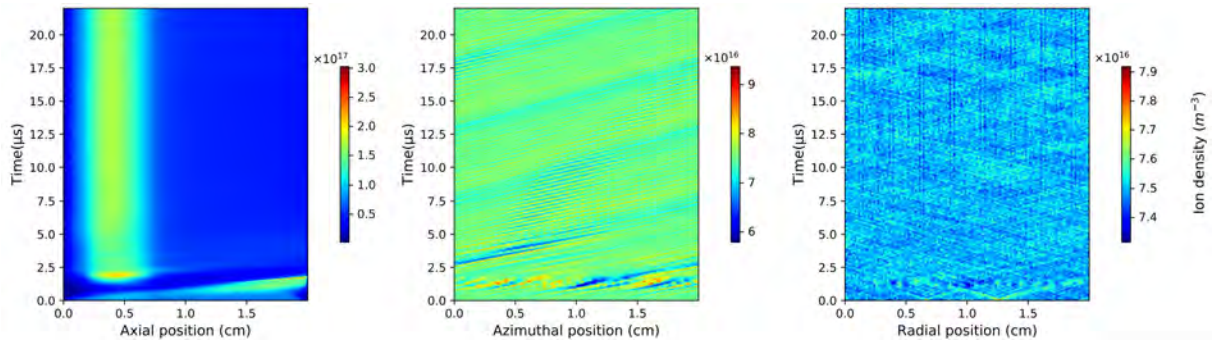

FIGURE 3.53: Spatially integrated ion density profiles in each direction.

The presence of the MHz wave can be seen on the azimuthal profile of the $n_i - n_e$ density in figure 3.54. The propagation of the azimuthal wave at MHz in the form of a wake of non-neutral plasma waves could be explained by the difference in time scale between the fast electron cyclotron perturbations and the ion plasma frequency. This notion of wake can be compared to that presented in chapter 8, dedicated to waves in Rax, 2005. The axial profile also shows the various transport zones defined above and their associated excess charge. Note that the amplitude of $n_i - n_e$ density fluctuations varies slightly with azimuthal position over time although they do not form a wave structure. This amplitude variation seems to be linked to the initial plasma evacuation, but not to the kHz propagation of the plasma deficit.

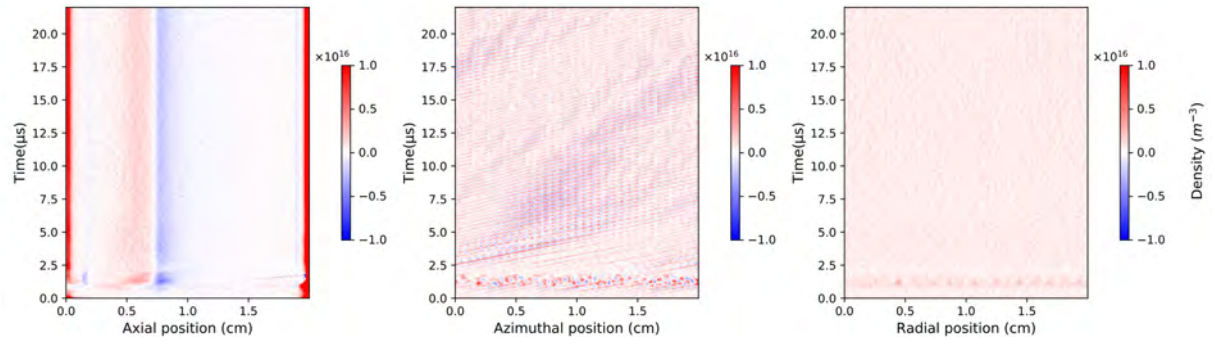

FIGURE 3.54: Spatially integrated density $n_i - n_e$ profiles in each direction.

The profiles of the axial component of the electric field shown in figure 3.55 also show the presence of a kHz wave in both the azimuthal and radial directions. In the azimuthal direction, the kHz wave propagates in the azimuthal direction with a period equal to the azimuthal length of the domain, and another kHz wave similar to that perceived in the radial direction is observed, but without propagation.

The kHz wave propagating in the azimuthal direction may be associated with the plasma deficit described above. The non-propagating wave is more difficult to determine.

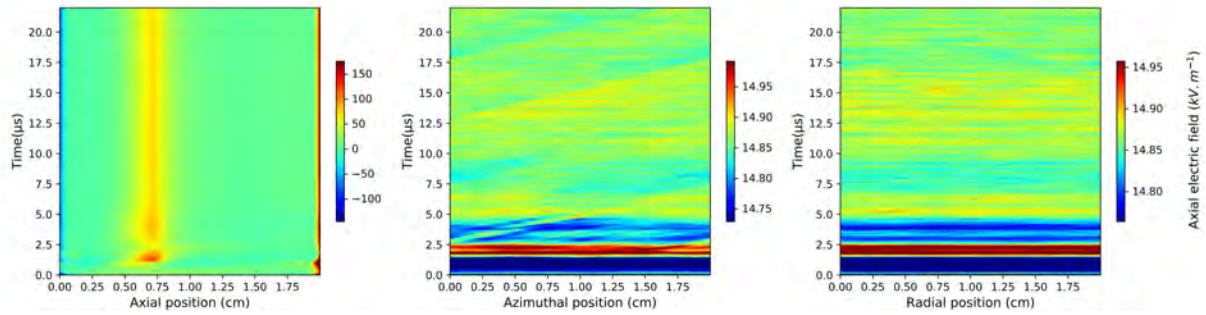

FIGURE 3.55: Spatially integrated axial electric field profiles in each direction.

The profiles of the azimuthal component of the electric field shown in figure 3.56 show the MHz wave propagating in the azimuthal direction with the same characteristics as those described in the ion density profile. The amplitude of the azimuthal electric field appears to vary with the amplitude of the $n_i - n_e$ density fluctuations in the azimuthal direction. We also note the presence of a non-zero value for the azimuthal component of the electric field in the radial direction, with a helical time structure from t = 7.5 μs onwards and a frequency of the order of 2 MHz, which is around twice lower than the average ion plasma frequency. It is difficult to explain the origin of this structure, but it may be linked to the vortices observed in the $(v_{azimuthal}, v_{radial})$ plane in the steady state (see figures 3.44 and 3.45 in section 3.7).

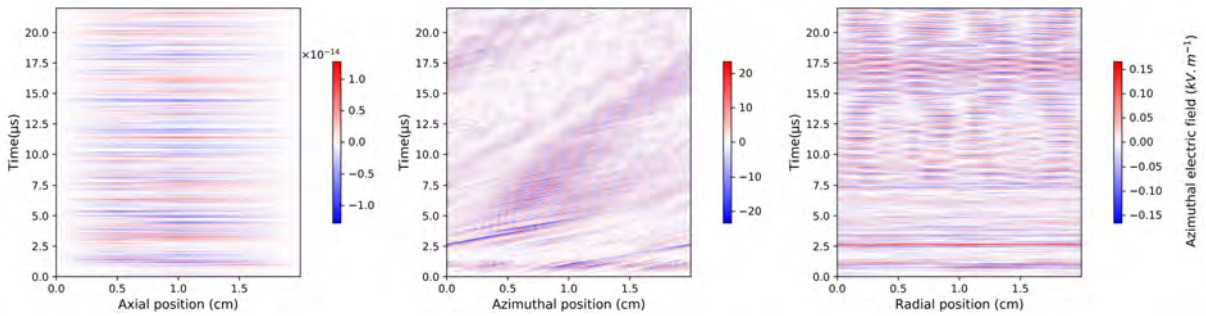

FIGURE 3.56: Spatially integrated azimuthal electric field profiles in each direction.

The profiles of the radial component of the electric field presented in figure 3.57 show above all, from t = 7.5 μs, the presence of a low-amplitude wave with a frequency of the order of 2 MHz, propagating in the azimuthal direction with an average wavelength of the order of a quarter of the azimuthal length of the domain, that is 5 mm. It could be coupled to the helical time structure of the azimuthal electric field in the radial direction.

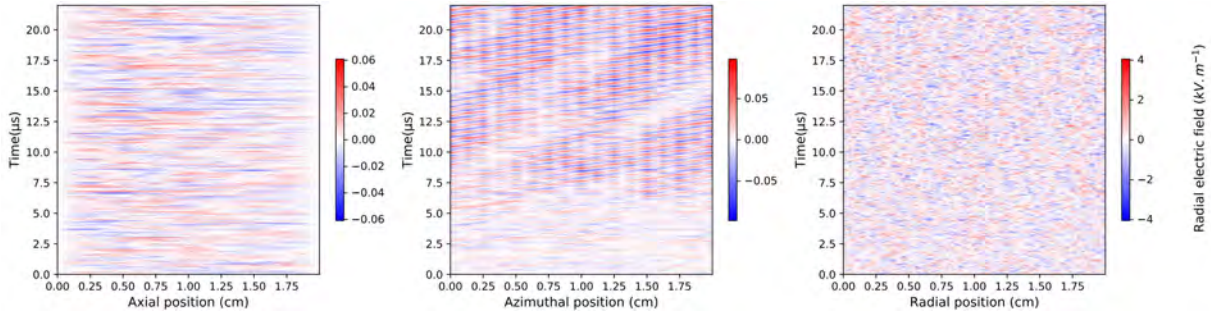

FIGURE 3.57: Spatially integrated radial electric field profiles in each direction.

A summary table of observed wavelengths and frequencies is given in table 3.5.

The observations made above and in the preceding sections can now be compared with the wave models usually used to describe instability in the Hall thruster. Alexandre Ducrocq's thesis (Ducrocq, 2006) establishes the three-dimensional dispersion relation under the following assumptions:

- collisionless plasma
- fluid model of cold, non-magnetized ions with zero mean ion velocity
- uniform magnetic field in the (Ox) direction (directions adapted to our conventions)
- uniform plasma
- constant azimuthal drift velocity v_d and static axial electric field E_z
- Maxwellian electron distribution function shifted by the drift velocity in the azimuthal velocity direction
- perturbed electric potential in all three spatial directions
- velocity perpendicular to the magnetic field and parallel velocity are invariants of motion

Under these assumptions, the general dispersion relation obtained by the method of characteristics is given by:

$$k^2\lambda_{De}^2\left(1-\frac{m_e}{m_i}\frac{\omega_{pe}^2}{\omega^2}\right)+1 + \frac{\xi^+ + \xi^-}{2}\left\{Z\left(\frac{\xi^+ + \xi^-}{2}\right)I_0(b)e^{-b} + \sum_{n=1}^{n=\infty}\left(Z\left(\xi^+\right)+Z\left(\xi^-\right)\right)I_n(b)e^{-b}\right\} = 0 \tag{3.23}$$

TABLE 3.5: Mean MHz and kHz frequencies and wavelengths observed in the ExB configuration.

	Frequency (MHz)	**Azimuthal wavelength (mm)**
Density	$f_{pi} = 4.8$	$\frac{c_s}{f_{pi}} = 1.4$
Azimuthal electric field	$f_{pi} = 4.8$	$\frac{c_s}{f_{pi}} = 1.4$
Radial electric field	$0.4 \times f_{pi} = 2$	$0.25 \times L_{azimuthal} = 5$

	Frequency (kHz)	**Azimuthal wavelength (mm)**
Density	200	$L_{azimuthal} = 20$
Axial electric field	200	(non propagating)
Axial electric field	200	$L_{azimuthal} = 20$
Azimuthal electric field	200	$L_{azimuthal} = 20$

	Frequency (MHz)	**Radial wavelength (mm)**
Azimuthal electric field	$0.4 \times f_{pi} = 2$	$0.5 \times L_{radial} = 10$

where we introduce the parameters $b = \frac{k_\perp^2 V_{th}^2}{\omega_{ce}^2}$ and

$$\xi^+ = \frac{\omega - k_y v_d + n\omega_{ce}}{k_x V_{th}\sqrt{2}} \tag{3.24}$$

$$\xi^- = \frac{\omega - k_y v_d - n\omega_{ce}}{k_x V_{th}\sqrt{2}} \tag{3.25}$$

The Z function is that of Fried and Conte, 1961 and the I_n functions are the modified Bessel functions.

$$Z(\xi) = \frac{1}{\sqrt{\pi}} \int_{-\infty}^{+\infty} \frac{e^{-\alpha^2}}{\alpha - \xi} d\alpha \tag{3.26}$$

$$I_n(b) = \frac{1}{\pi} \int_0^{\pi} exp(bcos(\theta))cos(n\theta)d\theta \tag{3.27}$$

This dispersion relation as it stands requires further assumptions to provide results. In the case of a purely azimuthal perturbation, Ducrocq, 2006 shows that the mode that has the highest probability of developing and maintaining itself is obtained for $\frac{k_y v_d}{\omega_{pe}} = 1.2$. It should be noted that the quasi-linear wave model does not take directly into account the wave saturation. It assumes that the mode developing faster has a higher chance to be dominant once the saturation is reached. This relation is important in that it shows that the dominant mode depends on the electron plasma frequency while resonances occur at multiples of the electron cyclotron harmonics for $k_y v_d = n\omega_{ce}$ ($n \in \mathbb{N}$). However, the observations in the previous sections

invalidate certain assumptions of the model presented above. In particular, the electron distribution function is not Maxwellian, and the velocities perpendicular and parallel to the magnetic field are not invariants of motion. Despite these differences, it is possible to take the results of this theoretical model as an order of magnitude to compare with the characteristics of the vortex structure observed in the $(z, v_{azimuthal})$ plane (see figure 3.38 in section 3.6). The center of this vortex could thus present the conditions for the azimuthal instability. We illustrate the non-Maxwellian nature of the electron distribution function (at least if considered for all electrons, though if we consider only the electrons from ionization, it is close to a perturbed Maxwellian distribution centered in the zero azimuthal velocity) by presenting its cut at the axial position associated with this vortex in figure 3.58.

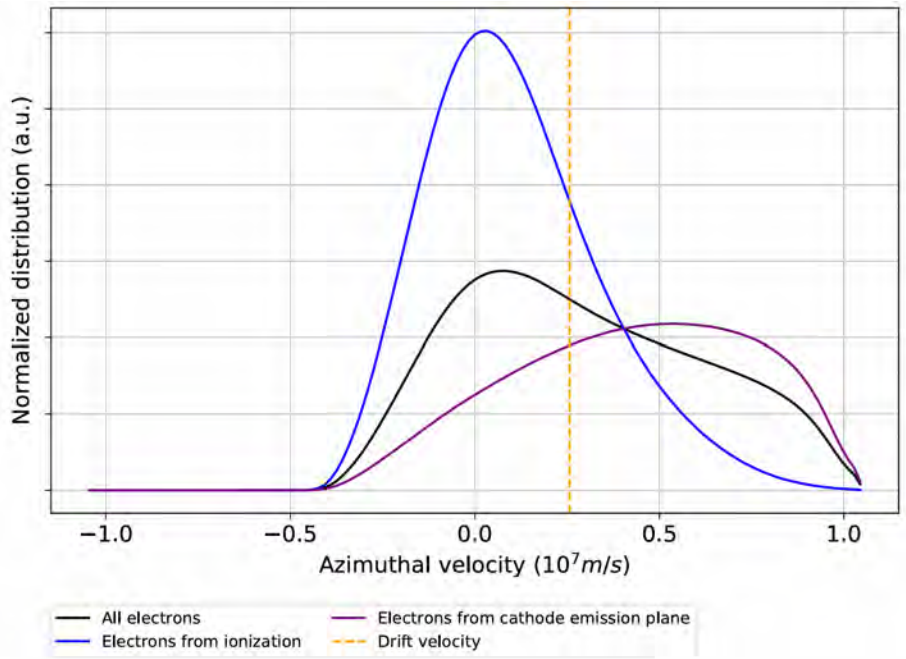

FIGURE 3.58: Azimuthal velocity distribution function at the axial position of the vortex structure for all electrons (black) and for each electron population (blue for electrons from ionization and purple for electrons from cathode emission): drift velocity value is represented in dashed orange line.

On the other hand, we present the vortex structure in the $(z, v_{azimuthal})$ plane, on which we have superimposed the v_d azimuthal drift velocity curve, the $\frac{\omega_{pe}}{k_y}$ velocity value averaged over the entire domain, the $\frac{\omega_{pe,cathode}}{k_y}$ velocity value where $\omega_{pe,cathode}$ is the electron plasma frequency considering only the population of electrons coming from the cathode emission plane, and the curve of velocity $\frac{n\omega_{ce}}{k_y}$ for n=7 in figure 3.59.

We observe that the center of the vortex structure is the crossover point such that $v_y = v_d = \frac{\omega_{pe,cathode}}{k_y} = \frac{7\omega_{ce}}{k_y}$. Contrary to the above model, if the center of the vortex corresponds to the constraints of the dominant azimuthal mode, it is not the

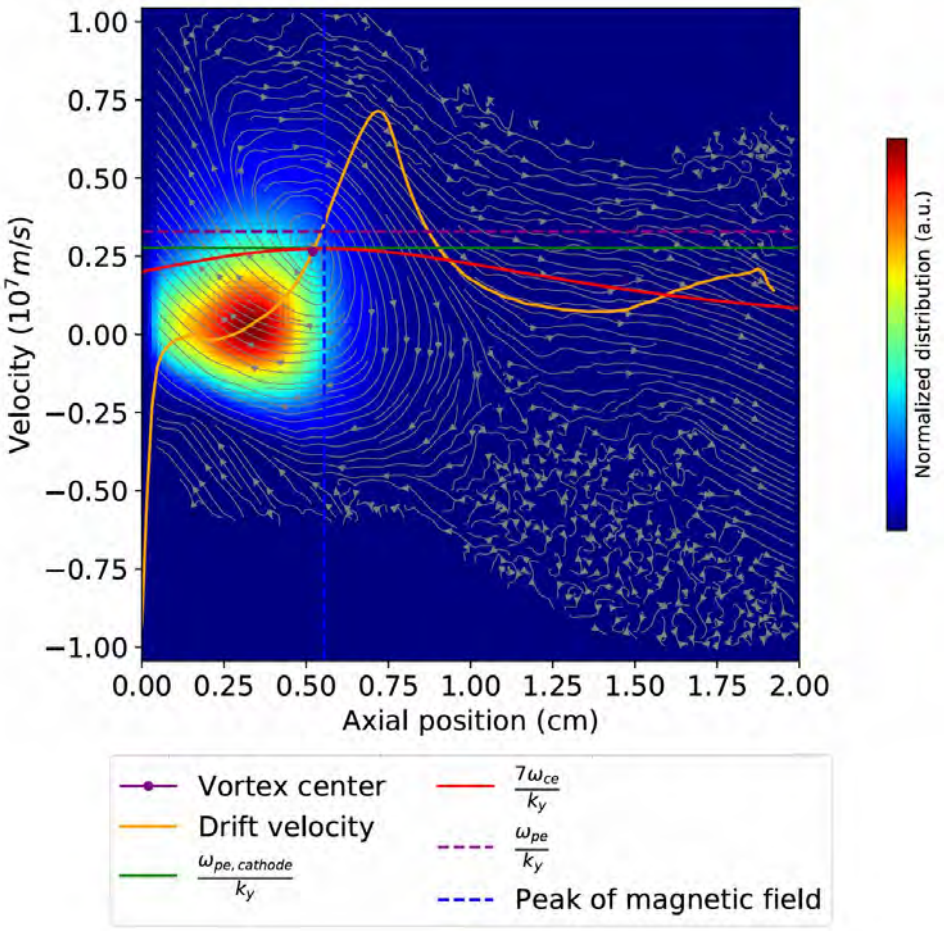

FIGURE 3.59: Axial profile of azimuthal velocity distribution $f(z, v_{azimuthal})$ in converged state: electrons from ionization (normalized distribution), the center of the vortex structure may be linked to the dominant azimuthal mode.

total electron plasma frequency that is at stake, but that of the electron population coming from the cathode emission plane. One possible interpretation is that the energy required to develop the azimuthal mode comes from the electrons ejected at the cathode. The saturation of the azimuthal mode would therefore be linked to the properties of these electrons. These electrons cross the zone of strong axial electric field, gain kinetic energy perpendicular to the magnetic field then transfer it to the electrons produced by ionization via the azimuthal wave mechanism as observed on particle trajectories derived from simulation in (z,v) space (see figures 3.40 and 3.41). This interpretation remains open to question, and further investigations are needed to confirm it.

3.10 Conclusions

The study of the ExB cross-field configuration in three dimensions, doubly periodic in the radial and azimuthal directions allowed us to compare the results of the Sparse-PIC-Φ method with the classical PIC and to validate the implemented code. A good match of the time-averaged axial profiles was found between the two methods, with deviations of the order of a few percent. Noise levels remained acceptable (below or around $10^{15} m^{-3}$ for electron density) for the Sparse-PIC method, despite the low number of particles.

A set of numerical diagnostics was then presented to provide a new perspective on the thruster's physics. Firstly, a separation of electrons according to their physical origin, produced by ionization or ejected at the cathode, has enabled us to distinguish two electron populations with singular properties in terms of axial density profile, temperature and pressure gradient. Several extrema and inflection points were shown to be linked to the peaks of magnetic field, azimutal drift velocity and electron density. It therefore seems that a three-fluid model (two electronic and one ionic) could be envisaged to theorize particle transport in greater detail.

On the other hand, diagnostics have been implemented to study waves through the temporal evolution of the average density and electric field quantities in the various spatial directions. The evolution of the electron and ion distribution functions in the transient and stationary regime, as well as the computation of fluid lines of motion in the various phase space planes were also added to give a better understanding of the plasma dynamics. The transient regime has shown the initial evacuation of the plasma associated with the formation of an axial "double layer" (DL) structure, an axial dipole enabling the static axial electric field to be established. A wave propagating at kHz in the azimuthal direction with a wavelength equal to the azimuthal dimension of the simulation domain is created following the initial plasma evacuation. It corresponds to the propagation of a plasma density dip, and could be similar to the "potential relaxation oscillations" observed in plasmas with a potential bias without a magnetic field (See references in section 3.5).

Another MHz wave, mainly affecting the azimuthal component of the electric field and density, has characteristics close to those of an ion acoustic wave in steady state, appears with the formation of the main DL and propagates with an average azimuthal wave vector of the order of 4500 $rad.m^{-1}$, equivalent to a wavelength λ_{MHz} of 1.4 mm. This azimuthal wave could be associated with the vortex structure of the streamlines observed in the $(z, v_{azimuthal})$ plane for electrons produced by ionization. This structure suggests that one azimuthal mode dominates and that its properties are connected to the azimuthal drift velocity, the electron cyclotron harmonics, and the density of electrons coming from the cathode in a similar condition than the one developed to determine the dominant mode in Ducrocq, 2006. This condition as well as the study of electron drift with regard to their cyclotron trajectory suggest that the electron cyclotron resonance mechanism is indeed at the origin of the main

azimuthal instability and the passage of electrons through the magnetic barrier. Resonances of a different nature at the ion plasma frequency, however, should explain the mobility of electrons out of the magnetic barrier.

The comparison between the quasi-linear wave theory and the simulation results is limited by the lack of saturation condition. In addition, the assumption of a Maxwellian electron distribution function and the assumption that velocities perpendicular and parallel to the magnetic field are invariants of motion in the wave models, are not verified in the simulation results. On the contrary, measured distribution functions and example trajectories from the simulation show that the azimuthal instability mechanism results in the exchange of energy perpendicular to the magnetic field $E_\perp = \frac{m_e v_\perp^2}{2} - e\Phi$ with or without conservation of total energy $E_{total} = \frac{m_e v_e^2}{2} - e\Phi$ between electrons produced by ionization and those ejected at the cathode. Saturation of the azimuthal dominant mode could therefore be linked to the properties of the energetic electron population coming from the cathode.

Minor perturbations of negligible amplitude compared with the azimuthal instability at ion plasma frequency have also been observed in the radial direction. Vortex structures observed in the $(v_{azimuthal}, v_{radial})$ plane in the main axial dipole zone could be linked to these perturbations.

The electron distribution functions in the steady state have shown an asymmetry in the direction of azimuthal velocities (Ov_y), resulting in a non-zero kinetic term in the first fluid moment equation (1.2). This kinetic term (3.13) shows that dynamics in the azimuthal direction play a major role in the axial electron transport. It also appears to be linked to the presence of a dipole axially centered on the position of the azimuthal drift velocity peak $v_d = \frac{E_z}{B_x}$, so that on average over time it is equal to the product of the cyclotron pulsation to the difference of density $n_i - n_e$, the sign depending on the axis conventions. Unfortunately, this relation does not allow us to conclude on a practical formulation of the electron transport in the Hall thruster. For this, we would need to know the relationship between the charge density or electric potential profile and the magnetic field configuration and voltage imposed on the electrodes, which could be the subject of future studies.

Several avenues of development for studying electronic transport in a Hall thruster have been proposed. They are based on results from the Sparse-PIC simulation. Their processing has revealed the complexity of the mechanisms involved. The kinetic aspect of the azimuthal instability is beyond doubt. Nonetheless, it should be possible to establish a fluid model, and certainly a three-fluid model, taking into account both electron populations and ions, and freeing ourselves from the assumption of a Maxwellian velocity distribution function. However, this requires sufficient analytical approximation of these distribution functions, and perhaps a better understanding of the exchange mechanisms taking place between the two electron populations.

Chapter 4

Influence of electronic secondary emission on the thruster

4.1 Electronic secondary emission models

Electronic secondary emission is the production of electrons by the impact of ions, protons or electrons on a material. Electron emission by ion impact can be explained by the tunnel effect as developed in Lieberman and Lichtenberg, 1994 (page 300), Amiaud, 2018 among others. It is considered negligible in the case of xenon, with a probability of emitting an electron of the order of 0.02 per ionic impact (Croes, 2017, page 99). The other type of electronic secondary emission is that linked to electron impacts on the material. The physical principle is still poorly described, but it seems to be linked to the untrapping of electrons previously trapped in the case of dielectrics. Previous works in Croes, 2017; Villemant, 2018; Tavant, 2019 have brought to light a multitude of experimental and analytical models to represent electronic secondary emission (Linear, Vaughan, Furman/Pivi, ...). Some of these have been developed within ONERA's OSMOSEE code (Inguimbert et al., 2017; Villemant et al., 2017). They consider several scenarii for incident electrons. They can either be reflected back into the domain with a lower energy and/or a different angle, or produce true secondary electrons with a kinetic energy of a few eV. In our study, we want to understand what happens to the secondary electron population once it has been emitted. We have chosen the simplest model: the linear model. This introduces the probability σ_e of emitting a secondary electron as a function of the incident energy ϵ of the electron, such that:

$$\sigma_e(\epsilon) = min(\sigma_0 + \frac{\epsilon}{\epsilon^\star}(1 - \sigma_0), \sigma_{max})$$

where $\epsilon^\star$ is a crossover energy parameter, σ_0 is the probability of attachment and σ_{max} the maximum probability of electronic secondary emission. The Croes et al., 2017 article gives parameter values for BN boron nitride, which are reproduced in table 4.1. Note that the probability introduced above may exceed unity. This means that several secondary electrons can be emitted for the same electron impact on the walls.

It is important to note that this probability here depends only on the particle's incident kinetic energy. It might be more accurate to consider the statistical weight of the particle in particle simulations and establish a collision cross-section so that the

TABLE 4.1: Linear model electron secondary emission parameters for the BN ceramic (from Croes et al., 2017).

Parameter	Value
$\epsilon^\star$ **(eV)**	35.04
σ_0	0.578
σ_{max}	2.9
Re-emission temperature (eV)	2

secondary emission process is also density-dependent. These developments require further investigation, which will not be carried out here.

4.2 Studied configuration

The case presented in chapter 3 considered doubly periodic conditions in the radial and azimuthal directions. In order to study the role of secondary electronic emission in a configuration close to the Hall thruster, we impose Dirichlet conditions in the radial direction. For the rest, the same conditions apply. A notable change is the use of absorbent walls in the radial direction in the sense that any particles captured by the walls disappear from the simulation domain. If the particle is an ion, it is re-injected with an electron into the ionization zone. This implies the creation of sheaths around the walls in the radial direction. Dielectrics are therefore not directly modeled, although they can significantly modify these radial sheaths. Electronic secondary emission is taken into account in the part of the simulation domain between the anode plane and the plane at the axial position of the magnetic field maximum. In this zone, any electron passing through a wall in the radial direction is assigned a probability of emitting one or more secondary electrons before disappearing from the simulation domain. This probability is calculated by the linear secondary electron emission model presented above. Secondary electrons are injected into the domain with a semi-Maxwellian velocity distribution in the incoming direction at a temperature of 2 eV. Their azimuthal and axial coordinates are the same as those of the incident electron. Their radial coordinate is shifted by two millionths of a centimeter so as not to be considered outside the simulation domain. The simulation boundary conditions are summarized in figure 4.1.

The area where electronic secondary emission is likely to occur is also shown in figure 4.2 on the axial profile of the radial magnetic field amplitude used.

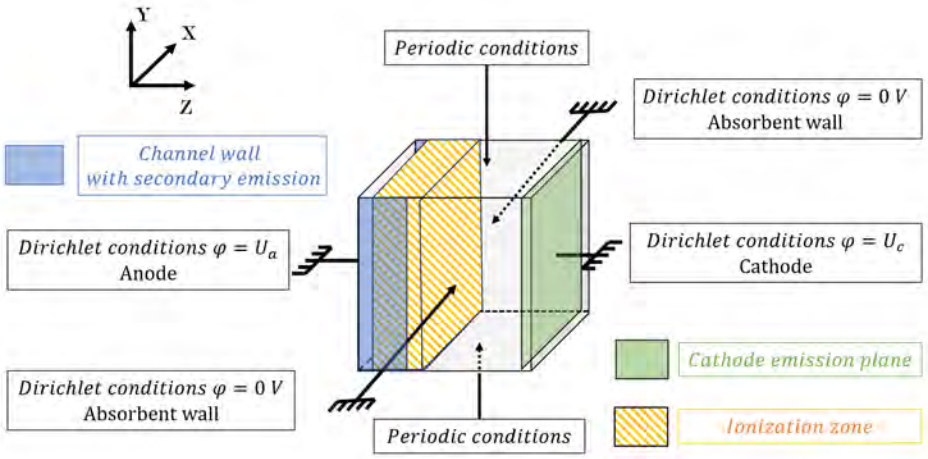

FIGURE 4.1: Schematics of three-dimensional simulation domain with boundary conditions.

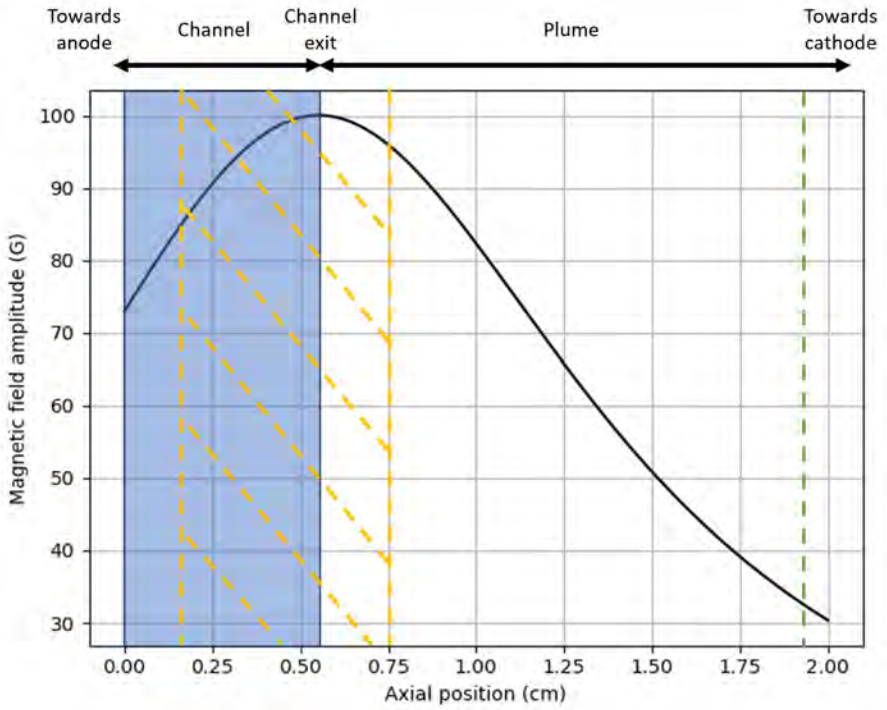

FIGURE 4.2: Axial profile of magnetic field amplitude: electron secondary emission can happen at the channel walls in blue zone, orange dashed zone is the ionization zone, green dashed line is the axial position of the cathode emission plane.

4.3 Time-averaged steady-state profiles

4.3.1 Comparison of doubly periodic profiles versus parietal with and without secondary emission

We first compare the axial profiles obtained in the previous chapter for the doubly periodic case with the results for the cases including radial walls without and with electronic secondary emission inside the channel for the same number of particles per sparse cell $n_{ppc,sparse} = 100$. This comparison enables us to assess the impact of the absorbent walls. Comparing the two cases with radial absorbent walls without and with electronic secondary emission allows us to study the effect of electronic secondary emission.

The axial electron flux profiles are shown in figure 4.3. A reduction in electron flux towards the anode is observed for both cases with radial absorbent walls, compared with the doubly periodic case. Between the doubly periodic case and the two cases with radial absorbent walls, the fluxes are equivalent in the positively charged zone of the dipole near the maximum drift velocity $v_d = \frac{E_z}{B_x}$ and differ mainly in the plume and in the channel zone. Note that the simulation conditions of the simplified model imply the presence of absorbent walls fixed at zero potential, even in the plume (see figure 4.1). The presence of these walls in the radial direction may explain the observed loss of electron flux. We note that the transport zones presented in figure 3.43 in the previous chapter are still relevant in cases with radial walls.

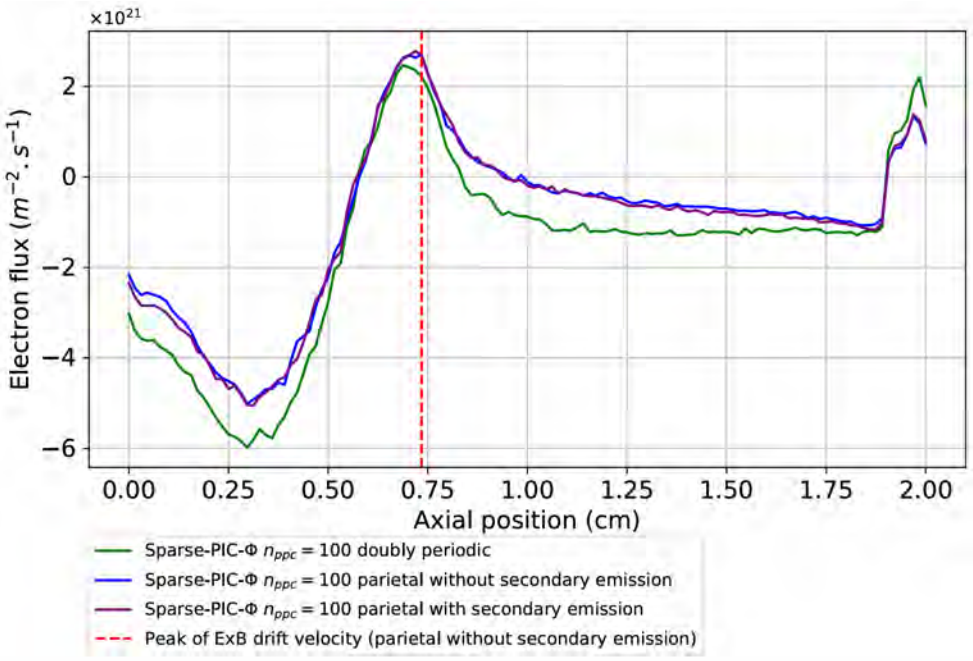

FIGURE 4.3: Axial profiles of electron flux doubly periodic versus parietal with and without secondary emission: results from Sparse-PIC-Φ for $n_{ppc} = 100$.

Electronic secondary emission does not seem to play an important role in axial electronic transport under our simulation conditions, although there is a slight increase in flux towards the anode (negative flux) near the anode zone compared to the case with radial walls and no secondary emission. The proportion of the electron current measured at the anode that is due to secondary electron emission is of the order of 6% at steady state, and is therefore negligible compared with the population of electrons produced by ionization (62%) and that coming from the cathode emission plane (32%). The negligible nature of secondary emission is in line with the results of the two-dimensional radial-azimuthal case (Croes et al., 2017). The ratio γ_{SEE} between the number of secondary electrons emitted and the number of electrons impacting the channel walls has been calculated for the two main electron populations. Its evolution over time for five microseconds of physical time in steady state is shown in figure 4.4. Sampling is similar to that of currents in chapter 3. We also compute a sliding average over 21 values, equivalent to a time average over 25 ns.

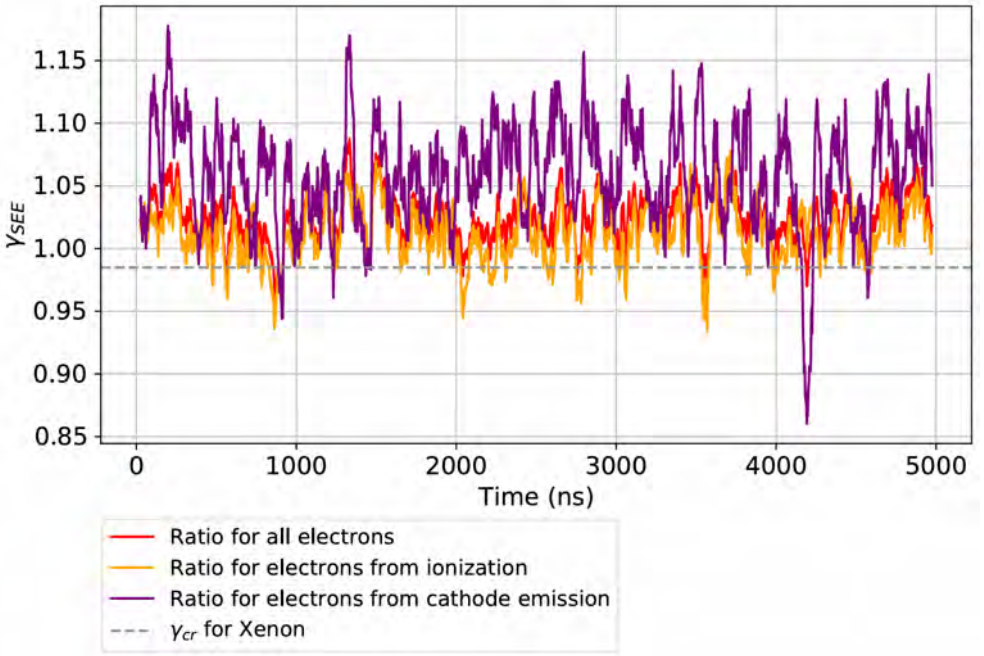

FIGURE 4.4: Evolution of electron secondary emission yield γ_{SEE} with time in stationary regime for all electrons, electrons from ionization and electrons from cathode emission plane. The critical value for xenon is also represented in grey, above which a space charge limited regime with sheath inversion can happen (Croes, 2017).

While the ratio γ_{SEE} is slightly higher for electrons from the cathode emission plane than for electrons produced by ionization, secondary electron production by impact of electrons from the cathode emission plane accounts for only 24% of secondary electron production, compared with 76% by impact of electrons produced by

TABLE 4.2: Ratio of secondary electrons emitted over impacting electrons γ_{SEE}.

Electron population	Mean value	Standard deviation
All electrons	1.02	0.02
Electrons from ionization	1.01	0.02
Electrons from cathode emission plane	1.06	0.03

ionization. A table summarizing the secondary emission yield values γ_{SEE} is available in table 4.2. Vivien Croes' thesis (Croes, 2017) shows that a space charge saturation regime exists when the ratio γ_{SEE} exceeds the critical value $\gamma_{cr} = 1 - \sqrt{\frac{2\pi m_e}{m_i}} \approx 0.985$ for xenon. This is the case here. The relatively stable value of the γ_{SEE} ratio around one could thus be explained by the appearance of sheath inversion linked to space charge saturation, as described in Croes, 2017. We note that dielectric modeling could lead to an increase in the observed emission by removing radial sheaths but keeping a γ_{SEE} ratio of the same order of magnitude. In other words, the production rate would be approximately the same, but the number of impacts would increase. Chapter 6 of Vivien Croes' thesis (Croes, 2017) indeed shows that adding dielectrics to the simulation maintains a γ_{SEE} ratio of the same order as without dielectrics. Only oscillations in this ratio are noisier, and sheath inversions linked to space charge saturation more pronounced.

Secondary electron production can also be compared with electron production by ionization and at the cathode emission plane. The number of secondary electrons produced per time step accounts for 0.6% of the number of electrons injected by ionization per time step. Similarly, it accounts for 0.4% of the number of electrons injected at the cathode emission plane per time step. The secondary electron population therefore remains negligible compared to the other two electron populations. The negligible role of secondary electron emission is confirmed by the axial profiles of ion density, ion and electron temperature and electric potential respectively in figures 4.5, 4.6, 4.7 and 4.8.

Secondary electronic emission does not lead to significant differences in ion density, potential and temperature profiles. However, it does lead to an increase in electronic temperature of the order of 10 eV in the anode zone. The main differences with the results of the previous chapter are due to the change of conditions in the radial direction with the introduction of radial absorbent walls. Compared with the doubly periodic case, the cases with radial walls show a decrease in ion density in the plume to the benefit of the channel, an increase in ion temperature of 1 to 2 eV with the appearance of a small temperature peak close to the anode sheath entrance, a drop in electron temperature up to 10 eV at its maximum, and a shift in the electric potential drop towards the cathode.

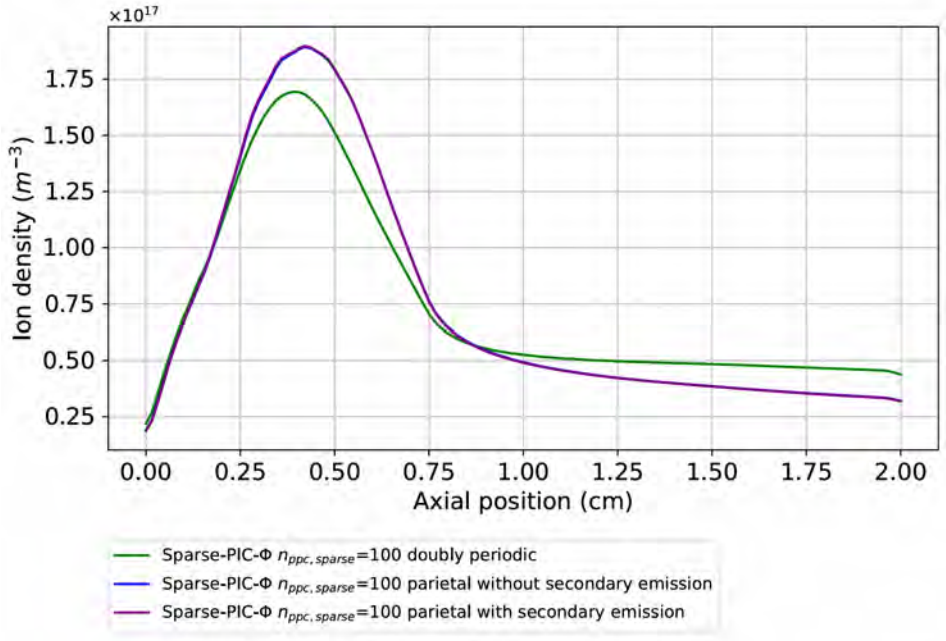

FIGURE 4.5: Axial profiles of ion density doubly periodic versus parietal with and without secondary emission: results from Sparse-PIC-Φ for $n_{ppc} = 100$.

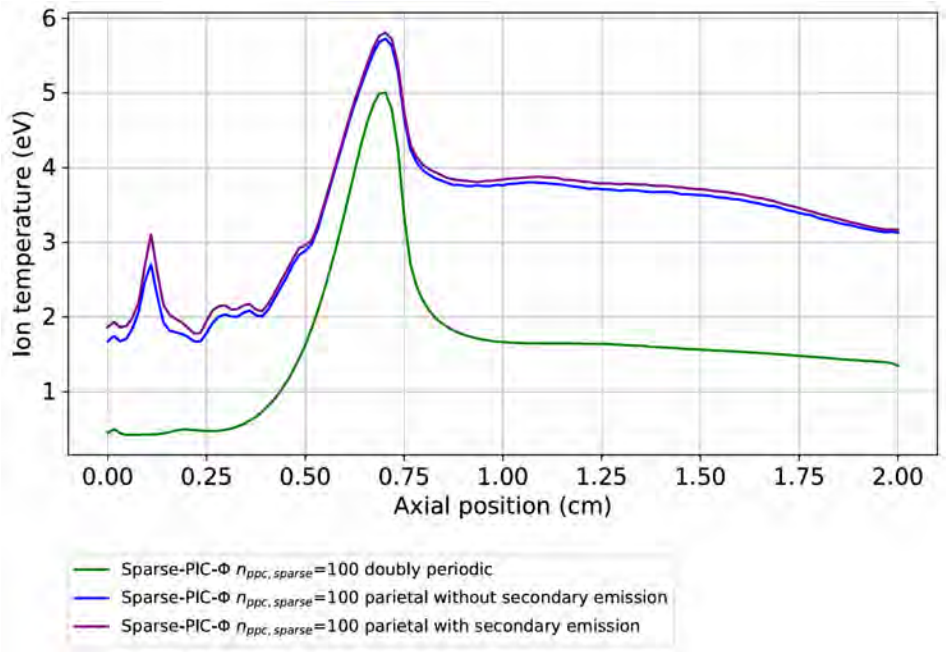

FIGURE 4.6: Axial profiles of ion temperature doubly periodic versus parietal with and without secondary emission: results from Sparse-PIC-Φ for $n_{ppc} = 100$.

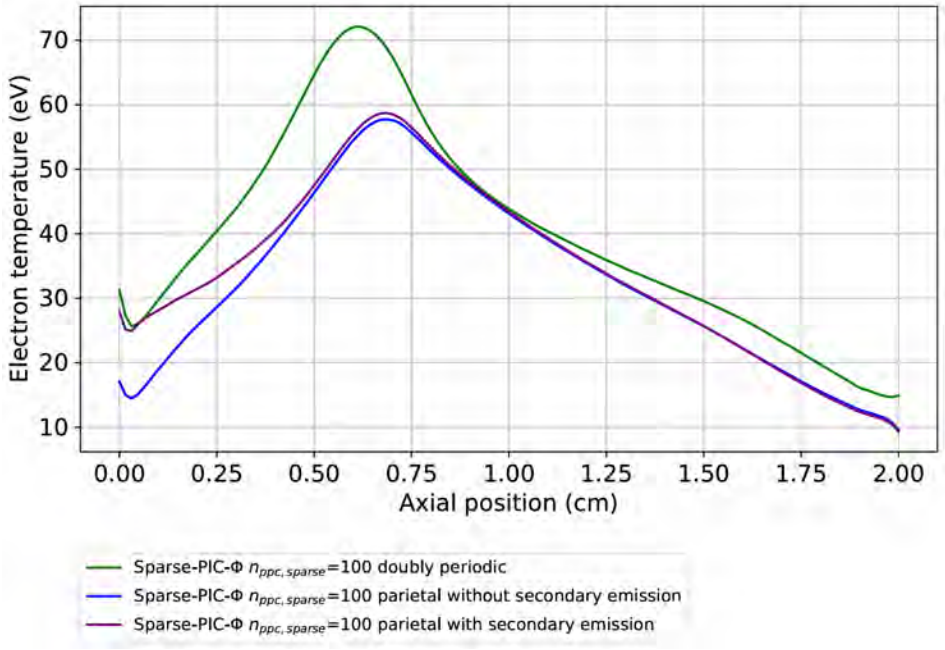

FIGURE 4.7: Axial profiles of electron temperature doubly periodic versus parietal with and without secondary emission: results from Sparse-PIC-Φ for $n_{ppc} = 100$.

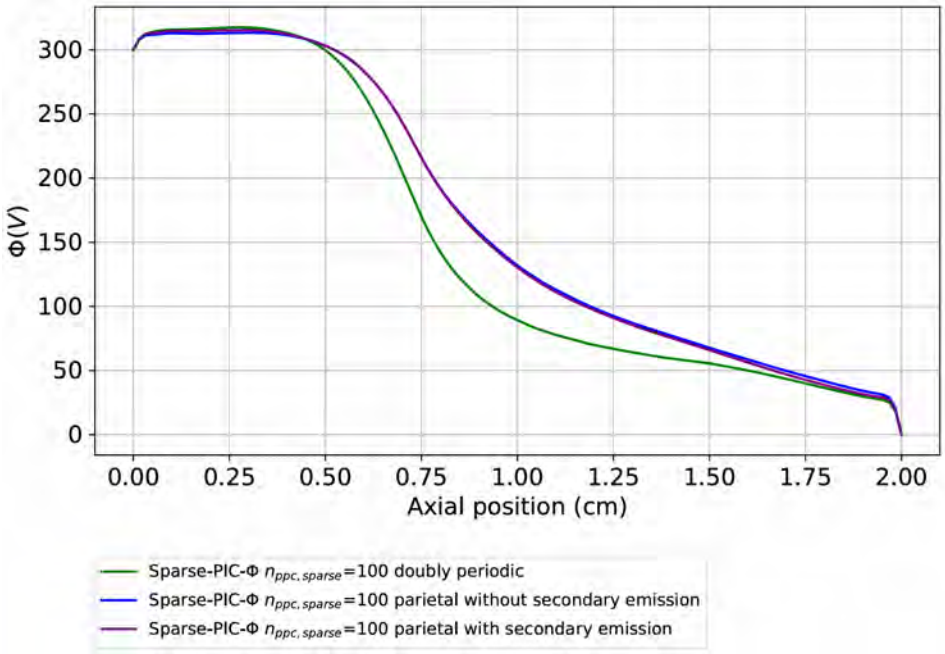

FIGURE 4.8: Axial profiles of electric potential doubly periodic versus parietal with and without secondary emission: results from Sparse-PIC-Φ for $n_{ppc} = 100$.

4.3.2 Details by electron population

We now detail the same profiles with the contributions of each electron population. Three are distinguished: those produced by ionization, those from the cathode emission plane and those from secondary electron emission. Figure 4.9 shows the electron fluxes of each population. Note that the contribution of electrons produced by secondary emission to electron flux is negligible outside the anode zone.

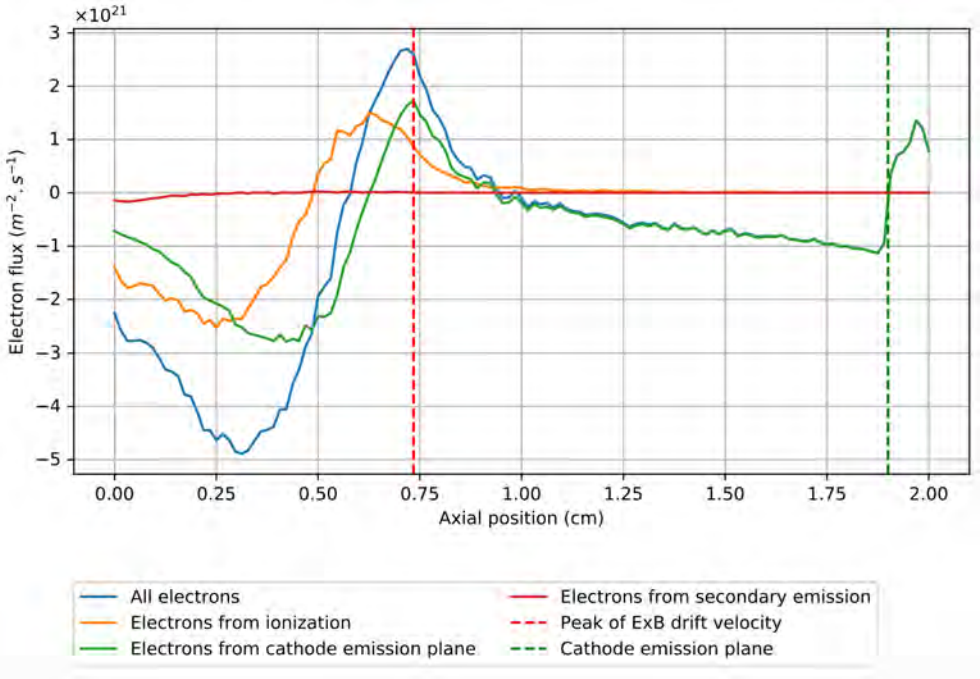

FIGURE 4.9: Axial profiles of electron flux with secondary emission for all electrons and each population.

Figures 4.10 and 4.11 show the axial electron density and temperature profiles for each electron population. It can be seen that the secondary electrons emitted have a much higher temperature than the other electrons in the channel. One explanation for this is that these electrons are injected into the radial sheaths, so they rapidly gain significant kinetic energy. The density of secondary electrons remains an order of magnitude lower than that of other electron populations. While under simulation conditions, secondary electron emission plays no significant role, it may nevertheless be interesting to examine their fate in position and velocity space, and to observe streamline structures in this space. This is what we do next.

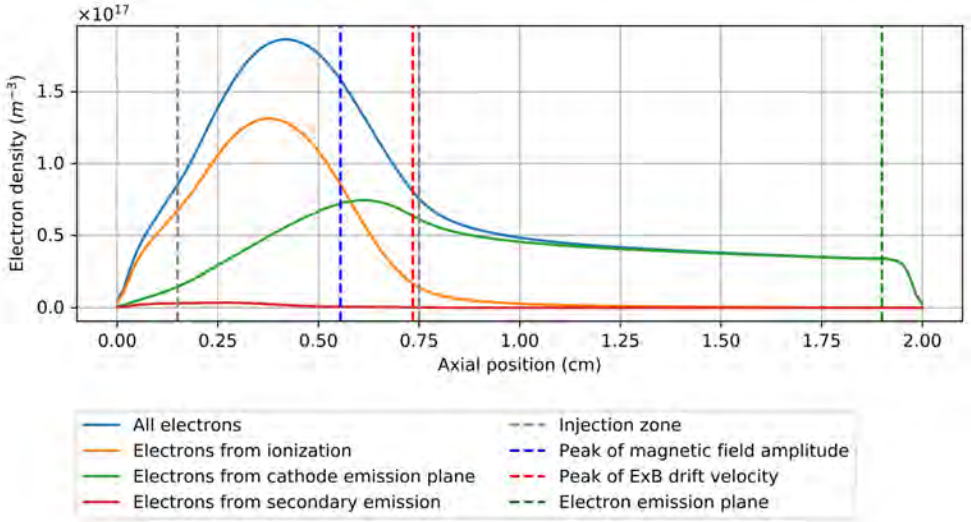

FIGURE 4.10: Axial profiles of electron density with secondary emission for all electrons and each population.

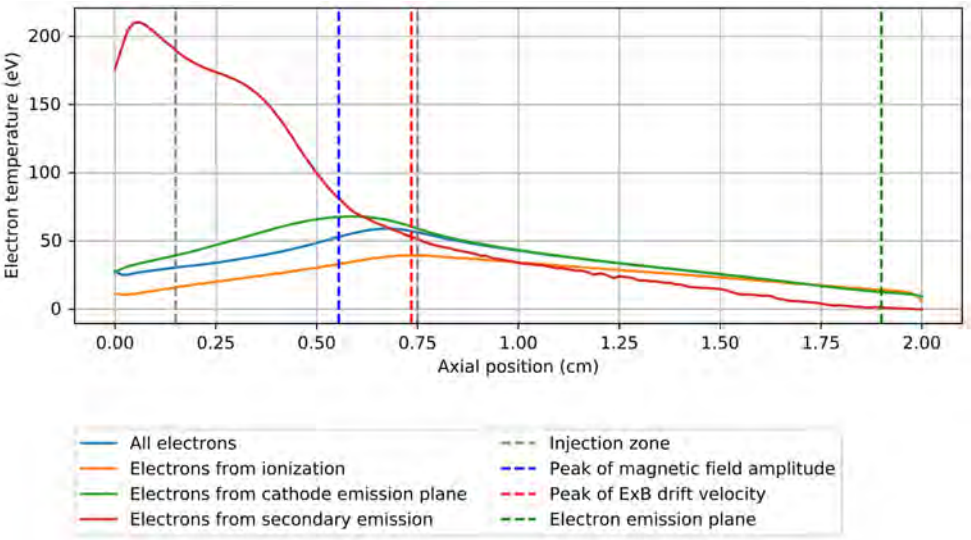

FIGURE 4.11: Axial profiles of electron temperature with secondary emission for all electrons and each population.

4.4 Behavior in velocity space

4.4.1 Velocity distribution profiles as a function of axial position

Velocity distribution profiles and streamlines are calculated in the same way as in the previous chapter. The case presented here is the one with radial absorbent walls and electronic secondary emission at the channel walls. In steady state, the profiles $f(z, v_{radial})$, $f(z, v_{azimuthal})$, $f(z, v_{axial})$, $f(z, v_{\perp})$, $f(z, |\vec{v}|)$ are similar to those observed in the doubly periodic case, and are shown in figure 4.12 for all electrons. The

main differences with the doubly periodic case are the appearance of circulation currents in the (z, v_{radial}) plane in the plume for radial velocities around $\pm 4 \times 10^6 m.s^{-1}$, a decrease in the diffusion of radial velocities, the appearance of streamlines in the $(z, v_\perp)$ and $(z, |\vec{v}|)$ planes which show fluid motions reducing the kinetic energy of electrons in the plume for velocities below $3 \times 10^6 m.s^{-1}$. These observations can be explained by the reflection of low-energy electrons at the radial sheaths that form due to Dirichlet conditions.

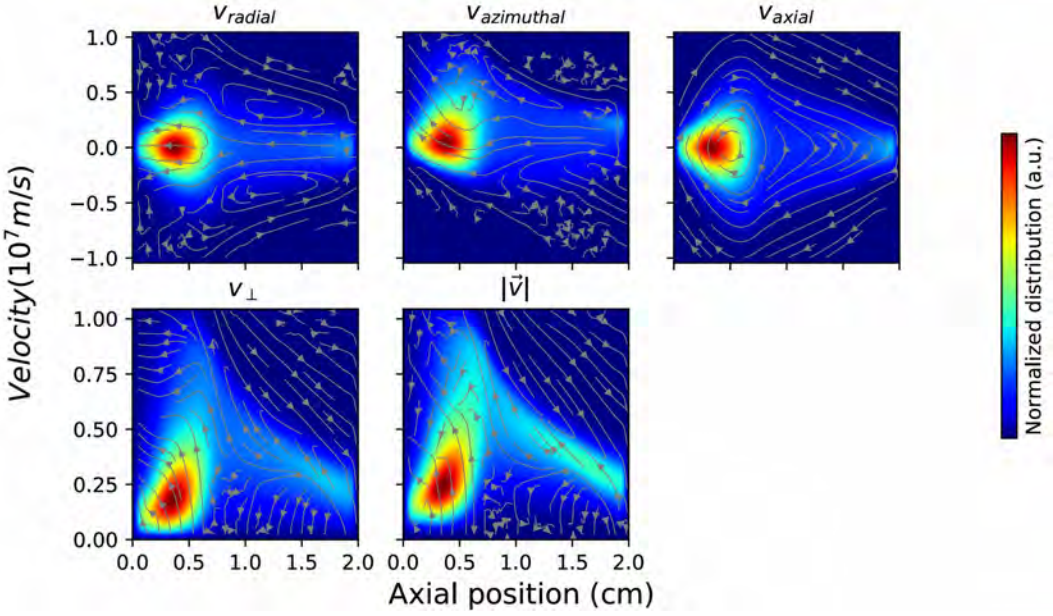

FIGURE 4.12: Axial profile of velocity distribution $f(z, v)$: all electrons (normalized distribution).

Similar radial structures are also observed in the channel and plume for electrons produced by ionization in figure 4.13 and in the plume only for electrons produced at the cathode emission plane in figure 4.14. Energy exchanges perpendicular to the magnetic field between these two populations are still suggested by the shape of the profiles. Note that the vortex in the $(z, v_{azimuthal})$ plane is still present in the profile of electrons produced by ionization in figure 4.13. The addition of radial walls and secondary electron emission appear to leave the main azimuthal instability mechanism unchanged.

The f(z,v) profiles obtained for the third electron population, that of secondary electrons emitted at the channel walls, are shown in figure 4.15. The reinjection of secondary electrons into the radial sheaths results in the appearance of a population of electrons with radial velocities greater than $10^7 m.s^{-1}$, but with velocities perpendicular to the magnetic field of the order of those of electrons produced by ionization. Some of these electrons appear to undergo the azimuthal instability mechanism, gaining energy perpendicular to the magnetic field $E_\perp$. The number of these electrons remains low compared with other populations, as can be seen from the density profiles presented in the previous sections.

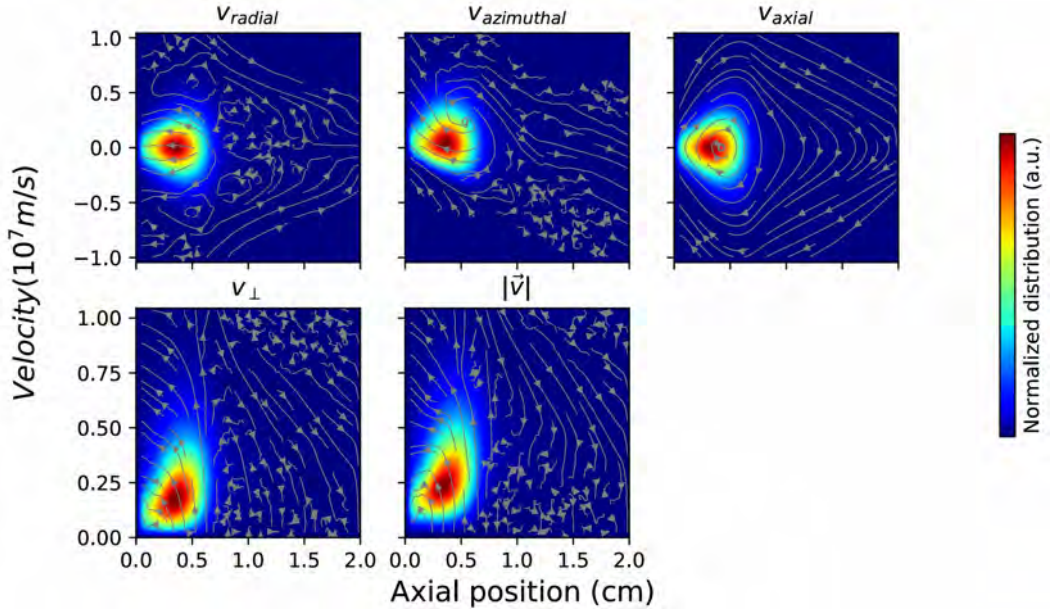

FIGURE 4.13: Axial profile of velocity distribution $f(z, v)$: electrons from ionization (normalized distribution).

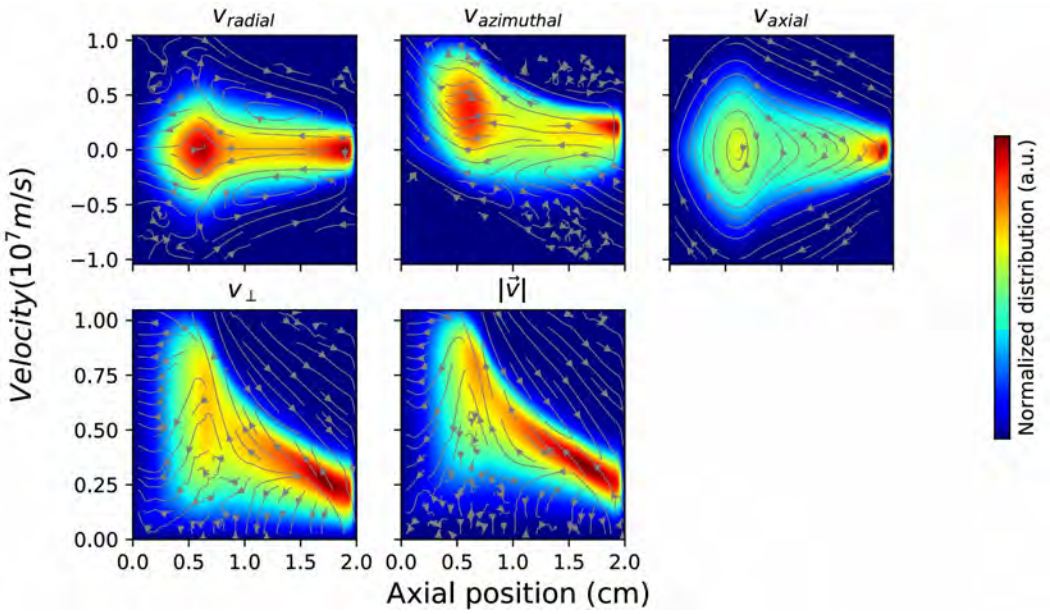

FIGURE 4.14: Axial profile of velocity distribution $f(z, v)$: electrons from cathode emission plane (normalized distribution).

It can be noted that the distribution function profiles f(z,v) obtained for ions in the steady state and presented in figure 4.16 are very similar to those observed in the doubly periodic case. One notable difference is the orientation of the streamlines in the (z, v_{radial}) plane along the (Ov_x) radial velocity axis, due to the presence of the radial sheaths.

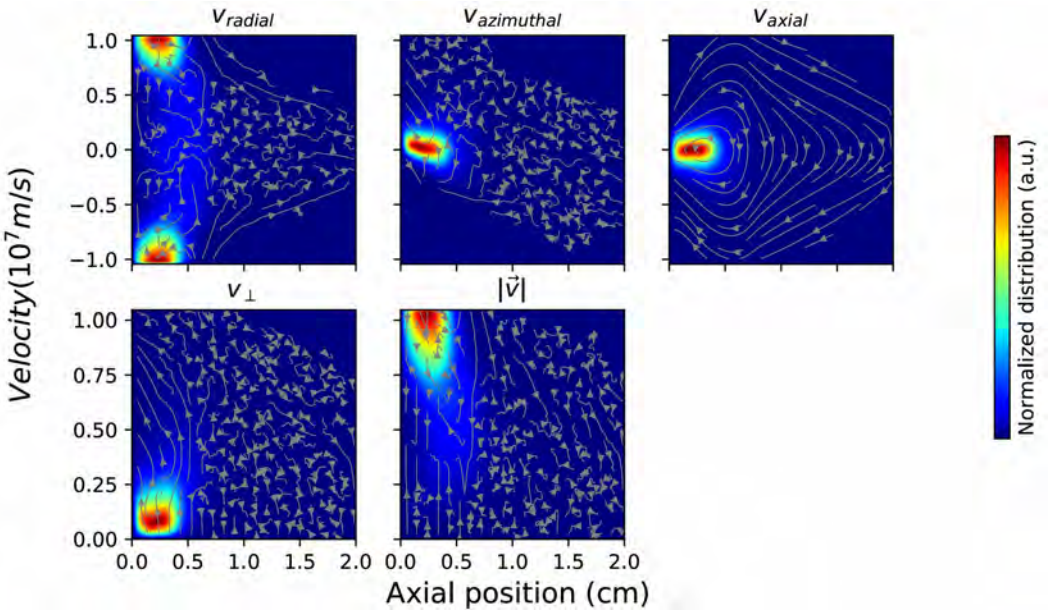

FIGURE 4.15: Axial profile of velocity distribution $f(z, v)$: electrons from secondary emission (normalized distribution).

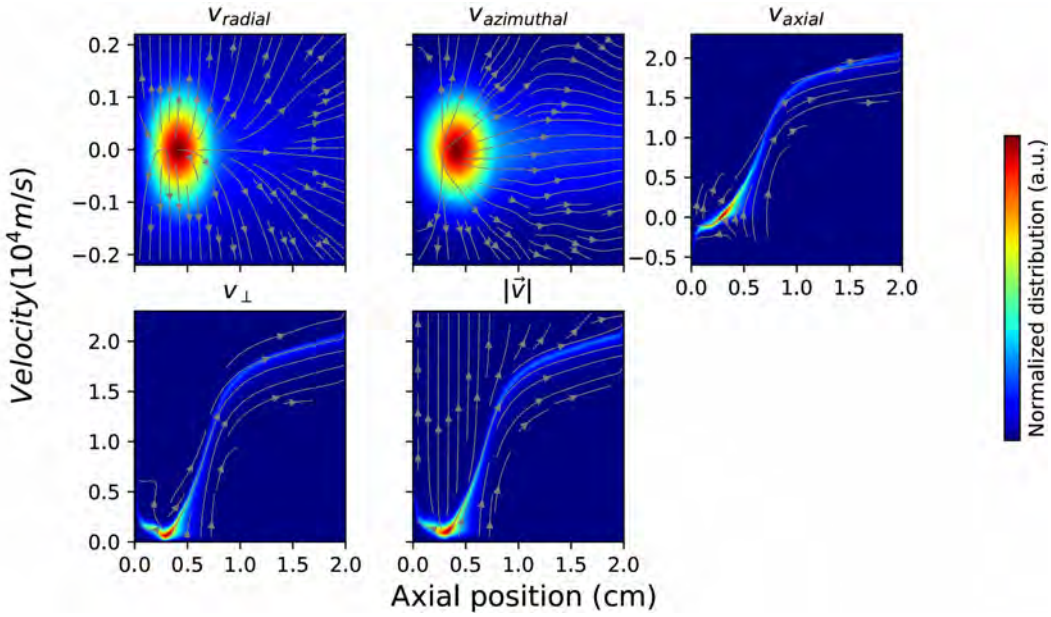

FIGURE 4.16: Axial profile of velocity distribution $f(z, v)$: ions (normalized distribution).

4.4.2 Profiles in velocity space by transport zone

In this subsection, we preserve the transport zone distinction of the previous chapter (see section 3.7 in chapter 3). This division is still valid, as the axial density and electron flux profiles are similar. The distribution function profiles in the $(v_{azimuthal}, v_{radial})$

plane for each electron population are shown in figures 4.17, 4.18 and 4.19. They allow to distinguish the vortex structures already visible in the doubly periodic case for electrons coming from the cathode emission plane in figure 4.18. These have their center at radial velocities of the order of $5 \times 10^6 m.s^{-1}$ in the positively charged zone of the dipole. For electrons produced by ionization, multiple structures are observed in figure 4.17. There appear to be traces of the vortices present in the doubly periodic case for radial velocities of the order of $2.5 \times 10^6 m.s^{-1}$ in the positively charged zone of the dipole. However, it is worth noting the appearance of new vortex structures that also correspond to the vortices observed for electrons coming from the cathode emission plane. Indeed, figure 4.17 shows vortices whose center is located at radial velocities of the order of $5 \times 10^6 m.s^{-1}$ in the positively charged zone of the dipole. Vortices located at lower radial velocities of the order of 1 to $2 \times 10^6 m.s^{-1}$ are also observed in the domain outside the sheaths for electrons produced by ionization and for electrons coming from the cathode emission plane. The nature of these structures remains to be investigated.

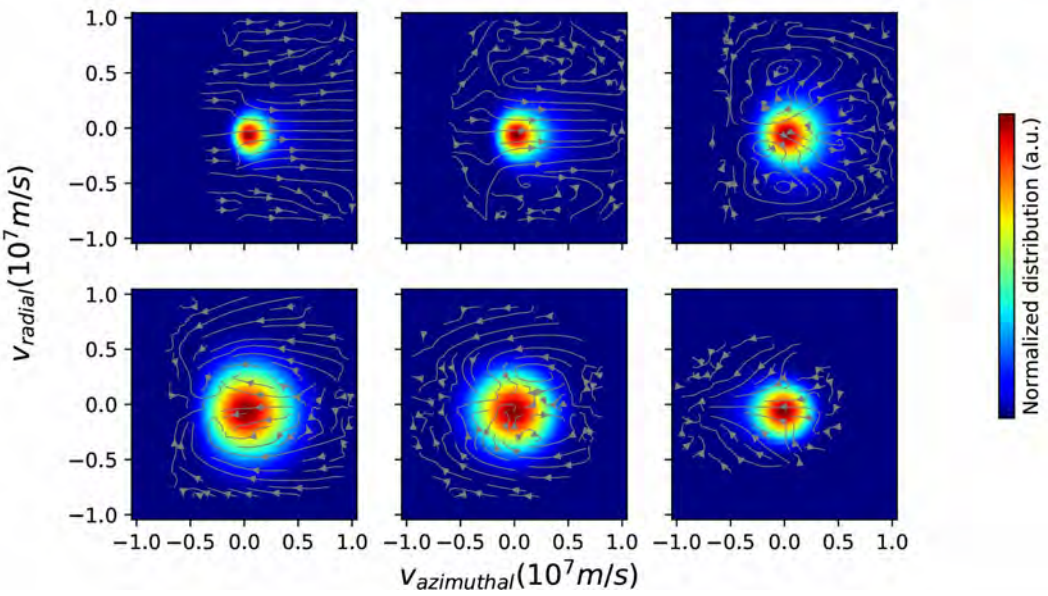

FIGURE 4.17: Azimuthal-radial profile of electron velocity distribution by transport zone for electrons from ionization: anode sheath (top left), secondary dipole (top middle), positively charged zone (top right), negatively charged zone (bottom left), almost constant electron flux (bottom middle), cathode sheath (bottom right).

Note that, for the population of emitted secondary electrons in figure 4.19, the vortex structures at radial velocities of the order of $5 \times 10^6 m.s^{-1}$ are difficult to distinguish in the positively charged zone of the dipole. The streamlines appear to be more disordered.

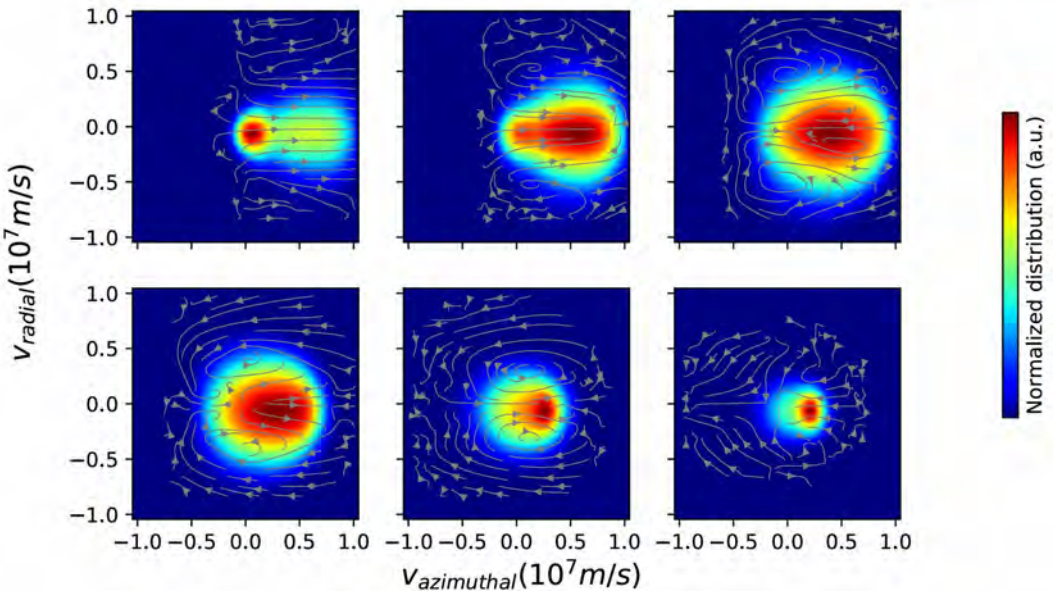

FIGURE 4.18: Azimuthal-radial profile of electron velocity distribution by transport zone for electrons from cathode emission: anode sheath (top left), secondary dipole (top middle), positively charged zone (top right), negatively charged zone (bottom left), almost constant electron flux (bottom middle), cathode sheath (bottom right).

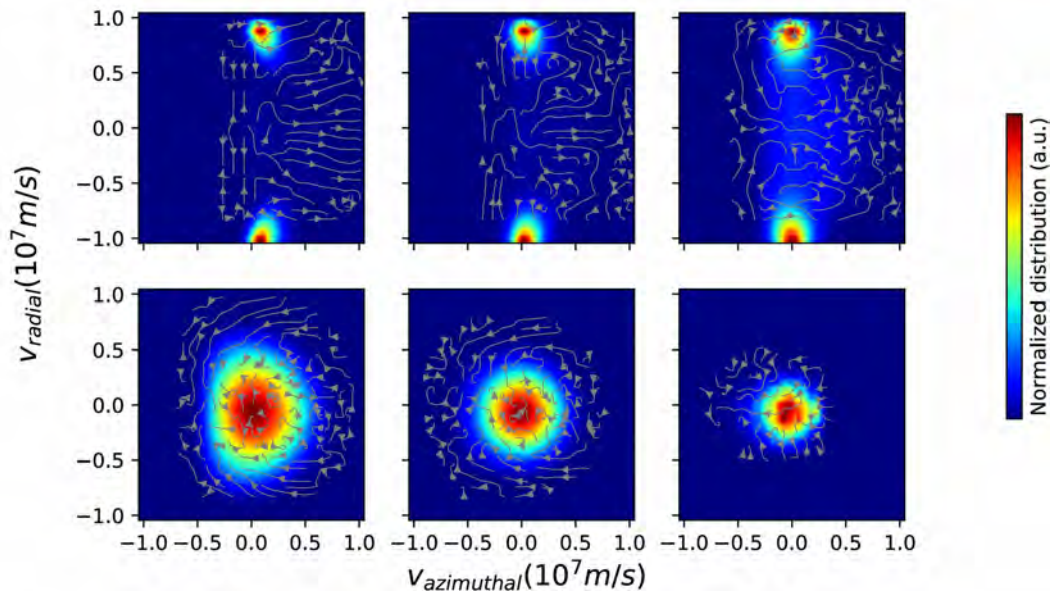

FIGURE 4.19: Azimuthal-radial profile of electron velocity distribution by transport zone for electrons from cathode emission: anode sheath (top left), secondary dipole (top middle), positively charged zone (top right), negatively charged zone (bottom left), almost constant electron flux (bottom middle), cathode sheath (bottom right).

4.5 Waves present in plasma

The sampling conditions for the diagnostics presented in this subsection are the same as in the previous chapter. It should be noted that the conclusions drawn for the doubly periodic case apply to the case with radial absorbent walls and electronic secondary emission. We focus in particular on the notable differences from the simulations in the previous chapter. Thus, it can be seen from the azimuthal profiles of ion density and secondary electron density shown in figures 4.20 and 4.21 that secondary electron production is accentuated after the passage of the plasma dip, which propagates in the azimuthal direction at kHz.

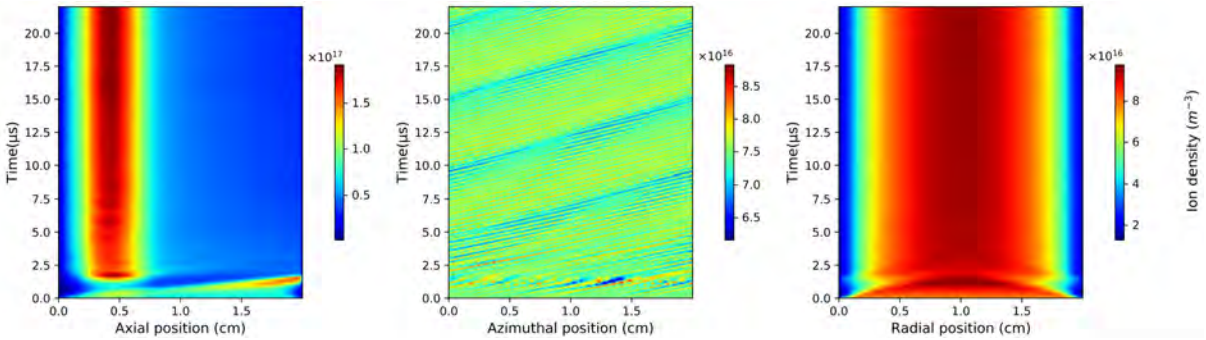

FIGURE 4.20: Spatially integrated ion density profiles in each direction.

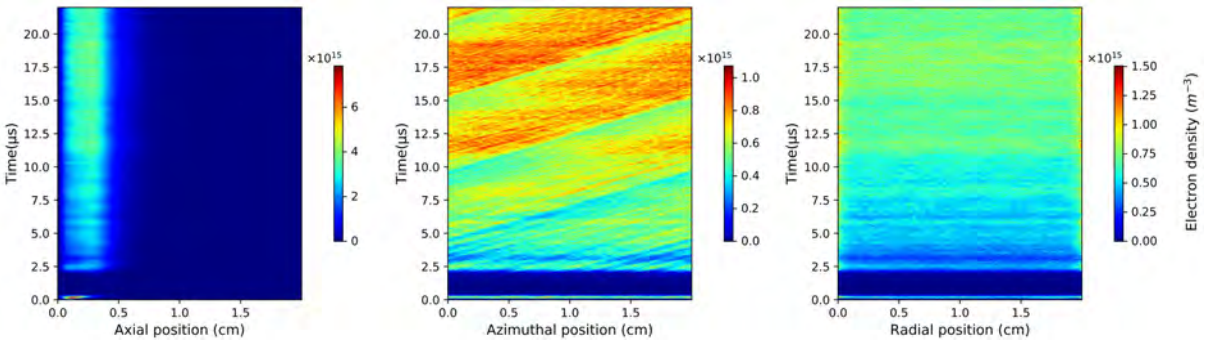

FIGURE 4.21: Spatially integrated electron density profiles in each direction: electrons from secondary emission.

In addition, the profile of the azimuthal component of the electric field presented in figure 4.22 shows, like figure 3.56 in the previous chapter, the presence of helixes in the (x,t) plane, but these are less pronounced than in the doubly periodic case. The branches of the helixes close to the walls tend to disappear. These perturbations remain negligible compared to the azimuthal perturbation at MHz.

We note that the same average frequencies and wavelengths are found in the parietal case with electronic secondary emission as in the doubly periodic case. Other profiles of electron density, electron velocities, and axial and radial electric field components are presented in Appendix C.

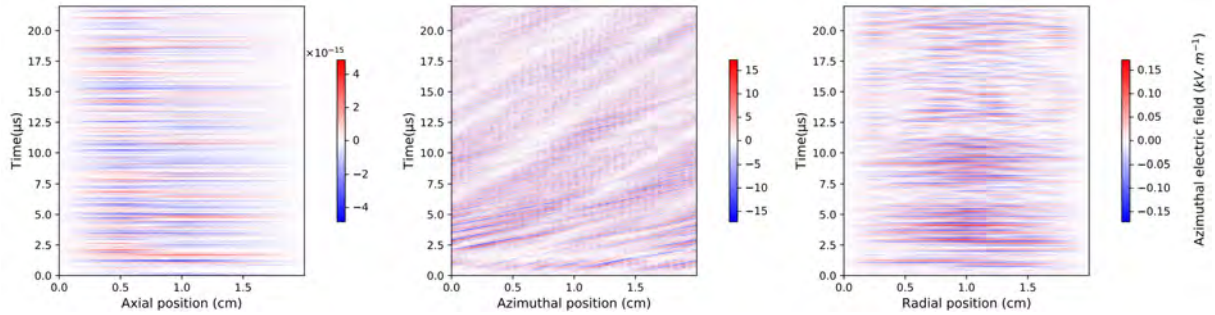

FIGURE 4.22: Spatially integrated azimuthal electric field profiles in each direction.

4.6 Conclusions on the role of electronic secondary emission on electronic transport

The study carried out in this chapter highlights, on one hand, the role of absorbent wall boundary conditions in the observed reduction in axial electron flow, and on the other hand, the low contribution of secondary electrons to axial electron flow compared with the two main electron populations, those coming from ionization and those from the cathode. These secondary electrons account for less than 6% of the electron flux at the anode, compared with 62% for electrons produced by ionization and 32% for electrons from the cathode emission plane under our simulation conditions. The ratio of emitted secondary electrons to the number of impacting electrons γ_{SEE} is of the order of 1.02 with a standard deviation of the order of 0.02, which is higher than the critical threshold given in Croes, 2017 for xenon ($\gamma_{cr} = 0.985$), but remains close to one. The charge saturation mechanism responsible for sheath inversions described in Croes, 2017 could explain the relatively stable value of this ratio. The distribution functions show that some secondary electrons appear to be affected by the azimuthal instability, gaining energy perpendicular to the magnetic field in the same way as electrons produced by ionization. The presence of radial absorbent walls and electronic secondary emission seem to have little effect on the dominant azimuthal mode observed through the vortex structure in the $(z, v_{azimuthal})$ plane. The conclusions on the azimuthal instability mechanism drawn in the previous chapter are thus still valid for the present case. These results are also in agreement with the observations made in Croes, 2017, which show that the characteristics of the azimuthal instability are little perturbed by the addition of electronic secondary emission. Other observations require further investigation to conclude. The propagation of the kHz plasma density dip in the azimuthal direction seems to lead to an increase in the production of secondary electrons emitted after its passage. New streamline vortex structures are observed in the $(v_{azimuthal}, v_{radial})$ plane, while some are similar to those observed in the doubly periodic case. The origin of these structures could be investigated assuming analytic waveforms or given distribution functions, but will be left to future work.

Chapter 5

Model-experiment comparison

We were given the opportunity to attend a part of the test campaign for a 1.5 kW PPS-1350ML thruster on the PIVOINE vacuum chamber in January 2021. The development of sparse grid tools within the PIC algorithm and that of the simulation code did not allow us to carry out the experimental measurements ourselves. Thibault Dubois, under the supervision of Sedina Tsikata, carried out the set-up and experimental measurements. It is these data presented in Dubois, 2023 that we attempt to explain with our simulation results.

5.1 Description of the experimental conditions

Laser diagnostic using incoherent Thomson scattering, and all experimental conditions are described in greater detail in chapter 4 of Thibault Dubois' thesis (Dubois, 2023). Readers are invited to refer to this chapter for an overview of the experimental set-up. A brief description of the operating principle of the laser diagnostic is given here.

The physical quantity measured is the light scattered by the plasma's free electrons. This type of scattering is called Compton scattering. When only elastic collisions between photons and free electrons are considered, it is called Thomson scattering. Where there is light scattering, there is a light source. This comes from the laser chosen for the experimental set-up. An optical fiber is used to recover the light scattered by the electrons and previously channeled through an optical lens. The use of a laser with a wavelength longer than the Debye length allows to study electron density fluctuations from the measured light spectrum. This is the coherent regime. In contrast, using a laser with a wavelength shorter than the Debye length allows to study the temperature, density and drift velocity of free electrons from the measured light spectrum. This is the incoherent regime.
A diagram adapted from figure 4.3 in Dubois, 2023 is shown in figure 5.1. The direction probed is that carried by the vector $\vec{k} = \vec{k}_s - \vec{k}_i$. where $\vec{k}_i$ is the laser beam direction and $\vec{k}_s$ is the beam direction captured by the optical fiber. A series of measurements is taken at 45 degrees on either side of the y-axis in the exit plane (Oxy), 1 mm from the thruster. This allows to establish the radial profiles of electron temperature, density and azimuthal drift velocity after post-processing of the measured spectra.

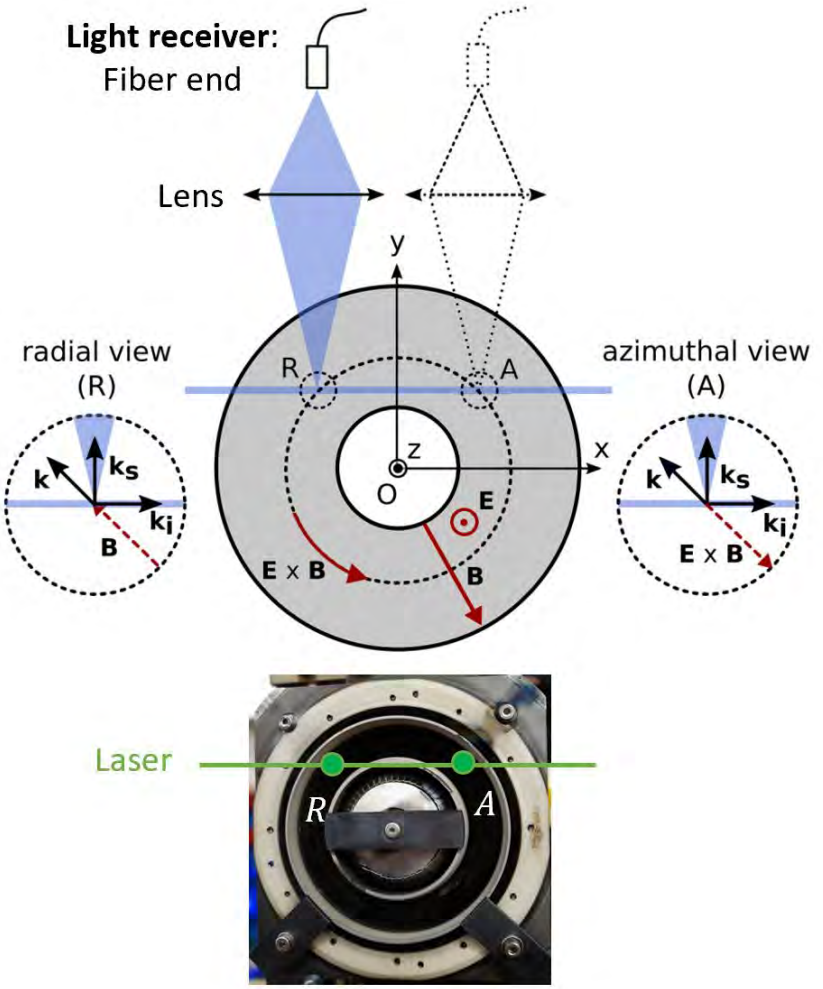

FIGURE 5.1: Front view scheme of experimental set-up for incoherent Thomson scattering measures: adapted from figure 4.3 in Dubois, 2023.

The test campaign on the 1.5 kW PPS-1350ML thruster was carried out under specific operating conditions. These conditions are presented in figure 5.2 for measurements obtained with krypton and xenon according to Dubois, 2023. The discharge voltage U_d is below nominal operating conditions (see table 3.1) but is sufficient to ensure plasma discharge.

	$\dot{m}_a$ (mg/s)	$\dot{m}_c$ (mg/s)	I_d (A)	U_d (V)	$B_{r,inner}$ (G)	$B_{r,center}$ (G)	$B_{r,outer}$ (G)
Kr	6.5	0.7	9.6	125	265	175	155
Xe	8	0.7	8.8	130	250	160	140

Table 4.1: *Operating conditions for incoherent Thomson scattering experiments with krypton and xenon. $\dot{m}_a$ and $\dot{m}_c$ are the gas flow rates to the anode and cathode, respectively. B_r is the radial magnetic field measured 1 mm outside the exit plane of the thruster at three radial locations: the inner ceramic edge, the center of the ceramic channel, and the outer ceramic edge.*

FIGURE 5.2: Low voltage operating conditions: after table 4.1 in Dubois, 2023.

5.2 Simulation with variation of the source term

The current capabilities of the computational code developed during the thesis enable the Sparse-PIC method to be applied to a cubic geometry, or a rectangular parallelepiped, or even a combination of these volumes (cf. sub-section on simulation domain extension in chapter 2). In order to take advantage of this simulation tool despite its geometric constraints and the simplifications of the thruster model developed in the previous two chapters, we focus on the influence of the shape of the ionization source term. Can the experimentally measured electron density profile be explained by a change in ionization in the channel? The article in Janes and Lowder, 1966 states:

> "Clearly, due to the small curvature of the ion trajectory away from the anode, nonuniform ionization near the anode would result in a nonuniform ion density everywhere down stream."

Unmagnetized ions follow a trajectory primarily guided by the axial profile of electric potential and therefore the axial electric field. Non-uniform ionization in the radial direction should therefore lead to a similar electron density profile at the thruster exhaust. This is what we verify by considering an arbitrary radially-biased ionization profile, as shown in figure 5.3. For the rest, we apply the same simulation conditions as in the previous chapter.

This profile is obtained by drawing a random number $r \in [0, 1]$ for the reinjection of electron-ion pairs at each exit of an ion from the domain, such that the radial position X_p of reinjection is equal to:

$$X_p = x_{min} + 2.5[mm] + (x_{max} - x_{min} - 5[mm]) \times log((e-1)r + 1)$$

where log is the logarithm function in base e, with e the value of the exponential function in 1, x_{min} the radial coordinate corresponding to the inner wall of the thruster and x_{max} the radial coordinate corresponding to the outer wall of the thruster. A margin of 2.5 mm is taken to avoid re-injecting into the radial sheaths, even though ionization is physically possible there. Radial profiles of electron density, temperature and azimuthal drift velocity taken at 1 mm from the thruster exit plane are shown respectively in figures 5.4, 5.5 and 5.6.

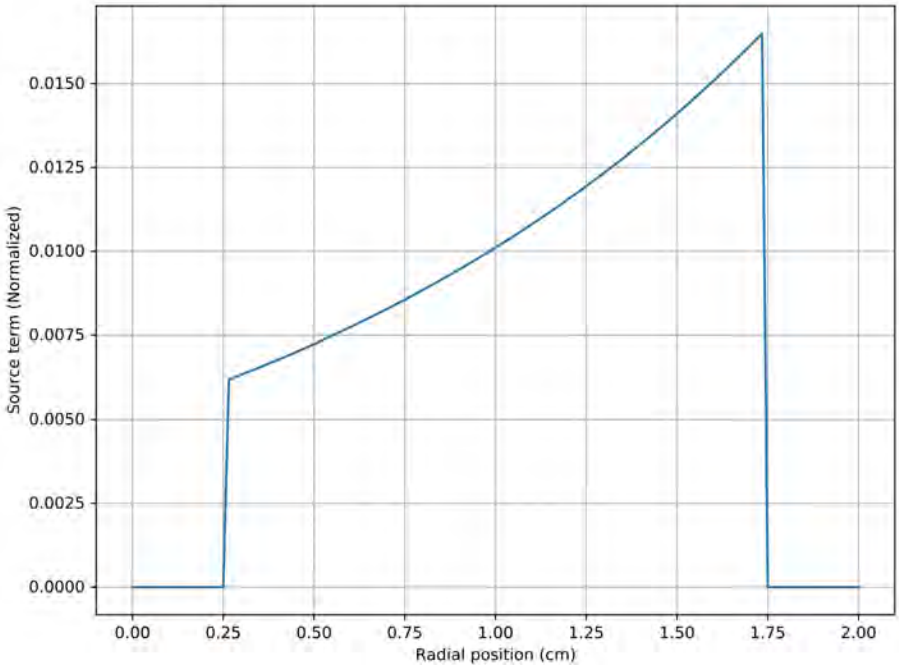

FIGURE 5.3: Radially-biased ionization source term.

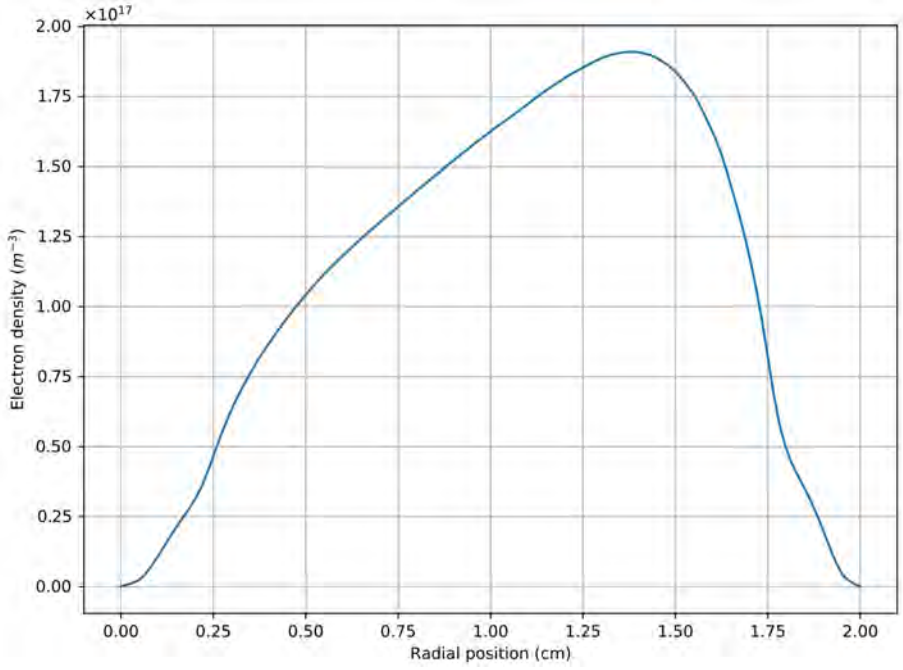

FIGURE 5.4: Electron density radial profile at 1 mm from channel exit plane for a radially-biased ionization source term.

We note that the radial bias of the ionization source term is reproduced in trend on the electron density profile at the thruster exhaust. The electron temperature is between 45 and 50 eV, with a minimum in the highest electron density zone. This

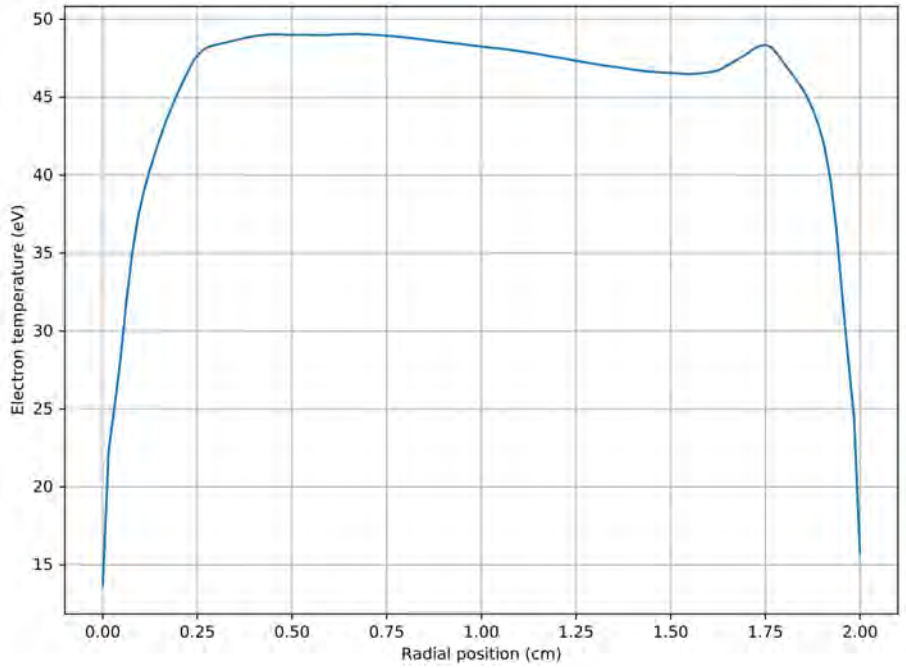

FIGURE 5.5: Electron temperature radial profile at 1 mm from channel exit plane for a radially-biased ionization source term.

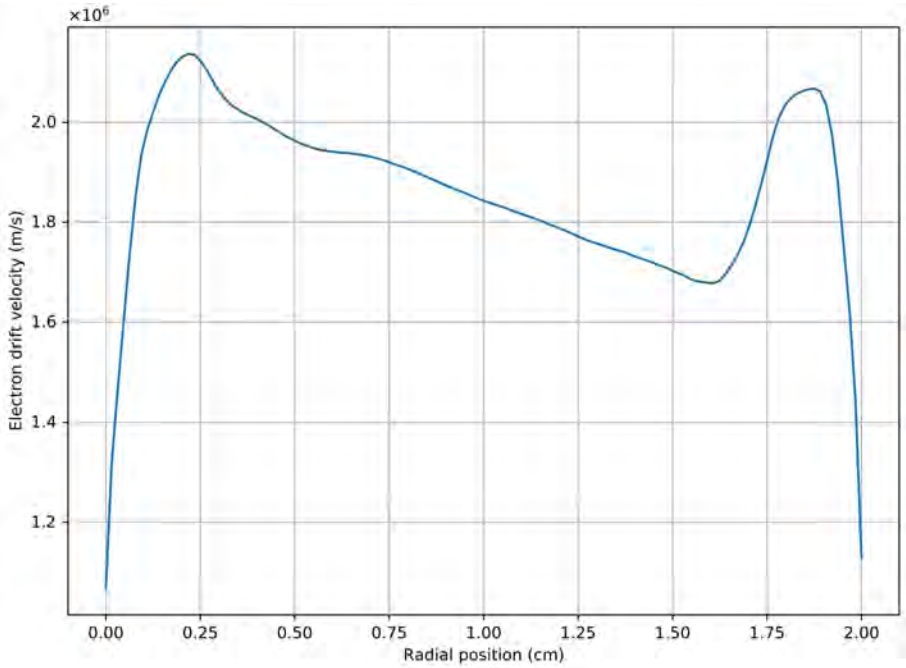

FIGURE 5.6: Electron azimuthal drift velocity radial profile at 1 mm from channel exit plane for a radially-biased ionization source term.

minimum electron temperature is also that of the electron azimuthal drift velocity.

It can be seen that the electron temperature and the electron azimuthal drift velocity have radial profiles which rise and then fall as they approach the walls in the sheaths. These two profiles follow each other in trend.

5.3 Interpretation of the experimental results

The results of the January 2021 campaign on PIVOINE are taken from Dubois, 2023 and represented here in figures 5.7, 5.8 and 5.9 for interpretation. The radial electron density profiles in figure 5.7 show a trend towards increasing electron density near the outer wall of the Hall thruster for both xenon and krypton. This suggests that ionization mainly takes place close to the outer wall of the thruster. This could be explained by the position of the external cathode on the outside of the thruster, as shown in figure 1.2. Primary electrons would enter the discharge close to the outer wall. Ionization would also be enhanced by increased secondary emission at the outer wall, thanks to the flow of electrons from the cathode.

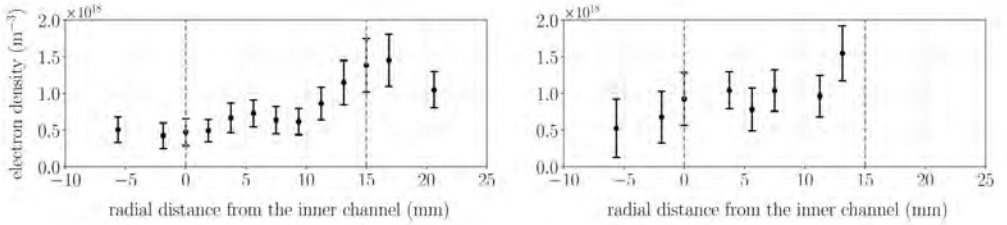

Figure 4.6: *Evolution of electron density in the radial direction, measured by incoherent Thomson scattering, for (left) krypton, and (right) xenon. The experimental conditions corresponding to these results are listed in Table 4.1.*

FIGURE 5.7: Electron density radial profile at 1 mm from channel exit plane for krypton and xenon: after figure 4.6 in Dubois, 2023.

Figure 5.8 shows the radial profile of electron temperature for krypton and xenon. Although data is lacking for xenon, it appears that the electron temperature increases at the outer wall. Such an increase is only seen in the simulation results because of the radial sheaths. In view of the electron distribution functions, however, it can be stated that that the hottest electrons are mainly those coming from the cathode.

Figure 5.9 shows the radial profile of electron azimuthal drift velocity for the two ion species tested. Although measurements for xenon near the outer wall of the thruster are also missing, it can be seen that the trend in the azimuthal drift velocity profile follows that of the electron temperature, which is consistent with previous simulation results. There is, however, a notable difference between the simulation results and those observed experimentally. Temperature and electron azimuthal drift velocity show an inverse trend to electron density outside the sheaths in the simulation results. On the contrary, experimental results show that all three profiles seem to follow the same radial trend. Such a difference could indicate an ionization source term in the simulations that is too important close to the inner wall of

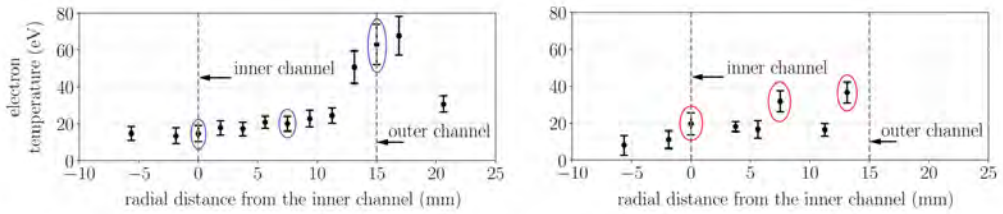

Figure 4.5: *Evolution of electron temperature in the radial direction, measured by incoherent Thomson scattering, for (left) krypton, and (right) xenon. The experimental conditions corresponding to these results are listed in Table 4.1. The points circled in blue and red are highlighted for the purpose of a later discussion in this chapter.*

FIGURE 5.8: Electron temperature radial profile at 1 mm from channel exit plane for krypton and xenon: after figure 4.5 in Dubois, 2023.

the thruster. Experimental conditions indicate operation at a lower discharge voltage (125-130 V vs. 300 V in the simulation) which also induces a lower azimuthal drift velocity. Electrons therefore drift less speedily, with an order of magnitude of $10^5 m.s^{-1}$ for the experimental results versus $10^6 m.s^{-1}$ for the simulation results. The radial variation in magnetic field amplitude, which is stronger near the inner wall than the outer wall under the experimental conditions may also explain the drop in temperature and azimuthal drift velocity observed towards the inner wall. Although the electron density conditions of the simulation are also an order of magnitude lower than the real conditions, this should not be a major factor in the observed differences. General improvement of the simulation conditions and further investigations could lead to a simulation closer to the observed experimental results. In particular, a simulation with a radial variation in magnetic field amplitude could be considered in future work.

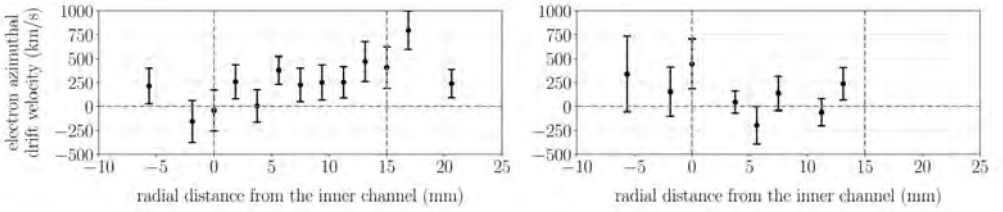

Figure 4.7: *Evolution of electron drift velocity in the radial direction, measured by incoherent Thomson scattering for (left) krypton, and (right) xenon. The experimental conditions corresponding to these results are listed in Table 4.1.*

FIGURE 5.9: Electron azimuthal drift velocity radial profile at 1 mm from channel exit plane for krypton and xenon: after figure 4.7 in Dubois, 2023.

A more physical interpretation of the experimental results from the January 2021 PIVOINE test campaign was given. In particular, the association between high electron temperature and the electron population from the cathode was highlighted for

measurements at the thruster exhaust. The radial ionization profile in the channel induces the ion and electron density profiles at the thruster exhaust. The position of the external cathode and the radial magnetic field profile could lead to non-uniformity of ionization in the channel.

Chapter 6

Conclusions

The whole thesis led us to study several scientific disciplines, including mathematics, algorithmics and plasma physics. Coupling these three main disciplinary fields with a view to creating a realistic and efficient simulation of the Hall thruster operation has guided our developments. Thus, the mathematical tools of sparse grids were applied to the Particle-In-Cell (PIC) algorithm in order to significantly improve the performance of the classical algorithm to the point of making accessible simulations previously considered too costly in computation time. This performance was achieved through efficient parallelization of computing resources on cpus architectures. The implemented three-dimensional Sparse-PIC algorithm was then applied to the Hall thruster model developed at LAPLACE. While the simulation results are far from the representation of numerical twins one might imagine, in other words models that faithfully represent the behavior of the thruster, they nevertheless offer many clues to the physical operation of the thruster. For greater clarity, the detailed conclusions are divided into two parts: the first is devoted to the Sparse-PIC method and the second on electronic transport in the Hall thruster.

6.1 Conclusions on the Sparse-PIC method

A first step in the verification of sparse grid tools was carried out by applying them to the solving of Poisson's equation. Several cases of manufactured solutions, including a density gradient case, spatial density oscillations and a mathematical approximation of the axial potential profile of a Hall thruster, have shown that the grid combination method derived from the sparse grid theory is well suited to this type of problem. For a channel length of the order of a few centimetres, the Sparse method can solve wavelengths of the order of a millimetre with grid levels greater than 7 in two and three dimensions. Not even mentioning coupling to the PIC algorithm, a time saving of a factor of 3 in two dimensions and 33 in three dimensions is obtained compared to a direct resolution of the Poisson equation.
The validity of the results of the coupled Sparse-PIC algorithm was confirmed by a benchmark with the results of the classical PIC method in three dimensions on an ExB cross-field configuration. Differences of just a few percent on the profiles of a few quantities of interest averaged over time after convergence of the results were obtained. The consistency of the physical results is ensured by a low level of fluctuations for the density of the order of $10^{15} m^{-3}$ and limited to a few volts for the electric potential.

Although data is lacking to compare the performance of the two algorithms, several orders of magnitude are available for the Sparse-PIC method. The cases presented in the last three chapters with a grid level of 7 were obtained in less than 13h on an architecture of 1440 cpus. A grid level of 9 would enable simulation with a plasma density ten times greater, closer to reality, but taking 17 days on the same cpus architecture. It may therefore be preferable to continue studying reduced three-dimensional models of the Hall thruster with representative numerical results of the physical phenomena available relatively quickly. It should be noted that the Sparse-PIC method can obtain more accurate results using higher-order numerical schemes at limited cost and with a modification of the grid combination method. The extension of the method to any type of geometry could be envisaged by means of adaptive refinement algorithms, transformations or sparse domain associations such as the T-shaped one tested during the thesis. Finally, we note that the sparse grid tools have already been applied to other algorithms in the GENE and EXAHD codes for adaptation to future exascale computing architectures. The coupling of the Sparse method and the PIC algorithm therefore seems consistent with the need to improve computational performance while maintaining an acceptable level of accuracy.

6.2 Conclusions on the electronic transport

The instabilities identified as being at the origin of anomalous electronic transport, that is, unrelated to collisions, in the thruster have encouraged us to study a collisionless model where ionization is a simulation parameter and neutrals are not taken into account. The orders of magnitude of collision frequencies discussed in chapter 3 justify this approximation to model the thruster acceleration zone. Modeling neutrals would above all enable us to refine the transport at plasma boundaries and the ionization source term. Significant additions from our simulation results concern, on the one hand, the distinction of electrons according to their origin (cathode, ionization or secondary emission at the walls) and, on the other hand, the representation of their distribution function and associated streamlines in velocity space as a function of axial position in particular. In the case of the Hall thruster, these diagnostics have made it possible to challenge two main assumptions of the electron drift (EDI) or the electron cyclotron drift (ECDI) instability models. On the one hand, the electron distribution functions are far from Maxwellian functions, are not centered around the electron drift velocity and even exhibit asymmetry in the direction of azimuthal velocities, implying terms of kinetic origin in the fluid equations. On the other hand, velocities perpendicular and parallel to the magnetic field are not invariants of motion. Electron trajectories in position and velocity space, as well as distribution functions, suggest exchanges of energy (kinetic plus potential) perpendicular to the magnetic field between the electron population produced by ionization and that coming from the cathode. The electrons produced by ionization would thus gain energy perpendicular to the magnetic field provided by the electrons coming from the cathode. For the most part, these exchanges would be "adiabatic" for the electrons coming from the cathode, that is, at constant total energy (perpendicular plus parallel to the magnetic field), and could explain the radial

velocity diffusion observed in our cases. For electrons produced by ionization, these exchanges also lead to an increase in total energy and contribute to the heating of this electron population.

The wave perceived in the simulation results at MHz propagates mainly in the azimuthal direction and has characteristics close to those of an ion acoustic wave in terms of frequency and wavelength. It seems to be linked to a vortex structure of the streamlines in the plane of the axial positions and azimuthal velocities associated with the electrons produced by ionization. The center of this structure is close to the axial position of the magnetic field maximum and coincides with the azimuthal drift velocity, the ratio of the seventh cyclotron harmonic to the azimuthal mean wavenumber, and the ratio of the partial electron plasma pulsation calculated with the density of electrons coming from the cathode to the azimuthal mean wavenumber. Such a condition suggests that an electron cyclotron resonance mechanism is at the origin of the azimuthal instability and that a single azimuthal mode dominates. Mode saturation could be linked to the population of electrons coming from the cathode, which is more energetic than the population of electrons produced by ionization, and which would provide the energy perpendicular to the magnetic field required for the exchanges suggested by the electron trajectories and distribution functions. Propagation in the form of a non-neutral wave in the simulation domain could be linked to the frequency difference between the electron cyclotron harmonics and the ion plasma frequency.

Perturbations in the radial direction with amplitudes negligible compared to the azimuthal perturbations were also observed. They could be linked to the vortex structures observed in the plane of radial and azimuthal velocities. Their understanding remains difficult, and further investigations are required.

Simulation results clearly indicate a kinetic origin of the azimuthal instability. The average characteristics of the two main electron populations (ionization, cathode), relative to the axial direction in terms of temperature, density and pressure gradient nevertheless seem to indicate an equilibrium between these two electron populations on a fluid scale. It would therefore be possible to consider a three-fluid model, with two electronic fluids (one for each electron population) and one ionic fluid, provided that the Maxwellian distribution function assumption is overcome and the kinetic terms are made explicit.

A contribution in this direction comes from the following observation: the time-averaged axial electron flux gradient is approximately equal to the product of the electron cyclotron pulsation by the difference between ion and electron density, the sign depending on axis conventions. This observation, based on simulation results, gives an approximate value to the term of kinetic origin in the first fluid moment which depends solely on the magnetic field and charge density configuration. Unfortunately, this is not enough to link the axial electron flux to the engineering parameters, namely the magnetic field configuration and the voltage imposed between the electrodes. For this, it is necessary to know the link between these parameters

and the charge density or electric potential profile, the conversion between the two being made by means of Poisson's equation.

It is important to note the proximity between the results of the cross-field configuration studied and the "double layer" configurations. A potential bias is imposed in the Hall thruster by means of electrodes. This type of bias introduces the formation of a non-neutral dipole structure in the plasma, enabling the establishment of a quasi-static axial electric field. Although the break in neutrality consists of a charge difference of less than two percent of the ion or electron density, its role in the axial electron transport seems non-negligible. In the case of the Hall thruster, the magnetic configuration alters the shape of the charge density profile and goes beyond the classical "double layer" framework. However, observations made on "double layers" of potential relaxation oscillation at kHz could be similar to the propagation in the azimuthal direction at kHz of a plasma density dip observed in the simulation results.

Changing the radial boundary conditions from periodic to radial absorbent wall seems to leave the azimuthal instability mechanism unchanged. It does, however, lead to a decrease in electron flux towards the anode and the appearance of other vortex structures in the plane of radial and azimuthal velocities. These latter structures could be linked to radial sheaths, but require further investigation. Using a simple linear model, the addition of secondary electronic emission plays no significant role in the simulation results. There is a slight increase in electron flux at the anode, but this remains negligible compared with the electron fluxes of the other electron populations. Secondary electron production depends mainly on the impact of electrons produced by ionization at the walls, but a quarter of them under our simulation conditions are produced by electron impact from the cathode emission plane. This secondary electron production accounts for less than one percent of the electrons produced by ionization or ejected at the cathode. The critical threshold for secondary electron production at the walls is reached and the space charge saturation regime described in Croes, 2017 could explain the relative stability of the secondary electron production rate by electron impact around one through the emergence of temporary sheath inversions. However, the physical phenomenon behind secondary electron emission by electron impact remains poorly described and it may be worth revisiting this parameter as our understanding of the phenomenon improves.

Interpretation of experimental results from the January 2021 test campaign on the PIVOINE vacuum chamber of a PPS-1350ML thruster highlights a potentially radially biased ionization due to a stronger magnetic field close to the inner wall than to the outer wall of the thruster. The external position of the cathode during measurements could also play an important role in this bias. Further simulations under conditions closer to the experimental ones, and in particular with a realistic magnetic configuration could bring simulation results closer to experimental observations.

The complexity of electronic transport in the cross-field configuration typical of a Hall thruster has been highlighted by Sparse-PIC simulation results. Numerous grey areas remain, and these will need to be resolved to achieve sufficient simulation to help design future electric thrusters.

6.3 Future prospects

As for the conclusions, future prospects concern the numerical tool of the Sparse-PIC method on the one hand, and further investigations of thruster physics on the other. There are three main tools for sparse grids: basis functions, a quadrature formula and a grid combination technique. Testing alternatives to these three parameters could improve the accuracy of results in certain configurations, as could the coupling to higher-order numerical schemes in the Sparse-PIC algorithm. An extension of the method to a variety of geometries is required to make it an industrial tool.

The results of the reduced thruster model suggest the development of multi-fluid models associated to the different electron populations, or theoretical developments based on fluid equations taking into account terms of kinetic origin. However, these developments often face the need for an analytical form of the electron distribution function, which could be the subject of further research. Another option is to determine the influence of engineering parameters such as discharge voltage and magnetic field configuration on the observed dipole. In this way, it would be possible to find an optimum of engineering parameters to reduce electron flux at the anode and thus power consumption, while maximizing ion flux.

A direct improvement to the model could be to take self-consistent ionization into account. The model could also be complemented by more realistic electrode models.

The observed vortex structures of streamlines in the space of positions and velocities could be explained by simulations introducing given waveforms such as plane progressive harmonic waves, and showing the evolution of distribution functions over time. These additional simulations would contribute to our understanding of the role of wave propagation on distribution functions.

Appendix A

Comparison between direct solver and Sparse methods.

A.1 Manufactured solutions: gradient without source term.

Here we consider $\Phi_{ref}(z) = (U_c - U_a)\frac{z}{L} + U_a$ with $U_a = 300V$, $U_c = 0V$, $L = 2cm$ and $\rho = 0$. Dirichlet conditions are set in (Oz) axis, periodic conditions in the other directions. Figures A.1,A.2 and A.3 show deviation from the exact solution of Poisson's equation for the potential, and the y-axis, z-axis components of the electric field in two dimensions. Figures A.4 and A.5 show deviation from the exact solution of Poisson's equation for the potential in three dimensions.

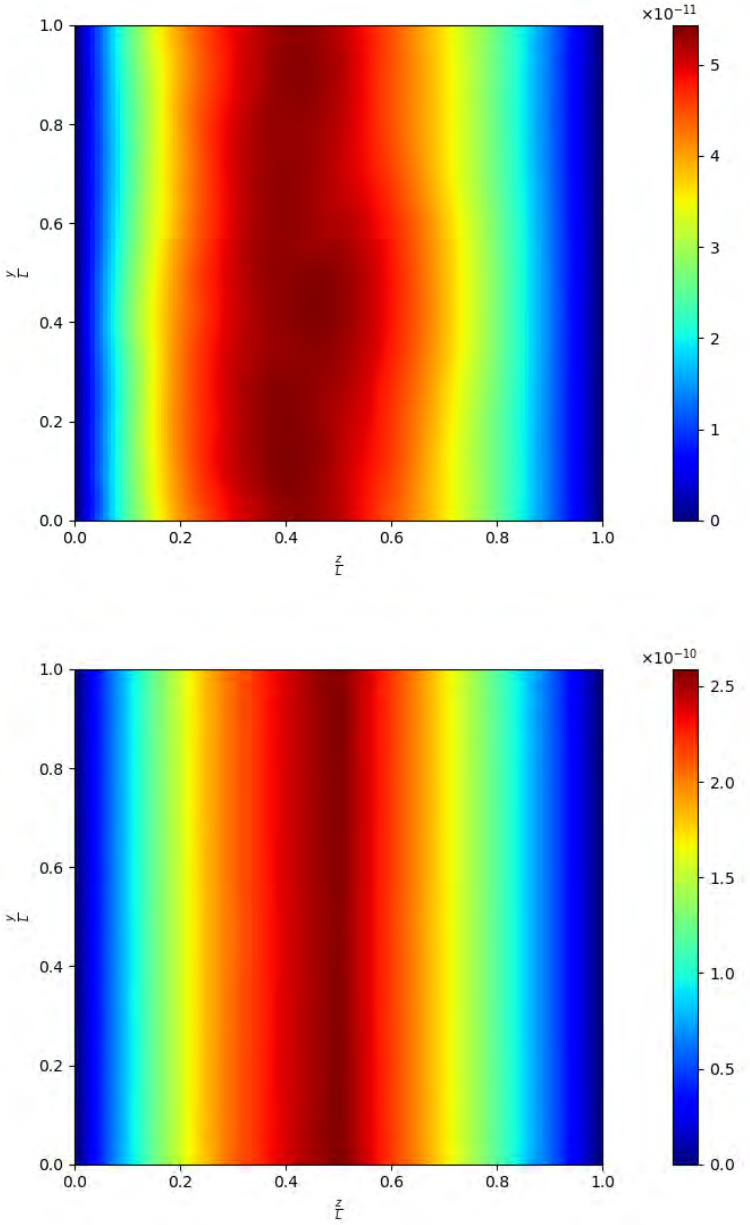

FIGURE A.1: Deviation from exact solution in 2D (absolute value in V): Pardiso direct solver (up), Sparse method (down).

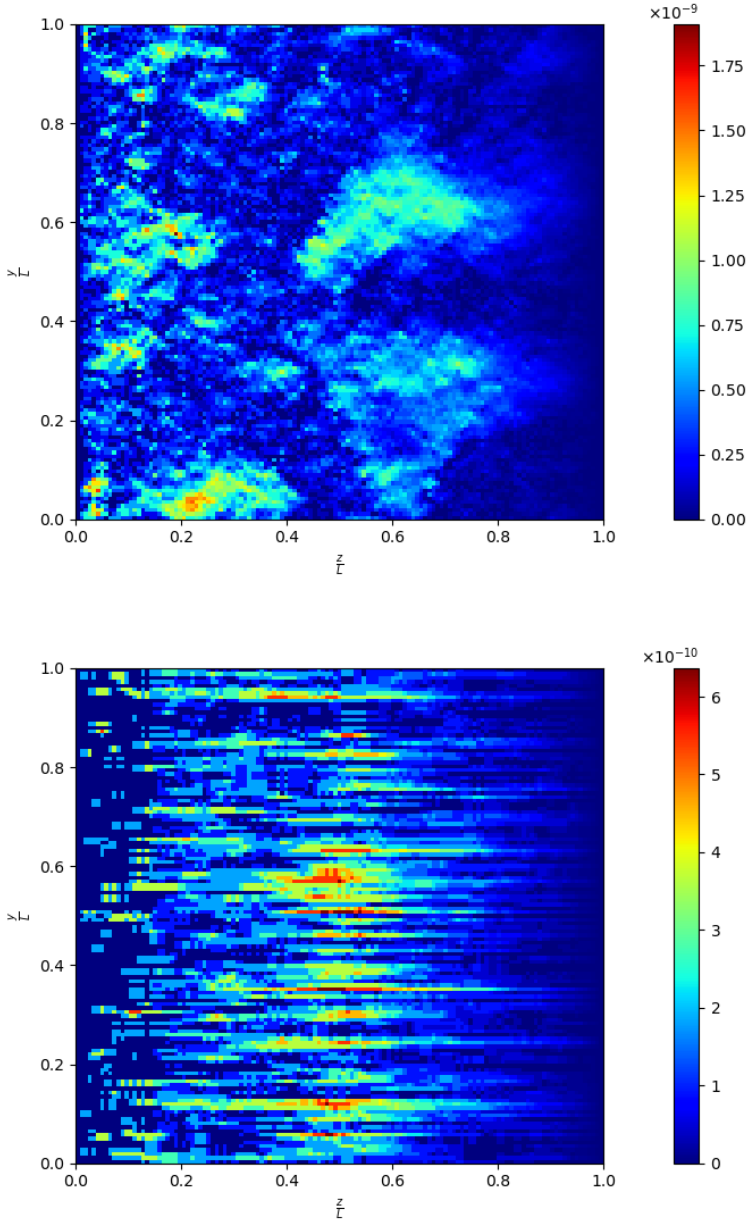

FIGURE A.2: Deviation from exact solution in 2D for y component of electric field (absolute value in V/m): Pardiso direct solver (up), Sparse method (down).

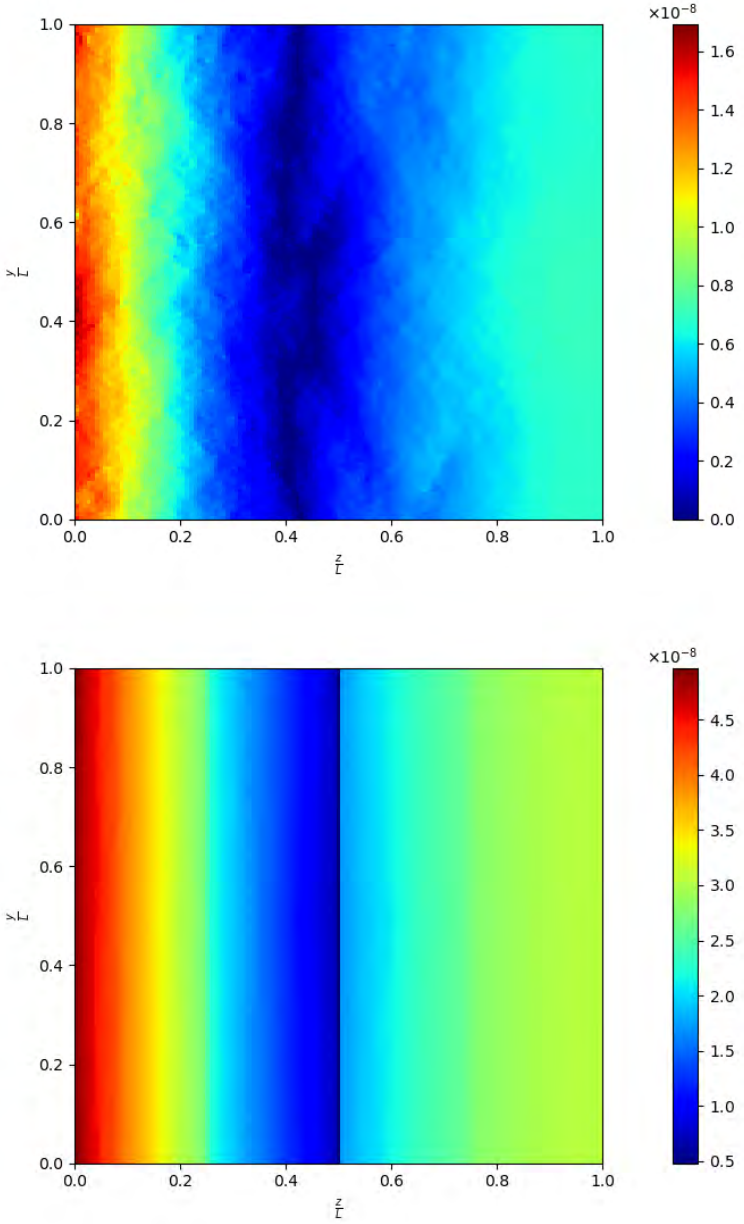

FIGURE A.3: Deviation from exact solution in 2D for z component of electric field (absolute value in V/m): Pardiso direct solver (up), Sparse method (down).

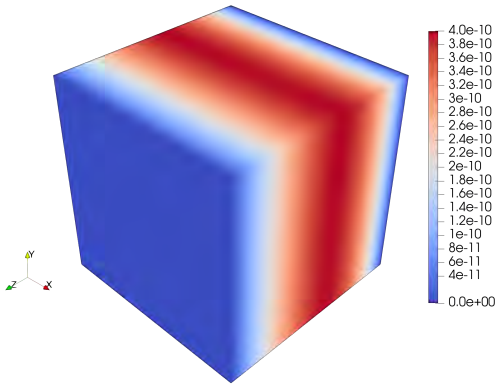

FIGURE A.4: Deviation from exact solution in 3D (absolute value in V): Pardiso direct solver.

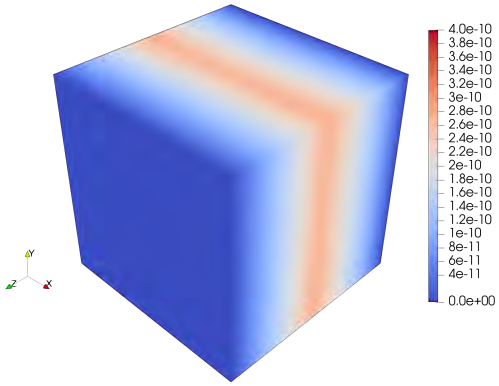

FIGURE A.5: Deviation from exact solution in 3D (absolute value in V): Sparse method.

A.2 Manufactured solutions: spatial oscillation with periodic conditions.

Here we consider $\Phi_{ref}(y,z) = \delta\Phi cos(k_y y)cos(k_z z)$ in 2D and $\Phi_{ref}(x,y,z) = \delta\Phi cos(k_x x)cos(k_y y)cos(k_z z)$ in 3D with $L = 2cm$, $\delta\Phi = 1V$, $k_x = k_y = k_z = \frac{2\pi}{L}$ and 256 cells in each direction. Periodic conditions are set in all directions. Due to full periodic conditions, potential is defined to whithin one constant. For relative error on the potential, we first substract mean value of the potential to the profile. Figures A.6,A.7 and A.8 show relative error from the exact solution of Poisson's equation for the potential, and the y-axis, z-axis components of the electric field in two dimensions.

Profiles of potential obtained for 12 n first modes with $k_x = k_y = k_z = \frac{2\pi n}{L}$ are also shown in figures A.9, A.10 and A.11 for grid levels 7, 8 and 9.

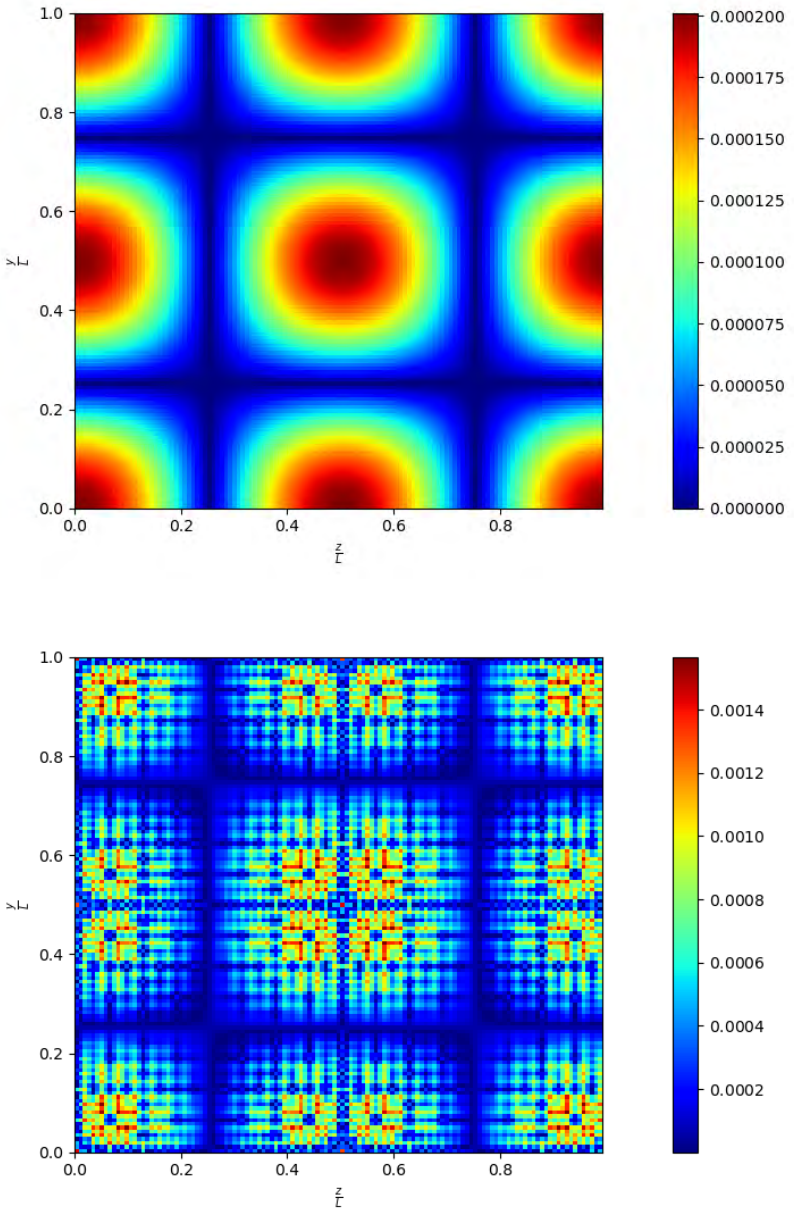

FIGURE A.6: Relative error in 2D for potential: Pardiso direct solver (up), Sparse method (down).

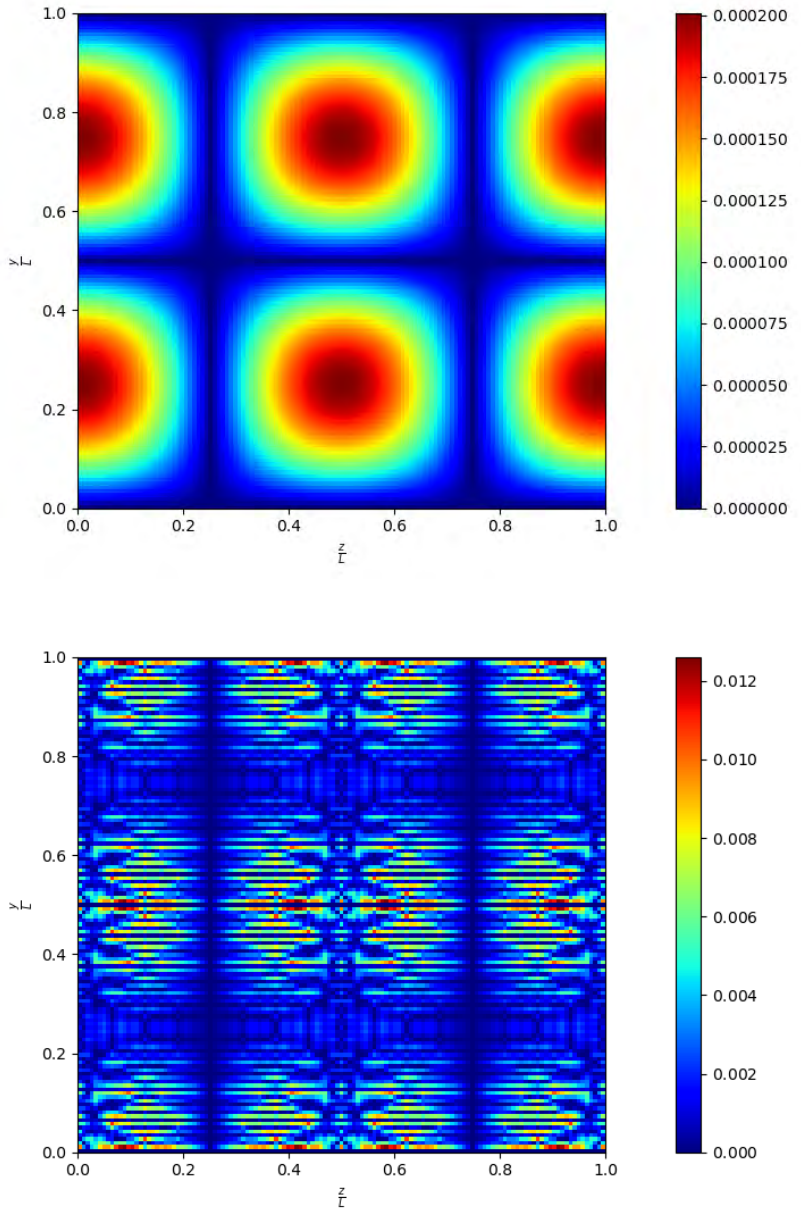

FIGURE A.7: Relative error in 2D for y component of electric field: Pardiso direct solver (up), Sparse method (down).

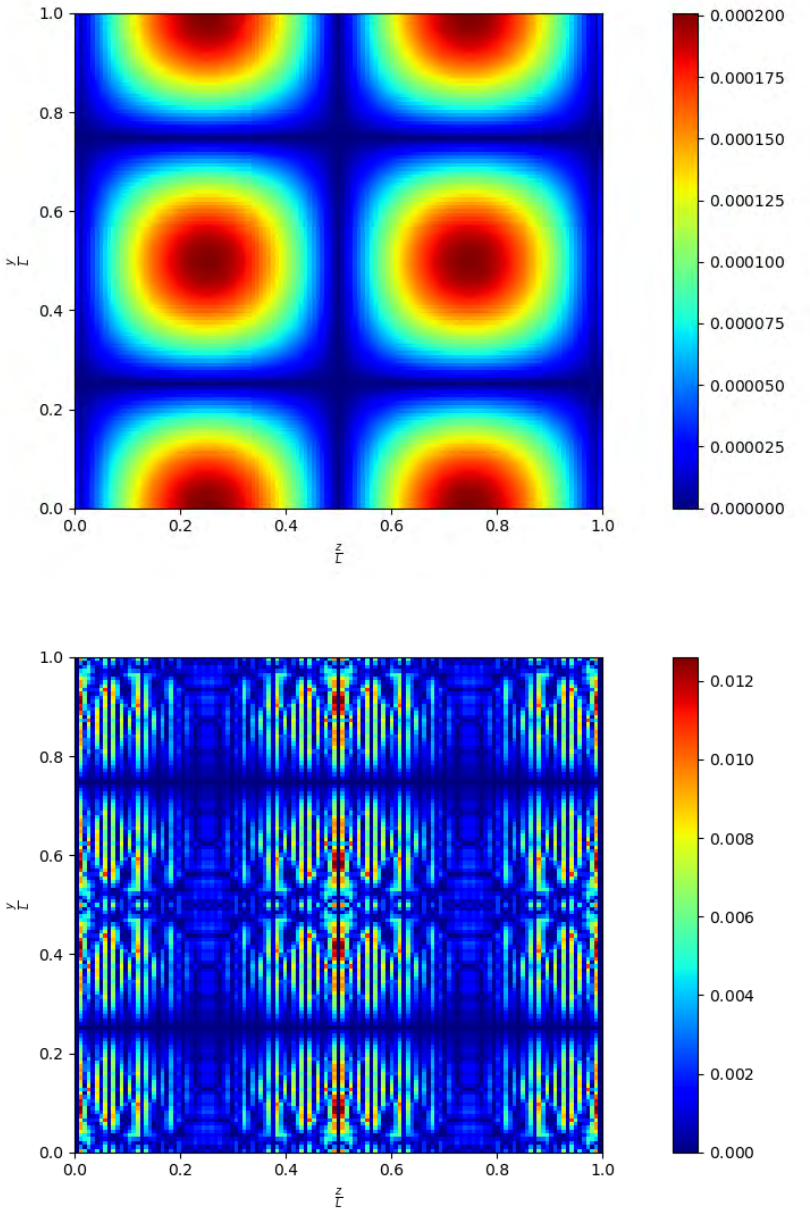

FIGURE A.8: Relative error in 2D for z component of electric field: Pardiso direct solver (up), Sparse method (down).

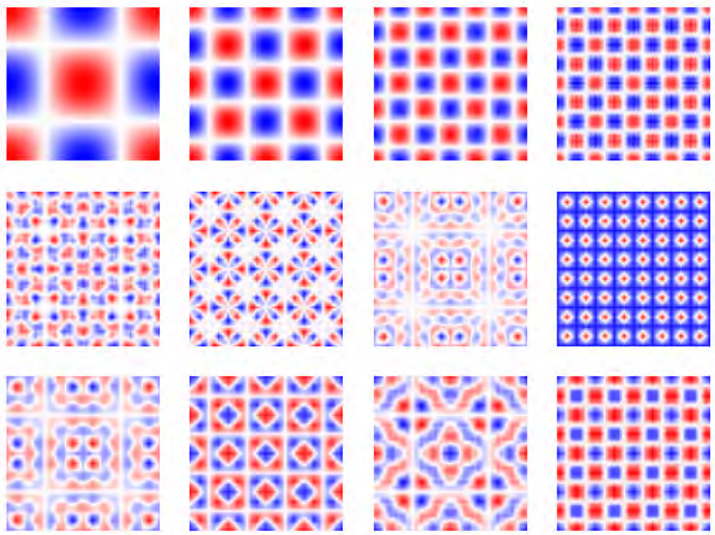

FIGURE A.9: Potential profiles for 12 first modes obtained with Sparse method for a 128^2-cells grid: periodic conditions.

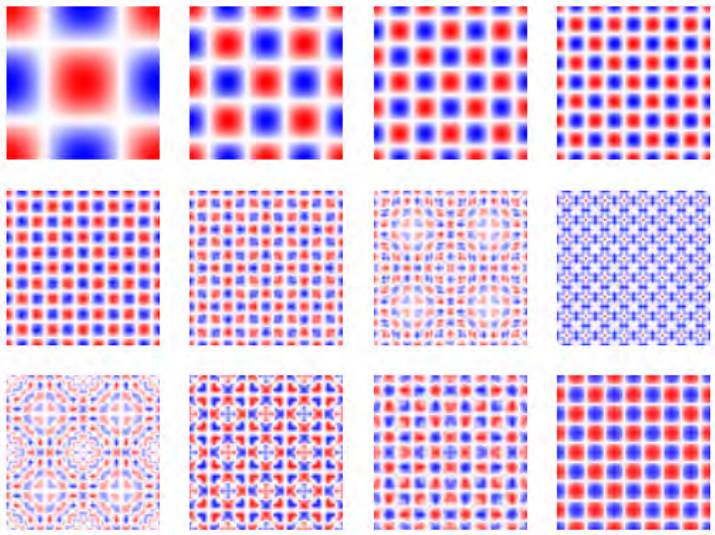

FIGURE A.10: Potential profiles for 12 first modes obtained with Sparse method for a 256^2-cells grid: periodic conditions.

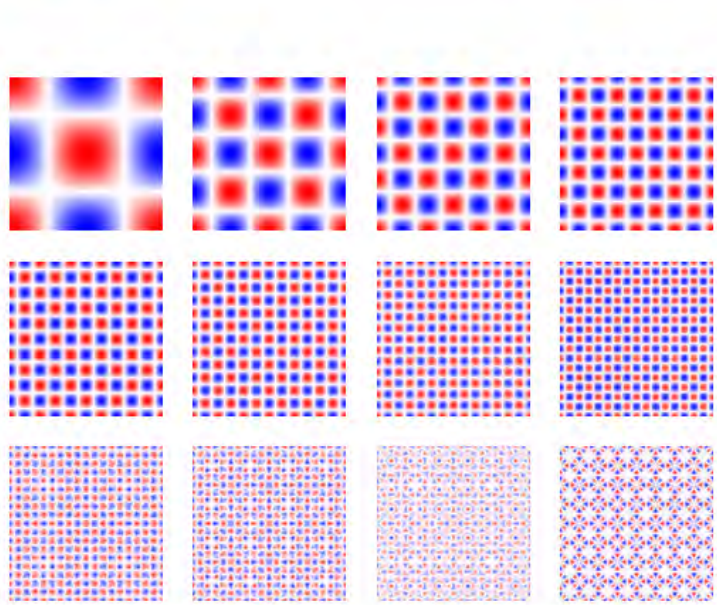

FIGURE A.11: Potential profiles for 12 first modes obtained with Sparse method for a 512^2-cells grid: periodic conditions.

A.3 Manufactured solutions: spatial oscillation with Dirichlet conditions.

Here we consider $\Phi_{ref}(y,z) = \delta\Phi sin(k_y y) sin(k_z z)$ in 2D and $\Phi_{ref}(x,y,z) = \delta\Phi sin(k_x x) sin(k_y y) sin(k_z z)$ in 3D. Profiles of potential obtained for 12 n first modes with $k_x = k_y = k_z = \frac{\pi n}{L}$ are also shown in figures A.12, A.13 and A.14 for grid levels 7, 8 and 9.

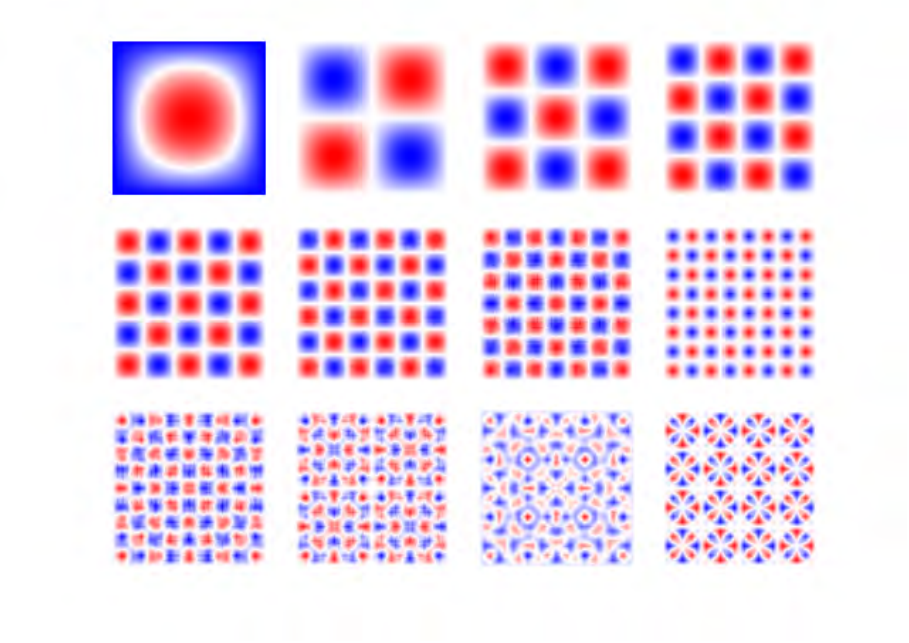

FIGURE A.12: Potential profiles for 12 first modes obtained with Sparse method for a 128^2-cells grid: Dirichlet conditions.

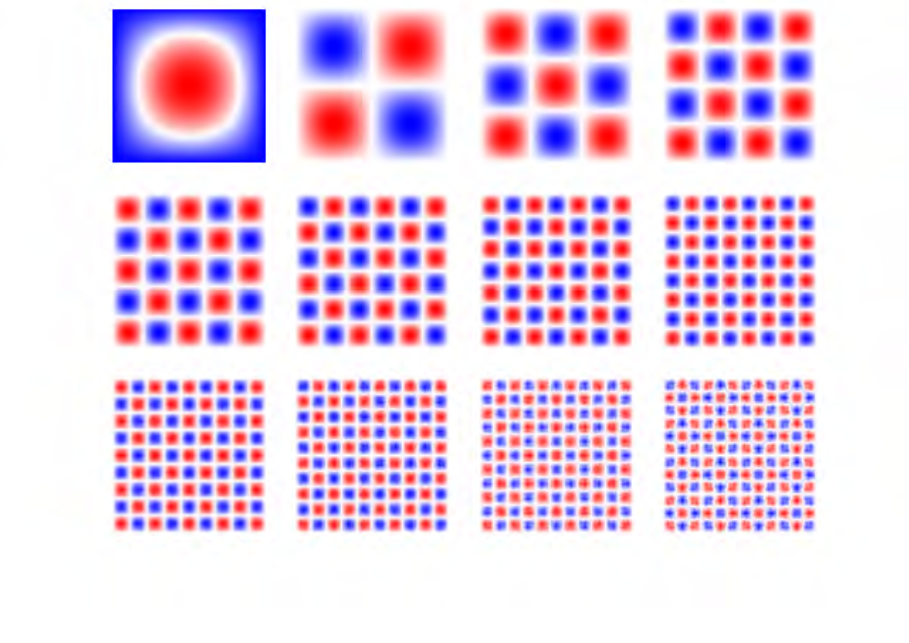

FIGURE A.13: Potential profiles for 12 first modes obtained with Sparse method for a 256^2-cells grid: Dirichlet conditions.

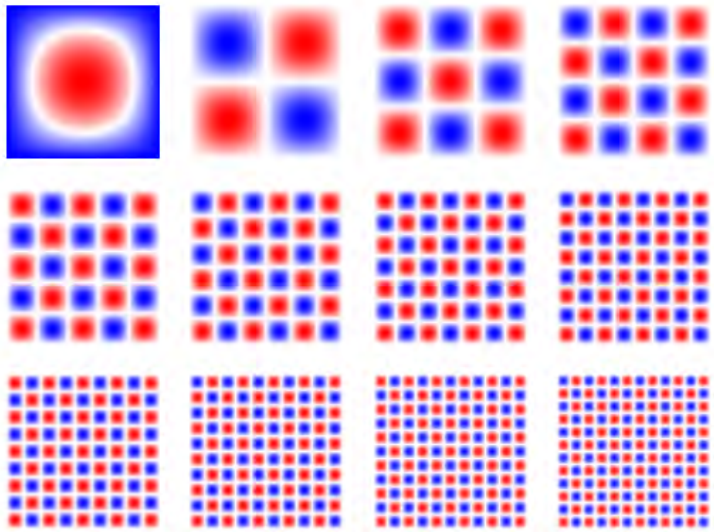

FIGURE A.14: Potential profiles for 12 first modes obtained with Sparse method for a 512^2-cells grid: Dirichlet conditions.

Appendix B

Results in ExB configuration: spatially integrated profiles.

Unidimensional profiles of values of interest with time are computed by integrating in the two other spatial directions. Samples are taken every 100 ns of simulation time. Electron density profiles for all electrons and each population are presented in figures B.1, B.2 and B.3. Axial, azimuthal and radial electron velocity profiles for all electrons are presented respectively in figures B.4, B.5 and B.6.

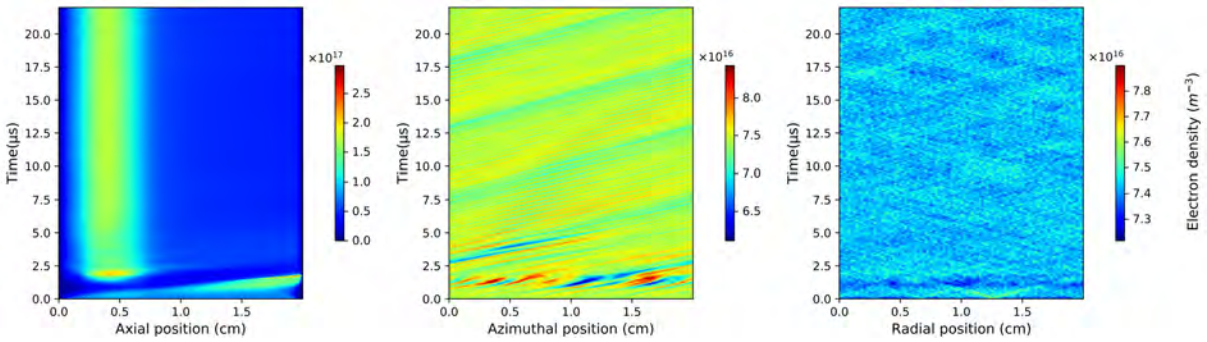

FIGURE B.1: Spatially integrated electron density profiles in each direction: all electrons.

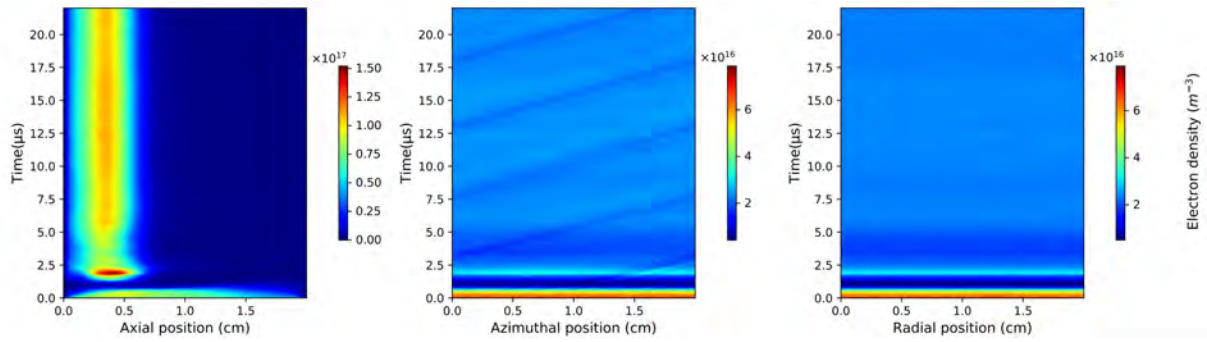

FIGURE B.2: Spatially integrated electron density profiles in each direction: electrons from ionization.

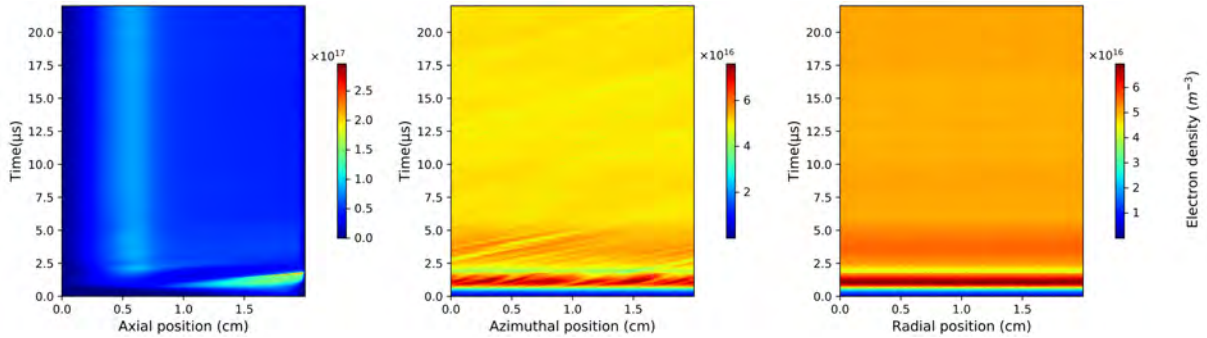

FIGURE B.3: Spatially integrated electron density profiles in each direction: electrons from cathode emission plane.

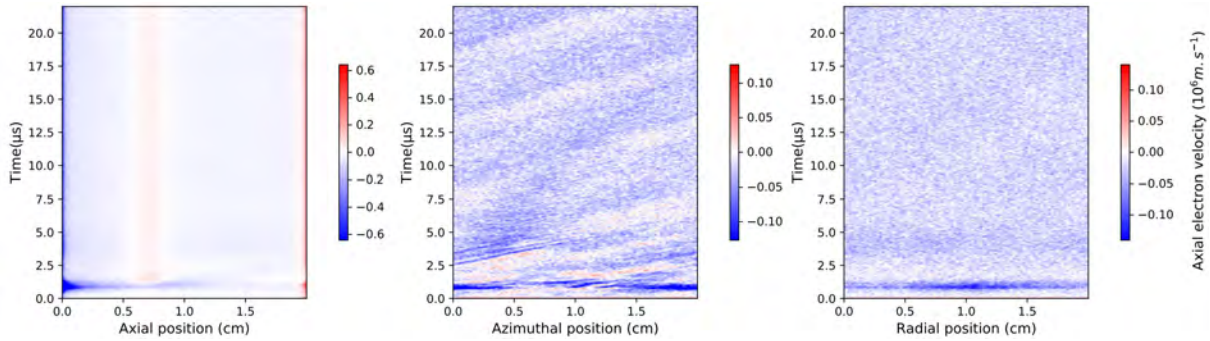

FIGURE B.4: Spatially integrated axial electron velocity profiles in each direction.

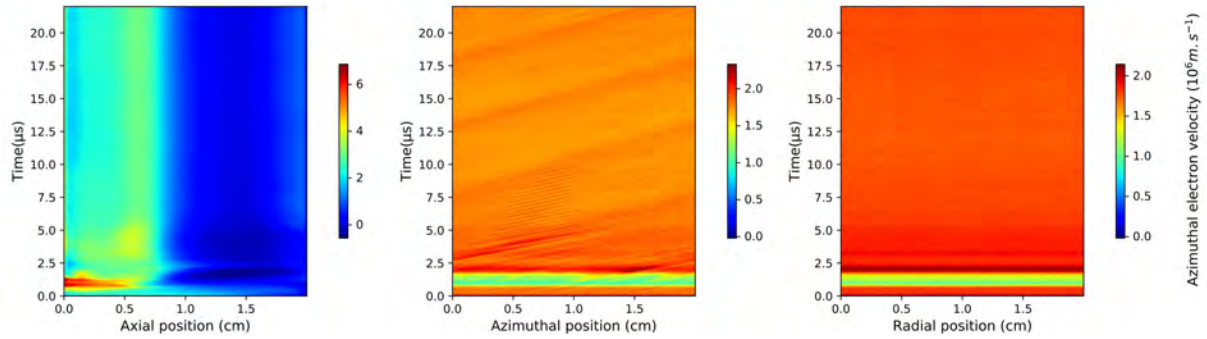

FIGURE B.5: Spatially integrated azimuthal electron velocity profiles in each direction.

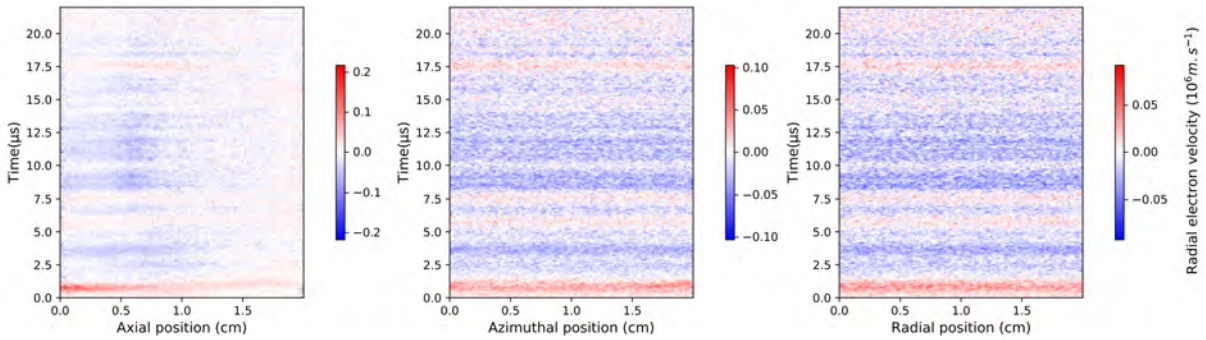

FIGURE B.6: Spatially integrated radial electron velocity profiles in each direction.

Appendix C

Results in ExB configuration: spatially integrated profiles with electron secondary emission.

We present here the same results than appendix B but with the effect of radial absorbent walls and electron secondary emission in the channel part of the simulation domain. Unidimensional profiles of values of interest with time are computed by integrating in the two other spatial directions. Samples are taken every 100 ns of simulation time. Electron density profiles for all electrons and each population are presented in figures C.1, C.2, C.3 and C.4. Axial, azimuthal and radial electron velocity profiles for all electrons are presented respectively in figures C.5, C.6 and C.7. Axial and radial components of electric field profiles are also presented here in figures C.8 and C.9.

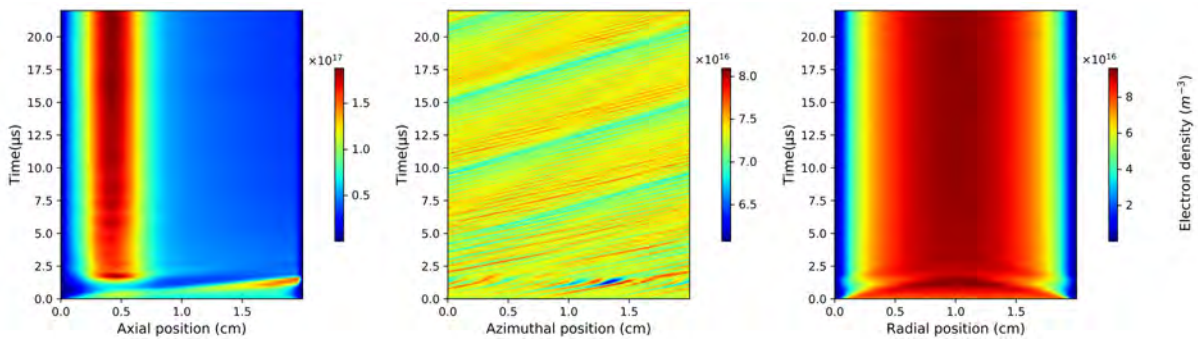

FIGURE C.1: Spatially integrated electron density profiles in each direction: all electrons.

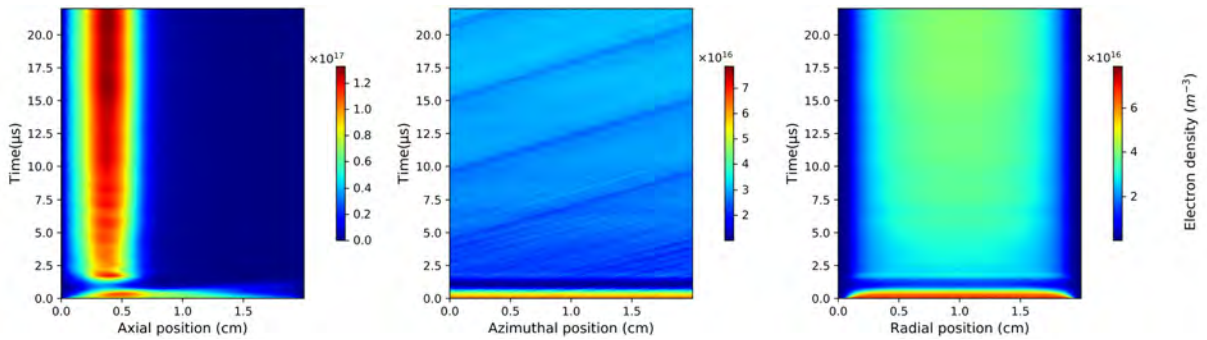

FIGURE C.2: Spatially integrated electron density profiles in each direction: electrons from ionization.

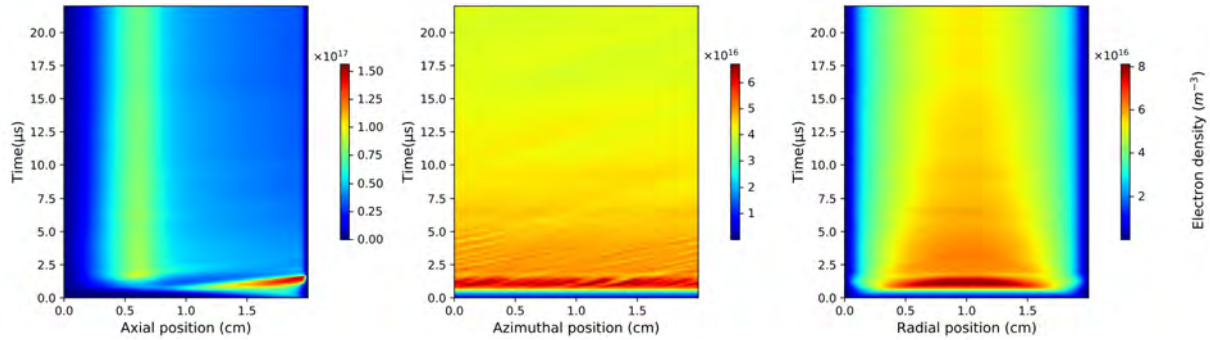

FIGURE C.3: Spatially integrated electron density profiles in each direction: electrons from cathode emission plane.

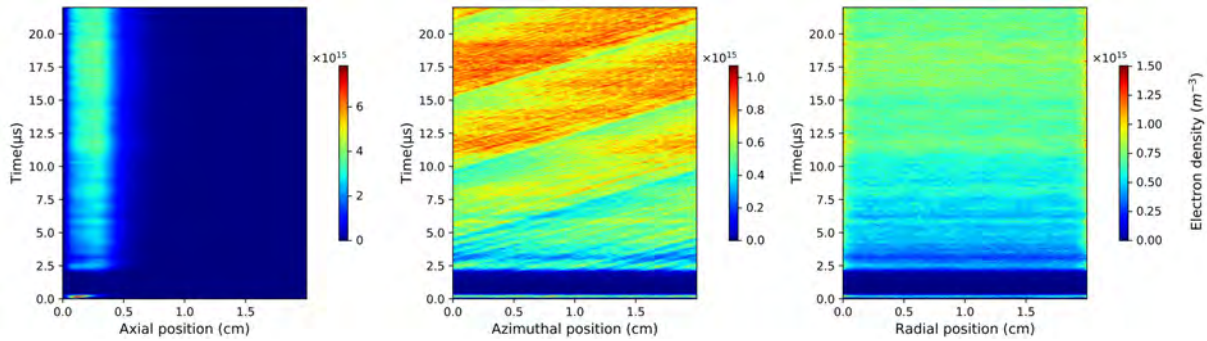

FIGURE C.4: Spatially integrated electron density profiles in each direction: electrons from secondary emission.

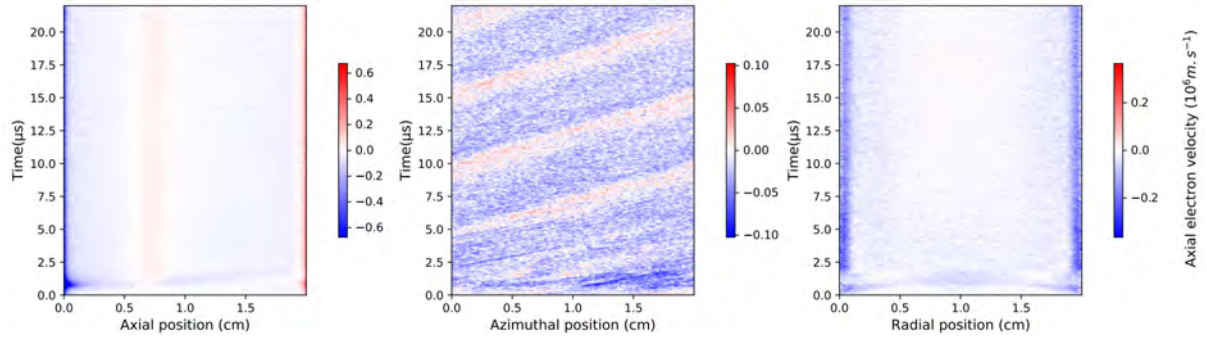

FIGURE C.5: Spatially integrated axial electron velocity profiles in each direction.

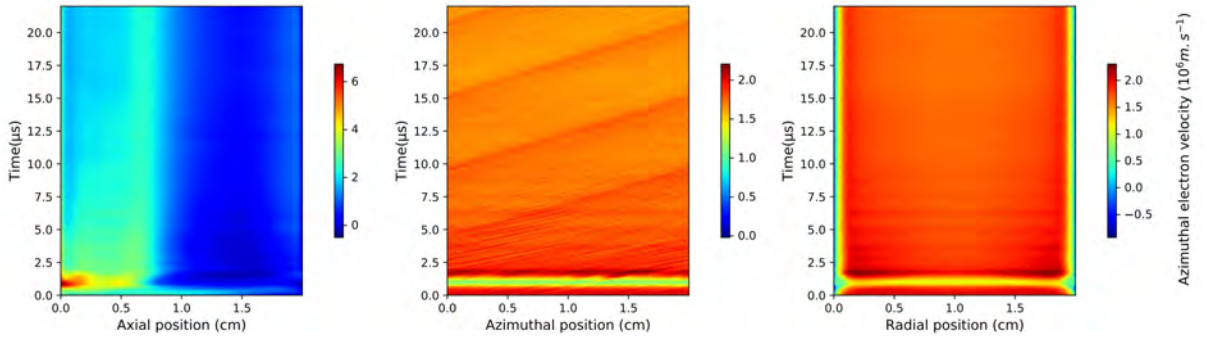

FIGURE C.6: Spatially integrated azimuthal electron velocity profiles in each direction.

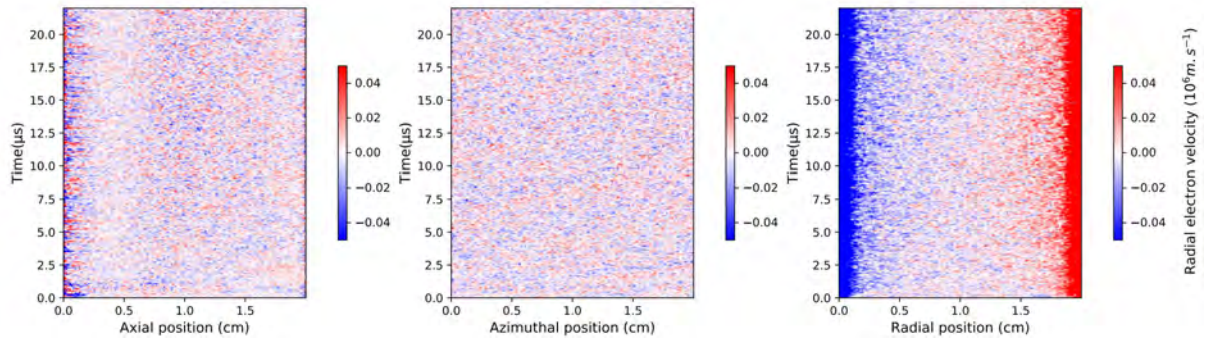

FIGURE C.7: Spatially integrated radial electron velocity profiles in each direction.

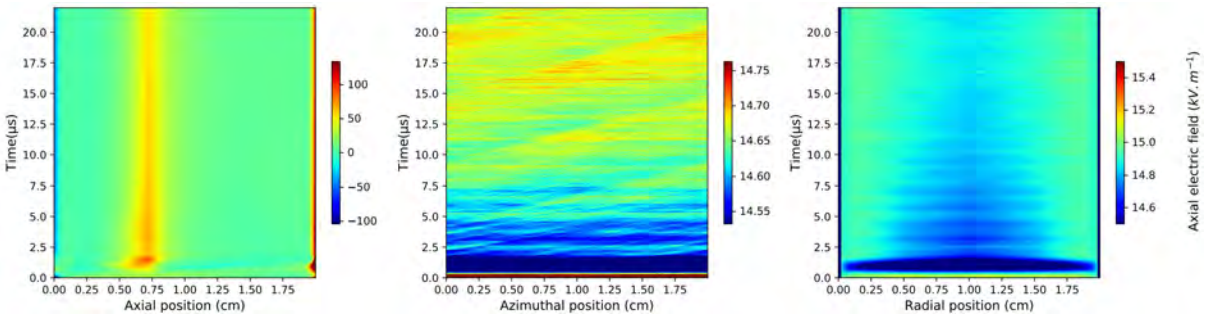

FIGURE C.8: Spatially integrated axial electric field profiles in each direction.

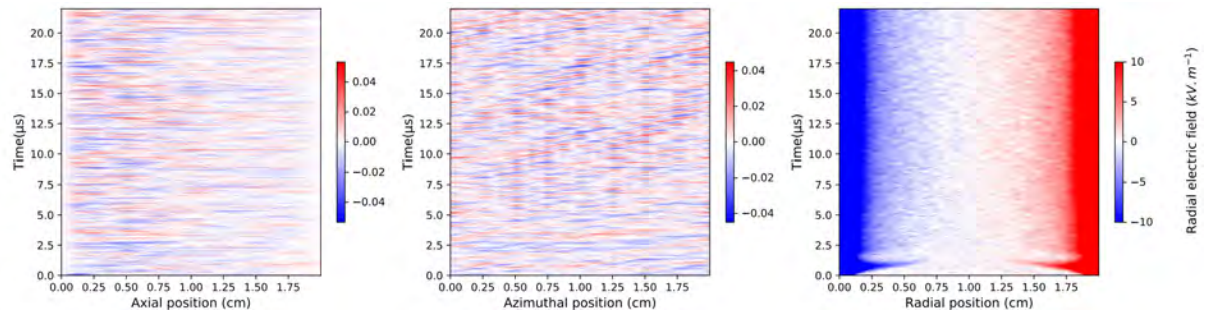

FIGURE C.9: Spatially integrated radial electric field profiles in each direction.

Bibliography

Adam, JC, A Héron, and G Laval (2004). "Study of stationary plasma thrusters using two-dimensional fully kinetic simulations". In: *Physics of Plasmas* 11.1, pp. 295–305.

Adam, JC et al. (2008). "Physics, simulation and diagnostics of Hall effect thrusters". In: *Plasma Physics and Controlled Fusion* 50.12, p. 124041.

Ahrens, James et al. (2005). "36-paraview: An end-user tool for large-data visualization". In: *The visualization handbook* 717, pp. 50038–1.

Amiaud, Anne-Charlotte (2018). "Modélisation du transport électronique et de l accumulation de la charge dans les isolants en couches minces". PhD thesis. Sorbonne université.

Balay, Satish et al. (1998). "PETSc, the portable, extensible toolkit for scientific computation". In: *Argonne National Laboratory* 2.17.

Bassner, H et al. (1994). "Flight test and ground investigation results of the RITA experiment on EURECA". In: *30th Joint Propulsion Conference and Exhibit*, p. 2848.

Birdsall, Charles K and A Bruce Langdon (2004). *Plasma physics via computer simulation*. CRC press.

Boeuf, Jean-Pierre (2017). "Tutorial: Physics and modeling of Hall thrusters". In: *Journal of Applied Physics* 121.1.

Boeuf, Jean-Pierre and Laurent Garrigues (2018). "E× B electron drift instability in Hall thrusters: Particle-in-cell simulations vs. theory". In: *Physics of Plasmas* 25.6.

Boeuf, Jean-Pierre and Andrei Smolyakov (2023). "Physics and instabilities of low-temperature E× B plasmas for spacecraft propulsion and other applications". In: *Physics of Plasmas* 30.5.

Bonnaud, Guy (2019). *Modélisation et simulation des plasmas*. Fédération Sciences Plasmas Fusion.

Bottino, A et al. (2007). "Nonlinear low noise particle-in-cell simulations of electron temperature gradient driven turbulence". In: *Physics of plasmas* 14.1.

Bungartz, Hans-Joachim and Michael Griebel (2004). "Sparse grids". In: *Acta numerica* 13, pp. 147–269.

Charoy, Thomas et al. (2019). "2D axial-azimuthal particle-in-cell benchmark for low-temperature partially magnetized plasmas". In: *Plasma Sources Science and Technology* 28.10, p. 105010.

Choueiri, Edgar Y. (2004). "A Critical History of Electric Propulsion: The First Fifty Years (1906-1956)". In: *American Institute of Aeronautics and Astronautics (AIAA)* AIAA-2004-3334.

Coche, Philippe (2013). "Modélisation cinétique d'un propulseur à effet Hall". PhD thesis. Toulouse 3.

Croes, Vivien (2017). "Modélisation bidimensionnelle de la décharge plasma dans un propulseur de Hall". PhD thesis. Université Paris Saclay (COmUE).

Croes, Vivien et al. (2017). "Study of electron transport in a Hall effect thruster with 2D radial-azimuthal Particle-In-Cell simulations". In: *Proceedings of the 35th International Electric Propulsion Conference. Atlanta, GA*.

Dagum, Leonardo and Ramesh Menon (1998). "OpenMP: an industry standard API for shared-memory programming". In: *Computational Science & Engineering, IEEE* 5.1, pp. 46–55.

Dawson, John M (1983). "Particle simulation of plasmas". In: *Reviews of modern physics* 55.2, p. 403.

Dong, Chuanfei et al. (2019). "Global ten-moment multifluid simulations of the solar wind interaction with mercury: From the planetary conducting core to the dynamic magnetosphere". In: *Geophysical Research Letters* 46.21, pp. 11584–11596.

Donoho, David L and Thomas Pok-Yin Yu (1999). "Deslauriers-Dubuc: ten years after". In: *Spline functions and the theory of wavelets (Montreal, PQ, 1996)* 18, pp. 355–370.

Dubois, Thibault (2023). "Rôle des ondes dans les sources plasmas à basses températures". PhD thesis. École doctorale Énergie, Matériaux, Sciences de la Terre et de l'Univers.

Ducrocq, Alexandre (2006). "Rôle des instabilités électroniques de dérive dans le transport électronique du propulseur à effet Hall." PhD thesis. Ecole Polytechnique X.

Dupree, Thomas H (1982). "Theory of phase-space density holes". In: *The Physics of Fluids* 25.2, pp. 277–289.

Eliasson, Bengt and Padma K Shukla (2006). "Formation and dynamics of coherent structures involving phase-space vortices in plasmas". In: *Physics reports* 422.6, pp. 225–290.

Farin, Gerald, Josef Hoschek, and M-S Kim (2002). *Handbook of computer aided geometric design*. Elsevier.

Fried, Burton D and Samuel D Conte (1961). "II—Properties of Z". In: *The Plasma Dispersion Function*, pp. 2–3.

Fubiani, Gwenaël et al. (2017). "Modeling of plasma transport and negative ion extraction in a magnetized radio-frequency plasma source". In: *New Journal of Physics* 19.1, p. 015002.

Garcke, Jochen (2013). "Sparse grids in a nutshell". In: *Sparse grids and applications*. Springer, pp. 57–80.

Garrigues, L and G Fubiani (2023). "Tutorial: Modeling of the extraction and acceleration of negative ions from plasma sources using particle-based methods". In: *Journal of Applied Physics* 133.4.

Garrigues, Laurent, G Fubiani, and Jean-Pierre Boeuf (2016). "Appropriate use of the particle-in-cell method in low temperature plasmas: Application to the simulation of negative ion extraction". In: *Journal of Applied Physics* 120.21.

Garrigues, Laurent, S Mazouffre, and G Bourgeois (2012). "Computed versus measured ion velocity distribution functions in a Hall effect thruster". In: *Journal of Applied Physics* 111.11.

Garrigues, Laurent et al. (2021a). "Application of sparse grid combination techniques to low temperature plasmas particle-in-cell simulations. I. Capacitively coupled radio frequency discharges". In: *Journal of Applied Physics* 129.15.

Garrigues, Laurent et al. (2021b). "Application of sparse grid combination techniques to low temperature plasmas Particle-In-Cell simulations. II. Electron drift instability in a Hall thruster". In: *Journal of Applied Physics* 129.15.

Garrigues, Laurent et al. (2024). "Acceleration of Particle-In-Cell Simulations using Sparse Grid Algorithms. II. Application to Partially Magnetized Low Temperature Plasma". In: *LAPLACE, Université de Toulouse, CNRS, INPT, UPS, Toulouse, France*.

Griebel, Michael (1998). "Adaptive sparse grid multilevel methods for elliptic PDEs based on finite differences". In: *Computing* 61, pp. 151–179.

Griebel, Michael et al. (1992). "The combination technique for parallel sparse-grid-preconditioning or-solution of PDE's on workstation networks". In: *International Conference on Vector and Parallel Processing*. Springer, pp. 217–228.

Guillet, Clément (2023). "Approche sur grilles parcimonieuses pour accélérer la méthode Particle-In-Cell". PhD thesis. Doctorat de l'Université de Toulouse.

Guo, Wei and Yingda Cheng (2016). "A sparse grid discontinuous Galerkin method for high-dimensional transport equations and its application to kinetic simulations". In: *SIAM Journal on Scientific Computing* 38.6, A3381–A3409.

Hakim, Ammar H (2008). "Extended MHD modelling with the ten-moment equations". In: *Journal of Fusion Energy* 27, pp. 36–43.

Hara, Kentaro (2019). "An overview of discharge plasma modeling for Hall effect thrusters". In: *Plasma Sources Science and Technology* 28.4, p. 044001.

Heene, Mario (2018). "A massively parallel combination technique for the solution of high-dimensional PDEs". PhD thesis. Universität Stuttgart.

Hofer, Richard R, Alec D Gallimore, and David Jacobson (2003). "Recent results from internal and very-near-field plasma diagnostics of a high specific impulse Hall thruster". In: *28th International Electric Propulsion Conference*. NASA/CR-2003-212604.

Hutchinson, Ian Horner (2017). "Electron holes in phase space: What they are and why they matter". In: *Physics of Plasmas* 24.5.

Inguimbert, C et al. (2017). "An analytical model for secondary electron emission". In: *MULCOPIM*.

Jackson, John David (1999). *Classical electrodynamics*.

Jacob, Riko (2014). "Efficient regular sparse grid hierarchization by a dynamic memory layout". In: *Sparse Grids and Applications-Munich 2012*. Springer, pp. 195–219.

Janes, GS and RS Lowder (1966). "Anomalous electron diffusion and ion acceleration in a low-density plasma". In: *The Physics of Fluids* 9.6, pp. 1115–1123.

Joncquières, Valentin (2019). "Modélisation et simulation numérique des moteurs à effet Hall". PhD thesis.

Kaganovich, Igor D et al. (2020). "Physics of E$\times$ B discharges relevant to plasma propulsion and similar technologies". In: *Physics of Plasmas* 27.12.

KERSLAKE, W and L IGNACZAK (1979). "SERT II 1979 extended flight thruster system performance". In: *14th International Electric Propulsion Conference*, p. 2063.

Lafleur, Trevor, SD Baalrud, and Pascal Chabert (2016). "Theory for the anomalous electron transport in Hall effect thrusters. II. Kinetic model". In: *Physics of Plasmas* 23.5.

Lago, Rafael et al. (2020). "EXAHD: A massively parallel fault tolerant sparse grid approach for high-dimensional turbulent plasma simulations". In: *Software for Exascale Computing-SPPEXA 2016-2019*. Springer International Publishing, pp. 301–329.

Lapenta, Giovanni (2012). "Particle simulations of space weather". In: *Journal of Computational Physics* 231.3, pp. 795–821.

Levchenko, I et al. (2020). "Perspectives, frontiers, and new horizons for plasma-based space electric propulsion". In: *Physics of Plasmas* 27.2.

Levchenko, Igor et al. (2018). "Space micropropulsion systems for Cubesats and small satellites: From proximate targets to furthermost frontiers". In: *Applied Physics Reviews* 5.1.

Lieberman, Michael A and Allan J Lichtenberg (1994). "Principles of plasma discharges and materials processing". In: *MRS Bulletin* 30.12, pp. 899–901.

Mazières, V et al. (2022). "Broadband (kHz–GHz) characterization of instabilities in Hall thruster inside a metallic vacuum chamber". In: *Physics of Plasmas* 29.7.

McDonald, MS and AD Gallimore (2009). "Cathode position and orientation effects on cathode coupling in a 6-kW Hall thruster". In: *31st International Electric Propulsion Conference*. Vol. 113.

Melzani, Mickaël (2017). "De l'équation cinétique de Vlasov aux équations fluides dans un plasma dilué". In: *Private typescript*.

Message Passing Interface Forum (June 2021). *MPI: A Message-Passing Interface Standard Version 4.0*. URL: https://www.mpi-forum.org/docs/mpi-4.0/mpi40-report.pdf.

Morozov, Alexander Yu, Andrey A Zhuravlev, and Dmitry L Reviznikov (2021). "Sparse grid adaptive interpolation in problems of modeling dynamic systems with interval parameters". In: *Mathematics* 9.4, p. 298.

Muralikrishnan, Sriramkrishnan et al. (2021). "Sparse grid-based adaptive noise reduction strategy for particle-in-cell schemes". In: *Journal of Computational Physics: X* 11, p. 100094.

Perez Luna, Jaime (2008). "Modélisation et diagnostics d'un propulseur à effet Hall". PhD thesis. Université de Toulouse, Université Toulouse III-Paul Sabatier.

Petronio, Federico et al. (2021). "Conditions of appearance and dynamics of the modified two-stream instability in E× B discharges". In: *Physics of Plasmas* 28.4.

Pflüger, Dirk et al. (2014). "EXAHD: an exa-scalable two-level sparse grid approach for higher-dimensional problems in plasma physics and beyond". In: *Euro-Par 2014: Parallel Processing Workshops: Euro-Par 2014 International Workshops, Porto, Portugal, August 25-26, 2014, Revised Selected Papers, Part II 20*. Springer, pp. 565–576.

Pflüger, Dirk Michael (2010). "Spatially adaptive sparse grids for high-dimensional problems". PhD thesis. Technische Universität München.

Pollinger, Theresa et al. (2023). "A stable and mass-conserving sparse grid combination technique with biorthogonal hierarchical basis functions for kinetic simulations". In: *Journal of Computational Physics* 491, p. 112338.

Pommier, David (2008). "Méthodes numériques sur des grilles sparse appliquées à l'évaluation d'options en finance". PhD thesis. Paris 6.

Rax, Jean-Marcel (2005). *Physique des plasmas: Cours et applications*. Dunod.

Ricketson, Lee F and Antoine J Cerfon (2016). "Sparse grid techniques for particle-in-cell schemes". In: *Plasma Physics and Controlled Fusion* 59.2, p. 024002.

Schamel, Hans (1986). "Electron holes, ion holes and double layers: Electrostatic phase space structures in theory and experiment". In: *Physics reports* 140.3, pp. 161–191.

Schenk, Olaf, Klaus Gärtner, and Wolfgang Fichtner (2000). "Efficient sparse LU factorization with left-right looking strategy on shared memory multiprocessors". In: *BIT Numerical Mathematics* 40, pp. 158–176.

Smolyak, Sergei Abramovich (1963). "Quadrature and interpolation formulas for tensor products of certain classes of functions". In: *Doklady Akademii Nauk*. Vol. 148. 5. Russian Academy of Sciences, pp. 1042–1045.

Sommerville, Jason and Lyon King (2007). "Effect of cathode position on Hall-effect thruster performance and cathode coupling voltage". In: *43rd AIAA/ASME/SAE/ASEE Joint Propulsion Conference & Exhibit*, p. 5174.

Straalen, B Van (2017). "A 4th-Order Particle-in-Cell Method with Phase-Space Remapping for the Vlasov–Poisson Equation". In: *SIAM Journal on Scientific Computing* 39.3, B467–B485.

Taccogna, F and Laurent Garrigues (2019). "Latest progress in Hall thrusters plasma modelling". In: *Reviews of Modern Plasma Physics* 3, pp. 1–63.

Tavant, Antoine (2019). "Study of the plasma/wall interaction and erosion on a plasma thruster of low power." PhD thesis. Université Paris Saclay (COmUE).

Tavassoli, Arash et al. (2023). "The electron cyclotron drift instability: A comparison of particle-in-cell and continuum Vlasov simulations". In: *Physics of Plasmas* 30.3.

Torvén, S, PJ Palmadesso, and K Papadopoulos (1979). "Wave Instabilities in Space Plasmas". In: *Palmadesso and Papadoulos(eds)* 109.

Tranquilli, Paul, Lee Ricketson, and Luis Chacón (2022). "A deterministic verification strategy for electrostatic particle-in-cell algorithms in arbitrary spatial dimensions using the method of manufactured solutions". In: *Journal of Computational Physics* 448, p. 110751.

Tsikata, Sedina et al. (2010). "Three-dimensional structure of electron density fluctuations in the Hall thruster plasma: E$\times$ B mode". In: *Physics of Plasmas* 17.11.

Tsiolkovsky, Konstantin Eduardovich (1903). "Exploration of the universe with reaction machines". In: *The Science Review* 5.

Turner, Miles M et al. (2013). "Simulation benchmarks for low-pressure plasmas: Capacitive discharges". In: *Physics of Plasmas* 20.1.

Vay, J-L et al. (2016). "Recent advances in high-performance modeling of plasma-based acceleration using the full PIC method". In: *Nuclear Instruments and Methods in Physics Research Section A: Accelerators, Spectrometers, Detectors and Associated Equipment* 829, pp. 353–357.

Vilamot, Raphaël (2012). "Optimisation de la configuration magnétique d'un propulseur à effet Hall par résolution du problème magnétostatique inverse". PhD thesis.

Villafana, Willca (2021). "Numerical Particle-In-Cell studies of Hall thrusters using unstructured grids". PhD thesis.

Villemant, M et al. (2017). "Electron emission model for hall thruster plasma modelling". In: *Proceedings of the 35th International Electric Propulsion Conference. Atlanta, GA*.

Villemant, Marc (2018). "Modélisation et caractérisation expérimentale de l'influence de l'émission électronique sur le fonctionnement des propulseurs à courant de Hall". PhD thesis. Institut supérieur de l'Aéronautique et de l'Espace (ISAE).

Vincent, Benjamin, Sedina Tsikata, and Stéphane Mazouffre (2020). "Incoherent Thomson scattering measurements of electron properties in a conventional and magnetically-shielded Hall thruster". In: *Plasma Sources Science and Technology* 29.3, p. 035015.

Wang, Liang et al. (2022). "Electron cyclotron drift instability and anomalous transport: two-fluid moment theory and modeling". In: *Plasma Sources Science and Technology* 31.10, p. 105001.

Weiman, Carl FR and George Chaikin (1979). "Logarithmic spiral grids for image processing and display". In: *Computer Graphics and Image Processing* 11.3, pp. 197–226.

Wirz, Richard E. et al. (2022). "Predictive Engineering Model for Life and Performance Assessment of High-Power Electric Propulsion Systems". In: *37th International Electric Propulsion Conference*. IEPC-2022-410.

Yoshikawa, S and DJ Rose (1962). "Anomalous diffusion of a plasma across a magnetic field". In: *The Physics of Fluids* 5.3, pp. 334–340.

Zenger, Christoph and W Hackbusch (1991). "Sparse grids". In: *Proceedings of the Research Workshop of the Israel Science Foundation on Multiscale Phenomenon, Modelling and Computation*, p. 86.

Titre : Transport électronique et émission secondaire électronique dans un propulseur de Hall

Mots clés : Simulation numérique, Grilles parcimonieuses, Particle-in-cell, Méthode d'accélération, Émission secondaire électronique, Propulsion pour satellites

Résumé : L'essor des activités spatiales pour satellite a permis le développement de nombreuses technologies de propulseurs électriques. Parmi elles, le propulseur à courant de Hall connaît un intérêt grandissant de par son coût, ses caractéristiques de poussée et d'impulsion spécifique. Si cette technologie existe depuis au moins cinquante ans, il n'en demeure pas moins que simuler et comprendre son fonctionnement reste hors de portée. La dynamique des particules chargées en configuration de champs croisés ExB est riche d'instabilités dont le rôle dans le fonctionnement du propulseur n'a pas atteint un consensus scientifique. Cette thèse propose de reprendre l'approche appelée "Particle-in-cell"(PIC) qui consiste à suivre les trajectoires individuelles de particules chargées dans l'espace des phases soumises à un champ électrique solution de l'équation de Poisson et calculé sur une grille de calcul. Cette méthode numérique dans sa version explicite doit répondre à des contraintes de pas d'espace et de temps qui se durcissent avec l'augmentation de la densité électronique. En trois dimensions de l'espace, l'algorithme classique PIC ne peut être appliqué aux conditions réelles d'un propulseur. Une approche récente permet de contourner ce problème au moyen de méthodes numériques de grilles parcimonieuses, appelée "Sparse-PIC". Elle repose sur le principe d'annulation des erreurs de grille lorsque l'on combine des sous-grilles de maillage grossier afin de représenter la solution sur la grille de maillage fin. Les performances de calcul obtenues avec le code implémenté pendant la thèse ont permis d'appliquer cette nouvelle approche à une configuration de champs croisés ExB dans un modèle réduit de propulseur de Hall.

Title: Electronic transport and secondary emission in a Hall thruster

Key words: Numerical simulation, Sparse grids, Particle-in-cell, Accelerating methods, Electronic secondary emission, Satellite propulsion

Abstract: The boom in satellite space activities has led to the development of numerous electric thruster technologies. Among these, the Hall current thruster is attracting growing interest due to its cost, thrust and specific impulse characteristics. Although this technology has been around for at least fifty years, simulating and understanding its operation remains out of reach. The dynamics of charged particles in the ExB cross-field configuration are rich in instabilities whose role in thruster operation has not yet reached scientific consensus. In this thesis, we propose to take up the "Particle-in-cell" (PIC) approach, which consists in tracking the individual trajectories of charged particles in phase space subjected to an electric field that is a solution of Poisson's equation and calculated on a computational grid. In its explicit version, this numerical method has to meet space and time step constraints that harden with increasing electron density. In three spatial dimensions, the classical PIC algorithm cannot be applied to real thruster conditions. A recent approach, called "Sparse-PIC", circumvents this problem by means of sparse grid methods. It is based on the principle of cancelling grid errors when combining coarse-mesh sub-grids to represent the solution on the fine-mesh grid. The computational performance obtained with the code implemented during the thesis has enabled us to apply this new approach to an ExB cross-field configuration in a reduced Hall thruster model.